Nonequilibrium dynamics in lattice gauge theories: disorder-free localization and string breaking

Dissertation
zur Erlangung des akademischen Grades
Doctor rerum naturalium (Dr. rer. nat.)

vorgelegt
der Fakultät Physik
Bereich Mathemathik und Naturwissenschaften
der Technischen Universität Dresden
von
Roberto Verdel Aranda
geboren am 21.10.1991 in Teloloapan, Mexiko

Max-Planck-Institut für Physik komplexer Systeme
Dresden, 2021

Wissenschaftlicher Betreuer:
Prof. Dr. Markus Heyl und Prof. Dr. Roderich Moessner

Eingereicht am 27.09.2021

Gutachter:
1. Prof. Dr. Roderich Moessner
2. Prof. Dr. Simone Montangero
3. Prof. Dr. Jan Carl Budich

Verteidigt am 11.02.2022

A mis padres

Acknowledgments

First of all, I would like to express my deepest gratitude to my supervisor Markus Heyl for his support, guidance, patience and kindness. I also thank him for always being available for scientific discussions related to my projects and beyond. Working with him has been a particularly enriching and enjoyable experience not only because of his broad knowledge and remarkable physical intuition, but also thanks to his great qualities as a person. I will always be grateful to Markus for all the things that he taught me and for sharing with me his enthusiasm for doing research.

The work presented in this thesis would not have been possible without the multiple efforts and insights of several people, with whom I had the pleasure to collaborate. In this respect, I am very grateful to Alexey V. Gorshkov, Yi-Ping Huang, Peter Karpov, Fangli Liu, Markus Schmitt and Seth Withsitt. Further, I extend my gratitude to Heiko Burau, Luis Colmenarez and Peter Karpov for proofreading several parts of this manuscript and for their valuable comments. My special thanks also go to Robin Schäfer and Pauline Glaß for kindly helping me to translate my Abstract into German.

Many thanks to all the members of our group as well as other members of the MPIPKS for all the interesting and cheerful conversations during the past years. In addition to those already mentioned above, here I would like to include Debasish Banerjee, Adrien Bolens, Nilotpal Chakraborty, Mani Jha, Reyhaneh Khasseh, Arkadiusz Kosior, Tiago Mendes, Daniele Trapin and Guo-Yi Zhu. I should also like to acknowledge the enlightening discussions with Guo-Yi on an ongoing project related to the work presented in this thesis.

I would like to thank Roderich Moessner for his support as director of the Condensed Matter Division at the MPIPKS. In particular, I am very grateful to him for allowing me to attend several summer schools and conferences, which played an important role in my doctoral studies. Many thanks as well to the IT department, the administrative staff and the Visitors Program of the MPIPKS for their kind help during these years.

My time in Dresden would not have been the same without all the nice people I met there. Hence, I also want to express my heartfelt gratitude to Adolfo, Ana, Robin, Omar, Piotr, Alberto, Amanda, Stefano, Charlie, Luis, Pauline, Manuel, Dora, Fabrizio, Christian, Ronnie, Ben and many others. Many thanks to all of them for their support, friendship and good times! Outside Dresden, my warm thanks go to my good friend *Fabri* and his family, who always make me feel at home whenever I visit them. I am also grateful to all my friends back in Mexico, who have shown me their support in all these years.

Finalmente, agradezco a mi familia por su apoyo incondicional, sin el cual me hubiera sido imposible haber llegado hasta aquí. En particular, quiero agradecer profundamente a mis padres por su gran amor, enseñanzas y por todos los sacrificios que han hecho para que yo pudiera alcanzar mis metas. También agradezco especialmente a mis hermanas, Erandi, Karina y Ariadna, por su constante apoyo y motivación. ¡Muchas gracias por estar tan cerca de mí aun con los miles de kilómetros de distancia que nos separan!

Abstract

Lattice gauge theories are crucial for our understanding of many physical phenomena ranging from fundamental particle interactions in high-energy physics to frustration and topological order in condensed matter. Hence, many equilibrium aspects of these theories have been studied intensively over the past decades. Recent developments, however, have shown that the study of nonequilibrium dynamics in lattice gauge theories also provides a very fertile ground for interesting phenomena.

This thesis is devoted to the study of two particular dynamical processes in lattice gauge theories and related quantum spin models. First, we show that an interacting two-dimensional lattice gauge theory can exhibit disorder-free localization: a mechanism for ergodicity breaking due to local constraints imposed by gauge invariance. This result is particularly remarkable as the stability in two dimensions of the more conventional (disorder-induced) many-body localization is still debated. Concretely, we show this type of nonergodic behavior in the quantum link model. Our central result is based on a bound on the localization-delocalization transition, which is established through a concomitant classical percolation problem. Further, we develop a numerical method dubbed "variational classical networks", to study the quantum dynamics in this system. This technique provides an efficient and perturbatively controlled representation of the wave function in terms of networks of classical spins akin to artificial neural networks. This allows us to identify distinguishing transport properties in the localized and ergodic phases, respectively.

In the second problem, we study the dynamics of string breaking, a key process in confining gauge theories, where a string connecting two charges decays due to the creation of new particle-antiparticle pairs. Our main result here is that string breaking can also be observed in quantum Ising chains, in which domain walls get confined either by a symmetry-breaking field or by long-range interactions. We identify, in general, two distinct stages in this process. While at the beginning the initial charges remain stable, the string can exhibit complex dynamics with strong quantum correlations. We provide an effective description of this string motion, and find that it can be highly constrained. In the second stage, the string finally breaks at a timescale that depends sensitively on the initial separation of domain walls. We observe that the second stage can be significantly delayed as a consequence of the dynamical constraints appearing in the first stage. Finally, we discuss

the generalization of our results to low-dimensional confining gauge theories.

As a general aspect of this work, we discuss how the phenomena studied here could be realized experimentally with current and future technologies in quantum simulation. Furthermore, the methods developed in this thesis can also be applied to other lattice gauge theories and constrained quantum many-body models, not only to address purely theoretical questions but also to provide a theoretical description of experiments in quantum simulators.

Zusammenfassung

Gittereichtheorien sind ein wichtiger Bestandteil im Verständnis vieler physikalischer Phänomene und Grundlage verschiedener Theorien, welche sich von der elementaren Wechselwirkungen in der Hochenergiephysik, Frustration in Spinmodellen bis hin zu topologischer Ordnung in der Festkörperphysik erstrecken. Die Eigenschaften von Eichtheorien im Gleichgewicht waren in den letzten Jahrzehnten ein zentraler Punkt der Forschung. Obwohl sich Untersuchungen der Dynamik jenseits des Gleichgewichs als eine große Herausfordung dargestellt haben, haben kürzliche Erkenntnisse gezeigt, dass die Dynamik in Gittereichtheorien überraschende und interessante Entdeckungen bereithält.

Diese Dissertation behandelt zwei zentrale dynamische Prozesse in Gittereichtheorien und verwandten Spinmodellen. Einerseits soll die Dynamik von zweidimensionalen und wechselwirkenden Gittereichtheorien untersucht werden im Falle des sogenannten Quanten-Link-Modells untersucht werden. Entgegen der Ergodenhypothese zeigt das System Lokalisierung ohne Unordnung aufgrund lokaler Zwangsbedingungen durch Eininvarianz. Dieses Ergebnis ist insofern bemerkenswert, als die gewöhnliche, durch Unordnung induzierte, Vielteilchenlokalisierung in zwei Dimensionen umstritten ist. Als ein Hauptergebnis finden wir einen Übergang zwischen einer lokalisierten und ergodischen Phase, dessen Existenz durch ein zugehöriges klassisches Perkolationsproblem gezeigt werden konnte. Die quantenmechanischen Transporteigenschaften, elementar verschieden in der lokalisierten und ergodischen Phase, werden charakterisiert und untersucht. Die Lösung der quantenmechanischen Zeitentwicklung wird durch eine methodische Weiterentwicklung der sogenannten „variationellen klassischen Netzwerke“ erreicht Diese Methode stellt eine perturbative, aber kontrollierte Repräsentation von zeitentwickelten quantenmechanischen Wellenfunktionen dar in Form von Netzwerken klassischer Spins, ähnlich wie bei einem künstlichen neuronalen Netz.

Im zweiten Teil untersuchen wir die Dynamik eines Schlüsselprozesses in Eichtheorien mit Confinement, welcher als „String-Breaking“ bezeichnet wird In diesem Prozess zerfällt der der Strang, der zwei elementare Ladungen verbindet, durch die Bildung neuer Teilchen-Antiteilchen-Paare. Ein Hauptresultat dieser Arbeit ist die Beobachtung dieses dynamischen Phänomens in Quantum-Ising-Ketten und damit in Systemen ohne Eichinvarianz.

Das Confinement entsteht dabei zwischen Domänenwänden entweder durch eine langreichweitige Wechselwirkung zwischen den beteiligten Spins oder durch symmetriebrechende Magnetfelder. Es wird gezeigt, dass während des „String-breaking“ Prozesses das Modell zwei Phasen durchläuft: Während zu Beginn die Anfangsladungen stabil bleiben, weist der Strang eine komplexe Dynamik mit starken Quantenkorrelationen auf. Für diese erste Phase wird eine effektive Beschreibung eingeführt, um die verschiedenen Aspekte zu analysieren und zu verstehen. Die Zeitskalen zur Destabilisierung des Strangs innerhalb einer zweiten Phase zeigen eine starke Abhängigkeit von der anfänglichen Trennung der Domänenwände. Es wird gezeigt, dass die zweite Phase als Konsequenz der dynamischen Beschränkungen der ersten Phase signifikant verzögert werden kann. Diese Resultate können in niedrigdimensionalen Eichtheorien verallgemeinert werden.

Weiterführend sollen die Ergebnisse als Grundlage einer experimentellen Realisierung durch Quantensimulationen dienen. Die entwickelten Methoden können auf andere Eichtheorien und verwandten Vielteilchenmodellen angewendet werden und bieten eine Plattform für weitere Ansätze.

List of Publications

The main results presented in this thesis appear in the following publications:

[1] **R. Verdel**, F. Liu, S. Whitsitt, A.V. Gorshkov, M. Heyl, *Real-time dynamics of string breaking in quantum spin chains*, Phys. Rev. B **102**, 014308 (2020).
`https://doi.org/10.1103/PhysRevB.102.014308`
Copyright (2020) by the American Physical Society.

[2] P. Karpov, **R. Verdel**, Y-P Huang, M Schmitt, M Heyl, *Disorder-Free Localization in an Interacting 2D Lattice Gauge Theory*, Phys. Rev. Lett. **126**, 130401 (2021).
`https://doi.org/10.1103/PhysRevLett.126.130401`
Copyright (2021) by the American Physical Society.

[3] **R. Verdel**, M Schmitt, Y-P Huang, P. Karpov, M Heyl, *Variational classical networks for dynamics in interacting quantum matter*, Phys. Rev. B **103**, 165103 (2021).
`https://doi.org/10.1103/PhysRevB.103.165103`
Copyright (2021) by the American Physical Society.

Un hombre se propone la tarea de dibujar el mundo. A lo largo de los años puebla un espacio con imágenes de provincias, de reinos, de montañas, de bahías, de naves, de islas, de peces, de habitaciones, de instrumentos, de astros, de caballos y de personas. Poco antes de morir, descubre que ese paciente laberinto de líneas traza la imagen de su cara.

El hacedor, Jorge Luis Borges

Contents

1 Introduction **1**
1.1 Outline 8

2 Lattice gauge theories in a nutshell **11**
2.1 Wilson-type LGTs in Hamiltonian formulation 13
2.1.1 Free fermions hopping on a lattice and U(1) global symmetry 13
2.1.2 Lattice fermions coupled to a background gauge field 14
2.1.3 Lattice fermions coupled to a dynamical gauge field 16
2.1.4 Lattice version of Gauss law and superselection sectors 17
2.1.5 Extension to the non-Abelian case 18
2.2 Quantum link models 20
2.2.1 The 2D U(1) QLM 20
2.2.2 Quantum dimer models 22
2.3 Ising gauge theories 24
2.3.1 Hamiltonian duality 25
2.4 Phases of LGTs 27
2.4.1 Strong coupling: confinement 27
2.4.2 Weak coupling: deconfinement 29
2.5 Quantum simulation of LGTs 30

3 Variational classical networks for quantum many-body dynamics **37**
3.1 The complexity of the quantum many-body dynamics problem 38
3.2 Exact diagonalization 39
3.2.1 Exact evolution 39
3.2.2 Prescription to perform an ED calculation 41
3.2.3 Lanczos time evolution 44
3.3 Time evolution with matrix product states 46
3.3.1 Matrix product states 46
3.3.2 Time evolution via a Trotter decomposition 50
3.4 Time evolution with classical networks 53

3.4.1 Classical networks as generative machines 53
3.4.2 Time-dependent variational principle 57
3.5 Variational classical networks 58
3.5.1 General settings 59
3.5.2 Building classical networks from a cumulant expansion 60
3.5.3 Variational ansatz 62
3.5.4 Benchmark: Quenches in the 1D TFIM model 63
3.6 Summary and further remarks 69

4 Disorder-free localization in an interacting 2D lattice gauge theory 73
4.1 The model 75
4.2 Disorder-free localization 76
4.3 VCNs for the QLM 77
4.3.1 First-order ansatz 78
4.3.2 Second-order ansatz 80
4.4 Quantum dynamics in the QLM 82
4.4.1 Initial states for unitary evolution 83
4.4.2 Benchmarks in quasi-1D ladders 84
4.4.3 Localized and ergodic dynamics in 2D 88
4.5 Bound on quantum dynamics by a correlated percolation problem 90
4.6 Summary and outlook 91

5 Real-time dynamics of string breaking in quantum spin chains 93
5.1 Models and quench dynamics 95
5.1.1 Quantum Ising chains 95
5.1.2 Quench protocol and measured observables 97
5.2 Summary of main results 98
5.3 First stage: string motion 100
5.3.1 Effective description of the string dynamics 100
5.3.2 Bound on particle production 104
5.3.3 Dynamics in resonant subspace 105
5.3.4 Typical timescale for the onset of string breaking 110
5.3.5 Field-theoretical approach and extended kinks in the short-range model 111
5.4 Second stage: string breaking 113
5.5 Summary and outlook 115

6 Conclusions and Outlook 117

A Schmidt decomposition and entanglement entropy 121

B Effective Hamiltonian for string breaking dynamics in short-range quantum Ising models **125**

Bibliography **127**

Chapter 1

Introduction

Gauge theories are field theories that are invariant under certain *local* symmetry transformations, which are obtained by promoting global symmetries to local ones. These theories constitute a cornerstone of many realms of modern physics ranging from particle physics, where all fundamental interactions—within the framework of the Standard Model—are mediated by gauge fields [4–6], to condensed matter [7, 8] and quantum information [9–11]. Gauge theories can also be defined on a spatial lattice (or even on a discretized Euclidean space-time) giving rise to *lattice gauge theories* (LGTs), in which the local gauge symmetries are now implemented on each lattice site. From the perspective of quantum field theory and high-energy physics, LGTs have established themselves as one of the most successful nonperturbative regularization schemes [12]. Further, the lattice also provides a direct connection between the aforementioned fields and statistical mechanics [13, 14], and brings these theories within reach of classical computer simulations with Monte Carlo techniques [15–17] and tensor network approaches [18–20]. Importantly, LGTs yield, in addition, a promising route towards the quantum simulation of gauge theories [18, 21–32], where a few remarkable experiments have already been carried out [11, 33–43]. In condensed matter, LGTs can also arise as effective low-energy descriptions of many interesting problems, such as spin-liquid states and quantum dimer models [7, 44–50], the fractional quantum Hall effect [51], and ferromagnetic superconductivity [52, 53]. On the other hand, some paradigmatic spin models in condensed matter physics can exhibit features analogous in phenomenology to some properties of LGTs such as confinement [54–77], where elementary excitations experience an attractive potential that rises linearly with the distance between them. Furthermore, LGTs are also relevant for topological quantum computation [9], as exemplified by Kitaev's toric code [10], a $\mathbb{Z}_2$ LGT used for topological quantum error correction, whose ground state has been recently realized on a superconducting quantum processor [11]. These as well as many other examples have boosted extensive investigations on LGTs, especially with regard to their static properties. Recent efforts, however, have also highlighted a plethora of interesting dynamical phenomena occurring in LGTs.

Among the different dynamical phenomena observed in LGTs, one that is particularly intriguing is *string breaking*. This phenomenon is at the core of confining theories such as quantum chromodynamics—the theory of strong interactions [4–6]. Confining theories have the defining feature that two static charges, such as a heavy quark-antiquark pair, are connected by a flux tube or string, whose energy increases linearly with the separation of the charges [78]. String breaking thus refers to the decay of the confining string at the expense of the creation of new particle-antiparticle pairs. In the particular context of quantum electrodynamics in one spatial dimension, this phenomenon is closely related to the Schwinger mechanism [79], which describes the process of vacuum decay by spontaneous fermion-antifermion pair production, of relevance, for instance, to studies with high-intensity lasers [80] and heavy-ion colliders [81]. While many equilibrium aspects of string breaking have been investigated extensively [82–89], the characterization of its dynamics has also started to attract attention [21, 31, 90–102], and will be considered later in this work as well. Further important topics regarding dynamics in LGTs include collisions and scattering events, where some recent studies have taken the first steps to address such processes in one-dimensional (1D) models [103–105], and the process of fermion number non-conservation or chirality breaking, which is relevant for highly energetic and dense matter environments like in the early universe [106].

The nonperturbative dynamical processes mentioned above are of fundamental importance to high-energy physics. However, the study of the nonequilibrium dynamics in LGTs has also proved important for other areas of physics. A notable example of this is given by *disorder-free localization*, a novel type of an ergodicity-breaking mechanism that has been recently observed in some homogeneous low-dimensional LGTs [107–114]. Typically, generic interacting quantum systems are expected to reach thermodynamic equilibrium during the course of their time evolution, thereby forgetting the details of the initial condition. On the other hand, systems featuring localization may fail to thermalize. This is normally reflected in an inefficient energy transfer across the microscopic degrees of freedom and deviations from linearity in the light-cone spreading of correlations [108]. A famous example of localization phenomena in interacting quantum systems is many-body localization [115–117], which depends crucially on the presence of strong disorder. Remarkably, many phenomenological aspects of disorder-free localization are similar to those of many-body localization but in the absence of any type of disorder. Instead, here, localization is caused by *local constraints* that are imposed by gauge invariance. Hence, this mechanism can be situated in the growing paradigm of ergodicity breaking due to local constraints, which includes systems featuring quantum many-body scars [118–122], fractonic systems [123–127], quantum models with East-like constraints [128–130], and systems with extremely slow relaxation due to dynamical constraints [131]. Thus, disorder-free localization offers new insights on fundamental aspects of ergodicity breaking in interacting quantum systems and LGTs, in particular. We shall discuss further aspects of this phenomenon in subsequent parts of this thesis.

Let us now mention some of the main tools used for the study of LGTs. Lattice Monte Carlo techniques [15–17] have proved quite successful for the investigation of equilibrium properties of LGTs. For example, the low-lying spectrum [132] and phase diagram [133–135] of quantum chromodynamics have been studied with the help of Monte Carlo computations. Besides, many static aspects of confinement and string breaking in non-Abelian[1] gauge theories [82, 85, 89, 136–138] have been investigated with such techniques too. Tensor network methods have also allowed us to explore not only several equilibrium properties of LGTs, see for instance Refs. [18–20, 139–147], but also some of their dynamical features, such as dynamical confinement and string breaking [92, 93, 95, 100, 102]. However, in general, accessing the nonequilibrium dynamics of LGTs poses a formidable challenge, as is in fact the case for most strongly interacting quantum systems. In particular, from the perspective of Monte Carlo methods, this is due to a fundamental sign problem [148, 149]. Importantly, this has stimulated theoretical and experimental efforts to simulate LGTs in real time using *quantum simulators* [150, 151], a field which has seen impressive progress in recent years.

Quantum simulators can be seen as special purpose quantum computers that can be either digital, with the unitary evolution of a quantum system being implemented as a circuit of single- and two-quibit gates (see for example Ref. [152]), or analog, with the Hamiltonian of the system of interest being directly mapped onto the Hamiltonian of the simulator (see for example Refs. [153, 154]). There are several platforms to construct quantum simulators, such as ultracold atoms in optical lattices [155], trapped ions [156, 157], superconducting circuits [158], and photons [159]. These technologies have thus allowed for the simulation of the unitary dynamics in closed quantum many-body systems, with an unprecedented level of control, as demonstrated in multiple experimental works [160–181]. Although LGTs pose a bigger challenge for quantum simulation, since gauge invariance is difficult to enforce, a few noticeable proof-of-principle experiments have already been performed in this direction [11, 33–43]. In this respect, let us highlight the pioneering experiment by Martinez et al. [33], which constitutes the first digital quantum simulation of an LGT using a trapped ion setup with four qubits. Concretely, the authors of this work studied the real-time dynamics of the process of spontaneous particle-antiparticle pair production in a discrete lattice version of the Schwinger model [78], a $(1+1)$-dimensional version of quantum electrodynamics; see Fig. 1.1. Dynamical processes, like the Schwinger mechanism mentioned above, give an example of the physics that cannot be accessed with conventional Markov Chain Monte Carlo methods. Crucial for the formulation of the protocol used in [33] is the fact that, for the model under consideration, the gauge degrees of

---

[1] A gauge theory is said to be *Abelian* if all the gauge group generators commute with each other and *non-Abelian* when this is not the case.

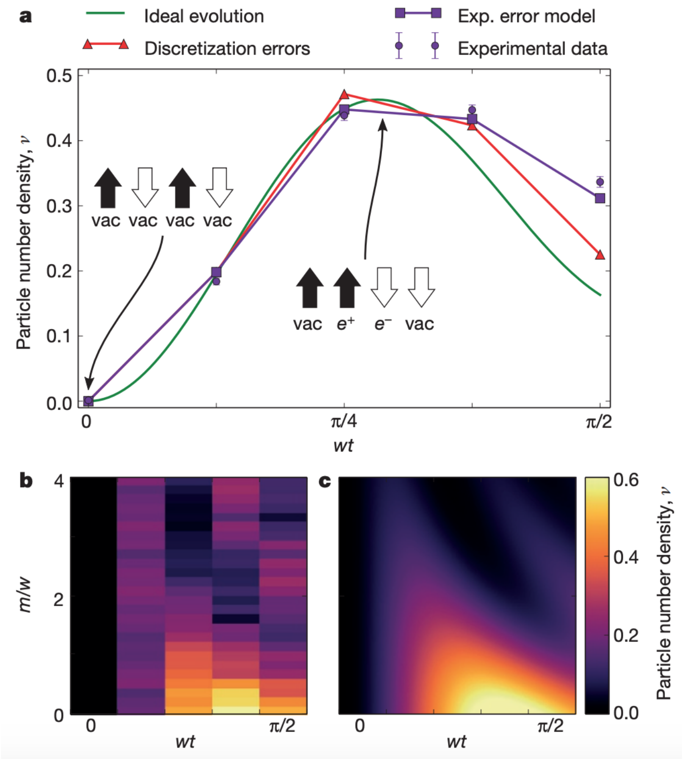

Figure 1.1: Digital quantum simulation of a 1D LGT: Real-time evolution of the Schwinger mechanism. The upper panel displays the time evolution of the particle number density (including experimental data), highlighting, in particular, the process of pair production out of the bare vacuum. Shown in the lower panel is (b) the experimental data and (c) the theoretical prediction for the dynamics of the particle number density as a function of time wt and particle mass m/w (in dimensionless units). [*Reprinted by permission from Springer Nature: Nature (Martinez et al. [33]) Copyright (2016);* `https://doi.org/10.1038/nature18318`.]

freedom can be integrated out analytically [28]. The resulting model contains only matter fields but it is still gauge invariant. Further, it can be recast as a nonconventional spin model with two-body terms and long-range interactions (which implicitly take into account the gauge fields). Trapped ions naturally feature long-range interactions [157] and are therefore well suited for the implementation of such a model.

Another relevant experiment in the field of quantum simulation was performed recently by Bernien et al. [169]. In this work, the quantum many-body dynamics of Ising-type systems was probed on a 51-qubit quantum simulator based on Rydberg atoms in a regime in which strong Rydberg interactions considerably constrain the dynamics of the system. This gives rise to anomalously slow dynamics as shown in Fig. 1.2. Although not envisioned with this purpose, this experiment turned out to be closely related to LGTs, as pointed out by Surace et al. [31]. Indeed, the latter authors found that, under the conditions considered in [169], the constrained dynamics of the simulated quantum spin chains exactly maps onto that of 1D LGTs. Moreover, it was also shown that the slow dynamics reported in Ref. [169] corresponds to a string-inversion mechanism (see Fig. 1.3), which is related to the process

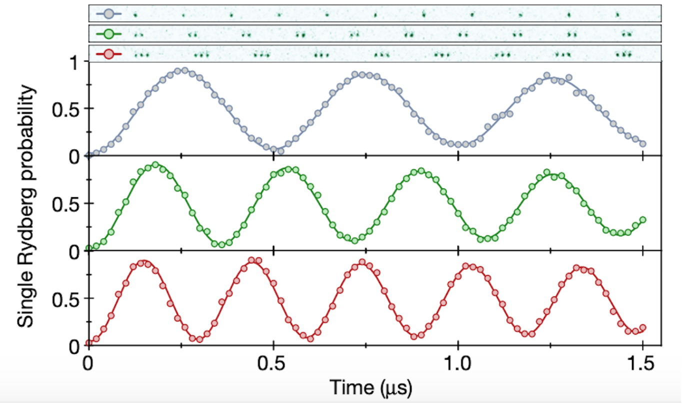

Figure 1.2: Slow dynamics in a 51-qubit quantum simulation using Rydberg atoms: Persistent oscillations in the many-body dynamics of a system of strongly interacting Rydberg atoms realizing Ising-type quantum spin models. As shown by Surace et al., in Ref. [31], the dynamics of such systems can be mapped onto the dynamics of certain 1D LGTs. [*Adapted by permission from Springer Nature: Nature (Bernien et al. [169]) Copyright (2017);* `https://doi.org/10.1038/nature24622`.]

of string breaking featured in some gauge theories.

Finally, let us briefly mention a recent experiment performed by Yang et al. [41], using a Bose-Hubbard quantum simulator with 71 sites. This work is not only remarkable for the considered system size, but also because it provides the first experimental quantification of gauge invariance during the real-time dynamics in a 1D LGT. In this experiment, the considered LGT is mapped onto the Hamiltonian of a system of ultracold bosons in a 1D optical lattice with 71 sites. By means of high-fidelity manipulation techniques, the authors of this experiment were able to quantify Gauss law violation by extracting probabilities of locally gauge-invariant states from correlated atom occupations (Fig. 1.4).

The examples discussed above show that LGTs offer quite a fertile ground for the study of nonequilibrium processes in gauge theories and the potential for their quantum simulation. It is also clear, however, that much more efforts are still needed to further characterize such phenomena and for the potential discovery of new intriguing physics in LGTs beyond equilibrium paradigms.

In this thesis, we study two particular nonequilibrium dynamical phenomena hosted in LGTs. First, we study a 2D interacting LGT of interest to both high-energy physics and condensed matter systems featuring valence bond configurations [44–46, 182], namely, a U(1) *quantum link model* (QLM) [23, 182, 183]. We provide strong numerical evidence showing that this model can exhibit disorder-free localization, an ergodicity-breaking mechanism due to the local constraints imposed by gauge invariance. As mentioned before, this mechanism has been recently observed in low-dimensional homogeneous LGTs [107–110, 112–114], including 2D noninteracting systems [111]. Here, on the other hand, we show that disoder-free localization is also possible in a 2D *genuinely interacting* model. The

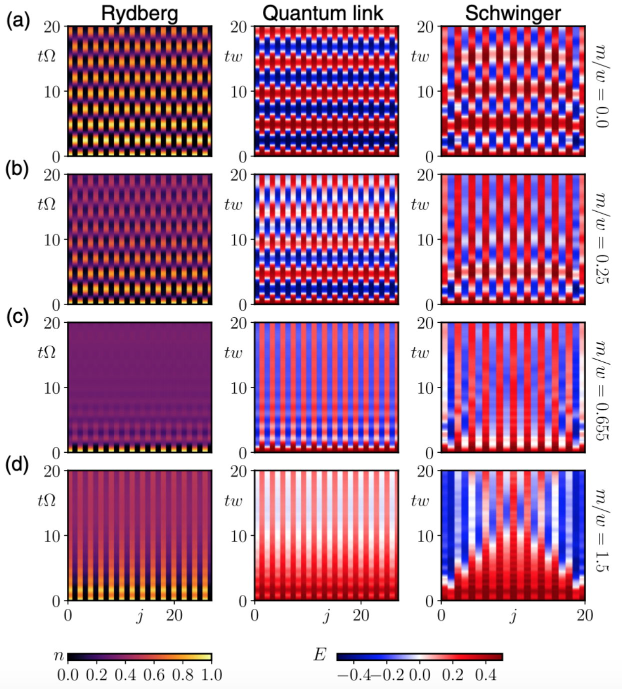

Figure 1.3: Relation between LGTs and Rydberg atom systems: Many-body dynamics of a Rydberg atom system (left column), in terms of the local density profile n, and a U(1) quantum link model (middle column) and the Schwinger model (right column), in terms of the local electric field profile E. The results for the first two systems are connected by a unitary transformation. The persistent oscillations in the Rydberg blockade setting considered in Ref. [169] can thus be related to the phenomenon of string inversion in LGTs, which is shown in the upper row. [*Figure from Ref. [31];* `https://doi.org/10.1103/PhysRevX.10.021041`.]

demonstration of robust nonergodic behavior in the 2D QLM appears quite remarkable in view of the fact that the stability of many-body localization [115–117]—a mechanism for nonergodic behavior in interacting quantum systems with disorder—is still debatable in 2D [168, 184–186]. The results presented in this part are based on a bound on the localization-delocalization transition that is obtained via an associated classical percolation problem. Moreover, such a percolation analysis also shows that, on the nonergodic side of the transition, the Hilbert space fragments into kinetically disconnected sectors. We further study the quantum dynamics of this system using a numerical method that is also presented in this thesis, namely, *variational classical networks* (VCNs). This approach provides an efficient encoding of the many-body wave function by means of complex networks of classical spins akin to artificial neural networks [3, 187–189]. The quantum dynamics simulations of the 2D QLM reveal a distinguishing signature of ergodic and nonergodic phases in the form of two different light cone structures arising from the propagation of an initial line defect. Let us also point out that VCNs constitute a general numerical framework that can be applied in a controlled manner to any quantum lattice model regardless of spatial dimensionality.

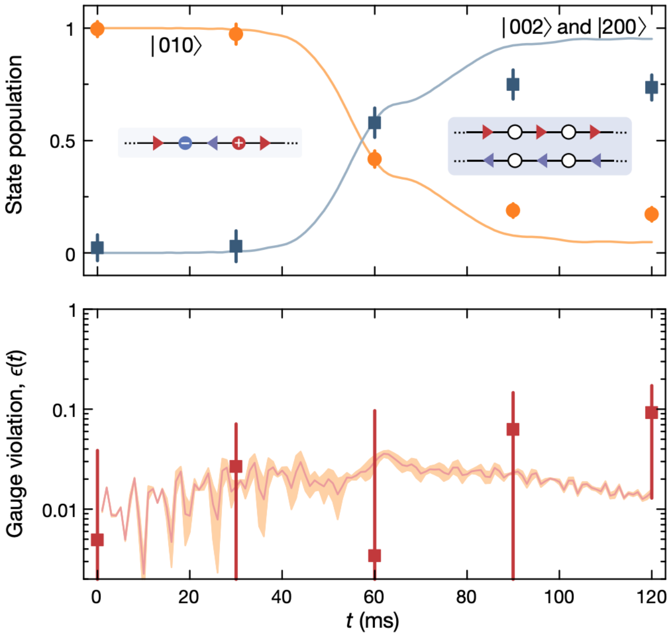

Figure 1.4: Observation of gauge invariance in a ultracold-atom quantum simulator with 71 lattice sites: Upper plot shows the population of gauge invariant states. These probabilities are then used to quantify gauge violation as a function of time $\epsilon(t) = 1 -$ (sum of prob. of gauge-invariant states), which is shown in the bottom plot. [*Adapted by permission from Springer Nature: Nature (Yang et al. [41]) Copyright (2020);* `https://doi.org/10.1038/s41586-020-2910-8`.]

In the second problem tackled in this thesis, we study the real-time dynamics of *string breaking* in quantum spin chains. As mentioned before, this phenomenon is of central importance in confining theories and occurs when the confining string becomes unstable to the creation of new particle-antiparticle pairs. Here, it is our main result that this process can also be observed in paradigmatic models in condensed matter physics, namely, quantum Ising chains where domain walls get confined either by a symmetry-breaking field [68] or by long-range interactions [70]. The general picture that we find is that string breaking occurs as a two-stage process. In the first stage, the initial charges remain, essentially, static and stable on a timescale, which can depend crucially on the initial domain wall separation. The connecting string, on the other hand, can develop some nontrivial dynamics. We construct an effective description of this motion, which turns out to exhibit strong kinetic constraints. Remarkably, the resulting reduced models allow us to obtain analytical access for instance on timescales of string breaking or on bounding the maximum number of particle-antiparticle pairs created during string motion. Furthermore, it is observed that the string motion also leads to a heterogeneous spatiotemporal profile of quantum correlations. While the regions outside of the string essentially remain uncorrelated, the string itself can develop strong quantum correlations. In the second stage, which can be severely delayed due to the dynamical constraints emerging from string motion, the string finally breaks at a timescale, which can grow by orders of magnitude upon increasing the separation of the initial domain walls. We finally comment on how the observations above can also generalize to low-dimensional confining gauge theories.

As a final remark, let us mention that the two problems studied in this thesis appear within reach of both current and future experiments with quantum simulators, as we will discuss later in this work. However, we can already anticipate that there are a few theoretical proposals for realizing the QLM using, for instance, Rydberg atoms [190, 191] or superconducting circuits [26], whereas the quantum Ising models relevant to our study on string breaking can be implemented with current technologies in Rydberg atoms [170, 171] and trapped ions [172, 181]. As already mentioned, the remarkable advances in the field of quantum simulation is one of the main motivations behind many of the theoretical works mentioned above, and indeed, of the two problems that are addressed in this thesis. In that respect, let us note that the method of VCNs, which is also one of the central contributions of this work, not only supplies a framework to address purely theoretical questions but could also be used to provide a theoretical description of experiments like the ones discussed above, in particular, those targeting two and higher spatial dimensions.

1.1 Outline

The remaining of this thesis is organized as follows.

- **Chapter 2**: This chapter presents a minimal introduction to LGTs. Concretely, in Section 2.1, we present the basic structure of an LGT following the pioneering approach due to Wilson [192] but in the so-called quantum Hamiltonian formulation. We consider free fermions on the lattice, fermions coupled to a background field, and fermions coupled to a dynamical gauge field, leading to the formulation of lattice quantum electrodynamics. We then review the lattice version of Gauss law and the concept of superselection sectors. We finish this section by briefly considering the non-Abelian extension that yields lattice quantum chromodynamics. Next, in Section 2.2, we present the quantum link formulation of LGTs with focus on Abelian U(1) gauge theories. Here, we consider the related quantum dimer model as well. We discuss Ising gauge theories in Section 2.3. Finally, we list a few aspects of the phases of LGTs in Section 2.4 and expand the discussion on the quantum simulation of LGTs in Section 2.5. No original results are discussed here. We believe, however, that this chapter should provide a minimal and adequate background for understanding the original results presented in this work.

- **Chapter 3**: We introduce the method of variational classical networks, which is the main tool used to study the quantum dynamics in the 2D QLM considered in

Chapter 4. In this chapter, we also present a short discussion about the complexity of the quantum many-body dynamics problem in Section 3.1 and revise some state-of-the-art numerical methods. In particular, exact diagonalization techniques are the subject of Section 3.2, while the time evolution with a particular type of tensor networks is briefly explained in Section 3.3. Next, in Section 3.4 we discuss how to study the time evolution of quantum systems with generic classical networks. We also mention some popular examples of such generative machines that have been used for this task, such as some particular types of artificial neural networks. Finally, in Section 3.5, we discuss in detail the formulation of variational classical networks and carry out some benchmarks in the 1D transverse-field Ising model. The latter section contains some of the original results presented in this work (see also Ref. [3]).

- **Chapter 4**: In this chapter we study the nonequilibrium dynamics of the 2D U(1) QLM, showing that such genuinely interacting model exhibits both localized and ergodic phases in the absence of disorder. To this end, we start by recalling the model Hamiltonian and its local symmetries in Section 4.1. Next, in Section 4.2, we briefly review the mechanism behind the ergodicity breaking in this system, namely, disorder-free localization. In Section 4.3 we work out in full detail the construction of variational classical networks for the problem at hand. Using such VCNs we compute the quantum dynamics in Section 4.4.3. The latter section also contains benchmark calculations in quasi-1D ladders, the definition of the observables of interest and the main results for the dynamics in the 2D case. Section 4.5 is focused on one of the central arguments to assert the existence of the localization-ergodic transition, namely, a bound on such transition that is obtained through a classical percolation problem. This analysis also implies a fragmentation of the Hilbert space into kinetically disconnected regions on the nonergodic side of the transition. Conclusions and a summary of this chapter are given in Section 4.6. This chapter comprises the first part of main results presented in this thesis (see also Ref. [2]).

- **Chapter 5**: We show that the dynamics of string breaking can also be observed and characterized in quantum spins chains relevant to the physics of LGTs. The considered models, measured observables and quench protocol are introduced in Section 5.1. The main results of this chapter are summarized for the sake of clarity in Section 5.2. The detailed discussion of these results is done in Sections 5.3 and 5.4. In the first of these sections, we describe the first stage of string breaking and work out some effective models, which give access to analytical predictions, such as a bound on particle production and the typical timescale for the final breaking of the string. An extension to the continuum is briefly presented in this section through a field-theoretical description. The second stage of string breaking is discussed in Section 5.4. Conclusions and a summary of this chapter are given in Section 5.5.

This chapter constitutes the second part of main results presented in this thesis (see also Ref. [1]).

- **Chapter 6**: Conclusions and possible extensions of the work presented in this thesis are discussed in this final chapter.

Chapter 2

Lattice gauge theories in a nutshell

Gauge theories are defined by their invariance with respect to local (gauge) symmetry transformations, which are obtained by promoting global symmetries to local ones. The invariance under the resulting local transformations is guaranteed by introducing a *gauge field* that dictates the form of the coupling or interactions in the theory. This important notion is known as *gauge principle* and has played a crucial role in the development of fundamental theories of particle interactions [4–6]. Gauge theories can also be defined on the lattice with the local symmetry transformations implemented at each lattice site. This approach gives rise to *lattice gauge theories*, and was first introduced in the 1970's in seminal works by Wilson [192] and Polyakov [193], as a solution to the problems of *quark and charge confinement*, respectively, and Wegner [194], who introduced Ising LGTs as an example of models that could undergo a phase transition without having a local order parameter. From the viewpoint of quantum field theories, LGTs are quite important for various reasons. First, they constitute one of the most successful nonpertubative regularization schemes [5, 6, 12]. Indeed, the lattice spacing introduces a natural cutoff in the theory, while the fact that path integrals are basically replaced by ordinary, finite-dimensional integrals means that nonperturbative effects become accessible. Moreover, the lattice formulation of gauge theories comes with the enormous advantage that it is amenable to computer simulations using, for example, conventional Monte Carlo techniques [15] or tensor network approaches [18–20]. Importantly, LGTs also provide a promising route towards quantum simulation of gauge theories in various setups [18, 23, 26–30], where a few notable experiments have already been carried out [33, 37–41]. As mentioned in the introduction, LGTs are not only important for high-energy physics; they also play a key role in other areas of physics such as condensed matter [7], topological quantum computation [9, 11], and even computer science [195]. Regarding condensed matter physics, many recent studies of strongly-correlated quantum matter have revealed that an understanding of the physics of such systems can be best achieved in the language of LGTs, which emerge in those instances as effective low-energy physics descriptions. Examples here include spin liquid states and quantum dimer models [7, 44–46, 48–50], the fractional quantum Hall effect [51], and ferromagnetic superconductivity [52, 53]. On the other hand, some paradigmatic quantum spin models in condensed matter physics can exhibit features analogous in phenomenology to some properties of LGTs. A prominent example of this is confinement, where particles with fractional quantum numbers bind together to form composite particles with integer quantum numbers, due to an attractive interaction whose strength rises linearly with the distance. It turns out that such phenomenon can also be exhibited in many condensed matter systems [54–77]. Thus, the symbiotic interaction between LGTs and condensed matter physics not only broadens the scope of the former towards the realm of quantum many-body theory, but it also makes the study of its phenomenology in quantum simulators more amenable. All in all, LGTs have evolved as a multidisciplinary and fruitful field for the study of many interesting physical phenomena.

The aim of this chapter is to present a brief overview of LGTs. It is not attempted to give a comprehensive review on the topic, for which there exist already several excellent examples in the literature; see for instance Refs. [13, 14, 18, 23, 27, 196]. Rather, we try to provide the essential theoretical background for the models studied in Chapters 4 and 5. Let us also point out that, in the following, we shall consider LGTs in the *Hamiltonian formulation* [197–199] (instead of the Wilson's Euclidean approach), where the theory is defined on a D-dimensional spatial lattice and it evolves in real (continuous) time. This approach has the advantage that it is conceptually similar to the setups found in condensed matter and atomic, molecular and optical physics. Also, we will mostly deal with *Abelian* LGTs, in which the gauge group generators commute with each other. However, we will briefly mention extensions to non-Abelian LGTs where relevant.

The organization of this chapter is as follows. In Section 2.1, we introduce LGTs following Wilson's approach [192] in the quantum Hamiltonian formulation of Kogut and Susskind [197]. We begin by considering the case of free fermions on the lattice, which are then coupled to an electromagnetic background field in Sections 2.1.1 and 2.1.2, respectively. Next, we promote such static gauge field to a dynamical one, leading to the lattice formulation of quantum electrodynamics (Section 2.1.3). Then, in Section 2.1.4, we discuss Gauss law on the lattice and review the concept of *superselection sectors*. Finally, we briefly mention the extension to non-Abelian LGTs and write down the Hamiltonian of lattice quantum chromodynamics (Section 2.1.5). The quantum link formulation of LGTs is revisited in Section 2.2. In particular, we focus on Abelian U(1) QLMs and the related quantum dimer model in Sections 2.2.1 and 2.2.2, respectively. Some aspects of the nonequilibrium dynamics of the U(1) QLM in two dimensions will be the subject of Chapter 4. Another important type of Abelian gauge theories are Ising or $\mathbb{Z}_2$ LGTs, which are discussed in Section 2.3. Ising LGTs are also relevant to some quantum spin models [7, 13, 47, 194, 199, 200]; in particular, they are related to the quantum Ising models studied in Chapter 5. Finally, we revise a few aspects of the phases of LGTs (Section 2.4) and present and overview of recent developments in the experemental realization of LGTs with quantum simulators (Section 2.5).

2.1 Wilson-type LGTs in Hamiltonian formulation

In this section, we show the basic structure of an LGT. We start by considering free fermions hopping on the lattice to illustrate a U(1) global symmetry. We then promote such symmetry to a U(1) local gauge symmetry and find the Hamiltonian description of staggered fermions coupled to a static background gauge field. Next, we consider dynamical gauge fields and write down a lattice version of quantum electrodynamics. Further, we discuss the extension of Gauss law to the lattice and the so-called superselection sectors. Finally, we briefly comment on a generalization to non-Abelian LGTs.

2.1.1 Free fermions hopping on a lattice and U(1) global symmetry

Let us start by considering the case of free fermions hopping on a 2D square lattice with lattice spacing a_0 (that we will normally set to 1). We denote lattice sites by $\mathbf{r} = (x, y)$, and the unit vectors of the lattice by $\hat{\mu} = \hat{\imath}, \hat{\jmath}$ (see Fig. 2.1). Thus, the Hamiltonian of the system reads

$$H = -t \sum_{\mathbf{r},\mu} (\psi^\dagger_{\mathbf{r}} \psi_{\mathbf{r}+\hat{\mu}} + \text{h.c.}) + \sum_{\mathbf{r}} m_{\mathbf{r}} \psi^\dagger_{\mathbf{r}} \psi_{\mathbf{r}}, \tag{2.1}$$

where t is the hopping constant, m is the mass of the particles, with $m_{\mathbf{r}} = (-1)^{x+y} m$ describing the so-called *staggered fermions* [201] (see Fig. 2.1), which is a way to adequately describe relativistic fermions on a lattice [23], and $\psi^\dagger_{\mathbf{r}}$ ($\psi_{\mathbf{r}}$) are fermionic creation (annihilation) operators satisfying canonical anti-commutation relations

$$\{\psi^\dagger_{\mathbf{r}}, \psi_{\mathbf{r}'}\} = \delta_{\mathbf{r},\mathbf{r}'}. \tag{2.2}$$

The Hamiltonian in Eq. (2.1) conserves the total number of fermions, that is, $[H, N_{\text{tot}}] = 0$, with $N_{\text{tot}} = \sum_{\mathbf{r}} \psi^\dagger_{\mathbf{r}} \psi_{\mathbf{r}}$, and hence, the system is invariant under global phase transformations:

$$\psi_{\mathbf{r}} \to \mathrm{e}^{i\alpha} \psi_{\mathbf{r}}, \quad \psi^\dagger_{\mathbf{r}} \to \mathrm{e}^{-i\alpha} \psi^\dagger_{\mathbf{r}}, \tag{2.3}$$

where α is any real number. In other words, H is invariant under the U(1) group,[1] whose elements are parametrized by the phases $\mathrm{e}^{i\alpha}$.

---

[1] U(n) describes the group of unitary $n \times n$ matrices.

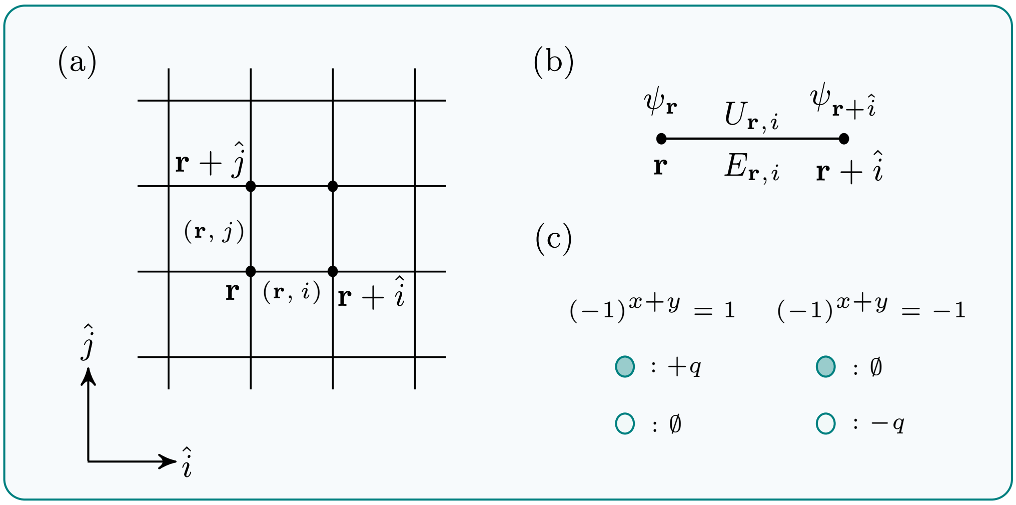

Figure 2.1: (a) The 2D square lattice where the links are labeled by the coordinates of a site $\mathbf{r}$ and the direction of a unit lattice vector $\hat{\mu}=\hat{i},\hat{j}$. (b) Matter fields $\psi^\dagger_\mathbf{r}/\psi_\mathbf{r}$ are put on lattice sites $\mathbf{r}$, while gauge fields $(U_{\mathbf{r},\mu},E_{\mathbf{r},\mu})$, are defined on the links. (c) Staggered fermion formulation where matter and antimatter fields are defined on a lattice bipartition: on the even (odd) sublattice, a full (empty) site represents a particle (antiparticle) with charge q $(-q)$.

2.1.2 Lattice fermions coupled to a background gauge field

As a next step, we now extend the global U(1) symmetry transformations in Eq. (2.3) to local ones. Namely,

$$\psi_\mathbf{r}\to \mathrm{e}^{i\alpha_\mathbf{r}}\psi_\mathbf{r},\quad \psi^\dagger_\mathbf{r}\to \mathrm{e}^{-i\alpha_\mathbf{r}}\psi^\dagger_\mathbf{r}, \tag{2.4}$$

where now the phase factors depend on the lattice site index.

It can be easily checked that, while the mass term in Eq. (2.1) remains invariant under these transformations, the hopping term does not. Intuitively, this is due to the fact that the hopping part does not conserve the number of particles on a local level. As mentioned in the introduction of this chapter, invariance under local transformations is guaranteed by introducing a gauge field. However, we need to figure out how to introduce a gauge field on the lattice. Since the gauge field $\mathbf{A}(\mathbf{r})$ of classical electromagnetism is a vector, it is natural to associate its lattice version $A_{\mathbf{r},\mu}$ with the directed *links* connecting neighboring lattice sites $\mathbf{r}$ and $\mathbf{r}+\hat{\mu}$ (see Fig. 2.1). For the time being, however, let us work with the continuum gauge field, for which we also know that it obeys a continuum gauge transformation: $\mathbf{A}(\mathbf{r})\to\mathbf{A}'(\mathbf{r})=\mathbf{A}(\mathbf{r})-\nabla\alpha(\mathbf{r})$, for some scalar function $\alpha(\mathbf{r})$. As this transformation involves derivatives and hence the infinitesimal vicinity of $\mathbf{r}$, it is convenient to integrate the continuum gauge field over the corresponding link in a fashion similar to that in Wilson's approach [23, 192]. Furthermore, it turns out that in LGT the natural gauge field operator is not $A_{\mathbf{r},\hat{\mu}}$, but rather its exponential [23, 53]. Thus, we consider the following gauge field operator:

$$U_{\mathbf{r},\mu} = \exp\left[i\int_{\mathbf{r}}^{\mathbf{r}+\hat{\mu}} d\mathbf{r}' \cdot \mathbf{A}(\mathbf{r}')\right]. \tag{2.5}$$

The gauge field operators in Eq. (2.5) are called *parallel transporters* [23] and can be viewed as connections in differential geometry that relate two local frames of the internal space of the matter field at neighboring sites $\mathbf{r}$ and $\mathbf{r}+\hat{\mu}$ [53]. Let us note that $U_{\mathbf{r},\mu}$ is an element of the Abelian U(1) gauge group. Also, the integral $\int_{\mathbf{r}}^{\mathbf{r}+\hat{\mu}} d\mathbf{r}' \cdot \mathbf{A}(\mathbf{r}')$ in Eq. (2.5) can be thought of as the phase accumulated by a charged particle moving from $\mathbf{r}$ to $\mathbf{r}+\hat{\mu}$ in the presence of a vector potential $\mathbf{A}(\mathbf{r})$ [26]. Under the continuum gauge transformation of $\mathbf{A}(\mathbf{r})$, the parallel transporter $U_{\mathbf{r},\mu}$ transforms as

$$\begin{aligned} U'_{\mathbf{r},\mu} &= \exp\left[i\int_{\mathbf{r}}^{\mathbf{r}+\hat{\mu}} d\mathbf{r}' \cdot \mathbf{A}'(\mathbf{r}')\right] \\ &= \exp\left[i\int_{\mathbf{r}}^{\mathbf{r}+\hat{\mu}} d\mathbf{r}' \cdot \big(\mathbf{A}(\mathbf{r}') - \nabla_{\mathbf{r}'}\alpha(\mathbf{r}')\big)\right] \\ &= \exp\left[i\int_{\mathbf{r}}^{\mathbf{r}+\hat{\mu}} d\mathbf{r}' \cdot \mathbf{A}(\mathbf{r}') + \alpha(\mathbf{r}) - \alpha(\mathbf{r}+\hat{\mu})\right]. \end{aligned} \tag{2.6}$$

Denoting the unitary elements of the U(1) gauge group by $V_{\mathbf{r}} = \exp(i\alpha(\mathbf{r}))$, the lattice gauge transformation above can be succinctly written as

$$U_{\mathbf{r},\mu} \to U'_{\mathbf{r},\mu} = V_{\mathbf{r}} U_{\mathbf{r},\mu} V^{\dagger}_{\mathbf{r}+\hat{\mu}}. \tag{2.7}$$

Thus, changing the Hamiltonian to

$$H = -t\sum_{\mathbf{r},\mu}(\psi^{\dagger}_{\mathbf{r}} U_{\mathbf{r},\mu}\psi_{\mathbf{r}+\hat{\mu}} + \text{h.c.}) + \sum_{\mathbf{r}} m_{\mathbf{r}}\psi^{\dagger}_{\mathbf{r}}\psi_{\mathbf{r}}, \tag{2.8}$$

invariance under the local gauge transformations, Eqs. (2.4) and (2.7), is restored. The Hamiltonian (2.8) thus describes staggered lattice fermions propagating in a classical electromagnetic background field. Let us mention that this is an important problem in condensed matter and cold atom physics, particularly, in context of topological quantum matter [18, 202]. In this respect, we notice the similarity to the Harper-Hofstadter model [203], which describes a system of non-interacting fermions in a 2D lattice, whose hopping carries a phase factor, such that when a fermion winds around an elementary plaquette its wave function picks up a phase factor given by the sum of the individual phases associated to the links of the plaquette. Such a phase factor thus plays the role of the flux of an effective magnetic field piercing each plaquette [18]. Let us also note that the Wilson's link variables introduced above have an infinite dimensional local Hilbert space, as they are continuous classical variables. In Section 2.2, we will study a different formulation of LGTs with finite-dimensional link Hilbert space.

2.1.3 Lattice fermions coupled to a dynamical gauge field

We now consider the case of staggered fermions coupled to a *dynamical* gauge field. In quantum field theory, this problem is described in a framework known as *quantum electrodynamics* [12]. Thus, the Hamiltonian of the corresponding LGT is required to (i) reduce to the Hamiltonian operator of quantum electrodynamics in the naive continuum limit $a_0 \to 0$, and (ii) satisfy the U(1) local gauge invariance that is inherited from the continuum theory. Let us see how to write down a reasonable Hamiltonian for the LGT according to these requirements. We start by considering the case without matter, in which the Hamiltonian of the continuum quantum electrodynamics reads

$$H = \frac{1}{2}\int d^3r(\mathbf{E}^2(\mathbf{r}) + \mathbf{B}^2(\mathbf{r})). \tag{2.9}$$

Let us point out that, in this expression, $\mathbf{E}$ and $\mathbf{B}$ are operators acting in a Hilbert space. In particular, the electric field operator is defined as the canonically conjugate momentum to the vector potential. The differential representation of the electric field operator in the lattice is then given by [23, 27, 53]

$$E_{\mathbf{r},\mu} = -i\frac{\partial}{\partial A_{\mathbf{r},\mu}}. \tag{2.10}$$

Although we defined the parallel transporters in Eq. (2.5) in terms of the continuum gauge field, we can also write it in terms of its lattice counterpart $A_{\mathbf{r},\mu}$, namely,

$$U_{\mathbf{r},\mu} = \exp\left(iA_{\mathbf{r},\mu}\right). \tag{2.11}$$

Thus, the electric field operator $E_{\mathbf{r},\mu}$ and the gauge field operator $U_{\mathbf{r},\mu}$ satisfy the commutation relations:

$$[E_{\mathbf{r},\mu}, U_{\mathbf{r},\mu'}] = \delta_{\mathbf{r},\mathbf{r}'}\delta_{\mu,\mu'}U_{\mathbf{r},\mu}, \quad [E_{\mathbf{r},\mu}, U^{\dagger}_{\mathbf{r},\mu'}] = -\delta_{\mathbf{r},\mathbf{r}'}\delta_{\mu,\mu'}U^{\dagger}_{\mathbf{r},\mu}. \tag{2.12}$$

Therefore, the lattice counterpart of the electric field term in Eq. (2.9) can be written as

$$\sum_{\mathbf{r},\mu} E^2_{\mathbf{r},\mu}. \tag{2.13}$$

We also need to consider a gauge-field self-interaction, which would be related to the magnetic part of LGT Hamiltonian. Due to gauge invariance, only products of group elements along closed paths are allowed [13, 27, 196, 197]. The smallest of such paths are formed around the elementary *plaquettes* of the square lattice (see Fig. 2.1). Thus, one can consider the plaquette product

$$U_\square = U_{\mathbf{r},i} U_{\mathbf{r}+\hat{i},j} U^\dagger_{\mathbf{r}+\hat{j},i} U^\dagger_{\mathbf{r},j}, \tag{2.14}$$

from which the magnetic field energy density is recovered in the continuum limit [53]. Thus, including the minimal coupling between the fermionic matter field and the gauge field derived in the previous sections, the mass term of the fermions, and the two terms generating the dynamics of the gauge field discussed above, one arrives at a lattice formulation of quantum electrodynamics, namely [23]:

$$\begin{aligned} H_{\text{QED}} = &-t \sum_{\mathbf{r},\mu} (\psi^\dagger_{\mathbf{r}} U_{\mathbf{r},\mu} \psi_{\mathbf{r}+\hat{\mu}} + \text{h.c.}) + \sum_{\mathbf{r}} m_{\mathbf{r}} \psi^\dagger_{\mathbf{r}} \psi_{\mathbf{r}} + \frac{q^2}{2} \sum_{\mathbf{r},\mu} E^2_{\mathbf{r},\mu} \\ &- \frac{1}{4q^2} \sum_\square (U_\square + U^\dagger_\square), \end{aligned} \tag{2.15}$$

where the proportionality factors are obtained by enforcing the desired continuum limit.

2.1.4 Lattice version of Gauss law and superselection sectors

The local gauge symmetry of classical electrodynamics is formulated in terms of the Gauss law:

$$\nabla \cdot \mathbf{E}(\mathbf{r}) = \rho(\mathbf{r}), \tag{2.16}$$

which relates the divergence of the electric field $\mathbf{E}$ and the density of matter charges ρ at *every* point in space. This constraint is expected to hold in quantum electrodynamics as well. In the lattice, one can define the discrete divergence of the electric field operator as $\sum_\mu E_{\mathbf{r},\mu} - E_{\mathbf{r}-\hat{\mu},\mu}$, while the charge density is $\psi^\dagger_{\mathbf{r}}\psi_{\mathbf{r}}$.[2] The Hermitian operator that generates an infinitesimal gauge transformation at a site $\mathbf{r}$ is [23, 27, 53]

$$G_{\mathbf{r}} = \sum_\mu (E_{\mathbf{r},\mu} - E_{\mathbf{r}-\hat{\mu},\mu}) - \psi^\dagger_{\mathbf{r}}\psi_{\mathbf{r}}, \tag{2.17}$$

or, for the particular case of staggered fermions [27, 145, 204, 205]:

$$G_{\mathbf{r}} = \sum_\mu (E_{\mathbf{r},\mu} - E_{\mathbf{r}-\hat{\mu},\mu}) - \left(\psi^\dagger_{\mathbf{r}}\psi_{\mathbf{r}} - \frac{1-(-1)^{x+y}}{2}\right). \tag{2.18}$$

One can then write a general gauge transformation by means of a unitary operator [23, 26]

$$V = \prod_{\mathbf{r}} \exp(i\alpha_{\mathbf{r}} G_{\mathbf{r}}), \tag{2.19}$$

---

[2] For staggered fermions, the charge density reads $\psi^\dagger_{\mathbf{r}}\psi_{\mathbf{r}} - (1-(-1)^{x+y})/2$ [27, 145, 204, 205].

which acts as

$$V\psi_{\mathbf{r}}V^{\dagger} = V_{\mathbf{r}}\psi_{\mathbf{r}}, \qquad V\psi_{\mathbf{r}}^{\dagger}V^{\dagger} = \psi_{\mathbf{r}}^{\dagger}V_{\mathbf{r}}^{\dagger}, \qquad VU_{\mathbf{r},\mu}V^{\dagger} = V_{\mathbf{r}}U_{\mathbf{r},\mu}V_{\mathbf{r}+\hat{\mu}}^{\dagger}. \tag{2.20}$$

Due to the gauge symmetry, the local gauge transformation generators $G_{\mathbf{r}}$ commute with the Hamiltonian, that is,

$$[H, G_{\mathbf{r}}] = 0, \qquad \forall \mathbf{r}. \tag{2.21}$$

This equation implies that the eigenvalues $\{Q_{\mathbf{r}}\}$ of the operators $G_{\mathbf{r}}$ are local constants of motion under the time evolution generated by H. One can give these conserved quantities the physical meaning of *static background charges*, which satisfy the the quantum lattice version of Gauss law:

$$G_{\mathbf{r}}|\psi(\{Q_{\mathbf{r}}\})\rangle = Q_{\mathbf{r}}|\psi(\{Q_{\mathbf{r}}\})\rangle. \tag{2.22}$$

Because of the conservation of the static charge configurations $\{Q_{\mathbf{r}}\}$, the Hilbert space splits into so-called *superselection sectors* [110, 205]:

$$\mathscr{H} = \bigotimes_{\{Q_{\mathbf{r}}\}} \mathscr{H}\big(\{Q_{\mathbf{r}}\}\big), \tag{2.23}$$

with each $|\psi(\{Q_{\mathbf{r}}\})\rangle \in \mathscr{H}\big(\{Q_{\mathbf{r}}\}\big)$ satisfying Eq. (2.22). Importantly, different superselection sectors are not mixed by the dynamics.

We note that, even in the absence of *dynamical charges*, the divergence of the electric field operator may not vanish. Thus, one finds sometimes in the literature that "physical" or gauge-invaraint states are those that obey $G_{\mathbf{r}}|\psi\rangle = 0$ for all $\mathbf{r}$ [18, 23, 53]. However, all states in $\mathscr{H}$ are in fact gauge invariant, albeit with different global phases that depend on the static charge configuration of the superselection sector to which they belong [205]. As we will see in posterior sections throughout this thesis, interesting physical phenomena may occur in different sectors of an LGT.

2.1.5 Extension to the non-Abelian case

In order to make the generalization to non-Abelian groups, it is convenient to introduce some notions of *Lie groups* (see for example Ref. [5]). For the purpose of this explanation, a Lie group can be regarded as a continuous group generated by a Lie algebra, which is a space with a basis consisting of $\mathcal{N}$ generators T^a, that are close under commutations:

$$[T^a, T^b] = i\mathcal{C}_{abc}T^c, \tag{2.24}$$

where the so-called *structure constants* $\mathcal{C}_{abc}$ are real numbers. Note that in an Abelian theory the generators commute with each other, that is, $\mathcal{C}_{abc} = 0$. Also, here we work in the fundamental representation of the group. A group element is written as

$$U_{\mathbf{r},\mu} = \exp\left(iA^a_{\mathbf{r},\mu}T^a\right), \tag{2.25}$$

where $A^a_{\mathbf{r},\mu}$ are called *group parameters*. The equation above reduces to Eq. (2.11) for the Abelian U(1) group of the previous sections.

For the generalized momenta, one can define two sets of operators that are conjugate to the group parameters [23, 27]. Namely,

$$L_{\mathbf{r},\mu} = -i\dot{U}_{\mathbf{r},\mu}U^\dagger_{\mathbf{r},\mu}, \quad R_{\mathbf{r},\mu} = -iU^\dagger_{\mathbf{r},\mu}\dot{U}_{\mathbf{r},\mu}. \tag{2.26}$$

In the Abelian case, we would have $E_{\mathbf{r},\mu} = -i\dot{U}_{\mathbf{r},\mu}U^\dagger_{\mathbf{r},\mu} = -iU^\dagger_{\mathbf{r},\mu}\dot{U}_{\mathbf{r},\mu}$, which written in the differential representation reads as in Eq. (2.10). We can express Eq. (2.26) in terms of the group generators, that is,

$$L_{\mathbf{r},\mu} = L^a_{\mathbf{r},\mu}T^a, \quad R_{\mathbf{r},\mu} = R^a_{\mathbf{r},\mu}T^a. \tag{2.27}$$

The operators $\{L^a_{\mathbf{r},\mu}\}$, $\{R^a_{\mathbf{r},\mu}\}$ are called *left and right* generators of the group, as they satisfy the group's algebra [23, 27]:

$$[L^a_{\mathbf{r},\mu}, U_{\mathbf{r},\mu}] = T^aU_{\mathbf{r},\mu}, \quad [R^a_{\mathbf{r},\mu}, U_{\mathbf{r},\mu}] = U_{\mathbf{r},\mu}T^a, \tag{2.28}$$

$$[L^a_{\mathbf{r},\mu}, L^b_{\mathbf{r},\mu}] = -i\mathcal{C}_{abc}L^c_{\mathbf{r},\mu}, \quad [R^a_{\mathbf{r},\mu}, R^b_{\mathbf{r},\mu}] = i\mathcal{C}_{abc}R^c_{\mathbf{r},\mu}, \tag{2.29}$$

$$[L^a_{\mathbf{r},\mu}, R^b_{\mathbf{r},\mu}] = 0. \tag{2.30}$$

Thus, in close analogy to the Hamiltonian written for lattice quantum electrodynamics in Eq. (2.15), one can write down a non-Abelian LGT as a lattice version of quantum chromodynamics (with the parallel transporters being elements of the non-Abelian gauge group SU(n)) [18, 23, 27]:

$$\begin{aligned} H_{\text{QCD}} = &-t\sum_{\mathbf{r},\mu}(\psi^\dagger_{\mathbf{r}}U_{\mathbf{r},\mu}\psi_{\mathbf{r}+\hat{\mu}} + \text{h.c.}) + \sum_{\mathbf{r}} m_{\mathbf{r}}\psi^\dagger_{\mathbf{r}}\psi_{\mathbf{r}} + \frac{g^2}{2}\sum_{\mathbf{r},\mu}\left[\Big(\sum_a L^a_{\mathbf{r},\mu}\Big)^2 + \Big(\sum_a R^a_{\mathbf{r},\mu}\Big)^2\right] \\ &- \frac{1}{4g^2}\sum_{\square}\text{Tr}(U_\square + U^\dagger_\square). \end{aligned} \tag{2.31}$$

This Hamiltonian is gauge invariant by construction as it commutes with the gauge transformation generators that now read

$$G^a_{\mathbf{r}} = \sum_\mu (L^a_{\mathbf{r},\mu} - R^a_{\mathbf{r}-\hat{\mu},\mu}) - \psi^{i\dagger}_{\mathbf{r}}T^a_{ij}\psi^j_{\mathbf{r}}, \tag{2.32}$$

$$[G^a_{\mathbf{r}}, G^b_{\mathbf{r}'}] = i\delta_{\mathbf{r},\mathbf{r}'}\mathcal{C}_{abc}G^c_{\mathbf{r}}. \tag{2.33}$$

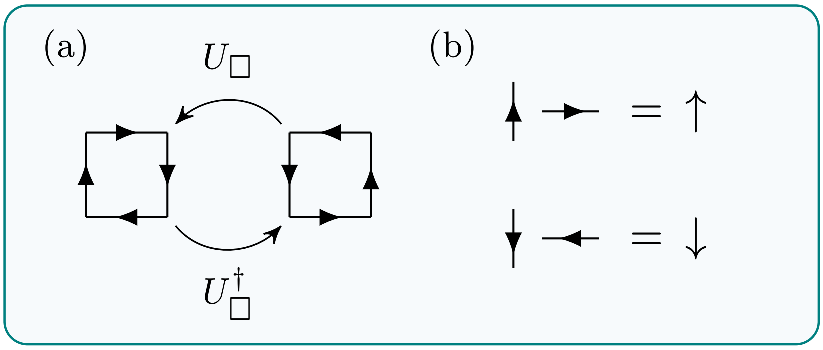

Figure 2.2: (a) In a flippable plaquette, the electric flux configuration winds around it, forming a loop. Such a plaquette can be 'flipped' upon applying the operators $U_\Box$ and $U_\Box^\dagger$, thereby reversing the direction of the electric flux loop, as illustrated here. (b) Convention to associate electric flux configurations with the spin states ↑ (flux pointing to the right or upward) and ↓ (flux pointing to the left or downward), in the $S = \frac{1}{2}$ QLM representation.

2.2 Quantum link models

The QLM formulation of LGTs can be seen as a generalization beyond Wilson's approach, in which Wilson's continuous classical parallel transporters are replaced by discrete quantum degrees of freedom, called *quantum links*. In spite of this, QLMs implement continuous gauge symmetries in an exact way [23]. While QLMs were firstly introduced in the context of high-energy physics [183, 206, 207], it turns out that they are also closely related to celebrated models in condensed matter physics such as quantum spin ice and quantum dimer models [23, 26, 44, 48, 49, 182]. From the experimental viewpoint, QLMs are well suited for both digital and analog quantum simulation using ultracold atomic gases in optical lattices, given the fact that, in this formulation, the link Hilbert space is finite-dimensional [23]. In this section, we introduce the Abelian U(1) QLM, whose nonequilibrium dynamics constitutes the subject of Chapter 4. We then study the connection to quantum dimer models, and finally, comment on the extension to non-Abelian QLMs.

2.2.1 The 2D U(1) QLM

The operators in a U(1) QLM are given by a finite-dimensional representation of the embedding algebra SU(2) [23, 26, 182], with both the quantum link operators and the electric field operators being defined in terms of quantum spin operators:

$$U_{\mathbf{r},\mu} = S^x_{\mathbf{r},\mu} + iS^y_{\mathbf{r},\mu} \equiv S^+_{\mathbf{r},\mu}, \quad U^\dagger_{\mathbf{r},\mu} = S^x_{\mathbf{r},\mu} - iS^y_{\mathbf{r},\mu} \equiv S^-_{\mathbf{r},\mu}. \tag{2.34}$$

$$E_{\mathbf{r},\mu} = S^z_{\mathbf{r},\mu}. \tag{2.35}$$

Thus, $U_{\mathbf{r},\mu}$ and $U^\dagger_{\mathbf{r},\mu}$ act as raising and lowering operators of the electric flux $E_{\mathbf{r},\mu}$, respectively. Due to the basic spin commutation relations: $[S^\alpha_{\mathbf{r},\mu}, S^\beta_{\mathbf{r}',\mu'}] = i\delta_{\mathbf{r},\mathbf{r}'}\delta_{\mu,\mu'}\epsilon_{\alpha\beta\gamma}S^\gamma_{\mathbf{r},\mu}$, the quantum link operators $U_{\mathbf{r},\mu}, U^\dagger_{\mathbf{r},\mu}$ and the electric field operator $E_{\mathbf{r},\mu}$ satisfy commutation relations of exactly the same form as those in Eq. (2.12) for Wilson's theory. Consequently, the Hamiltonian for the Abelian U(1) LGT in Eq. (2.15), the local gauge transformation generators in Eqs. (2.17) and (2.18), and the gauge transformations in Eq. (2.20), all retain their previous form. However, a significant difference with respect to Wilson's theory where $[U_{\mathbf{r},\mu}, U^\dagger_{\mathbf{r}',\mu'}] = 0$, is that in the U(1) QLM we have instead $[U_{\mathbf{r},\mu}, U^\dagger_{\mathbf{r}',\mu'}] = 2\delta_{\mathbf{r},\mathbf{r}'}\delta_{\mu,\mu'}E_{\mathbf{r},\mu}$, which again follows from the spin commutation relations. Besides, as we have mentioned, in the QLM formulation the link Hilbert space is finite-dimensional. To be precise, for a given finite-dimensional spin-S representation, the link Hilbert space has dimension $(2S+1)$. Remarkably, these differences do not alter the U(1) gauge symmetry of the theory.

In the U(1) QLM formulation, one can consider a 2D gauge-field Hamiltonian of the form [23, 26, 182]:

$$H_{\text{QLM}} = \frac{g^2}{2}\sum_{\mathbf{r},\mu} E^2_{\mathbf{r},\mu} - \sum_{\square}\Big[\mathcal{J}(U_\square + U^\dagger_\square) - \lambda(U_\square + U^\dagger_\square)^2\Big], \tag{2.36}$$

with $U_\square = S^+_{\mathbf{r},i}S^+_{\mathbf{r}+\hat{i},j}S^-_{\mathbf{r}+\hat{j},i}S^-_{\mathbf{r},j}$, and where we have also put a potential energy λ for flippable plaquettes, that is, plaquettes with a loop of electric flux winding around them (see Fig. 2.2). In the minimal $S = \frac{1}{2}$ representation, the electric-field energy is just an additive constant $E^2_{\mathbf{r},\mu} = (S^z_{\mathbf{r},\mu})^2 = \frac{1}{4}$, and hence can be omitted in the Hamiltonian (2.36). The magnetic-flux term, proportional to $\mathcal{J}$, acts as a kinetic-energy term, which inverts the electric flux around flippable plaquettes, while it annihilates non-flippable plaquettes. On the other hand, the potential-energy term, proportional to λ favors states with a larger number of flippable plaquettes for $\lambda < 0$. These terms are known in the literature as "ring-exchange" and "Rokhsar-Kivelson" interactions, respectively [23, 26].

The generators of infinitesimal U(1) gauge transformations, with which the Hamiltonian in Eq. (2.36) commutes, are in this case

$$G_{\mathbf{r}} = \sum_{\mu}(E_{\mathbf{r},\mu} - E_{\mathbf{r}-\hat{\mu},\mu}). \tag{2.37}$$

We will come back to this model in Section 4.1. However, let us mention here some of its equilibrium properties (see Fig. 2.3). At zero temperature, the model is confining for $\lambda/\mathcal{J} < 1$, while at high temperatures, $T > T_c$ it has a deconfining phase. Moreover, at some critical coupling λ_c, the model undergoes a weak first-order quantum phase transition that separates two confined phases with spontaneously broken translation symmetry. The phase at $\lambda < \lambda_c$ has also a spontaneously broken charge conjugation symmetry [23, 26, 182].

Let us also point out that for $D > 1$, a *pure* LGT, that is, an LGT with only gauge fields, such as that in Eq. (2.36), is in general a truly *interacting* theory, with the gauge fields exhibiting nontrivial dynamics even though there is no coupling to matter fields.

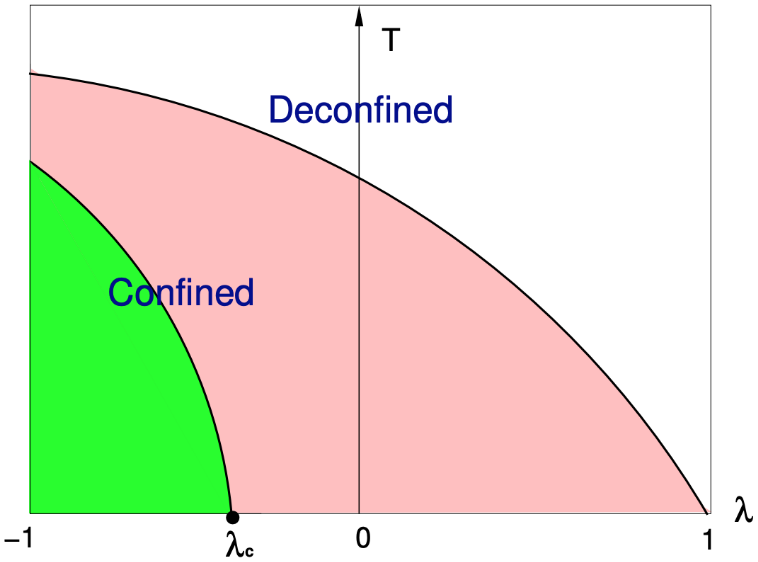

Figure 2.3: Schematic sketch of the equilibrium phase diagram in the T-λ plane. Here, $\mathcal{J}$ sets the energy scale. [*Adapted by permission from John Wiley and Sons: Annalen der Physik (Wiese [23]) Copyright (2013);* `https://doi.org/10.1002/andp.201300104`.]

This is to be contrasted to the continuum case, where for example the Hamiltonian in Eq. (2.9) describes an ensemble of free photons [53]. Pure LGTs have attracted quite some attention in condensed matter physics, where the quantum dimer model discussed below is a good example.

For an account on non-Abelian QLMs, the reader is referred to the specialized literature; see for example Refs. [23, 208].

2.2.2 Quantum dimer models

Quantum dimer models are effective descriptions of the short-range resonating-valence-bond states introduced by Anderson [209], which can realize valence-bond crystal or quantum spin liquid phases [7, 26]. The valence-bond picture was proposed to describe situations where the local couplings in a microscopic spin model are very strong, such that a spin wave-based picture is not expected to work. Instead, one considers that spins pair up into singlet pairs or valence bonds. When a valence-bond state has all valence bonds with sites at the same relative distance entering with the same amplitude, it then forms a resonating-valence-bond state [7]. Moreover, when the valence bonds in such a state are restricted to nearest-neighboring sites, one gets a short-range resonating-valence-bond state, whose underlying valence-bond configurations turn out to have a one-to-one correspondence with configurations of classical dimers such as the one in Fig. 2.4(a). Note that, in this model, the number of valence bonds is conserved, but the dimers can rearrange

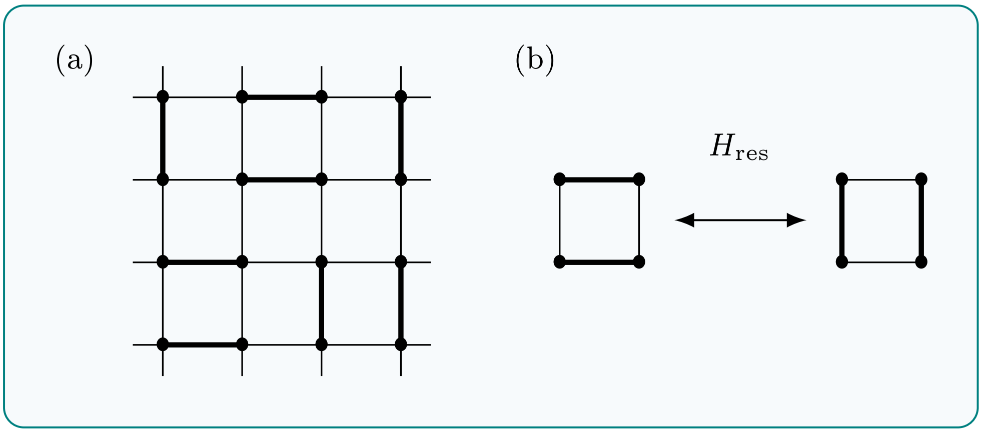

Figure 2.4: (a) A short-range valence-bond state on the 2D lattice. The thicker lines represent valence bonds or dimers. (b) The resonance process induced by the kinetic-energy term in Eq. (2.39).

themselves in a way that each site shares exactly one dimer with one of the neighboring sites [7, 26].

In quantum dimer models the degrees of freedom live on the links and are represented by integer-valued variables $D_{\mathbf{r},\mu}$, that can take either the value zero (no dimer) or the value one (dimer). According to the dimer covering constraint, every site has to belong to one and only one dimer; yet, dimers can be located at opposite links of a lattice plaquette (here, we restrict ourselves to a 2D square lattice, however, analogous constructions can be made for different geometries [7]). In general, the Hamiltonian of a quantum dimer model is the sum of a resonance term (kinetic energy) and a diagonal term (potential energy), that is,

$$H_{\text{QDM}} = H_{\text{res}} + H_{\text{diag}}. \tag{2.38}$$

The structure of such Hamiltonian will depend on the type of lattice. For the 2D square lattice, the resonance and diagonal terms are given by [44]:

$$H_{\text{res}} = -\mathcal{J} \sum_{\square} \Big(|=\rangle\langle \Vert| + |\Vert\rangle\langle =| \Big), \tag{2.39}$$

and

$$H_{\text{diag}} = \lambda \sum_{\square} \Big(|=\rangle\langle =| + |\Vert\rangle\langle \Vert| \Big). \tag{2.40}$$

In these equations, $|=\rangle$ and $|\Vert\rangle$ denote states with two dimers placed horizontally or vertically, respectively, on opposite links of a plaquette. The resonant term in Eq. (2.39) annihilates plaquettes with no dimer or only one dimer, since such states are orthogonal [7]. It also induces the resonance process illustrated in Fig. 2.4(b). On the other hand, the diagonal term in Eq. (2.40) assigns an energy λ to a pair of neighboring parallel dimers, while it gives an energy 0 to a plaquette in all states with no dimer or only one dimer on that plaquette. Now we proceed to reveal the relation between this model and the U(1) QLM of the last section in the $S = \frac{1}{2}$ representation. Indeed, one can map the flux variables $E_{\mathbf{r},\mu} = \pm\frac{1}{2}$ onto the dimer variables $D_{\mathbf{r},\mu} = 0, 1$, such that [182]

$$E_{\mathbf{r},\mu} = (-1)^{x+y}\Big(\frac{1}{2} - D_{\mathbf{r},\mu}\Big), \tag{2.41}$$

which, together with the dimer covering constraint $\sum_\mu (D_{\mathbf{r},\mu} + D_{\mathbf{r}-\hat{\mu},\mu}) = 1$, lead to a modified lattice divergence of the electric flux:

$$G_\mathbf{r} = \sum_\mu (E_{\mathbf{r},\mu} - E_{\mathbf{r}-\hat{\mu},\mu}) = (-1)^{x+y}. \tag{2.42}$$

Thus, the quantum dimer model can be described by exactly the same Hamiltonian of the QLM, but with an "unconventional" Gauss law corresponding to a staggered background of static charges ±1 [23, 182].

2.3 Ising gauge theories

Another important class of Abelian LGTs is that of $\mathbb{Z}_N$ LGTs, where we now consider a *discrete* gauge group. It turns out that this type of theories are also important for many interesting problems. For example, in high-energy physics, the $\mathbb{Z}_3$ case is relevant for the confinement in quantum chromodynamics [27, 199]. Besides, in condensed matter physics, $\mathbb{Z}_2$ or Ising LGTs are related to the QLM and quantum dimer model discussed above [7, 46, 47]. Furthermore, Kitaev's toric code model [10] is also a $\mathbb{Z}_2$ LGT that is relevant in the context of topological quantum computation. In this section, we focus only on $\mathbb{Z}_2$ or Ising LGTs. These theories were firstly introduced in 1971 by Wegner [194], whose main motivation was to show examples of phase transitions without a local order parameter, taking inspiration in the 2D planar model [13, 210, 211]. It is indeed found that in lattice theories endowed with a local invariance group, cannot spontaneously break. This is result is known as Elitzur's theorem [212] and applies not only to $\mathbb{Z}_2$ LGTs but also to theories with a continuous local symmetry group [13], such as the Abelian U(1) LGTs considered in previous sections.

As before, here we consider the quantum Hamiltonian formulation [13, 198, 199]. The Hamiltonian of the $\mathbb{Z}_2$ LGT is the sum of two parts: one acting on individual links ("kinetic-energy" term) and the other acting on plaquettes ("potential-energy" term), namely,

$$H_{\mathbb{Z}_2\mathrm{LGT}} = -g\sum_{\mathbf{r},\mu} \sigma^x_{\mathbf{r},\mu} - \frac{1}{g}\sum_{\mathbf{r}} \sigma^z_{\mathbf{r},i}\sigma^z_{\mathbf{r}+\hat{i},j}\sigma^z_{\mathbf{r}+\hat{j},i}\sigma^z_{\mathbf{r},j}, \tag{2.43}$$

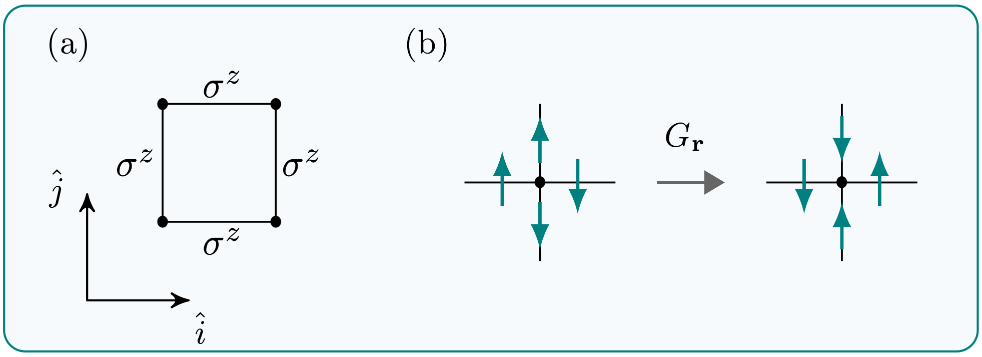

Figure 2.5: (a) Magnetic (flip) term in the $\mathbb{Z}_2$ LGT Eq. (2.43). (b) Local gauge transformation at site $\mathbf{r}$ generated by the operator $G_{\mathbf{r}}$ in Eq. (2.44), with the degrees of freedom (gauge fields) depicted as green arrows.

where $\sigma^x_{\mathbf{r},\mu}$, $\sigma^z_{\mathbf{r},\mu}$ are, respectively, the off-diagonal and diagonal Pauli matrices acting on the link $(\mathbf{r},\mu)$. The first term of this Hamiltonian is also referred to as the "electric-field" term, while the second term is a "magnetic" term (see Fig. 2.5).

The generators of $\mathbb{Z}_2$ local gauge transformations flip the values of σ^z on all links emanating from a given site $\mathbf{r}$ (see Fig. 2.5) and are given by

$$G_{\mathbf{r}} = \prod_{\pm\mu} \sigma^x_{\mathbf{r},\mu} = \sigma^x_{\mathbf{r},i}\sigma^x_{\mathbf{r}-\hat{i},i}\sigma^x_{\mathbf{r},j}\sigma^x_{\mathbf{r}-\hat{j},j}, \tag{2.44}$$

where $\sigma^x_{\mathbf{r},-\mu} = \sigma^x_{\mathbf{r}-\hat{\mu},\mu}$. For all sites $\mathbf{r}$, we have that these local operators commute with each other $[G_{\mathbf{r}}, G_{\mathbf{r}'}] = 0$ and with the Hamiltonian $[G_{\mathbf{r}}, H_{\mathbb{Z}_2\text{LGT}}] = 0$. Furthermore, the generators are Hermitian and obey $G^2_{\mathbf{r}} = \mathbf{1}$. Hence, their eigenvalues are ±1. This in turn means that here, the generalized Gauss law reads

$$G_{\mathbf{r}}|\psi\rangle = |\psi\rangle. \tag{2.45}$$

The eigenstates of the Hamiltonian (2.43) which satisfy this constraint are again referred to as the physical (gauge-invariant) states.

It is known [7, 13, 198] that the $\mathbb{Z}_2$ LGT in $D \geq 2$ has two phases: a weak-coupling, $g < g_c$, deconfiend phase, and a strong-coupling, $g > g_c$, confined phase. We will comment more on these phases in Section 2.4, but now let us analyze another important aspect of Ising gauge theories, namely, the *duality* with conventional Ising models.

2.3.1 Hamiltonian duality

Duality is a powerful concept in physics. In particular, it can be used to understand the phase structure and topological properties of an LGT [7, 13, 198]. Here we will see that a $\mathbb{Z}_2$ theory has a dual theory defined on the so-called dual lattice. This result actually applies to both global and local $\mathbb{Z}_2$ symmetries. One very well known example is 1D transverse-field Ising model, which is in fact self-dual [13, 198]. On the other hand, the Ising LGT defined by equation (2.43) has as dual theory the 2D transverse-field Ising model, as we will see below.

We start by finding the dual lattice, which for the square lattice it is also a square lattice with sites labeled by $\tilde{\mathbf{r}} = \mathbf{r} + (\hat{\imath} + \hat{\jmath})/2$. We then define the dual operators on the sites of the dual lattice. First, we have the so-called magnetic monopole operator [7, 13, 198], which for the present case is given by

$$\tau^z_{\tilde{\mathbf{r}}} = \prod_{(\mathbf{r}',\mu)\in\tilde{\gamma}(\tilde{r})} \sigma^x_{\mathbf{r}',\mu}, \tag{2.46}$$

where $\tilde{\gamma}$ is an open path in the dual lattice with endpoint at the dual site $\tilde{\mathbf{r}}$. Let us also define the plaquette operator as follows

$$\tau^x_{\tilde{\mathbf{r}}} = \sigma^z_{\mathbf{r},i}\sigma^z_{\mathbf{r}+\hat{\imath},j}\sigma^z_{\mathbf{r}+\hat{\jmath},i}\sigma^z_{\mathbf{r},j}. \tag{2.47}$$

It is a simple exercise to verify that the dual operators obey the same algebra of the Pauli matrices. Moreover, the Gauss law constraint of Eq. (2.45) is automatically satisfied by these definitions. Thus, writing the Hamiltonian in terms of the dual operators, one gets

$$H = -g\sum_{\tilde{\mathbf{r}},\mu} \tau^z_{\tilde{\mathbf{r}}}\tau^z_{\tilde{\mathbf{r}}+\hat{\mu}} - \frac{1}{g}\sum_{\tilde{\mathbf{r}}} \tau^x_{\tilde{\mathbf{r}}}, \tag{2.48}$$

which we identify with the anticipated 2D transverse-field Ising model.

Let us write the duality relation found above as follows

$$H_{\mathbb{Z}_2\mathrm{LGT}}(g) \equiv H_{\mathrm{TFIM}}(1/g). \tag{2.49}$$

This equation makes more explicit a very important general feature of duality transformations, namely, that they relate weakly coupled theories to strongly coupled theories. Let us note that thsi duality maps the broken symmetry phase of the Ising model onto the confined phase of the gauge theory ($g > g_c$), and the order parameter of the Ising model onto the $\mathbb{Z}_2$ magnetic-charge operator of the gauge theory. Therefore, one can picture the confining phase of the Ising gauge theory as a “condensate” of $\mathbb{Z}_2$ magnetic monopoles [7, 13, 198]. Let us finally point out that the sort of duality transformations discussed here for the 2D case can also be established in other dimensions. In particular, in $D = 3$ the $\mathbb{Z}_2$ LGT is actually self-dual [13, 194, 198]. Besides, Balian, Drouffe and Itzykson [200] also showed that a similar duality can be established between Ising gauge theories and Ising models when a external (longitudinal) field is added. The latter theory actually shares more connections with LGTs. Indeed, around the same time, McCoy and Wu [54, 55] build a quantum field theory based on the Ising model in a longitudinal field that was shown to be relevant for the problem of quark confinement.

2.4 Phases of LGTs

Although we have already mentioned a few properties regarding the phase diagram of the LGTs reviewed so far, in this section we revise in slightly more detail some of the main features of the confining and deconfining phases in Abelian LGTs.

2.4.1 Strong coupling: confinement

We first focus on the strong-coupling regime. Let us start with the $\mathbb{Z}_2$ LGT with Hamiltonian (2.43). The strong-coupling limit here refers to $g \gg 1$, and hence, one can treat the second term in Eq. (2.43) perturbatively in $1/g$. Clearly, when $g \to \infty$, the ground state is an eigenstate of the electric field operators $\{\sigma^x_{\mathbf{r},\mu}\}$. In this basis, the ground state is the state with $\sigma^x = +1$ on all links. Because of Gauss law [Eq. (2.45)], we note that gauge-invariant states must have, at most, an even number of links with $\sigma^x = -1$ at every lattice site. Moreover, the magnetic term in the Hamiltonian (2.43), will flip the values of σ^x around a plaquette from $+1$ to -1. Therefore, the excited states are closed loops of length ℓ on the lattice, on which $\sigma^x = -1$ [7, 198]. Now, since the energy cost of a single excited link is $2g$, the total energy of such a excited state is $\Delta E = 2g\ell$. Note that the energy of an elementary plaquette excitation is $\Delta E_\Box = 8g$, and thus, in this limit, the theory has a spectrum of excited states with a finite and large energy gap. For finite but large g, the most general ground state is a superposition of states with loops of varying length [7, 198]. For sufficiently large g the predominant contributions come from small loops, while loops of increasingly larger size become more relevant as the quantum phase transition at g_c is approached, with their size diverging as $g \to g_c$ [7].

To see that the system exhibits confinement in the strong-coupling phase, we compute the energy difference between the vacuum state (no electric charges) and that of an elementary *string*, that is, the ground state of a sector with two electric charges located at positions $\mathbf{r}_1$ and $\mathbf{r}_2$ (see Fig. 2.6). Such sector is defined by $Q = -1$ at $\mathbf{r}_1$ and $\mathbf{r}_2$, and $Q = +1$ anywhere else, with $Q_\mathbf{r}$ being the eigenvalue of the operator $G_\mathbf{r}$ [see Eq. (2.44)], and the ground state is a state with $\sigma^x = +1$ on every link, except on those along the shortest path $\gamma(\mathbf{r}_1, \mathbf{r}_2)$ connecting the two charges at $\mathbf{r}_1$ and $\mathbf{r}_2$. The energy of this string with respect to the vacuum is

$$\Delta E_{\text{string}} = \sigma \ell_{\text{string}}, \tag{2.50}$$

where $\sigma = 2g + \mathcal{O}(1/g)$ is the *string tension* (it has units of energy per unit length) and ℓ_{string} is the length of the string (in lattice units). This property, that the energy of the string connecting two charges grows linearly with the distance is known as *confinement*, as

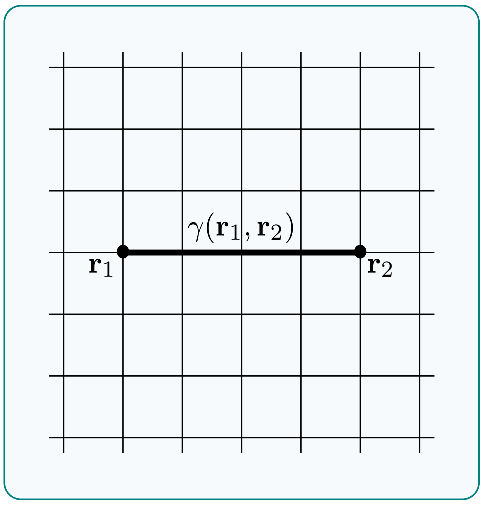

Figure 2.6: Confinement in the $\mathbb{Z}_2$ LGT: Schematic representation of the vacuum state plus two $\mathbb{Z}_2$ charges, $Q = -1$ (thereby respecting the global $\mathbb{Z}_2$ symmetry), placed at $\mathbf{r}_1$ and $\mathbf{r}_2$, which are connected by a string along the path $\gamma(\mathbf{r}_1, \mathbf{r}_2)$ that has $\sigma^x = -1$ on each link. In the confining phase of the theory, this string has an energy that grows linearly with the distance.

already mentioned. Considering a large but finite g will have the effect of inducing string fluctuations and decreasing the string tension [198], which should vanish as $g \to g_c$ [7].

Similar arguments apply to the other Abelian LGTs studied in this chapter. For instance, we can consider the U(1) LGT in Eq. (2.15). In fact, for simplicity, let us just consider the gauge-field part, that is,

$$H_{\mathrm{U(1)LGT}} = g \sum_{\mathbf{r},\mu} E^2_{\mathbf{r},\mu} - \frac{1}{g} \sum_{\mathbf{r},\mu} \cos(A_{\mathbf{r},i} + A_{\mathbf{r}+\hat{\imath},j} - A_{\mathbf{r}+\hat{\jmath},i} - A_{\mathbf{r},j}), \tag{2.51}$$

where we simplified the magnetic term, in a way that is possible for the Abelian case [13, 27]. The generators of the local gauge transformations in this case read

$$G_{\mathbf{r}} = \sum_{\mu} (E_{\mathbf{r},\mu} - E_{\mathbf{r}-\hat{\mu},\mu}). \tag{2.52}$$

Just like in the $\mathbb{Z}_2$ example, here we work in a basis in which the electric field operators $E_{\mathbf{r},\mu}$ are diagonal, and treat the magnetic term perturbatively in $1/g$. Since we consider a *compact* U(1) LGT, that is, $A_{\mathbf{r},\mu} \in [0, 2\pi)$, the eigenvalues of the electric field operators $E_{\mathbf{r},\mu}$, denoted by $e_{\mathbf{r},\mu}$, take values on the integers [27]. Thus, in the limit $g \to \infty$, the ground state has $e_{\mathbf{r},\mu} = 0$ everywhere. Moreover, the sources of the electric field, $Q_{\mathbf{r}}$ [eigenvalues of $G_{\mathbf{r}}$ in Eq. (2.52)], are also integer valued and satisfy the generalized Gauss law written in Eq. (2.22). We now consider once again two charges $\pm Q \in \mathbb{Z}$ (thereby respecting the global U(1) symmetry of the theory) placed at sites $\mathbf{r}_1$ and $\mathbf{r}_2$ as in Fig. 2.6. The ground state in this particular sector has $e_{\mathbf{r},\mu} = 0$ everywhere, except on the links on the shortest path $\gamma(\mathbf{r}_1, \mathbf{r}_2)$ connecting the two sources. Instead, on the links of such path

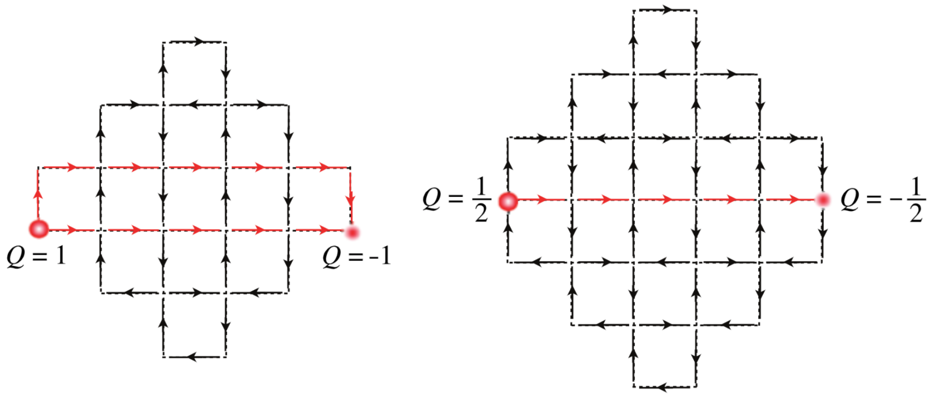

Figure 2.7: Confinement in the 2D U(1) QLM: Schematic illustration of possible strings of electric flux between a charge-anticharge pair, with $Q = \pm 1$ (left) and $Q = \pm\frac{1}{2}$ (right). [*Reprinted by permission from Elsevier: Annals of Physics (Marcos et al. [26]) Copyright (2014);* `https://doi.org/10.1016/j.aop.2014.09.011`.]

we have $e = Q$. The energy of this state is found to be once more a linear function of the distance between the static charges, and therefore, this theory is also confining in the strong-coupling regime.

Finally, as for the 2D U(1) QLM in Eq. (2.36) (in the $S = \frac{1}{2}$ representation), let us just mention that here the confining strings may display unusual features [23]. For example, the strings connecting two external charges $Q = \pm 2$ separate into four mutually repelling strands, each one carrying a fractional electric flux $\frac{1}{2}$ [23]. Similarly, strings connecting static charges $Q = \pm 1$ split into two strands as schematically illustrated in Fig. 2.7.

2.4.2 Weak coupling: deconfinement

We now consider the weak-coupling limit $g \ll 1$. Let us consider again the $\mathbb{Z}_2$ LGT. At $g = 0$ the unperturbed Hamiltonian is now the magnetic term in Eq. (2.43), and thus it is convenient to work in the basis of eigenstates of the vector potentials $\{\sigma^z_{\mathbf{r},\mu}\}$. The ground state thus lives in the sector where all plaquette operators are equal to one on all the plaquettes and "magnetic excitations" are created by the monopole operator $\tau^z_{\mathbf{r}}$ [Eq. (2.46)] [7], which creates a couple of deconfined $\mathbb{Z}_2$ "monopoles" at the ends of the string $\tilde{\gamma}(\tilde{\mathbf{r}})$. This corresponds to flipping the plaquettes at the ends of such string from $+1$ to -1. Besides, the theory has also "electric excitations". To see this, it is convenient to work in the basis of eigenstates of $\{\sigma^x_{\mathbf{r},\mu}\}$. As we said for the confined case, the most general ground state is a superposition of closed loops on which $\sigma^x = -1$. In the strong-coupling regime, such loops are typically of finite size, however, as we approach the deconfining phase, bigger and bigger loops start to "proliferate" [7, 198]. In the extreme case $g = 0$, the vacuum state is thus an equal-weight superposition of loops of all sizes [7]. It turns out that this is closely related to the fact that the deconfined phase of the $\mathbb{Z}_2$ gauge theory is in fact a *topological phase* [7, 213]. To see that this phase is actually deconfining, let us note that for the configuration with two sources at sites $\mathbf{r}_1$ and $\mathbf{r}_2$, the most general ground state consists of a linear superposition of all possible closed loops and all possible strings connecting the charges (as opposed to the confining phase that only includes the shortest of such strings), since the plaquette operator only deforms the string when acting on it [7, 198]. At $g = 0$, this state has exactly the same energy as the vacuum state, and hence, there is no energy cost of placing two charges at a distance R from each other, that is, $\Delta E(R) = 0$. At finite but small g, we get a finite energy cost when adding corrections to the expansion in powers of g^2. Concretely, the following long-range behavior is found [7]:

$$\Delta E(R) = 2E_0(g) + V(g, R), \tag{2.53}$$

where $E_0(g) \sim g^2 + \mathcal{O}(g^4)$, is the self-energy of the charges and vanishes as $g \to 0$, and $V(g, R)$ is an *effective interaction* between the charges that, for the case at hand, is short-ranged [7]. Since $E_0(g)$ does not depend on the distance and $V(g, R)$ is exponentially small at large R, separating the charges costs a finite amount of energy and we say that this phase is *deconfined*.

In the case of a U(1) Wilson's gauge theory, the weak coupling regime corresponds to the Coulomb phase [13, 53]. In this phase, the fluctuations of the gauge field are suppressed by the plaquette term in the LGT Hamiltonian. Moreover, it can be proved that the potential of a pair of sources with opposite charge separated by a distance R is given by Coulomb law

$$V(R) \sim \frac{1}{R}, \tag{2.54}$$

in a three-dimensional space [53, 214]. In fact, using a renormalization group argument, Peskin [215] showed that the Coulomb law is expected as a universal feature in all dimensions at the quantum critical point.

As for the U(1) QLM, we have already said that at high temperatures there exists a deconfed phase as well (see Fig. 2.3). In fact, in 3D it has been found that the model has a Coulomb phase, too, at least for a sufficiently large spin representation [216], which is interpreted as a spin liquid in the condensed matter context [23, 48].

2.5 Quantum simulation of LGTs

One of the main motivations in recent years behind many theoretical studies in quantum many-body theory, in general, is the remarkable progress achieved in experiments in the field of quantum simulation [150, 151], which can be roughly defined as simulating a quantum system by quantum mechanical means [151], a pioneering idea initially proposed by Feynman [217]. As mentioned in the introduction, there are two main avenues when it comes to quantum simulation: analog and digital. In analog quantum simulation, the Hamiltonian to be simulated H_{sys} is directly mapped onto the Hamiltonian of the simulator

H_{sim}, that is,

$$H_{\text{sys}} \leftrightarrow H_{\text{sim}}. \tag{2.55}$$

On the other hand, in digital quantum simulation the unitary evolution is implemented through a sequence of short quantum operations. This can be achieved by decomposing the time-evolution operator e^{-iHt} using the Trotter expansion [18, 33, 151]:

$$\mathrm{e}^{-iHt} \simeq \left(\prod_{\kappa=1}^{M} \mathrm{e}^{-iH_\kappa t/n} \right)^n, \qquad H = \sum_{\kappa=1}^{M} H_\kappa, \tag{2.56}$$

where the individual terms H_κ describe local interactions. Thus, we can think of the time evolution of the system as a sequence of local gates acting on a few qubits.

Among the different platforms for building quantum simulators, we encounter ultracold atoms in optical lattices [155], trapped ions [156, 157], superconducting circuits [158], and photons [159]. While these technologies have allowed for a highly controllable and precise simulation of several types of closed quantum many-body systems out-of-equilibrium; see for instance Refs. [160–181], the realization of LGTs still represents a big challenge for quantum simulation, since enforcing gauge invariance is a very difficult task. There are, however, some recent noticeable proof-of-principle examples of quantum simulating LGTs [33–41]. In this section we briefly discuss the strategies for implementing LGTs in quantum simulators and review the main achievements reported in some of the latter experiments as well as other experiments dealing with phenomenology related to LGTs.

Let us comment on some of the main strategies for engineering gauge symmetries in quantum simulation. One approach consists of imposing an *energy penalty* to gauge variant states, such that the low-energy physics takes place only on the gauge invariant Hilbert space [18]. This is achieved as follows. Given a set of commuting gauge symmetry generators $\{G_{\mathbf{r}}\}$, one considers a Hamiltonian with the following form:

$$H = VH_0 + \lambda H_1, \qquad H_0 := \sum_{\mathbf{r}} G_{\mathbf{r}}^2, \tag{2.57}$$

with $V > 0$. Thus, in the limit $V \gg \lambda$ all states that violate Gauss law have an energy $E \geq V$ and the low-energy physics is confined to the gauge invariant sector of the Hilbert space. The dynamics in this regime is driven by H_1, which can be gauge variant. In this case, the gauge-invariant Hamiltonian is obtained perturbatively [18]. This means gauge invariance is not perfectly implemented. In fact, for Abelain LGTs, such as the U(1) and $\mathbb{Z}_2$ theories, it is found that when gauge-variant terms are present, gauge violation will accumulate perturbatively at short times before proliferating at very long times [218]. However, by putting an energy penalty to processes that drive the dynamics away from the initial gauge-invariant sector, such proliferation can be suppressed up to infinite times [218] (Fig. 2.8).

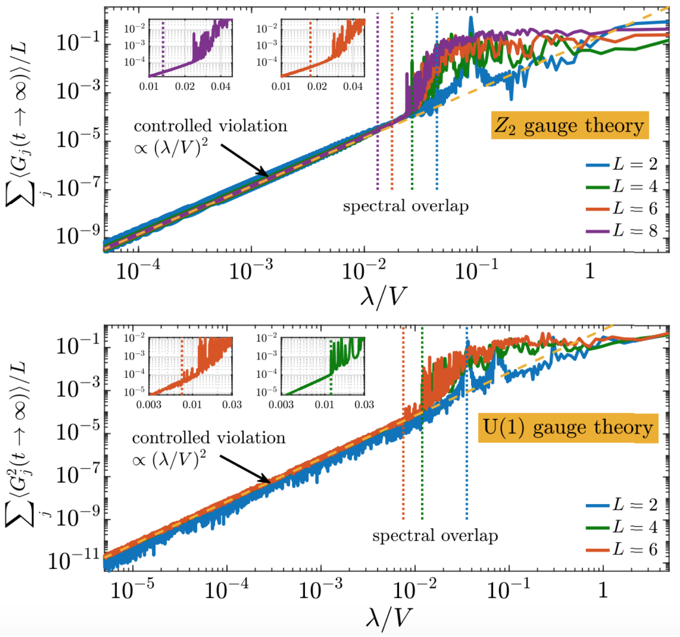

Figure 2.8: Plots of the infinite-time Gauss law violation for $\mathbb{Z}_2$ and U(1) LGTs in one dimension similar to the theories studied in this chapter. These numerical results for fixed λ show how energy penalties can keep the gauge invaraince violation under control in the infinite-time limit. This is the regime at large V where the gauge invariance violation is controlled and scales down with $(\lambda/V)^2$. [*Figure from Ref. [218]*; `https://doi.org/10.1103/PhysRevLett.125.030503`.]

This approach was, for example, used in a recent experiment by Yang et al. [41], mentioned in the previous chapter, where gauge invariance was quantified for the first time experimentally for a 1D QLM in the $S = \frac{1}{2}$ QLM representation:

$$H_{\text{1D-QLM}} = -iw \sum_r (\psi_r^\dagger S^+_{r,r+1} \psi_{r+1} + \text{h.c.}) + m \sum_r (-1)^r \psi_r^\dagger \psi_r. \tag{2.58}$$

While the approach of energy punishment is easily applied to Abelian LGTs, the situation becomes considerably more complicated for non-Abelian theories, where fine-tunning problems may arise due to the fact that generators do not commute with each other [18].

Another type of protocols to protect gauge invariance use classical noise, which is introduced in a controlled manner via external fields or via intrinsic dissipation channels. In the context of constrained models, and LGTs in particular, the *quantum Zeno dynamics* approach can be used to engineer constraints corresponding to Gauss law in both Abelian and non-abelian cases [18, 219]. Another approach for analog quantum simulation exploits *microscopic symmetries* of the simulator and combines them with spatially arranged potentials in such a way that the emerging dynamics is gauge invariant up to very high energy scales [18, 21, 22, 25].

Let us also mention here a coupled of experiments in analog quantum simulation using interacting bosons on dynamical lattices [30]. In particular, $\mathbb{Z}_2$ Bose-Hubbard-type models have been formulated and studied both theoretically [220] and experimentally with ultracold atoms in periodically driven double-well potentials [39]. This type of models are very rich, even in the absence of gauge invariance, as they might host interesting topological features [30, 221, 222]. Another experiment in similar setting and also using a Floquet engineering approach (periodic driving) was reported in Ref. [38], where density-dependent Peierls phases were realized and measured through the coupling of dynamical gauge fields to matter.

Regarding digital quantum simulation, there is no need to enforce local constraints, since the Hamiltonian is gauge invariant by definition. There is however one main difficulty with this approach, namely, to efficiently decomposed multi-spin interactions into a sequence of local gates [18]. Nevertheless, this approach has been used successfully for the quantum simulation of LGTs. One prominent example is the pioneering experiment by Martinez et al., reported in Ref. [33]. This experiment constitutes the first digital quantum simulation of an LGT in a trapped ion setup. Concretely, the authors of this experiment considered the Schwinger model in the Kogut–Susskind Hamiltonian formulation, that is, the 1D version of the Hamiltonian in Eq. (2.15) without the plaquette term:

$$H_{\text{Schwinger}} = -iw\sum_r (\psi_r^\dagger U_{r,r+1}\psi_{r+1} + \text{h.c.}) + J\sum_r E_r^2 + m\sum_r (-1)^r \psi_r^\dagger \psi_r, \tag{2.59}$$

with the generators of the local gauge symmetry given by Eq. (2.18).

It turns out that for this 1D theory, the gauge degrees of freedom can be integrated out analytically thanks to Gauss law [28] (see also Section 4.2), giving rise to a pure matter model. Further, using a Jordan-Wigner transformation the resulting model can be recast as a unconventional spin model with single-spin, two-spin and long-range spin-spin terms (the gauge fields are included implicitly in the long-range interactions). In this experiment the real-time dynamics of the spontaneous particle-antiparticle pair creation from the bare vacuum could be accessed; see Fig. 1.1. This particularly remarkable as such dynamical process is out of reach for conventional Markov Chain Monte Carlo methods due to a sign problem [148, 149].

Let us note that trapped-ion quantum simulators are well suited for the implementation of long-range interacting models like the one encoding the Schwinger model [28, 33]. Also, the experiment was done in four lattice sites, that is, using 4 qubits (although the protocol can be realized in a scalable fashion), and implemented each time step with a sequence of over 200 gate operations [28, 33]. Further, since the experiment dealt with a small system size, it was possible to compute the entanglement generated during the process of particle production using a measurement of the density matrix for the associated spin system.

Another quantum simulation of the Schwinger model and the process of spontaneous creation and destruction of pairs of charges was performed by Kokail et al. [37], in an experiment in which a programmable trapped-ion quantum computer with 20 quibits was employed as a quantum co-processor. This work constitutes an example of a *hybrid classical–quantum variational algorithm* (see for instance Ref. [30]), in which a feedback loop is introduced between a classical computer and a quantum co-processor to produce the result.

A recent experiment that attracted attention in the field of quantum simulation was carried out by Bernien et al. [169]. In this work, the many-body dynamics of a Ising-type system was probed on a 51-qubit quantum simulator based on Rydberg atoms. Concretely, the Hamiltonian of such system is

$$H_{\text{Rydberg}} = \sum_i (\Omega\sigma_i^x + \delta\sigma_i^z) + \sum_{i<j} V_{i,j} n_i n_j, \tag{2.60}$$

where $n_i = (\sigma_i^z+1)/2$, $\sigma_i^{x/z}$ are the Pauli matrices at site i, 2Ω and 2δ are the Rabi frequency and the detuning of the laser excitation, respectively, and $V_{i,j}$ is the interaction strength between atoms at sites i, j in their Rydberg states [31, 169]. For this kind of systems, the interaction is strong at short distances and decays as $1/R^6$ at large distances. Particularly, the situation considered in [169] was such that the nearest-neighbor term $V_{i,i+1}$ was much larger than all other energy scales. This gives rise to the so-called Rydberg blockade effect [223], in which neighboring atoms cannot be simultaneously in their excited Rydberg state. This can be written as a local constraint $n_i n_{i+1} = 0$ [31]. In this regime, the Hamiltonian in Eq. (2.60) reduces to the Fendley, Sengupta, and Sachdev Hamiltonian [31]:

$$H_{\text{FFS}} = \sum_i (\Omega\sigma_i^x + 2\delta n_i). \tag{2.61}$$

The focus of the original work by Bernien et al. [169] was on probing the many-body dynamics of this type of systems. In particular, they observed phase transitions into spatially ordered states that break various discrete symmetries and found a very slow dynamics when performing rapid quantum quenches across the phase transition (left panel in Fig. 1.2). It turns out that the system in Eq. (2.61) can be exactly mapped, by means of a unitary transformation, to a 1D U(1) QLM like the one in Eq. (2.58), as reported in Ref. [31]. In particular, this allowed to link the persistent oscillations in the Rydberg system to the phenomenon of string inversion in the LGT (right panel in Fig. 1.2).

Finally, let us mention the recent experiment by Tan et al. [181]; see Fig. 2.9. As we have already mentioned, it turns out that quantum Ising models share deep connections with LGTs. In particular, the phenomenon of *dynamical confinement* can be realized in quantum Ising chains where domain walls get confined by either symmetry-breaking fields [55, 57, 68] or long-range interactions [70] (see also Chapter 5). A crucial consequence of such connections is that they make it simpler to experimentally study the

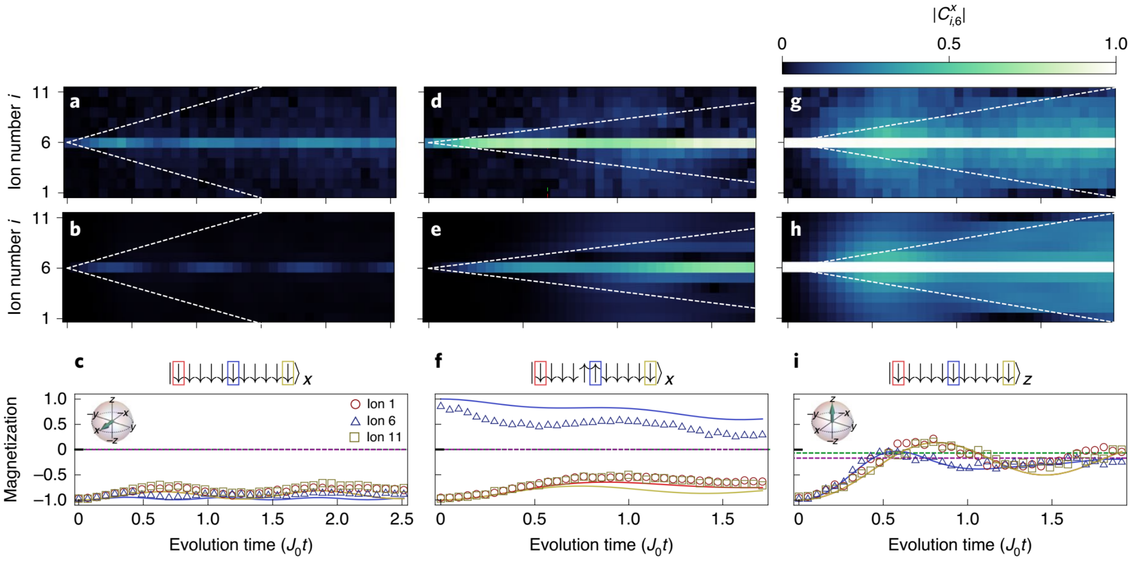

Figure 2.9: Confinement dynamics in a long-range Ising model realized in a trapped-ion quantum simulator. Domain wall get confined due to the long-range interactions in analogy to the phenomenon of quark confinement in high-energy physics. This confinement can be directly observed in the form a bend light cone of correlations shown in the upper panel. [*Adapted by permission from Springer Nature: Nature Physics (Tan et al. [181]) Copyright (2021);* `https://doi.org/10.1038/s41567-021-01194-3.`]

phenomenology of LGTs with quantum simulators, since the dynamics in spin chains are simpler to implement in this type of settings, and have, in fact, already been successfully studied in various quantum simulator experiments [167, 169–172, 174–176, 179]. Particularly, the experiment in Ref. [181] reported the observation for the first time of domain-wall confinement in a long-range Ising model [see Eq. (5.2) in Section 5.1.1] implemented in a trapped-ion quantum simulator. This work thus further demonstrates the capability and versatility for studying the phenomenology of LGTs with quantum simulators, with future perspectives in phenomena such as string breaking dynamics, which is the subject of Chapter 5 (see also Ref. [1]), and particle collisions that have also been investigated in quantum Ising models [103–105].

Chapter 3

Variational classical networks for quantum many-body dynamics

Some parts of this chapter are based on Ref. [3].

Most of the LGTs and quantum spin models that we have encountered so far, form part of the broader class of *strongly correlated quantum systems*. As such, apart from rather exceptional cases, in general, it is practically impossible to obtain exact analytical results and one must make use of numerical calculations. This is particularly the case when solving the nonequilibrium dynamics in such strongly interacting systems. In the last decades the development of powerful computational techniques has seen, indeed, impressive progress, largely motivated by experimental progress in realizing and controlling isolated quantum systems far away from equilibrium [33, 37–41, 160–181]. The majority of the advances have been achieved for 1D systems, for which there exist now a set of reliable methods that can simulate efficiently the dynamics of lattice models. The primary example of such techniques is tensor network algorithms such as the time-dependent density matrix renormalization group (tDMRG)—or its variants: time-evolving block decimation (TEBD) and time-evolved matrix product states (tMPS)—[224–231], which uses a matrix product state [232–234] representation of the wave function and solves the dynamics, for instance, via a Trotter decomposition of the evolution operator. However, this approach is generally restricted due to a rapid growth of entanglement, and a substantial increment of its computational complexity in higher dimensions. A recent alternative consists of encoding quantum states in various types of networks of classical degrees of freedom, such as artificial neural networks (ANNs) [188, 189, 235–241] and perturbative classical networks (pCNs) [187]. In addition to these methods, one can also employ exact diagonalization (ED) techniques; see for example [242], which allow for a numerically exact solution for arbitrary long times, although it is limited to relatively small system sizes. On the other hand, the description of quantum dynamics in higher dimensions faces, in general, even more severe limitations. In spite of a few very recent efforts in two dimensions using tensor networks [243–252], artificial neural networks [189, 237–239], or numerical linked cluster expansion [253], solving the quantum dynamics of 2D (and higher-dimensional) interacting systems remains one of the central challenges in computational quantum physics.

In this chapter, we present a numerical framework that allows for an efficient solution of the dynamics of quantum lattice models in one and higher dimensions. In this method, the many-body wave function amplitudes are represented in terms of complex network of classical spins akin to ANNs. The links or couplings among the spins in these networks are taken as variational parameters, which are optimized via a time-dependent variational principle (TDVP) [188, 254] (see also Section 3.4.2). The variational wave functions introduced in this approach are dubbed *variational classical networks* (VCNs). We will study VCNs at length in the last part of this chapter, namely, in Section 3.5. Before reaching this point, however, we will revise some other state-of-the-art computational methods. Concretely, exact diagonalization techniques constitute the subject of Section 3.2; next, the main ideas of time evolution with matrix product states are explained in Section 3.3; finally, we discuss the framework for computing time evolution with classical networks, in general, in Section 3.4, preparing the stage for the last section on VCNs, which is the method of choice to study the quantum dynamics of a 2D interacting LGT in Chapter 4.

3.1 The complexity of the quantum many-body dynamics problem

The problem at hand consists of solving the many-body time-dependent Schrödinger equation

$$H|\psi(t)\rangle = i\hbar\frac{\partial}{\partial t}|\psi(t)\rangle, \tag{3.1}$$

where H is the Hamiltonian[1] of the system under study and $|\psi(t)\rangle$ is the many-body wave function. In the following, we will consider units in which $\hbar = 1$. The inherent problem in solving Eq. (3.1) is that, the computational effort required to find a numerically exact solution, in general, grows *exponentially* with the number of degrees of freedom. Indeed, let us say that we attempt a direct numerical integration of Eq. (3.1) after expressing it in an adequate basis. Then, to perform the numerical integration, we would need to make a discretization on a d-dimensional grid, where we take M points on each direction. Thus, the total number of points to be considered is M^{dN}, for a system of N particles.

Another way to look at this problem is to expand the wave function in a given basis. Let us consider, for example, a system of N spin-1/2 degrees of freedom and use the computational basis of spin configurations $s = (s_1, s_2, \cdots, s_N)$, with $s_i = \uparrow, \downarrow$. The wave function can be written as

---

[1] Here, we will only consider time-independent Hamiltonians.

$$|\psi(t)\rangle = \sum_{\{s\}} \psi(s,t)|s\rangle, \tag{3.2}$$

where the *amplitudes* $\psi(s,t) := \langle s|\psi(t)\rangle$ contain the full information about the system, from which, in principle, all physical quantities can be computed. The sum in Eq. (3.2) runs over all spin configurations, which means that one would need to compute and store 2^N amplitudes $\psi(s,t)$ for the considered system with N spin-1/2 degrees of freedom.

The exponential complexity exposed above also appears when dealing with stationary problems. Thus, overcoming such an exponential wall is one of the main challenges in quantum many-body theory and related fields. In the following sections, we present a short introduction to some of the most successful and promising methods for solving the real-time dynamics of strongly interacting quantum models. Let us mention that, our discussion will be restricted to *closed*[2] quantum systems, since this is the class of models that we will be dealing with in the rest of this thesis.

3.2 Exact diagonalization

We begin our review on numerical techniques by presenting what is perhaps the most direct approach (besides the direct numerical integration scheme briefly sketched in the previous section), namely, *exact diagonalization.* In short, the idea behind ED consists of constructing a complete representation of the computational basis and the Hamiltonian matrix, which is then diagonalized numerically. When this is achieved, one has then access to the full knowledge of the system under consideration, since any static or dynamical observable can be computed if we have at our disposal all the eigenvalues and eigenstates of the Hamiltonian. Let us understand how this works for the case of the real-time evolution. In the presentation given below, we follow Refs. [242, 255].

3.2.1 Exact evolution

The eigenvalue problem for the Hamiltonian at hand is

$$H|\alpha\rangle = \epsilon_\alpha|\alpha\rangle, \tag{3.3}$$

where $\{\epsilon_\alpha\}$ and $\{|\alpha\rangle\}$ are the eigenvalues and eigenstates of H, respectively.

Now the formal solution to Eq. (3.1) is given by

$$|\psi(t)\rangle = \mathrm{e}^{-iHt}|\psi(0)\rangle. \tag{3.4}$$

---

[2] A *closed* quantum system is a quantum system that is not in contact with an external reservoir or measuring device.

Let us suppose that we have solved the eigenvalue problem in Eq. (3.3). Then, we can expand the initial state $|\psi(0)\rangle$ in terms of eigenstates $\{|\alpha\rangle\}$, as they form a complete basis. We have

$$|\psi(0)\rangle = \sum_{\alpha} a_{\alpha}|\alpha\rangle, \tag{3.5}$$

where $a_{\alpha} := \langle\alpha|\psi(0)\rangle$. Inserting Eq. (3.5) into Eq. (3.4) and using Eq. (3.3), one gets

$$|\psi(t)\rangle = \sum_{\alpha} a_{\alpha}\mathrm{e}^{-i\epsilon_{\alpha}t}|\alpha\rangle. \tag{3.6}$$

Hence, having access to all the eigenvalues and eigenstates would allows us to compute the real-time evolution of any observable using Eq. (3.6) in the expectation value of the corresponding Hermitian operator $\langle\psi(t)|O|\psi(t)\rangle$.

From a practical point of view, however, we would need to express the eigenvalue problem in Eq. (3.3) in a matrix form. Let us denote by $\mathsf{H} \equiv \{H_{mn} := \langle m|H|n\rangle\}$ the matrix representation of the Hamiltonian H in some arbitrary, complete basis $\{|n\rangle\}$ (which could be, for example, the computational basis). The eigenvalue problem is then solved numerically for this matrix using standard libraries. The output the set of eigenenergies $\{\epsilon_{\alpha}\}$ and eigenvectors $\{|\alpha\rangle\}$. The change of basis that diagonalizes H is then written using a unitary matrix S whose columns are the normalized eigenvectors $|\alpha\rangle$, that is, $\mathsf{S}_{n\alpha} := \langle n|\alpha\rangle$ is the n-th component of the α-th eigenvector, and we get

$$\mathsf{S}^{\dagger}\mathsf{H}\mathsf{S} = \mathrm{diag}(\epsilon_{\alpha}). \tag{3.7}$$

In practice, one also starts normally with the initial state expressed in terms of the considered basis

$$|\psi_0\rangle = \sum_{n}\langle n|\psi_0\rangle|n\rangle \equiv \sum_{n} c_n|n\rangle. \tag{3.8}$$

We want to find the time-evolved amplitudes $c_n(t)$ that give the solution $|\psi(t)\rangle$ in this basis as well

$$|\psi(t)\rangle = \sum_{n} c_n(t)|n\rangle. \tag{3.9}$$

This is achieved using the spectral decomposition, Eq. (3.6). One gets

$$|\psi(t)\rangle = \sum_{n}\sum_{\alpha} a_{\alpha}\mathrm{e}^{-i\epsilon_{\alpha}t}|n\rangle\langle n|\alpha\rangle = \sum_{n}\Big(\sum_{\alpha}\mathsf{S}_{n\alpha}a_{\alpha}\mathrm{e}^{-i\epsilon_{\alpha}t}\Big)|n\rangle. \tag{3.10}$$

Comparison with Eq. (3.9) then yields

$$c_n(t) = \sum_{\alpha}\mathsf{S}_{n\alpha}a_{\alpha}\mathrm{e}^{-i\epsilon_{\alpha}t}. \tag{3.11}$$

Also, note that

$$a_\alpha = \langle\alpha|\psi_0\rangle = \sum_n \langle\alpha|n\rangle\langle n|\psi_0\rangle = \sum_n \mathsf{S}^*_{\alpha n} c_n. \tag{3.12}$$

We have now a well-formulated numerical problem. In summary, we start by numerically diagonalizing the matrix H. This allows us to construct the matrices S and $\mathrm{diag}(\mathrm{e}^{-i\epsilon_\alpha t})$. Next, the solution, Eq. (3.9), is found by performing the matrix multiplications in Eqs. (3.11) and (3.12).

3.2.2 Prescription to perform an ED calculation

Let us explain now the basic steps to perform an ED calculation. To fix ideas, we shall consider the 1D transverse-field Ising model (TFIM):

$$H = -J \sum_{i=0}^{N-1} \sigma_i^z \sigma_{i+1}^z - h \sum_{i=0}^{N-1} \sigma_i^x, \tag{3.13}$$

where the coupling J sets the overall energy scale, h is the strength of the transverse field, and $\sigma_i^{x/z}$ are the Pauli matrices acting on site i.

The steps to follow in an ED implementation would be as listed below.

1. Find an adequate basis set representation.
2. Generate the matrix representation of the Hamiltonian, denoted by H, and of the relevant observables. If symmetries are taken into account, one would need to build H in a block-diagonal.
3. Numerically diagonalize (or block-diagonalize) H to obtain the set of eigenvalues $\{\epsilon_n\}$ and eigenvectors $\{|n\rangle\}$.
4. Compute the evolution of the vector state and relevant observables as described in the previous section.

Let us go through some of these points for the considered example.

Representation of the computational basis

As said before, for systems of spin-1/2 degrees of freedom, it is convenient to work in the computational basis $s = (s_1, s_2, \cdots, s_N)$, with $s_i = \uparrow, \downarrow$. For the purposes of ED, this basis is particularly simple, as one can directly use a *bit representation* of spin states. Indeed, the local states $s_i = \uparrow, \downarrow$ are naturally represented in a computer using the bit values 0 and 1 of an integer. Thus, the 2^N spin configurations s can be regarded as a binary representation of the integers $I = 0, 1, 2, \cdots, 2^N - 1$. The bit $I[i]$, with $i = 0, 1, \cdots, 31$, of an integer

I,[3] then corresponds to the spin at site i, that is, $I[i] \equiv s_i$. For example, for a system of $N = 3$ spins, one would use the dictionary in Table 3.1.

Basis state	Bit representation	Integer
$\vert\downarrow\downarrow\downarrow\rangle$	000	0
$\vert\downarrow\downarrow\uparrow\rangle$	001	1
$\vert\downarrow\uparrow\downarrow\rangle$	010	2
$\vert\downarrow\uparrow\uparrow\rangle$	011	3
$\vert\uparrow\downarrow\downarrow\rangle$	100	4
$\vert\uparrow\downarrow\uparrow\rangle$	101	5
$\vert\uparrow\uparrow\downarrow\rangle$	110	6
$\vert\uparrow\uparrow\uparrow\rangle$	111	7

Table 3.1: Bit representation of the computational basis states for a system with $N = 3$.

For hard-core bosons or spinless fermions, a similar basis representation as the one explain here can directly be used. For higher-spin systems, one could use, for example, a larger number of bits to label the internal states of each spin.

Generation of the Hamiltonian matrix

The Hamiltonian matrix is a $\mathcal{D} \times \mathcal{D}$ square matrix, where $\mathcal{D}$ is the dimension of the corresponding Hilbert space. For the model under consideration, Eq. (3.13), we have $\mathcal{D} = 2^N$. The role of symmetries, which yield a block-diagonal structure, will be addressed below. For the time being, let us consider the full Hamiltonian matrix $\mathsf{H} = \{H_{ab} := \langle a|H|b\rangle\}$. Here, we directly use the integer representation of the basis states, that is, $a, b = 0, 1, \cdots, 2^N - 1$. The first term in Eq. (3.13) is purely diagonal, so we only need to consider the matrix elements $\langle a|\sigma_i^z \sigma_{i+1}^z|a\rangle$, whose value only depends on whether the bits $a[i]$ and $a[i+1]$ are the same or different. Namely, $\langle a|\sigma_i^z \sigma_{i+1}^z|a\rangle = 1$ if $a[i] = a[i+1]$, and $\langle a|\sigma_i^z \sigma_{i+1}^z|a\rangle = -1$ if $a[i] \neq a[i+1]$. The second term in Eq. (3.13) is off-diagonal, as it acts as a spin-flip operator for σ^z, that is, $\sigma_i^x|a\rangle = |b\rangle$, where $|b\rangle$ differs from $|a\rangle$ just in that the spin (bit) at site i has been flipped. Therefore, $\langle b|\sigma_i^x|a\rangle = 1$ if $b[i] \neq a[i]$ and $b[j] = a[j]$ for all $j \neq i$, and $\langle b|\sigma_i^x|a\rangle = 0$ otherwise. We can generate all states $|b\rangle$ that give rise to nonzero matrix elements $\langle b|\sigma_i^x|a\rangle$, using the bitwise "exclusive-or" (XOR) operation. Indeed, consider an auxiliary state represented by the integer $c = 2^i$, with all bits set to 0 but the i-th bit that is set to 1. If we denote as $\mathbf{bitXOR}(a, b)$ the pseudocode function implementing the bitwise XOR operation of the integers a and b, then the integer $b = \mathbf{bitXOR}(a, 2^i)$ gives the integer that differs from a by having the i-th bit flipped.

---

[3] For a "long" integer, we would use $i = 0, 1, \cdots, 63$.

Below, we give a pseudocode algorithm to build the matrix representation of the Hamiltonian in Eq. (3.13), using periodic boundary conditions.

Algorithm 1: Hamiltonian matrix for the 1D transverse-field Ising model

```
for $a \leftarrow 0$ to $2^N - 1$ do
    for $i \leftarrow 0$ to $N - 1$ do
        $j = \mathbf{mod}(i + 1, N)$; (periodic boundary conditions)
        (diagonal part)
        if $\mathbf{bitGet}(a, i) = \mathbf{bitGet}(a, j)$ then
            $\mathsf{H}(a, a) = \mathsf{H}(a, a) - J$;
        else
            $\mathsf{H}(a, a) = \mathsf{H}(a, a) + J$;
        end
        (off-diagonal part)
        $b = \mathbf{bitXOR}(a, 2^i)$;
        $\mathsf{H}(a, b) = \mathsf{H}(a, b) - h$;
    end
end
```

The pseudocode function **bitGet**(a, i) simply gets the i-th bit of the integer a. For the example of $N = 3$, the resulting matrix is given below

$$\mathsf{H} = \begin{pmatrix} -3J & -h & -h & 0 & -h & 0 & 0 & 0 \\ -h & J & 0 & -h & 0 & -h & 0 & 0 \\ -h & 0 & J & -h & 0 & 0 & -h & 0 \\ 0 & -h & -h & J & 0 & 0 & 0 & -h \\ -h & 0 & 0 & 0 & J & -h & -h & 0 \\ 0 & -h & 0 & 0 & -h & J & 0 & -h \\ 0 & 0 & -h & 0 & -h & 0 & J & -h \\ 0 & 0 & 0 & -h & 0 & -h & -h & -3J \end{pmatrix}. \tag{3.14}$$

At this point, we are ready to carry out a numerical diagonalization of H using standard libraries. We can see, however, that because the number of basis states grows exponentially with N, this method is rather limited to small system sizes. This limitation is particularly restrictive for the full diagonalization scheme described so far. To illustrate this point, a system with 40 spin-1/2's would require about 4 TB of classical memory for storage [151]. In the remaining of this section, we discuss how one can refine an ED calculation in order to tackle nontrivial system sizes.

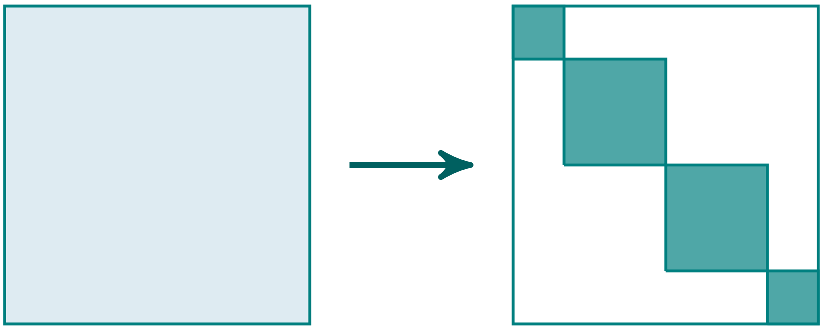

Figure 3.1: Schematic representation of the use of symmetries to bring the Hamiltonian matrix into a block-diagonal form. The resulting blocks can be labeled by the different conserved quantum numbers concomitant to the symmetries.

Remark on symmetries

A first step to reduce the numerical overhead mentioned above, consists of employing the symmetries of the problem. It is an elementary result of quantum mechanics that when symmetries are explicitly taken into account, one can reduce the Hamiltonian matrix into a block-diagonal form, see Fig. 3.1. The blocks are then labeled by the different conserved quantum numbers associated to the symmetries. Importantly, each block can be diagonalized independently of the others. By using symmetries and high-performance computational resources, it is now possible to study the low-energy sector of certain spin-$1/2$ systems with up to $N = 48$ sites [256]. Providing a detailed description of how to implement the similarity transformations needed to account for the relevant symmetries goes beyond the scope of the present work. Therefore, we refer the reader to the literature for a in-depth study of this crucial point (see, for example, Ref. [242]).

3.2.3 Lanczos time evolution

Let us consider the formal solution in Eq. (3.4), and expand it to M-th order

$$|\psi(t)\rangle = \mathrm{e}^{-iHt}|\psi(0)\rangle \approx \sum_{k=0}^{M-1} \frac{(-it)^k}{k!} H^k |\psi_0\rangle. \tag{3.15}$$

The set of functions on the right-hand side, formed by successive applications of the Hamiltonian onto the initial state, spans a subspace of the Hilbert space, which is known as the *Krylov subspace*: $\mathcal{K}_M = \mathrm{span}\big\{|\psi_0\rangle, H|\psi_0\rangle, H^2|\psi_0\rangle, \cdots, H^{M-1}|\psi_0\rangle\big\}$.

Let us make a couple of remarks. First, up to the timescale for which the truncated expansion in Eq. (3.15) is valid, it is a good approximation to consider that the time-evolved state $|\psi(t)\rangle$ belongs to the Krylov subspace. Second, the functions $\{H^k|\psi_0\rangle\}$ are not orthogonal with each other. However, one can build systematically an orthonormal basis of the Krylov subspace using the Lanczos method [257], which is sketched next.

Let $|\phi_0'\rangle = H|\psi_0\rangle$, $\tilde{\alpha}_0 = \langle\phi_0'|\psi_0\rangle$, with this, we construct a first element of the Lanczos basis, namely, $|\phi_0\rangle = |\phi_0'\rangle - \tilde{\alpha}_0|\psi_0\rangle$. The remaining elements are obtained recursively as prescribed below [242, 258].

Algorithm 2: Recursive construction of the Lanczos basis

```
for $k \leftarrow 1$ to $M-1$ do
    $\tilde{\beta}_k = ||\phi_{j-1}|| := \sqrt{\langle\phi_{k-1}|\phi_{k-1}\rangle}$;
    $|\psi_k\rangle = |\phi_{k-1}\rangle/\tilde{\beta}_k$;
    $|\phi_k'\rangle = H|\psi_k\rangle$;
    $\tilde{\alpha}_k = \langle\phi_k'|\psi_k\rangle$;
    $|\phi_k\rangle = |\phi_k'\rangle - \tilde{\alpha}_k|\psi_k\rangle - \tilde{\beta}_k|\psi_{k-1}\rangle$;
end
```

One can then prove [258] that with the Lanczos construction the Hamiltonian matrix (in the Krylov subspace) acquires a $M \times M$ tridiagonal form

$$\mathsf{H}_M = \begin{pmatrix} \tilde{\alpha}_0 & \tilde{\beta}_0 & 0 & \cdots & 0 & 0 \\ \tilde{\beta}_0 & \tilde{\alpha}_1 & \tilde{\beta}_1 & \cdots & 0 & 0 \\ 0 & \tilde{\beta}_1 & \tilde{\alpha}_2 & \cdots & 0 & 0 \\ \vdots & \vdots & \vdots & \ddots & \vdots & \vdots \\ 0 & 0 & 0 & \cdots & \tilde{\alpha}_{M-2} & \tilde{\beta}_{M-2} \\ 0 & 0 & 0 & \cdots & \tilde{\beta}_{M-2} & \tilde{\alpha}_{M-1} \end{pmatrix}. \tag{3.16}$$

Now let us denote by $\mathbf{f}(t)$ the vector of coefficients of the vectors $\{|\phi_k\rangle\}_M$, where the subscript M indicates that these vectors are elements of the subspace $\mathcal{K}_M$. One finds that the solution is given by [258]

$$\mathbf{f}(t) = \mathrm{e}^{-i\mathsf{H}_M t}\mathbf{f}(0), \tag{3.17}$$

with $\mathbf{f}(0) = (1, 0, 0, \cdots)^{\mathbf{t}}$. The desired time-dependent coefficients $c_n(t)$, can then be obtained by a simple change of basis.

Clearly, working in the reduced subspace $\mathcal{K}_M$ reduces the overall computational overhead and allows us to reach bigger system sizes. Let us finish by noting that the starting point given by the expansion in Eq. (3.15), is a good approximation if the considered time interval is small. In order to go to longer timescales, one could split the time evolution into small time steps δt and apply the procedure above iteratively. Therefore, in practical applications, one must check convergence in terms of the two control parameters, M and δt.

3.3 Time evolution with matrix product states

Given the importance of tensor-network-based algorithms for the simulation of quantum many-body systems, in this section, we briefly summarize the main ideas of this approach. For simplicity, we will focus on 1D systems, for which the aforementioned techniques have proven particularly successful; see for example Ref. [234] and references therein. In this case, there is a particularly important class of tensor-network wave functions, namely *matrix product states* (MPS) [232–234], which can encode quite efficiently quantum states with low and moderate *entanglement*. Therefore, MPS-based calculations have been used extensively for ground-state problems[4] in low-dimensional systems. This approach is known as the density matrix renormalization group (DMRG) [259]. When it comes to dynamics, one can use the time-dependent version of this algorithm, which is referred to as tDMRG (or its variants: TEBD and tMPS) [224–231]. It turns out that MPS can also capture efficiently the evolution of quantum states, provided that the entanglement stays moderate during the course of the evolution. We follow Refs. [234, 260] for the presentation given below.

3.3.1 Matrix product states

Let us consider again a system with N spins, with local Hilbert space dimension d_l. In the computational basis, one can write an arbitrary state in a fashion similar to Eq. (3.2), that is,

$$|\psi\rangle = \sum_{\{s\}} \psi(s)|s\rangle, \tag{3.18}$$

Let us recall that s is a shorthand notation for the collection of all spins: $s = (s_1, s_2, \cdots, s_N)$. This means that we can also think of $\psi(s)$ as an object with N indices, namely, $\psi(s) \equiv \psi^{s_1 \cdots s_N}$.

As the name suggests, the main idea of MPS consists, basically, in replacing the amplitudes $\psi^{s_1 \cdots s_N}$ by a product of matrices as follows:

$$\psi^{s_1 \cdots s_N} \to M^{s_1} M^{s_2} \cdots M^{s_N}, \tag{3.19}$$

where the matrices M^{s_i} have dimensions $(1 \times D_1), (D_1 \times D_2), \ldots, (D_{L-2} \times D_{L-1}), (D_{L-1} \times 1)$, and d_l matrices M^{s_i} are introduced at each site. Thus, an MPS has the general form

$$|\psi\rangle = \sum_{\{s\}} M^{s_1} M^{s_2} \cdots M^{s_N} |s\rangle. \tag{3.20}$$

---

[4] So-called *area laws* tell us that low-entanglement states are crucial for describing low-temperature properties [234].

Product states constitute a simpler type of wave functions, with the form given in Eq. (3.20) but with all the matrices having dimension $D = 1$. Entangled states are, by definition, those states that cannot be written as a product state. Thus, we see that a generic MPS like in Eq. (3.20) can represent an entangled state. In fact, as we will see shortly, *any* quantum state can be *exactly* written as an MPS, although such representation may not be numerically efficient. Below, we explain how to represent an arbitrary quantum state by an MPS.

Representing an arbitrary state by an MPS

We show how to write any quantum state as an MPS. The key ingredient for this construction is a linear algebra factorization known as the *singular value decomposition* (SVD),[5] which works as follows. Let A be an arbitrary $(m \times n)$-matrix. The SVD of A reads

$$A = U\Sigma V^{\dagger}, \tag{3.21}$$

where U has dimensions $(m \times k)$ and its columns are orthogonal, $V^{\dagger}$ has dimensions $(k \times n)$ and its rows are orthogonal, and Σ is a $(k \times k)$ diagonal matrix, whose entries on the diagonal are real and non-negative and are called singular values. In these expressions $k = \min(m, n)$. Note also that U, V will be unitary if $k = m$ or $k = n$, respectively. Before continuing, let us point out that the SVD in Eq. (3.21) is also behind another important factorization, the so-called Schmidt decomposition, which in turn is useful for computing a measurement of entanglement in the form of the von Neumann entropy (see Appendix A).

Coming back to the task at hand, the d_l^N-dimensional state vector $\psi^{s_1 \cdots s_N}$ can be reshaped as a rectangular matrix of dimension $(d_l \times d_l^{N-1})$, which is then SV decomposed, that is,

$$\psi^{s_1 \cdots s_N} \rightarrow A_{s_1, s_2 \cdots s_N} = \sum_{\alpha_1=1}^{r_1} U_{s_1,\alpha_1} \Sigma_{\alpha_1,\alpha_1} V^{\dagger}_{\alpha_1, s_2 \cdots s_N}, \tag{3.22}$$

with the rank $r_1 \leq d_l$. The matrix U can now be "sliced" into d_l row vectors or $(1 \times r_1)$-dimensional matrices, that is, $U_{s_1,\alpha_1} = A^{s_1}_{1,\alpha_1}$, and hence Eq. (3.22) becomes

$$\psi^{s_1 \cdots s_N} = \sum_{\alpha_1=1}^{r_1} A^{s_1}_{1,\alpha_1} \psi^{\alpha_1 s_2 \cdots s_N}, \tag{3.23}$$

with $\psi^{\alpha_1 s_2 \cdots s_N} = \Sigma_{\alpha_1,\alpha_1} V^{\dagger}_{\alpha_1, s_2 \cdots s_N}$, which is also reshaped and SV decomposed as follows:

$$\psi^{\alpha_1 s_2 \cdots s_N} \rightarrow A_{\alpha_1 s_2, s_3 \cdots s_N} = \sum_{\alpha_2=1}^{r_2} U_{\alpha_1 s_2, \alpha_2} \Sigma_{\alpha_2,\alpha_2} V^{\dagger}_{\alpha_2, s_3 \cdots s_N}, \tag{3.24}$$

---

[5] In practice, one can also use a QR factorization, which may be faster than a SVD [234, 260].

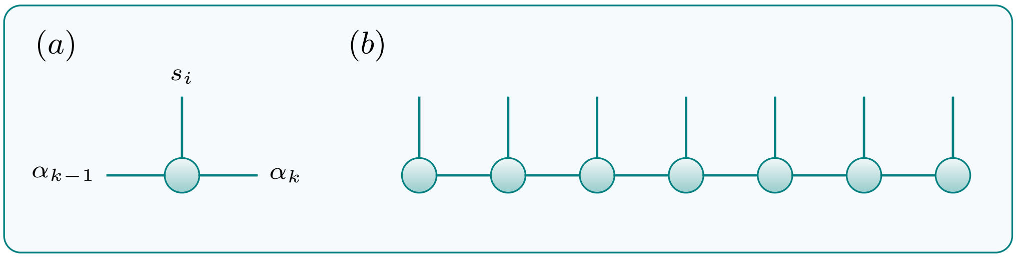

Figure 3.2: (a) Graphical representation of one of the matrices $A^{s_i}_{\alpha_{k-1},\alpha_k}$ forming an MPS, with physical indices as vertical lines and row and column indices as horizontal lines. (b) Graphical representation of the entire MPS wave function. Note that the indices that only take the value 1 are not drawn. With this convention, complex conjugation of objects like in (a) and (b) would have them with the vertical lines pointing downward.

with $r_2 \leq r_1 d_l \leq d_l^2$. Once again, we sliced U into d_l $(r_1 \times r_2)$-dimensional matrices: $U_{\alpha_1 s_2,\alpha_2} = A^{s_2}_{\alpha_1,\alpha_2}$. Letting $\psi^{\alpha_2 s_3 \cdots s_N} = \Sigma_{\alpha_2,\alpha_2} V^{\dagger}_{\alpha_2,s_3\cdots s_N}$, and inserting Eq. (3.24) into Eq. (3.23) yields

$$\psi^{s_1\cdots s_N} = \sum_{\alpha_1,\alpha_2} A^{s_1}_{1,\alpha_1} A^{s_2}_{\alpha_1,\alpha_2} \psi^{\alpha_2 s_3\cdots s_N}. \tag{3.25}$$

At this point, it should already be clear that upon performing further steps like these, one arrives at

$$\psi^{s_1\cdots s_N} = \sum_{\alpha_1,\ldots,\alpha_N} A^{s_1}_{1,\alpha_1} A^{s_2}_{\alpha_1,\alpha_2} \cdots A^{s_{N-1}}_{\alpha_{N-2},\alpha_{N-1}} A^{s_N}_{\alpha_{N-1},1}. \tag{3.26}$$

This construction then shows us that any quantum state can be written in an MPS form such as Eq. (3.20). We emphasize that so far, this procedure is exact. However, the exponential complexity discussed in Section 3.1 is still present as the dimensions of the matrices in Eq. (3.26) also grow exponentially with N. To be more concrete, the maximum possible dimensions are $(1 \times d_l), (d_l \times d_l^2), \ldots, (d_l^{N/2-1} \times d_l^{N/2})(d_l^{N/2} \times d_l^{N/2-1}), \ldots (d_l^2 \times d_l), (d_l \times 1)$. Therefore, in order to have a numerically “useful” method one must make an approximation and restrict the maximum dimension of the matrices to some value D_M, which allows for sufficiently accurate calculations within the limits of feasible computational resources and computation time.

Finally, let us mention that there is a quite convenient and hence widely used graphical representation of MPS, which saves us from writing expressions with many indices as the ones above. The rules and building blocks are very simple: each matrix is represented by a circle that has horizontal and vertical lines sticking out of it. Here we use the convention that horizontal lines correspond to row and column indices, whereas vertical lines represent physical indices. This is illustrated in Fig. 3.2, where we also show how to represent a full MPS. For the graphical construction of the latter and other more complicated objects, one needs to bare in mind just one rule: connected lines are *contracted*, that is, the joint index is summed over.

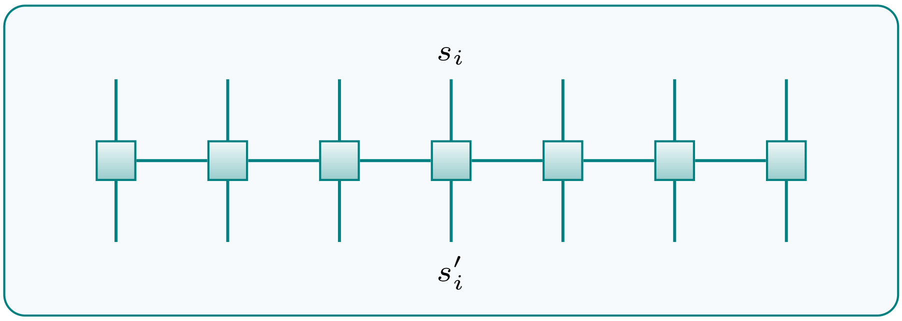

Figure 3.3: Graphical representation of a generic MPO.

Generalization to operators

The MPS representation discussed above can be generalized to represent operators, too, giving rise to *matrix product operators* (MPO). The idea is sketched in the following. Let us consider an arbitrary operator O written in the computational basis, namely,

$$O = \sum_{\{s\}} \sum_{\{s'\}} a^{s_1 \cdots s_N, s_1' \cdots s_N'} |s\rangle\langle s'|. \tag{3.27}$$

Upon reshuffling of the indices, the coefficient $a^{s_1 \cdots s_N, s_1' \cdots s_N'}$ can also be written as $a^{s_1 s_1' s_2 s_2' \cdots s_N s_N'}$, and a "mean-field-like approximation"[6] would consist of making the following factorization:

$$a^{s_1 s_1' s_2 s_2' \cdots s_N s_N'} \approx a^{s_1 s_1'} a^{s_2 s_2'} \cdots a^{s_N s_N'}. \tag{3.28}$$

Taking this as our starting point, we now promote the coefficients on the right-hand side of Eq. (3.28) to matrices to get the most general form of an MPO, namely,

$$O = \sum_{\{s\}} \sum_{\{s'\}} M^{s_1 s_1'} M^{s_2 s_2'} \cdots M^{s_N s_N'} |s\rangle\langle s'|. \tag{3.29}$$

Let us remark that, as it happens, this kind of representation is actually exact for many operators of interest, ranging from local operators such as σ_i^z to full Hamiltonians [234, 260]. Furthermore, the dimension of the matrices in Eq. (3.29) is typically small, as opposed to what happens with MPS. Also, the graphical representation of an MPO is analogous to that of an MPS, with the difference that now we have "ingoing" [primed variables in Eq. (3.29)] and "outgoing" vertical lines, as illustrated in Fig. 3.3. As a final remark, let us note that applying an MPO to an MPS results in a new MPS, as it can be readily seen. The resulting MPS will have matrices whose dimensions are basically the product of the dimensions of the matrices in the original MPS and the MPO. Since we have seen that, at least, the matrix dimensions of an MPS can quickly take large values, when applying an MPO to an MPS one normally needs to implement a “compression” procedure [231, 234, 260], via a SVD with a *cutoff* of singular values, such that the resulting MPS has manageable matrix dimensions.

---

[6] The mean-field approximation of an MPS has all matrices in Eq. (3.20) with dimension 1, and gives rise to product states, as mentioned before.

3.3.2 Time evolution via a Trotter decomposition

We now turn to problem of computing the time evolution using the language of MPS and MPO. As before, we consider time-independent Hamiltonians. As we have seen, the solution to the time-dependent Schrödinger equation can be obtained by applying the time-evolution operator e^{-iHt} to the initial state $|\psi(0)\rangle$; see Eq. (3.4). Now in the current formulation, the initial state is assumed to be in an MPS representation, either built by hand or by means of an auxiliary DMRG calculation ($|\psi(0)\rangle$ could be the ground state of a different Hamiltonian, as typically done in quantum quenches). Therefore, the “only” problem we have is to represent the unitary operator e^{-iHt} as an MPO. While we cannot fully solve this problem because it is not known how to write down such a representation in an exact and efficient manner, there are a few strategies available to solve the dynamics approximately. Here we will focus on a scheme based on the *Trotter decomposition.*

As a first step, we split the total time interval $[0,t]$ into N_t small time steps δt, such that $N_t \cdot \delta t = t$. Ideally, we would take infinitesimal time steps and $N_t \to \infty$, but of course in practice δt is finite. Next, we assume that the Hamiltonian can be written as a sum of local terms, just like the TFIM Hamiltonian in Eq. (3.13). In fact, we will restrict ourselves to the case of Hamiltonians with only nearest-neighbor interactions, which are generically written as

$$H = \sum_{i=1}^{N} h_i. \tag{3.30}$$

Once again, for the TFIM in Eq. (3.13), we would have that $h_i = \sigma_i^z \sigma_{i+1}^z$, with onsite terms distributed in the two consecutive h_i's that share the corresponding site. In either case, the time-evolution operator can be written as

$$\mathrm{e}^{-iHt} = \prod_{\tau=1}^{N_t} \mathrm{e}^{-iH\delta t} = \prod_{\tau=1}^{N_t} \mathrm{e}^{-i\sum_{j=1}^{N-1} h_j \delta t}. \tag{3.31}$$

The problem would be tractable *if* we could factorize the last exponential as a product of time-evolution operators over two sites, $\mathrm{e}^{-ih_j\delta t}$. However, we know that such factorization is incorrect when dealing with non-commuting operators, for which we have

$$\mathrm{e}^{\mathcal{A}\mathcal{B}} = \mathrm{e}^{\mathcal{A}}\mathrm{e}^{\mathcal{B}}\mathrm{e}^{\frac{1}{2}[\mathcal{A},\mathcal{B}]}, \tag{3.32}$$

where $[\mathcal{A},\mathcal{B}] := \mathcal{A}\mathcal{B} - \mathcal{B}\mathcal{A}$ is the usual commutator. Since in our case the operators under consideration have a factor of δt in front, we see that the last term in Eq. (3.32) scales as

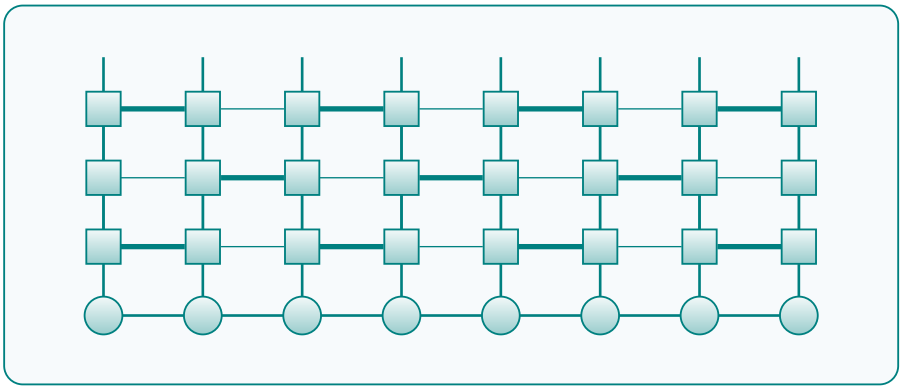

Figure 3.4: Graphical representation of the MPO time-evolution operator applied to some MPS (sitting at the bottom) using the Trotter scheme explained in the text. We first apply all the odd bond MPOs (thick lines on odd bonds) and then all the even bond MPOs (thick lines on even bonds). Thin lines represent MPOs with dimension 1, due to the factorization of the time evolution.

δt^2. Therefore, for $\delta t \to 0$, we can approximate

$$\mathrm{e}^{-iH\delta t} \approx \mathrm{e}^{-ih_1\delta t}\mathrm{e}^{-ih_2\delta t}\cdots\mathrm{e}^{-ih_{N-2}\delta t}\mathrm{e}^{-ih_{N-1}\delta t} + \mathcal{O}(\delta t^2), \tag{3.33}$$

which is known as the first-order Trotter decomposition.

Because of the restriction to only nearest neighbors, we further notice that two-site evolution operators on odd (even) bonds commute with each other. Therefore, within the Trotter approximation it is customary to write $\mathrm{e}^{-iH\delta t} = \mathrm{e}^{-iH_{\text{odd}}\delta t}\mathrm{e}^{-iH_{\text{even}}\delta t}$, with $\mathrm{e}^{-iH_{\text{odd}}\delta t} = \prod_{j\ \text{odd}} \mathrm{e}^{-ih_j\delta t}$ and $\mathrm{e}^{-iH_{\text{even}}\delta t} = \prod_{j\ \text{even}} \mathrm{e}^{-ih_j\delta t}$, and perform the bond time evolution on all odd (even) bonds at the same time. Let us note that, in practice, it is advisable to use a higher-order scheme. For instance, the second-order Trotter decomposition [228]:

$$\mathrm{e}^{-iH\delta t} \approx \mathrm{e}^{-iH_{\text{odd}}\delta t/2}\mathrm{e}^{-iH_{\text{even}}\delta t}\mathrm{e}^{-iH_{\text{odd}}\delta t/2} + \mathcal{O}(\delta t^3). \tag{3.34}$$

However, for the sake of simplicity, let us stick to the first-order decomposition. Our task now is to build the MPO of a single two-site time-evolution operator for odd bonds and another one for even bonds. This can be easily done with the same strategy that we followed for MPS. For instance, for the first bond, the time-evolution operator reads

$$\mathcal{U}^{s_1 s_2, s_1' s_2'} := \langle s_1 s_2 | \mathrm{e}^{-ih_1\delta t} | s_1' s_2' \rangle. \tag{3.35}$$

We then reshuffle indices and perform a SVD. This yields

$$\mathcal{U}^{s_1 s_2, s_1' s_2'} = \tilde{\mathcal{U}}_{s_1 s_1', s_2 s_2'} = \sum_\alpha U_{s_1 s_1', \alpha} \Sigma_{\alpha,\alpha} V^\dagger_{\alpha, s_2 s_2'}. \tag{3.36}$$

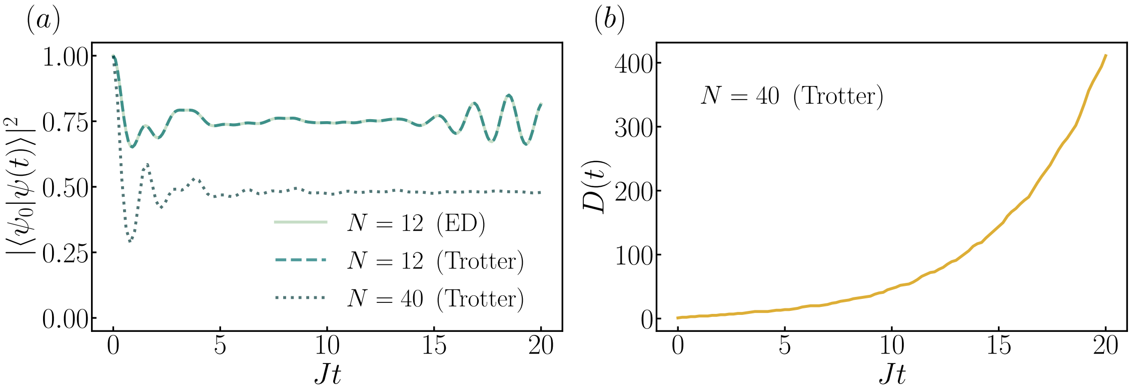

Figure 3.5: Dynamics in the 1D TFIM [Eq. (3.13) with $J = 1, h = 0.35$]. (a) Return probability for $N = 12, 40$, starting from the product state $|\psi_0\rangle = |\uparrow\downarrow\uparrow\downarrow \cdots \uparrow\downarrow\uparrow\downarrow\rangle$. For $N = 12$, we also show the full ED result (solid line). (b) Largest bond dimension $D(t)$ as a function of time in the MPS simulation with $N = 40$.

Finally, we absorb the singular values on the left and right matrices and slice the resulting matrices so as to get

$$\mathcal{U}^{s_1 s_2, s_1' s_2'} = \sum_\alpha M_{1,\alpha}^{s_1 s'} M_{\alpha,1}^{s_2 s_2'}, \tag{3.37}$$

where the matrices on the right-hand side have dimensions $(1 \times d_l^2)$ and $(d_l^2 \times 1)$, respectively (and the other way around for even bonds). Thus, if the maximum *bond dimension* of the MPS is set to be D_M, then after one Trotter time step the resulting dimension will grow to $d_l^2 D_M$, leading to an exponential growth upon further time steps. Hence, one has to constantly compress the time-evolved MPS to keep its bond dimension no larger than D_M. The graphical representation of the "Trotterized" time-evolution operator e^{-iHt} applied to some MPS is shown in Fig. 3.4.

While the algorithm described before seems to be applicable to arbitrary long times with a fixed accuracy, there is a fundamental restriction to be taken into account, namely, the growth of entanglement during time evolution. Indeed, Lieb-Robinson bounds [261] tell us that entanglement generally grows up to linearly as the system evolves in time. A linear growth is, in fact, obtained when studying *global quantum quenches*, where the dynamics is computed after a sudden change in the Hamiltonian [262]. On the other hand, an MPS of dimension D can encode at most an entanglement $S = \ln(D)$ (see Appendix A). Therefore, in the worst case scenario, one would need to increase *exponentially* the bond dimension of the evolving MPS to keep the same accuracy. This is illustrated in Fig. 3.5, where we show the dynamics after a global quench in a one-dimensional TFIM: starting from a product state $|\psi_0\rangle = |\uparrow\downarrow\uparrow\downarrow \cdots \uparrow\downarrow\uparrow\downarrow\rangle$, we compute the dynamics generated by the Hamiltonian in Eq. (3.13) with $J = 1, h = 0.35$, using open boundary conditions. Panel (a) shows the return probability $|\langle\psi_0|\psi(t)\rangle|^2$ for two system sizes $N = 12, 40$, which after a brief transient settles to a steady value that decreases with system size. For $N = 12$ we see the appearance of revivals at $Jt \gtrsim 15$, due to the finite system size. Here we also show the result obtained with full ED (see previous section); we see that both curves lie on top of each other. Panel (b) shows the exponential growth of the bond dimension as a function of time in the simulation with $N = 40$. For the MPS simulations, we used the second-order Trotter decomposition [Eq. (3.34)] with a time step $\delta t = 0.01$ and a truncation error of the order of $\epsilon = 10^{-12}$.[7] The latter computations were done using the software *ITensor* [263].

3.4 Time evolution with classical networks

In this section, we discuss a recent alternative to the previous techniques, which consists of encoding quantum states in various types of networks of classical degrees of freedom. This approach received increased attention, when general-purpose ANNs were proposed as *generative models* in a seminal work by Carleo and Troyer [188]. As we will see, however, this idea can be generalized to other types of classical networks. In the following, we discuss the general idea of this approach and revise a few examples of classical networks that have been used for the task of time-evolution simulations. Moreover, we explain the general procedure to optimize such networks, the so-called time-dependent variational principle (TDVP). The content of this section works as a prelude for the main subject of this chapter, VCNs, which we shall address in the next section.

3.4.1 Classical networks as generative machines

Generative machines provide an alternative, efficient way to encode the many-body wave function. The basic idea is that, instead of storing the exponentially many time-dependent amplitudes $\psi(s,t)$, which appear as expansion coefficients in Eq. (3.2), a generative machine approximates them *on the fly*, see Fig. 3.6. For the time being, let us consider a generic generative machine, which in the present context, will define a class of variational wave functions $\psi_\eta(s) \equiv \psi(s;\eta(t))$, endowed with a set of complex-valued, time-dependent variational parameters $\eta(t) = (\eta_1(t), \eta_2(t), \cdots, \eta_K(t)) \in \mathbb{C}^K$. The goal is to carry out an optimization procedure such that this variational wave function gives a good approximation to the exact wave function, that is,

$$\psi_\eta(s) \approx \psi(s,t). \tag{3.38}$$

Before giving concrete examples of such variational wave functions and explaining the optimization procedure with which one may achieve the desired approximation, Eq. (3.38), we explain how to compute physical quantities of interest. In the computational basis,

---

[7] This value for the truncation error is rather small and should yield very high accuracy. Yet, it implies a large bond dimension. In practice, for more demanding calculations, one allows for a larger truncation error, say $\epsilon \sim 10^{-9}$, which will typically yield a good accuracy. Of course, convergence must checked from case to case.

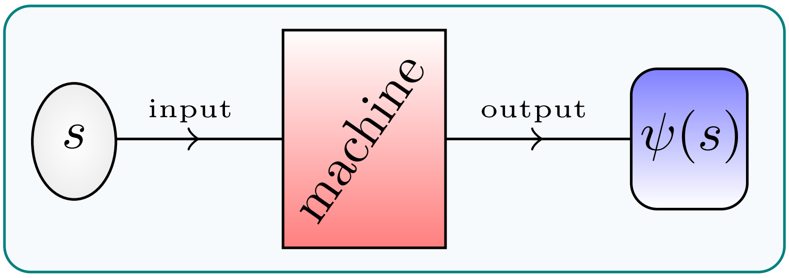

Figure 3.6: Schematic representation of a generative machine that takes as input a spin configuration s, and computes on-the-fly an approximation of the corresponding wave function amplitude $\psi(s)$. Examples of such machines are artificial neural networks or variational classical networks (see Section 3.5).

the expectation value of an observable O with matrix elements $\langle s|O|s'\rangle =: Oss'$, can be written as

$$\langle\psi_\eta|O|\psi_\eta\rangle = \sum_{\{s\}} |\psi_\eta(s)|^2 O_\eta(s), \tag{3.39}$$

where

$$O_\eta(s) := \sum_{\{s'\}} O_{ss'} \frac{\psi_\eta(s')}{\psi_\eta(s)}. \tag{3.40}$$

Let us note that typical local observables are such that $\langle s|O|s'\rangle$ is sparse. Consequently, getting $O_\eta(s)$ in Eq. (3.40) requires only a polynomial computational overhead. Hence, assuming a normalized wave function, the expectation value in Eq. (3.39) can be calculated efficiently via a Monte Carlo sampling of the distribution $|\psi_\eta(s)|^2$; see for example Refs. [264, 265]. Note that a compression of the wave function in the form of $\psi_\eta(s)$, will be efficient as long as the overall number K of parameters is significantly less than the dimension of the Hilbert space.

In general, a generative machine refers to a model that can generate samples according to some target distribution, which in this case is $|\psi(s,t)|^2$. Remarkably, generative machines such as that in Eq. (3.38), which we shall regard in the following, not only achieve the task mentioned above but also give direct access to the complex amplitudes $\psi(s,t)$.

As it will become clear in the following, most of the generative models considered in the present context, can be written as "Boltzmann-like functions"

$$\psi_\eta(s) = \mathrm{e}^{\mathcal{H}_\eta(s)}, \tag{3.41}$$

where $\mathcal{H}_\eta(s) \equiv \mathcal{H}(s;\eta(t))$ is a complex energy function or Hamiltonian defining certain classical spin system with couplings given by the variational parameters η. As we will exemplify below, such classical spin models can be visualized as networks, hence the term *classical networks*.

Now with a classical network of the form (3.41), Eqs. (3.39) and (3.40) become

$$\langle\psi_\eta|O|\psi_\eta\rangle = \sum_{\{s\}} \mathrm{e}^{\tilde{\mathcal{H}}_\eta(s)} O_\eta(s), \tag{3.42}$$

$$O_\eta(s) = \sum_{\{s'\}} \mathfrak{Re}\left[O_{ss'}\left(\mathrm{e}^{\mathcal{H}_\eta(s')} - \mathrm{e}^{\mathcal{H}_\eta(s)}\right)\right], \tag{3.43}$$

where $\tilde{\mathcal{H}}_\eta(s) := 2\mathfrak{Re}[\mathcal{H}_\eta(s)]$. Note that, for the particular case of a diagonal observable $\langle s|O|s'\rangle = Os\delta_{ss'}$, Eq. (3.42) simplifies to

$$\langle\psi_\eta|O|\psi_\eta\rangle = \sum_{\{s\}} \mathrm{e}^{\tilde{\mathcal{H}}_\eta(s)} O_s. \tag{3.44}$$

A few examples of classical networks are given in the following.

The Jastrow ansatz

One of the simplest classical networks is given by Jastrow-like wave functions [266], which have been widely used in the context of time-dependent variational Monte Carlo to tackle dynamical problems [267–270]. A Jastrow-like classical network for a spin model can, in general, be written as

$$\mathcal{H}_J(s;\eta(t)) = \sum_{i,j} \eta_{i,j}(t) s_i s_j. \tag{3.45}$$

Restricted Boltzmann machines

Recently, it was realized that ANNs could provide a versatile and powerful class of variational wave functions, like the one discussed here. In the seminal paper by Carleo and Troyer [188], it was proposed to represent the wave function using a particular type of ANNs, namely, *restricted Boltzmann machines* (RBMs); see for example Ref. [271]. An RBM is a classical network that contains two layers of classical spin variables: a “visible” layer with the physical degrees of freedom $s = (s_1, s_2, \cdots, s_N)$ and a “hidden” layer with ancillary variables $(h_1, h_2, \cdots, h_M)$, with $h_j = \pm 1$. The architecture of this kind of model is called “restricted” in the sense that there are no couplings between spins within one of the two layers. There are only inter-layer connections, see Fig. 3.7. Concretely, the RBM energy function is

$$\mathcal{H}_{\mathrm{RBM}}(s,h;\eta(t)) = \sum_i a_i(t) s_i + \sum_j b_j(t) h_j + \sum_{i,j} W_{i,j}(t) s_i h_j, \tag{3.46}$$

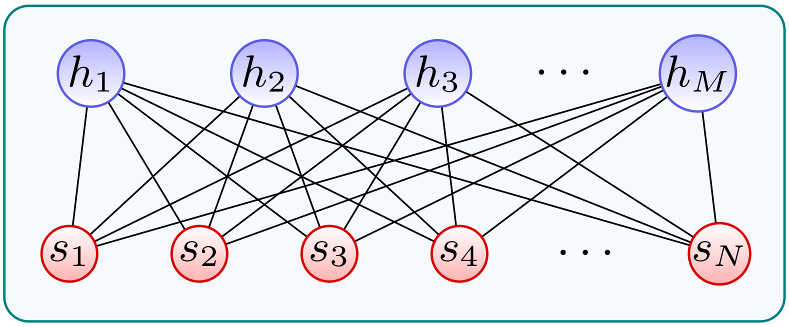

Figure 3.7: Example of an RBM architecture with visible spins s_i coupled to hidden degrees of freedom h_j. This type of architecture is said to be *restricted* because there are no couplings between visible spins, nor between hidden ones.

where we denote by $\eta = \{a_i, b_j, W_{ij}\}$ the whole set of variational parameters. The corresponding wave function amplitude is given by

$$\psi_{\mathrm{RBM}}(s;\eta(t)) = \sum_{\{h\}} \mathrm{e}^{\mathcal{H}_{\mathrm{RBM}}(s,h;\eta(t))}. \tag{3.47}$$

Moreover, due to the fact that there are no intra-layer couplings, one can easily integrate out the hidden variables analytically, yielding

$$\psi_{\mathrm{RBM}}(s;\eta(t)) = \mathrm{e}^{\sum_i a_i(t) s_i} \times \prod_{j=1}^{M} 2\cosh\left[b_j + \sum_i W_{ij} s_i\right]. \tag{3.48}$$

Another crucial advantage of working with RBMs is the fact that such type of ANNs is known to be a *universal approximator* [272], that is, for a sufficiently large number of hidden spins, an RBM is, in principle, capable of approximating any target function to arbitrary accuracy. Let us mention that RBMs have also been used, even more widely, for ground state searching problems, see for example Ref. [271] and references therein. Recently, some other ANN architectures, with a richer structure and potential representational power, have been employed for representing quantum states. We mention one example next.

Convolutional neural networks

Without entering into details, let us simply mention another type of ANN architecture, which has been recently proposed by Schmitt and Heyl [189] for representing quantum states in the context of quantum many-body dynamics, namely, *convolutional neural networks* (CNNs). As opposed to RBMs, CNNs are *deep* neural networks, meaning that they include multiple layers. In addition, a CNN can be defined with arbitrary activation functions and sparse connectivity. Importantly, CNNs satisfy the properties of locality and causality [189]. In a way, CNNs can be regarded as a generalization to RBMs, which are included as a particular case of fully connected, single-layer CNNs with fixed activation function.

Let us note that it has been identified [189] that the ANNs discussed above, generally, face *numerical instabilities*, which, in many situations, make it hard to reliably use these networks to extract the dynamics at longer timescales.

Finally, let us explain how classical networks, in general, can be optimized to serve the purpose of providing a good approximation to the time-evolved wave function; see Eq. (3.38). This procedure is the TDVP, which is discussed below.

3.4.2 Time-dependent variational principle

The TDVP [188, 254] is a procedure for optimizing a time-dependent variational ansatz $\psi_\eta(s)$, as the classical networks considered above. In essence, the TDVP establishes an equivalence between the time-dependent Schrödinger equation and a system of first-order differential equations that govern the dynamics of the variational parameters, namely,

$$\sum_{k'} \mathcal{S}_{kk'} \dot{\eta}_k' = -iF_k, \tag{3.49}$$

where the overdot denotes differentiation with respect to time and with the following definitions:

$$\mathcal{S}_{kk'} := \langle O_k^* O_{k'} \rangle - \langle O_k^* \rangle \langle O_{k'} \rangle, \tag{3.50}$$

which is the so-called covariance matrix, and

$$F_k := \langle E_{\text{loc}} O_k^* \rangle - \langle E_{\text{loc}} \rangle \langle O_k^* \rangle. \tag{3.51}$$

These quantities are expressed in terms of the local energy $E_{\text{loc}}(s) := \frac{\langle s|H|\psi_\eta\rangle}{\langle s|\psi_\eta\rangle}$, and the variational derivatives, $O_k(s) := \frac{\partial \ln \psi_\eta(s)}{\partial \eta_k}$, and $\langle \cdot \rangle$ stands for the statistical average with respect to the distribution $|\psi_\eta(s)|^2$, just like in Eq. (3.39).

In order to quantify the accuracy of the TDVP, one commonly introduces the Fubini-Study metric $\mathscr{D}_{\text{FS}}$, which measures the distance between the exact evolution during a small time interval δt: $\mathrm{e}^{-i\delta t H}|\psi_\eta\rangle$, and the variational evolution $|\psi_{\eta+\delta\dot{\eta}}\rangle$. Its definition is the following

$$\mathscr{D}_{\text{FS}}(\varphi, \phi)^2 := \arccos\left(\sqrt{\frac{\langle\varphi|\phi\rangle\langle\phi|\varphi\rangle}{\langle\varphi|\varphi\rangle\langle\phi|\phi\rangle}}\right)^2. \tag{3.52}$$

Thus, one can define a relative residual error as [188, 189]

$$r^2(t) := \frac{\mathscr{D}_{\text{FS}}(|\psi_{\eta+\delta\dot{\eta}}\rangle, \mathrm{e}^{-i\delta t H}|\psi_\eta\rangle)^2}{\mathscr{D}_{\text{FS}}(|\psi_\eta\rangle, \mathrm{e}^{-i\delta t H}|\psi_\eta\rangle)^2} \tag{3.53}$$

which can be measured, too, by performing a Monte Carlo sampling of $|\psi_\eta(s)|^2$. We shall use the integrated residual error:

$$R^2(t) := \int_0^t dt' r^2(t'), \tag{3.54}$$

to quantify errors in later parts of this thesis, when we perform calculations with VCNs. Alternatively, one could also use the error production rate [267], which is defiened as

$$\Delta^2(t) := \sum_{\{s\}} \left| \dot{\Phi}(s,t) - \dot{\Psi}(s,t) \right|^2 = \sum_{\{s\}} |\psi_\eta(s)|^2 \left| \sum_k O_k(s)\dot{\eta}_k + iE_{\mathrm{loc}}(s) \right|^2, \tag{3.55}$$

where $|\Phi\rangle = |\psi_{\eta+\delta\dot{\eta}}\rangle$ and $|\Psi\rangle = \mathrm{e}^{-i\delta t H}|\psi_\eta\rangle$. Finally, let us mention that, Eq. (3.49) can be derived by minimizing the numerator in Eq. (3.53) or Δ^2 in Eq. (3.55), with respect to $\dot{\eta}^*$. More details of such derivation can be found in Refs. [188, 189, 267].

3.5 Variational classical networks

VCNs constitute another family of variational wave functions that can be used as generative machines to efficiently solve quantum many-body dynamics problems in one and higher dimensions. In this method, the many-body wave function is represented as a complex network of classical spins akin to the ANNs revised above, with couplings among the spins that are taken as variational parameters, and which are then optimized with the TDVP of the previous section (see Section 3.4.2). Let us already mention here that one of the key advantages of VCNs over ANNs is the fact that the former do not face the numerical instabilities that have been observed for latter [189].

The architecture of VCNs can be derived systematically. More specifically, the structure of VCNs is inspired by the construction in their relative *perturbative classical networks* (pCNs) [187]. Thus, a crucial property of VCNs is that they inherit the *controlled* character that arises from the perturbative nature of pCNs. In addition, the optimization step introduced with the TDVP allows us to mitigate several inherent drawbacks of pCNs, such as being forcibly limited to weak quantum fluctuations and short timescales. Furthermore, there exist situations, as discussed subsequently, where VCNs may bear a reduced computational complexity compared to similar state-of-the-art techniques, while still yielding sufficiently accurate results.

In the following, we will explain in detail the procedure to construct VCNs. Moreover, we will illustrate the workings of the method by studying several quenches in the 1D quantum Ising model [see Eq. (3.13)]. In Chapter 4, we will employ VCNs to study the dynamics of the more challenging 2D QLM.

3.5.1 General settings

We consider again systems of N spin-$1/2$ degrees of freedom and choose to work in the computational basis $s = (s_1, s_2, \ldots, s_N)$, with $s_i = \uparrow, \downarrow$. Moreover, we consider the following family of Hamiltonians

$$H = H_0 + \gamma V, \tag{3.56}$$

where H_0 represents a classical system in the sense that it is diagonal in the computational basis,

$$H_0 |s\rangle = E_s |s\rangle, \tag{3.57}$$

and the off-diagonal perturbation γV, with γ playing the role of a small parameter, accounts for quantum fluctuations that induce transitions between the eigenstates of H_0.

We are interested in the nonequilibrium dynamics generated by the Hamiltonian (3.56). This can be obtained by solving the time-dependent Schrödinger equation, which admits the formal solution given by Eq. (3.4), which we repeat here for convenience

$$|\psi(t)\rangle = \mathrm{e}^{-iHt} |\psi_0\rangle, \tag{3.58}$$

where $|\psi_0\rangle \equiv |\psi(t=0)\rangle$ denotes the initial state.

In general, it is challenging to determine the action of the evolution operator e^{-iHt} onto the basis vectors. However, whenever the Hamiltonian H can be split as in Eq. (3.56), it is possible to carry out a perturbative treatment by working in the interaction picture, in which the evolution operator can be written as

$$\mathrm{e}^{-iHt} = \mathrm{e}^{-iH_0 t} W_\gamma(t), \tag{3.59}$$

where

$$W_\gamma(t) = \mathcal{T} \exp\Big[- i\gamma \int_0^t dt' V(t') \Big], \tag{3.60}$$

where $\mathcal{T}$ is the time-ordering operator, and with $V(t)$ satisfying the equation of motion:

$$- i \frac{d}{dt} V(t) = [H_0, V(t)]. \tag{3.61}$$

Within these settings, the many-body wave function amplitudes are given by

$$\psi(s,t) = \mathrm{e}^{-iE_s t} \langle s | W_\gamma(t) | \psi_0 \rangle. \tag{3.62}$$

The task now is to calculate the right-hand side Eq. (3.62). Classical networks provide a possible solution, as detailed below.

3.5.2 Building classical networks from a cumulant expansion

The right-hand side of Eq. (3.62) can be computed in a controlled way by means of a cumulant expansion [273, 274], namely,

$$\langle s|W_\gamma(t)|\psi_0\rangle = \langle s|\psi_0\rangle \exp\left[\sum_{n=1}^{\infty} \frac{(-i\gamma)^n}{n!} \int_0^t dt_1 \int_0^t dt_2 \cdots \int_0^t dt_n \langle \mathcal{T} V(t_1)V(t_2)\cdots V(t_n)\rangle_c\right], \tag{3.63}$$

where $\langle\cdot\rangle_c$ denotes the cumulant average. For example, for the lowest-order corrections, we have

$$\langle A\rangle_c \equiv \frac{\langle s|A|\psi_0\rangle}{\langle s|\psi_0\rangle}, \tag{3.64}$$

$$\langle AB\rangle_c \equiv \frac{\langle s|AB|\psi_0\rangle}{\langle s|\psi_0\rangle} - \frac{\langle s|A|\psi_0\rangle\langle s|B|\psi_0\rangle}{\langle s|\psi_0\rangle^2}. \tag{3.65}$$

This expansion allows us to write down the wave function as

$$\psi(s,t) = \mathrm{e}^{\mathcal{H}_{\text{eff}}(s,t)}, \tag{3.66}$$

with $\mathcal{H}_{\text{eff}}(s,t)$ defined by Eqs. (3.62) and (3.63).

We observe that this is exactly the form given in Eq. (3.41), and thus, this cumulant-expansion-based procedure allows us to derive a perturbative class of classical networks or pCNs, which were first introduced by Schmitt and Heyl recently; see Ref. [187]. Below, we will show how to promote this approach into a variational one, so that we can use the ideas of the previous section. Before, though, let us gain some insight about the physical content of the function $\mathcal{H}_{\text{eff}}(s,t)$. To this end, let us restrict ourselves for a moment to a simple initial product state, namely, an equally weighted superposition of the spin configurations:

$$|\psi_0\rangle = |{\rightarrow}\rangle \equiv \bigotimes_{i=1}^{N} \frac{1}{\sqrt{2}}\big[|{\uparrow_i}\rangle + |{\downarrow_i}\rangle\big]. \tag{3.67}$$

This initial state is particularly convenient as $\psi_0(s) = 2^{-N/2}$ for all s, and hence $\psi_0(s)$ drops out in all the cumulant averages. In this scenario, and upon performing the integrals in the cumulant expansion (3.63), the function $\mathcal{H}_{\text{eff}}$ adopts, in general, the following form

$$\mathcal{H}_{\text{eff}}(s,t) = \sum_l C_l(t)\Phi_l(s). \tag{3.68}$$

That is, $\mathcal{H}_{\text{eff}}$ can be regarded as the effective Hamiltonian of a classical spin system with complex couplings $C_l(t)$, and with spin interactions given by the functions $\Phi_l(s)$, which are local provided that the quantum Hamiltonian is local, too. Situations where quenches from the initial state (3.67) are of physical interest are discussed in posterior sections (see

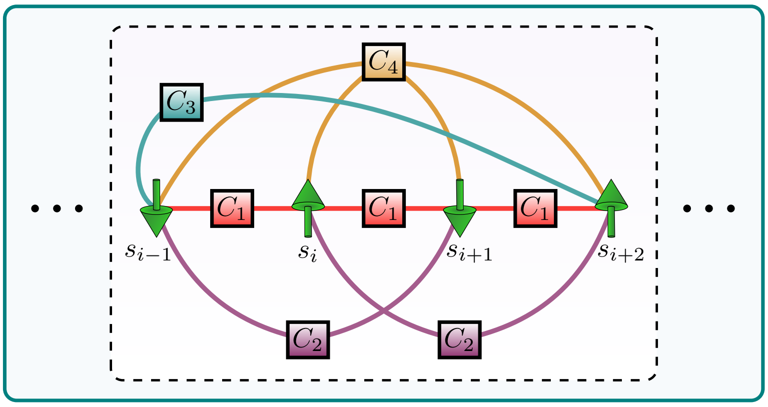

Figure 3.8: Local structure of a classical network for the 1D TFIM in a translationally invariant lattice, containing up to second-order terms. The network's connectivity is defined by functions such as those in Eq. (3.68) [see also Eqs. (3.81) and (3.82) for this particular example]. The nodes of the network correspond to classical spins s_i, whereas the links of the network are specified by the couplings C_l.

for example Sections 3.5.4 and 4.4).

Let us point out that in some cases, it is possible to recast the systems defined by Eq. (3.68), as conventional classical statistical mechanical models. For example, the effective model corresponding to the 1D TFIM to be discussed in Section 3.5.4, contains, up to first order in the cumulant expansion, the following terms [187]:

$$\Phi_1(s) = \sum_i s_i s_{i+1}, \quad \Phi_2(s) = \sum_i s_i s_{i+2}, \tag{3.69}$$

which define a 1D classical Ising model with nearest and next-to-nearest neighbor interactions.

Moreover, as we have already said, systems such as (3.68) can also be visualized as *networks* of classical spins with connectivity specified by the functions $\Phi_l(s)$. In Fig. 3.8, we display the network representation, up to second order, of the classical spin model that emerges when considering a translationally invariant 1D TFIM.

Let us emphasize that the approach presented here works as well for initial states other than the equally weighted superposition (3.67). Importantly, this is true not only for translationally invariant initial states but also for nonuniform ones, as will be shown later. To consider a more general case, let us assume that the perturbation consists of a sum of local terms, namely, $V = \sum_\alpha v_\alpha$, where the overall number of terms is polynomial in system size. Thus, we can write an equation of motion for each of the individual terms:

$$-i\frac{d}{dt}v_\alpha(t) = [H_0, v_\alpha(t)] = \mathrm{e}^{iH_0t}[H_0, v_\alpha]\mathrm{e}^{-iH_0t}. \tag{3.70}$$

Note that the commutator $[H_0, v_\alpha]$ measures, essentially, the energy difference between two eigenstates of H_0 in a transition induced by v_α, i.e., $v_\alpha|s_1\rangle = |s_2\rangle$. Indeed, one can readily prove that

$$[H_0, v_\alpha]|s_1\rangle = (E_{s_2} - E_{s_1})v_\alpha|s_1\rangle. \tag{3.71}$$

Therefore, Eq. (3.70) can be rewritten as

$$\frac{d}{dt}v_\alpha(t) = i\Omega_\alpha v_\alpha(t), \tag{3.72}$$

with Ω_α being a diagonal operator in the computational basis, which measures the energy difference in a transition induced by v_α. This equation admits the formal solution

$$v_\alpha(t) = \mathrm{e}^{i\Omega_\alpha t}v_\alpha. \tag{3.73}$$

Thus, if the effective Hamiltonian is written as $\mathcal{H}_{\text{eff}} = \sum_{n=0}^{\infty}\mathcal{H}^{(n)}$, where the zeroth-order term is $\mathcal{H}^{(0)}(s,t) := -iE_s t + \ln(\psi_0(s))$, and the subsequent orders are defined by Eq. (3.63), one can write, for example, the first-order correction as

$$\mathcal{H}^{(1)}(s,t) = -i\gamma\sum_{\{s'\}}\frac{\psi_0(s')}{\psi_0(s)}\sum_\alpha\langle s|v_\alpha|s'\rangle\int_0^t dt'\mathrm{e}^{i\Omega_\alpha(s)t'}, \tag{3.74}$$

and likewise for higher-order terms. Note that the matrix $\langle s|v_\alpha|s'\rangle$ is typically sparse for physical systems with few-body couplings.

Let us remark that the cumulant expansion (3.63) goes beyond conventional time-dependent perturbation theory, since the corrections considered here effectively account for a resummation of several terms that appear in a standard perturbative expansion [187]. However, pCNs face their own limitations, too. In particular, they are inherently restricted to weak quantum fluctuations (small γ) to ensure that we can safely truncate the expansion (3.63). Besides, the description of the evolution of observables will eventually break down, since resonant processes may be present, giving rise to secular terms that limit a correct description to timescales of order $\mathcal{O}(1/\gamma)$ [187]. Nonetheless, one can still benefit from the framework introduced here, while mitigating the drawbacks mentioned before. This is achieved by constructing adequate *variational* wave functions with a network architecture that is inherited from a corresponding pCN, as argued in the following.

3.5.3 Variational ansatz

Let us now carry out the program already outlined in the previous paragraph, namely, let us consider classical networks with a network structure defined by a cumalant expansion as explained above. We aim now to promote such networks to variational ones. A straightforward possibility to achieve this goal, which we will use in the following, is to replace the set of couplings $\{C_l\}$ in the effective Hamiltonian defining the network, such as the one in Eq. (3.68), by a set of variational parameters $\{\eta_l\}$. The resulting classical networks are called *variational classical networks* or VCNs, as we have already mentioned. An important remark is that the resulting VCNs will inherit the controlled character of the cumulant expansion, in that the accuracy of the approximation can be improved systematically by reducing the value of γ, or by taking into account higher-order cumulants.

For concreteness, let us consider a classical network like the one given by Eq. (3.68). The corresponding VCN would then be defined by the following effective Hamiltonian:

$$\mathcal{H}_{\mathrm{VCN}}(s;\eta(t)) = \sum_l \eta_l(t)\Phi_l(s). \tag{3.75}$$

We reiterate that the structure of this network is basically determined by the functions $\Phi_l(s)$, which arise from the underlying cumulant expansion.

In the more general case such as Eq. (3.74), one can build the corresponding VCN by noting that $\Omega_\alpha(s)$ take a finite number of discrete values for any s. Thus one can simply introduce a variational parameter for each value of $\Omega_\alpha(s)$. To fix ideas let us consider the first-order correction given in Eq. (3.74), and let us denote as Λ_{Ω_α} the set of all possible values of $\Omega_\alpha(s)$. After rewriting the integral

$$\int_0^t dt' \mathrm{e}^{i\Omega_\alpha(s)t'} = \sum_{\Omega\in\Lambda_{\Omega_\alpha}} \delta_{\Omega_\alpha(s),\Omega} \int_0^t dt' \mathrm{e}^{i\Omega t'}, \tag{3.76}$$

we can introduce a set of variational parameters so that the corresponding first-order variational effective Hamiltonian reads

$$\mathcal{H}^{(1)}_{\mathrm{VCN}}(s;\eta(t)) = -i\gamma \sum_{\{s'\}} \frac{\psi_0(s')}{\psi_0(s)} \sum_\alpha \langle s|v_\alpha|s'\rangle \times \sum_{\Omega\in\Lambda_{\Omega_\alpha}} \delta_{\Omega_\alpha(s),\Omega}\eta^{(1)}_\Omega(t). \tag{3.77}$$

and likewise for higher-order terms. In either case, the concomitant wave function amplitudes take the form

$$\psi_{\mathrm{VCN}}(s;\eta(t)) = \mathrm{e}^{\mathcal{H}_{\mathrm{VCN}}(s;\eta(t))}, \tag{3.78}$$

which is time-evolved with the TDVP described in Section 3.4.2.

3.5.4 Benchmark: Quenches in the 1D TFIM model

In this section we show how to build VCNs in a concrete example and benchmark their performance for computing the quantum many-body dynamics. To this end, we study several quenches in the 1D TFIM; see Eq. (3.13). First, however, let us recall some features of the model in Eq. (3.13). First of all, the 1D TFIM is integrable by means of a Jordan-Wigner transformation [275]; hence, comparison with analytical solutions is at our disposal. Moreover, this model features both equilibrium [276] and dynamical [277] quantum phase transitions. Indeed, the Hamiltonian (3.13) undergoes an equilibrium quantum phase transition at $h_c/J = 1$ [276], where the critical point separates a ferromagnetic phase

($h < h_c$) from a paramagnetic one ($h > h_c$). Its dynamical quantum phase transition is signaled by non-analyticities in the many-body dynamics [277, 278], and occurs when a global quench is performed across the underlying equilibrium quantum phase transition. For example, when quenching from the paramagnetic point $h_0 = \infty$, which corresponds to the initial state in Eq. (3.67), to a point within the ferromagnetic phase ($h < h_c$). Although it is not our aim to probe dynamical quantum phase transitions, we shall consider the aforementioned quench, as well as quenches within the paramagnetic phase only (see details below). Let us point out that from an experimental point of view, both probing the dynamics of the 1D TFIM and engineering the relevant initial state in Eq. (3.67) are now feasible tasks with current technologies in quantum simulators in various settings [163, 169, 170]. We start by showing how to construct the VCNs for the 1D TFIM.

VCNs for the 1D TFIM

The corresponding perturbative CNs for TFIMs have been recently derived elsewhere [187]. Here, we review the main steps of such calculations. Taking the exchange constant J as the overall energy scale, we let the Ising term be reference Hamiltonian $H_0 \equiv -\sum_{i=1}^{N} \sigma_i^z \sigma_{i+1}^z$, and the transverse-field term be the perturbation $\gamma V \equiv -h/J \sum_i \sigma_i^x$ (identifying $\gamma = -h/J$). Also, in the following, we consider periodic boundary conditions.

Using the basic commutation relations of the Pauli matrices, one can readily show that

$$[H_0, \sigma_j^x] = -2(\sigma_{j-1}^z + \sigma_{j+1}^z)\sigma_j^z \sigma_j^x, \tag{3.79}$$

where we emphasize again that this commutator measures the change in energy in a transition induced by σ_j^x, between eigenstates of H_0. The solution to the equation of motion Eq. (3.72) for $\sigma_j^x(t)$ therefore reads

$$\begin{aligned} \sigma_j^x(t) &= \mathrm{e}^{-2i(\sigma_{j-1}^z + \sigma_{j+1}^z)\sigma_j^z Jt} \sigma_i^x \\ &= \left[\cos^2(2Jt) - \sin^2(2Jt)\sigma_{j-1}^z \sigma_{j+1}^z - \frac{i}{2}\sin(4Jt)(\sigma_{j-1}^z + \sigma_{j+1}^z)\sigma_j^z\right]\sigma_i^x, \end{aligned} \tag{3.80}$$

where the second step follows from Euler's formula. This solution leads to a first-order pCN of the form anticipated in Eq. (3.69). Indeed, plugging the solution (3.80) in Eq. (3.74) and using the fact that $\psi_0(s) = 2^{-N/2}$ for all s, for the initial state in Eq. (3.67), one gets

$$\mathcal{H}_{\mathrm{TFIM}}^{(1)} = C_0^{(1)}(t)N + C_1^{(1)}(t)\sum_{i=1}^{N} s_i s_{i+1} + C_2^{(1)}(t)\sum_{i=1}^{N} s_i s_{i+2}, \tag{3.81}$$

where the explicit form of the coefficients $C_l^{(1)}$ can be easily deduced from Eqs. (3.80) and (3.74). As previously explained, the classical network defined above can be turned into a VCN, simply by regarding the couplings $C_l^{(1)}$ as variational parameters.

The perturbatively motivated structure of the VCN can be systematically expanded by straightforwardly plugging Eq. (3.80) into higher-order terms in Eq. (3.63). By potentiating $\sum_j \sigma_j^x(t)$, more and more nonlocal couplings are generated. In fact, at order k couplings up to distance $k+1$ are generated (see Ref. [187] for details). Hence, we can systematically increase the VCN by adding all distinct classical coupling terms up to a given distance d, which are compatible with the system's symmetries. For example, when considering second-order corrections, the terms

$$\mathcal{H}_{\text{TFIM}}^{(2)} = C_1^{(2)}(t) \sum_{i=1}^{N} s_{i-1}s_i s_{i+1}s_{i+2} + C_2^{(2)}(t) \sum_{i=1}^{N} s_i s_{i+3}, \tag{3.82}$$

that respect $\mathbb{Z}_2$ and lattice symmetries, and which expand up to a distance $d = 3$, would be added to the effective Hamiltonian, $\mathcal{H}_{\text{TFIM}} = \mathcal{H}_{\text{TFIM}}^{(1)} + \mathcal{H}_{\text{TFIM}}^{(2)}$ (see Fig. 3.8).

Notice that the possible number of coupling terms in the classical network at $d = N$ equals the dimension of the Hilbert space of the quantum system. In the presence of translational invariance, lattice inversion symmetry, and $\mathbb{Z}_2$ symmetry, the symmetry allowed couplings can be obtained by generating the corresponding symmetry reduced computational basis and then identifying the domain wall configuration in each computational basis state with a coupling term in the variational wave function. In the absence of $\mathbb{Z}_2$ symmetry the computational basis configurations themselves correspond to coupling terms. Finally, let us point out that the classical networks presented here for the 1D TFIM can be mapped onto certain types of ANNs [187].

Quench protocol and results

As mentioned before, quenches in the 1D TFIM across the critical point comprise a dynamical quantum phase transition. In that respect, an interesting class of quenches consists of going from the paramagnetic to the ferromagnetic phase in the parameter space. Here, we concentrate precisely on this situation as well as on quenches within the paramagnetic phase. In particular, we consider the initial state $|{\rightarrow}\rangle$ given in Eq. (3.67), which corresponds to the point $h_0 = \infty$. Next, we compute the unitary dynamics generated by the Hamiltonian in Eq. (3.13) with $h/J < 1$ (ferromagnetic) and $h/J > 1$ (paramagnetic).

We compare results for the dynamics of the TFIM obtained in three different ways: exact, pCN, and VCN. For the exact solution we exploit the integrability of the model. Via a Jordan-Wigner transformation the spin system is mapped to a model of noninteracting fermions [275], for which closed form expressions can be obtained for all quantities of interest [276]. The results shown here are for a translationally invariant chain in the thermodynamic limit. With pCN and VCN, we consider systems with $N = 50$ sites and periodic boundary conditions. On the timescales shown there is no finite-size effect in the observables. To obtain the time-evolved VCN we initialize all network couplings with zero

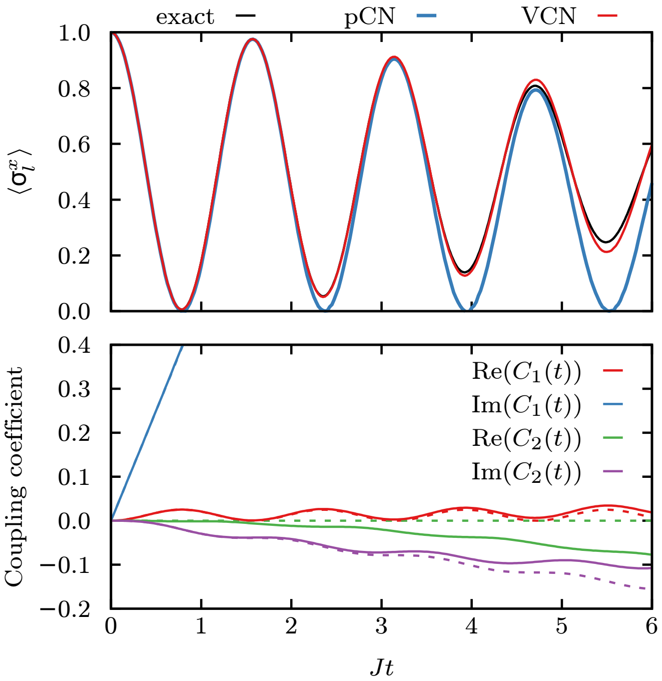

Figure 3.9: Comparison of first-order pCN, first-order VCN and the exact solution of the TFIM with $N = 50, h/J = 0.1$. Top: Dynamics of the transverse magnetization $\langle\sigma_l^x\rangle$. The black curve shows the exact solution obtained via fermionization in the thermodynamic limit. Bottom: Evolution of the perturbative (dashed lines) and variational (solid lines) couplings of the classical network defined in Eq. (3.81).

and integrate the TDVP equation using a second-order consistent integrator with adaptive time step. Expectation values with respect to $|\psi(s)|^2$ are estimated using 8×10^4 samples generated by a single-spin-flip Markov chain Monte Carlo.

The results of the quench dynamics are shown in Figs. 3.9–3.12. First, in Fig. 3.9, we compare the performance of the first-order pCN given in Eq. (3.81) and its associated VCN, in a quench to $h/J = 0.1$. As illustrated for the dynamics of the transverse magnetization $\langle\sigma_l^x\rangle$, both approaches capture very accurately the short-time behavior. However, it is the variational ansatz that yields a much more accurate description at longer times. Interestingly, when looking at the evolution of the perturbative and variational couplings, Fig. 3.9 (bottom), we can see that their dynamics start to differ approximately at the point where discrepancies in the evolution of observables are first noted.

In Fig. 3.10, we study the overall performance of various VCNs with different coupling distance d, when quenching to the ferromagnetic phase ($h/J = 0.3$) and the paramagnetic one ($h/J = 3$), left and right columns in Fig. 3.10, respectively. As a principal result, we observe that the accuracy is systematically improved upon increasing the coupling distance of the VCNs. This is not only observed from the real-time evolution of the transverse magnetization $\langle\sigma_l^x\rangle$, and the next-to-nearest neighbor correlation function $\langle\sigma_l^z\sigma_{l+2}^z\rangle$, but also from the integrated residuals $R^2(t)$, which show a systematic error convergence by

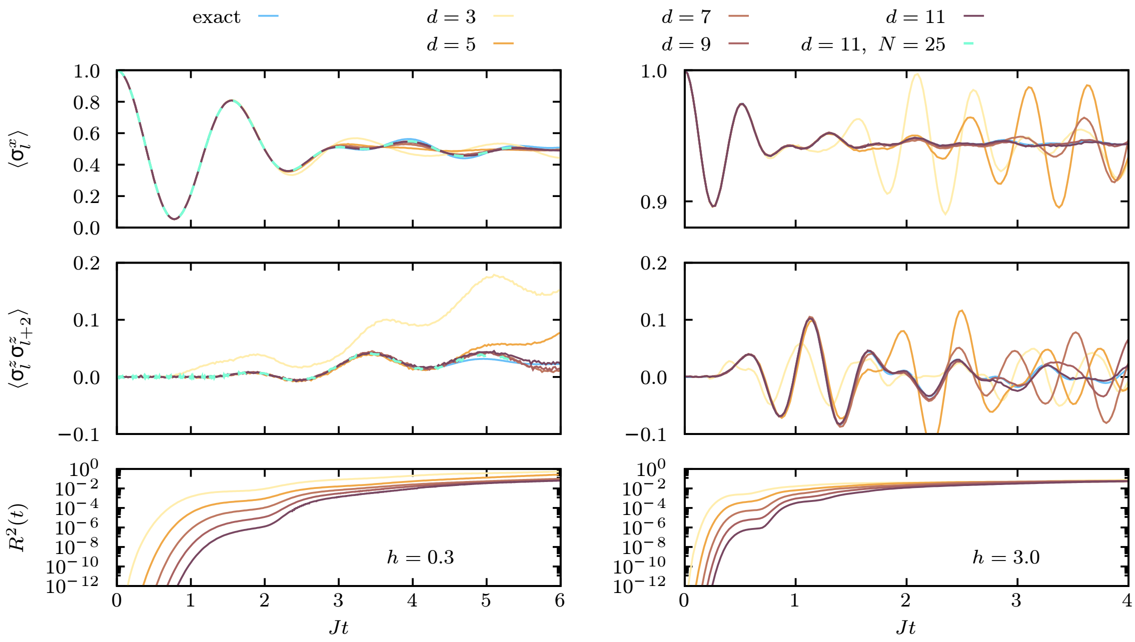

Figure 3.10: Dynamics of the TFIM in quenches from $h_0 = \infty$ to $h/J = 0.3$ (left column) and $h/J = 3$ (right column), with $N = 50$. Convergence of VCN solution to the exact dynamics is shown as a function of the coupling distance d (see main text). Upper panels: Transverse magnetization $\langle \sigma_l^x \rangle$. Middle panels: Next-to-nearest neighbor correlation function $\langle \sigma_l^z \sigma_{l+2}^z \rangle$. Lower panels: Integrated relative residual $R^2(t)$. Results for a different system size ($N = 25$) are also shown in the quench to $h/J = 0.3$ (left column) for the VCN with $d = 11$.

increasing d. Next, focusing on the transverse magnetization $\langle \sigma_l^x \rangle$, we see that, in both quenches, it quickly relaxes to a steady-state value: While at weak transverse field this feature can be well captured by all the considered VCNs, the situation becomes more challenging when the value of h/J is large. Nevertheless, even in the latter case, the dynamics computed with the VCNs with the largest coupling distances regarded here ($d = 9, 11$) follow very closely the actual relaxation of $\langle \sigma_l^x \rangle$. As for the next-to-nearest neighbor correlation function $\langle \sigma_l^z \sigma_{l+2}^z \rangle$, it is found that correlations at this distance are rather small in the quench to the ferromagnetic phase, whereas they are larger and oscillate between positive and negative values before decaying to zero in the quench within the paramagnetic phase. In both cases, however, it is again the highest-order VCNs that yield a better description of this correlation function, as expected. In Fig. 3.10 results corresponding to a different system size ($N = 25$) are also shown for comparison in the quench to $h/J = 0.3$, with $d = 11$. There are no appreciable finite-size effects observed up to the accessed timescales.

The accuracy of correlations as a function of the coupling distance d is analyzed in Fig. 3.11, for the two quenches considered before. In this figure we plot the deviation of the TDVP results from the exact dynamics $\Delta \langle \sigma_l^z \sigma_{l+r}^z \rangle$, in terms of two-point correlation

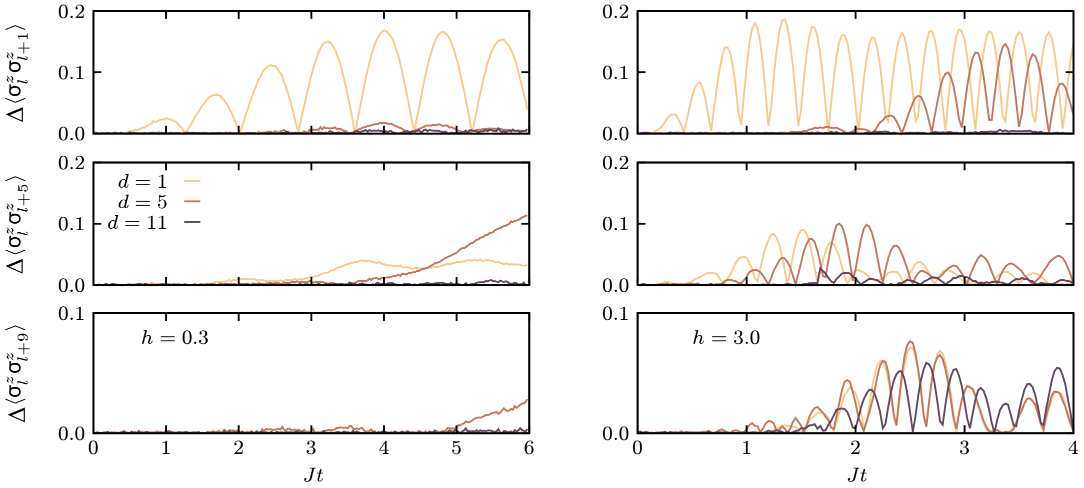

Figure 3.11: Accuracy of correlations in the TFIM at different distances in the quench to $h/J = 0.3$ (left column) and $h/J = 3$ (right column): The quantity $\Delta\langle\sigma_l^z\sigma_{l+r}^z\rangle$ denotes the absolute value of the difference between the TDVP result and the exact result from free fermions.

functions $\langle\sigma_l^z\sigma_{l+r}^z\rangle$, at various distances r. As a general remark, we observe that the deviations from the exact result are systematically decreased by increasing the coupling distance d, in agreement with the results in Fig. 3.10. Also, it should be noted that the smaller the coupling distance d is, the earlier the deviations from the exact dynamics occur, as expected from the underlying perturbatively-motivated structure of the VCNs. Moreover, we observe that in the case of large transverse field the deviations, in general, grow more than in the quench to weak fields. This is due to the fact that in the dynamics with a large transverse field, correlations develop significantly at all the considered distances in the relevant timescales, see Fig. 3.12 below, whereas at weak transverse field the dynamics is more local and hence correlations at large distances are rather small (see, for instance, the correlation function on the left column of Fig. 3.10). Lastly, note that the oscillations observed for some of the deviations arise from the fact that the variational results oscillate around the exact solution, as can be seen in Fig. 3.10.

Finally, it is instructive to look at the correlation spreading when using VCNs with different coupling distance d. This is illustrated in Fig. 3.12 for the quench to $h/J = 3$, with three VCNs with $d = 1, 5, 11$, as well as the exact solution. The results shown on this figure reveal another crucial feature of VCNs: The distance for which a VCN can adequately capture the propagation of correlations is exactly determined by the coupling distance d. Thus, we see that the spreading of correlations can be well captured in a controlled manner by increasing the coupling distance in the structure of the VCN. Although this result is obtained for the Ising model, we expect that it holds in general.

3.6 Summary and further remarks

In this chapter, we have introduced a numerical variational scheme for the study of dynamics in correlated quantum systems in one and higher dimensions. This method relies on an efficient representation of the many-body wave function in terms of complex networks of classical spin variables. This class of variational wave functions, termed VCNs, is similar to ANNs. Crucially, VCNs can be constructed according to a controlled prescription as it has been underlined and explicitly shown in this chapter for the 1D TFIM; see Section 3.5. We have, however, presented VCNs as a general numerical framework that can be applied to any interacting quantum lattice model, regardless of spatial dimensionality, provided that an expansion around a well-defined classical limit is possible. In the next chapter, we will show how to use this method to study the nonequilibrium dynamics in a more challenging 2D interacting LGT. On the other hand, in the present chapter we have also reviewed some other state-of-the-art techniques for the study of the nonequilibrium quantum dynamics quantum many-body systems. In particular, we explained the main ideas of ED methods in Section 3.2 and of time evolution with MPS in Section 3.3.

Coming back to the VCN approach, we showed in this chapter the way in which the method works and its range of applicability by studying quantum quenches in the paradigmatic 1D TFIM, which serves as an ideal testing ground for our method as it can be solved exactly [275]. Moreover, the 1D TFIM presents the advantage that the resulting VCNs have a relatively simple and intuitive form, which is in fact, that of classical Ising models. Further, for this example we have shown, in a rather intuitive manner, how the perturbatively motivated architecture of VCNs can be systematically built upon by incorporating classical couplings that expand over a certain coupling distance, which is closely related to the order of the underlying cumulant expansion. Then, we characterized the performance of various VCNs in terms of the real-time evolution of two-point correlation functions at varying distance, local off-diagonal observables, and the integrated residuals. In general,

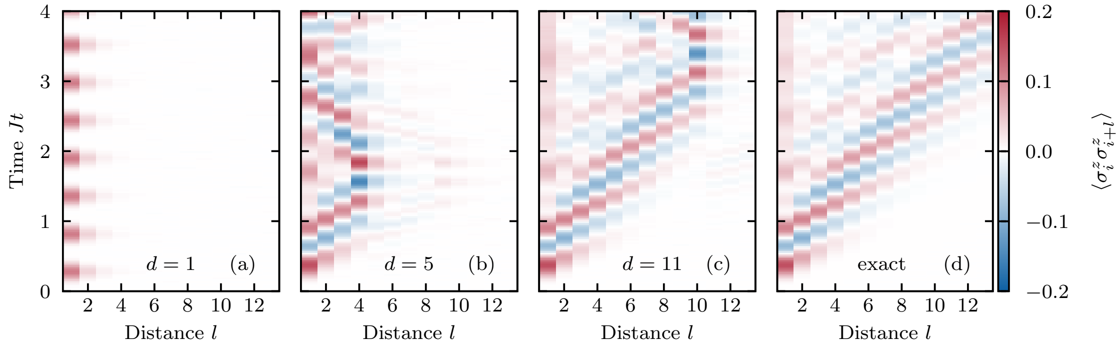

Figure 3.12: Correlation spreading in the Ising model for the quench to $h/J = 3$, with VCNs with (a) $d = 1$, (b) $d = 5$, (c) $d = 11$: Spreading is only captured up to the coupling distance. The exact correlation dynamics is also shown in (d).

we found that the basic architecture of VCNs allows for a systematic improvement in the accuracy of such results by adding higher-order terms according to the controlled procedure referred to above. We have verified that this statement remains true when varying system size and quenching to different points in the parameter space of the associated Hamiltonian.

Overall, the quantum quenches discussed above have allowed us to characterize the accuracy and versatility of our methodology. As a principal observation, we note that upon adding higher-order couplings in the structure of a VCN, its accuracy can be improved in a controlled way. In addition, higher-order couplings also account for another crucial feature: correlation spreading is properly captured up to a spatial scale determined by the maximum coupling distance included in the architecture of the VCN. On the other hand, at a fixed order of the cumulant expansion, the accuracy can also be systematically increased by reducing the strength of the off-diagonal perturbation. As a rule of thumb, we expect a low-order VCN to give sufficiently accurate results up to a timescale set by the inverse of the perturbation strength [187]. However, such timescales can be further prolonged when considering higher-order VCNs. Besides, for a given order of the cumulant expansion, in general, a VCN outperforms its corresponding pCN at all relevant timescales, and in some cases, the former can account for important features of the quantum dynamics, which are just beyond the scope of the latter, such as the relaxation of observables towards a steady-state value. We have checked that all the remarks made above also hold when varying system size, and quenching to different points in the parameter space of the studied Hamiltonian. As it has been already mentioned, in Chapter 4, we will make use of VCNs to study the quantum dynamics in a 2D interacting LGT. We point out that the remarks made above also hold in this case.

Naturally, our method is not exempt from limitations and drawbacks, which can be understood from the considerations made in the previous paragraph. First and foremost, the addition of higher-order terms is accompanied by an exponential growth in complexity, so in practice, we are limited to a given order of the cumulant expansion. Moreover, we also know that a VCN will fail at capturing correlations beyond their maximum coupling distance, as illustrated very clearly in Fig. 3.12. Such coupling distance is also determined by the order of the cumulant expansion. Also, in general, we expect a breakdown in the description of the evolution of observables after a timescale set by the inverse of the perturbation strength, at least, as far as low-order VCNs are concerned.

Regarding possible further applications, there are several interesting routes that one could explore employing VCNs. A particularly promising one consists of formulating hybrid approaches that combine VCNs with ANNs, so as to mitigate some of the drawbacks sustained by both kinds of generative machines. Also, as we have already mentioned, the applicability of VCNs is not fundamentally restricted by spatial dimensionality. Thus, in this respect, it would be interesting to use this approach to study the nonequilibrium dynamics in 2D and 3D systems. In next chapter, we describe precisely one of such applications when we study the quantum dynamics in a 2D QLM with only gauge fields. However, other potential applications could be: 2D TFIMs, 2D bosonic and fermionic Hubbard models, 2D QLMs in the presence of a dynamical matter field, 3D quantum spin ice models, as well as other kinetically constrained models. Lastly, regarding VCNs as generative machines also raises the possibility of employing them for tasks other than solving the real-time dynamics of quantum many-body systems. In particular, VCNs could be used for addressing ground-state search problems, with an optimization procedure guided by a conventional variational principle that minimizes the energy functional, rather than using a TDVP.

Chapter 4

Disorder-free localization in an interacting 2D lattice gauge theory

The content of this chapter is mainly based on Refs. [2, 3].

In this chapter, we study the nonequilibrium dynamics of one of the LGTs previously introduced in Chapter 2. Namely, the U(1) quantum link model in two dimensions; see Eq. (4.1) and Fig. 4.1. It is our central result that this system exhibits nonergodic behavior in the form of *disorder-free localization*, which has been recently introduced as a mechanism for ergodicity breaking in low-dimensional homogeneous lattice gauge theories caused by *local constraints* imposed by gauge invariance [107–114]. In this respect, it is worth emphasizing the role of local constraints. Indeed, systems with local constraints play an important role in various physical contexts ranging from strongly correlated electrons [44, 52] and frustrated magnets [114, 279, 280] to quantum information [10] and fundamental theories of matter such as quantum electrodynamics and chromodynamics [4–6], where constraints take the form of local gauge symmetries, as we have seen in Chapter 2 (see in particular Section 2.1.4). The equilibrium properties of such systems have been extensively studied over the last decades, but only recently their nonequilibrium dynamics has moved into focus. In particular, local constraints have emerged as a new paradigm for ergodicity breaking, besides the two known archetypical scenarios caused by localization due to strong disorder or integrability. Systems with local constraints can exhibit rare nonergodic eigenstates, termed quantum many-body scars [118–122], or extremely slow relaxation [128–131], whereas dipole conservation can prevent thermalization of large parts of the spectrum in one-dimensional fractonic systems [123–127]. Disorder-free localization can be placed in this list as a generic mechanism for nonergodic behavior hosted in LGTs where local constraints emerge naturally due to the local gauge symmetry, leading to an extensive number of local conserved quantities. Specifically, this can lead to the absence of ergodicity in 1D LGTs with discrete [108, 109, 112] and continuous [110, 113] gauge symmetries or for higher-dimensional systems in the low-energy limit [107] or when they are non-interacting [111]. However, it has remained a key challenge to identify nonergodic behavior in genuinely interacting quantum systems beyond one spatial dimension.

Here we show that the 2D U(1) quantum link model features both localized and ergodic phases in the absence of disorder. This result appears especially remarkable since for the more conventional disorder-induced many-body localization [115–117] it is debated whether interactions destroy localization in 2D, as it follows from the theoretical arguments [184, 185], or not, as suggested by experiment [168] and numerics [186]. Thus, we show that the constraint-induced disorder-free localization provides an alternative and robust localization mechanism surviving in the higher dimensions in presence of interactions. In particular, we demonstrate nonergodic behavior in the QLM by obtaining a bound on the localization-delocalization transition through a classical correlated percolation problem implying a fragmentation of Hilbert space on the nonergodic side of the transition. The localization-delocalization transition in the QLM is further supported by investigating the quantum dynamics of the model. Specifically, we identify a distinguishing quantum dynamical signature of the two phases by studying the propagation of an initial line defect, which leads to two different light cone structures. For this part of this study, we make use of the varaitional classical networks introduced in the previous chapter. We show in full detail how to construct first- and second-order VCNs for the QLM and provide specific benchmarks for the problem at hand in quasi-1D geometries, where one can still access the dynamics via exact diagonalization. Importantly, our theoretical analysis could potentially be the subject of future experiments with quantum simulators, following remarkable proof-of-principle experimental realizations of 1D LGTs [33, 37–41].

The structure of this chapter is the following. In Section 4.1, we recall the Hamiltonian of the U(1) QLM and the definition of its superselection sectors. The mechanism of disorder-free localization is explained in Section 4.2. We illustrate it in the 1D Schwinger model in which disorder-free localization can be shown in a rather elegant manner. Next, in section 4.3, we build in detail the VCNs for the QLM. Specifically, we construct first- and second-order VCNs, whose effective Hamiltonians turn out to be highly nonconventional spin models. We benchmark extensively the resulting VCNs (and also a partial third-order ansatz) in quasi-1D ladder systems where one can still access the dynamics via exact diagonalization methods. This is done in Section 4.4.2. The main results regarding the quantum dynamics are presented in Section 4.4.3, where we look at the spreading of line defects with a subextensive energy contribution and identify distinctive light cone structures in the localized and ergodic phases. We then derive a bound on this transition by studying a correlated classical percolation problem in Section 4.5. Section 4.6 contains a summary and conclusions of this chapter.

4.1 The model

We study the 2D U(1) QLM [23, 182, 183] that we have introduced in Section 2.2.1. Once again, we consider a pure gauge theory, that is, without coupling to matter fields, and with gauge fields represented by spin-1/2 operators that are defined on the links of a square lattice Fig. 4.1(a). Let us remind that in our notation a link connecting the vertices $\mathbf{r} = (x, y)$ and $\mathbf{r} + \hat{\mu}$ (here $\hat{\mu} = \hat{\imath}, \hat{\jmath}$ is one of the two unit vectors of the lattice), is labeled by the coordinates of the site $\mathbf{r} = (x, y)$ and the direction μ. For convenience, let us also write here the Hamiltonian of the theory, namely,

$$H = -\mathcal{J} \sum_{\square} (U_{\square} + U_{\square}^{\dagger}) + \lambda \sum_{\square} (U_{\square} + U_{\square}^{\dagger})^2, \tag{4.1}$$

where we have omitted the electric-field term, since it only enters as an additive constant in the $S = \frac{1}{2}$ representation. Also, $U_{\square} = S^{+}_{\mathbf{r},i} S^{+}_{\mathbf{r}+\hat{\imath},j} S^{-}_{\mathbf{r}+\hat{\jmath},i} S^{-}_{\mathbf{r},j}$ induces a collective flip of all spins on plaquette $\square$, and $S^{\pm}_{\mathbf{r},\mu}$ denote the raising and lowering operators. The first (kinetic-energy) term induces coherent dynamics and the second (potential-energy) term counts the number of flippable plaquettes. For what follows, we will consider periodic boundary conditions and the case of a strong potential term with $\mathcal{J}/\lambda = -0.1$. As mentioned in Section 2.2, the QLM in Eq. (4.1) not only appears in the context of high-energy physics, but also shares strong connections to condensed matter systems featuring quantum spin ice phases or quantum dimer models [23, 26, 44, 48, 49, 182]. On the experimental side various proposals have explored the potential realization of the QLM in quantum simulators within the past years [26, 190, 191].

The local gauge symmetry of the QLM is generated by the operators

$$G_{\mathbf{r}} = \sum_{\mu} (S^z_{\mathbf{r},\mu} - S^z_{\mathbf{r}-\hat{\mu},\mu}), \tag{4.2}$$

counting the total inflow of the electric field to the vertex $\mathbf{r}$. Since $[G_{\mathbf{r}}, H] = 0$ for all lattice points and $[G_{\mathbf{r}}, G_{\mathbf{r}'}] = 0$, eigenstates of H can be classified by the respective eigenvalues $q_{\mathbf{r}} \in \{-2, -1, 0, 1, 2\}$ of $G_{\mathbf{r}}$. The set of $\mathbf{q} = \{q_{\mathbf{r}}\}$ defines the so-called superselection sector of states $|\psi_{\mathbf{q}}\rangle$ with $G_{\mathbf{r}}|\psi_{\mathbf{q}}\rangle = q_{\mathbf{r}}|\psi_{\mathbf{q}}\rangle$, so that each of the $q_{\mathbf{r}}$ can be given a physical meaning in terms of static background charges located at $\mathbf{r}$ (see Section 2.1.4).[1] The QLM further has global conserved quantities given by

$$\Phi_x = \sum_{y} S^z_{\mathbf{r},i}, \qquad \Phi_y = \sum_{x} S^z_{\mathbf{r},j}, \tag{4.3}$$

which define the flux sectors.

---

[1] To follow the notation in Ref. [2], here we denote static charges by $q_{\mathbf{r}}$, rather than the symbol $Q_{\mathbf{r}}$ used in Chapter 2.

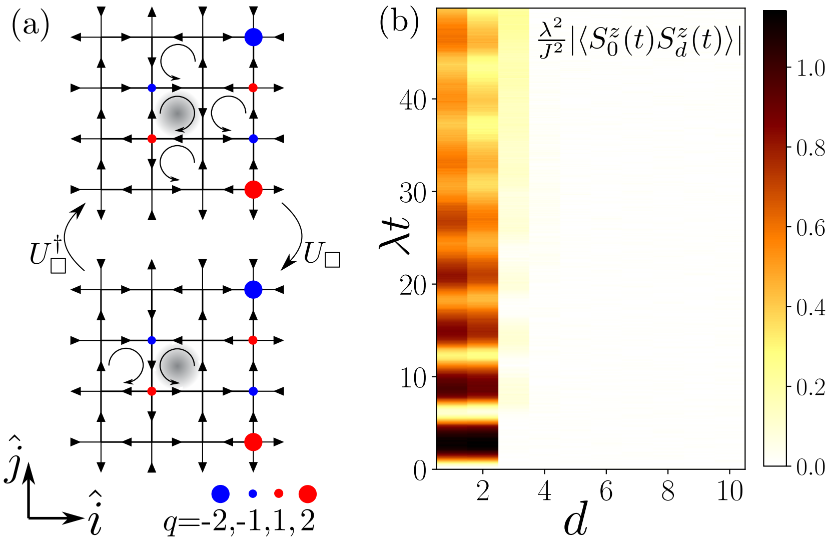

Figure 4.1: a) Illustration of the $U(1)$ quantum link model (QLM) with spin-$1/2$'s located on the links of the square lattice. Spins pointing → or ↑ correspond to $S^z = +1$ and ← or ↓ to $S^z = -1$, respectively. Kinetics is introduced by plaquette-flip operators $U_\square, U_\square^\dagger$ (shown for the darkened central plaquette) whenever the spins on a plaquette are oriented clockwise or counterclockwise. Flippable plaquettes are denoted by circular arrows. Background charges with nonzero inflow or outflow of electric field at a given vertex are indicated by red a blue dots. b) Spatiotemporal buildup of quantum correlations $|\langle S^z_{\mathbf{r},y}(t)S^z_{\mathbf{r}+\mathbf{d},y}(t)\rangle| \equiv |\langle S_0^z(t)S_d^z(t)\rangle|$ ($\mathbf{d} = d\hat{i}$) starting from $|\psi(\alpha = 0)\rangle = |{\rightarrow}\rangle$ in the localized phase of the QLM for $\mathcal{J}/\lambda = -0.1$ and a system of size 80×80, that is, 12800 spins.

4.2 Disorder-free localization

The existence of the superselection sectors, protected by gauge invariance, can lead to an unconventional scenario for ergodicity breaking. Consider a homogeneous superposition state

$$|\psi\rangle = \sum_{\mathbf{q}} C_{\mathbf{q}}|\psi_{\mathbf{q}}\rangle, \tag{4.4}$$

involving many superselection sectors. As the Hamiltonian and typical observables are block-diagonal, that is, $H|\psi_{\mathbf{q}}\rangle = H_{\mathbf{q}}|\psi_{\mathbf{q}}\rangle$, the expectation values of an operator O during dynamics become equivalent to

$$\langle O(t)\rangle = \sum_{\mathbf{q}} |C_{\mathbf{q}}|^2 \langle\psi_{\mathbf{q}}|\mathrm{e}^{iH_{\mathbf{q}}t} O \mathrm{e}^{-iH_{\mathbf{q}}t}|\psi_{\mathbf{q}}\rangle, \tag{4.5}$$

resembling an effective disorder average with the disorder strength determined by the random background charges in the typical superselection sectors [110]. This can, in principle, lead to nonergodic behavior of $\langle O(t)\rangle$, although both the initial state and the Hamiltonian are homogeneous leading to the notion of disorder-free localization [108]. For illustrative purposes, we show, following Ref. [110], what the Hamiltonians $H_{\mathbf{q}}$ look like in a one-dimensional U(1) LGT, namely, the Schwinger model in Eq. (2.59) that we rewrite here for convenience:

$$H_{\text{Schwinger}} = -t\sum_r (\psi_r^\dagger U_{r,r+1}\psi_{r+1} + \text{h.c.}) + m\sum_r (-1)^r \psi_r^\dagger \psi_r + J\sum_r E_r^2, \tag{4.6}$$

with the generators of the local gauge symmetry given by Eq. (2.18). It turns out that in this case, it is possible to integrate out analytically the gauge fields thanks to Gauss law [28]. To see this, we apply a Jordan-Wigner transformation to the staggered fermions: $\psi_r^\dagger \psi_r = (\sigma_r^z + 1)/2$ [110], and assume a zero background field. Then, Gauss law yields the relation

$$E_r = E_{r-1} + \frac{\sigma_r^z + (-1)^r}{2} + q_r, \tag{4.7}$$

and hence the gauge fields can be sequentially integrated out. After integration of the gauge fields, the corresponding Hamiltonian in each superselection sector is given by the sum of two terms: $H_{\mathbf{q}} = H^1 + H^2_{\mathbf{q}}$. The first one has to do with the matter-gauge coupling and is independent of the static charges. The second term has to do with the electric field energy term and contains a long-range spin-spin interaction (H^{ZZ}), and a single-spin term ($H^Z_{\mathbf{q}}$), which, crucially, depends on the background charges [110]:

$$H^Z_{\mathbf{q}} = \frac{J}{2}\sum_{r=1}^{N-1}\left(\sum_{l=1}^{r}\sigma_l^z\right)\left[\left(\sum_{j=1}^{r} q_j\right) - r \bmod 2\right]. \tag{4.8}$$

Thus, when considering an initial state of the form (4.4), one precisely obtains a charge distribution average like in Eq. (4.5), with the terms $H^Z_{\mathbf{q}}$ affectively acting as a correlated "disorder" for the spin dynamics [110].

The 1D model in Eq. (4.6) is thus somewhat special in the sense that the gauge fields can be integrated out exactly. Therefore, it is a fair question to ask whether this mechanism is also present in higher-dimensional interacting LGTs, in which such kind of simplifications are not possible. As mentioned before, the investigation of such question in the 2D QLM is the central goal for this part of the present thesis. We will answer it partly by studying the quantum dynamics of this model, which is computed with the VCN method introduced previously in Section 3.5. Thus, below we discuss how to build the relevant VCNs for the problem at hand.

4.3 VCNs for the QLM

In order to study the nonequilibrium dynamics of the QLM, we use the method of VCNs that was introduced in Section 3.5 of the previous chapter. Following the general settings discussed in Section 3.5.1, we start by identifying the classical limit of the theory under consideration. For the Hamiltonian in Eq. (4.1), such a term is $H_0 \equiv \sum_\square (U_\square + U_\square^\dagger)^2$. On the other hand, quantum fluctuations are induced by the term $\gamma V \equiv -\frac{\mathcal{J}}{\lambda}\sum_\square (U_\square + U_\square^\dagger)$, where we recognize $\gamma = -\frac{\mathcal{J}}{\lambda}$. Next, we solve the equation of motion for the operator $U_\square$, that is, $-i\frac{\mathrm{d}}{\mathrm{d}t}U_\square(t) = [H_0, U_\square]$ (and likewise for $U_\square^\dagger$). We get,

$$U_\square(t) = \mathrm{e}^{i\lambda\Omega_\square t}U_\square, \quad U_\square^\dagger(t) = \mathrm{e}^{-i\lambda\Omega_\square t}U_\square^\dagger, \tag{4.9}$$

where the operator $\Omega_\square$ commutes with both $U_\square$ and $U_\square^\dagger$, and is given by

$$\Omega_\square = \sum_{p\in\mathcal{P}_\square}(-\mathcal{A}_p + \mathcal{B}_p), \tag{4.10}$$

where $\mathcal{P}_\square = \{a, b, c, d\}$ denotes the set of neighboring plaquettes around a given plaquette (see Fig. 4.2), and the operators $\mathcal{A}_p$ and $\mathcal{B}_p$ are given by

$$\mathcal{A}_a = P^\uparrow_{a,1}P^\uparrow_{a,2}P^\downarrow_{a,4}, \quad \mathcal{B}_a = P^\downarrow_{a,1}P^\downarrow_{a,2}P^\uparrow_{a,4}, \tag{4.11}$$

$$\mathcal{A}_b = P^\uparrow_{b,1}P^\uparrow_{b,2}P^\downarrow_{b,3}, \quad \mathcal{B}_b = P^\downarrow_{b,1}P^\downarrow_{b,2}P^\uparrow_{b,3}, \tag{4.12}$$

$$\mathcal{A}_c = P^\uparrow_{c,2}P^\downarrow_{c,3}P^\downarrow_{c,4}, \quad \mathcal{B}_c = P^\downarrow_{c,2}P^\uparrow_{c,3}P^\uparrow_{c,4}, \tag{4.13}$$

$$\mathcal{A}_d = P^\uparrow_{d,1}P^\downarrow_{d,3}P^\downarrow_{d,4}, \quad \mathcal{B}_d = P^\downarrow_{d,1}P^\uparrow_{d,3}P^\uparrow_{d,4}. \tag{4.14}$$

In these definitions, the operators $P^{\uparrow,\downarrow}_{p,i}$ are projectors onto one of the components of the spins defined on the bonds of the four neighboring plaquettes; for instance, $P^\uparrow_{a,2} = (1 + S^z_2)/2$, projects onto the $S^z_2 = +1$ component of the spin living on the second link of plaquette a, which lies underneath the reference plaquette as in Fig. 4.2. Note that the very same spin of this example is also the fourth one in the plaquette on the right side of a. The convention for enumerating the spins in a given plaquette and labeling neighboring plaquettes is shown in Fig. 4.2.

As the QLM in Eq. (4.1) can be regarded as a spin model akin to condensed matter models, in the following, we will work in the computational basis as in previous sections.

4.3.1 First-order ansatz

The first-order (perturbative) effective Hamiltonian [see Eq. (3.74)] for the problem at hand is

$$\mathcal{H}^{(1)}_{\mathrm{pert}} = i\frac{\mathcal{J}}{\lambda}\sum_\square\left(\frac{\psi_0(s_\square)}{\psi_0(s)}\mathcal{F}_\square(s)^2\int_0^t \mathrm{d}t'\mathrm{e}^{i\lambda\omega_\square(s)t'}\right), \tag{4.15}$$

where $\omega_\square(s) := \mathcal{F}_\square(s)\Omega_\square(s)$, and $\mathcal{F}_\square := U_\square U_\square^\dagger - U_\square^\dagger U_\square$, is a diagonal operator with possible matrix elements $\mathcal{F}_\square(s) = +1, -1, 0$, when the reference plaquette (indicated by the subscript $\square$) is flippable and has an anticlockwise orientation $(+1)$, a clockwise orientation (-1), or it is not flippable (0). Also, we denote spin configurations by $|s\rangle$ and use the notation $|s_\square\rangle \equiv (U_\square + U_\square^\dagger)|s\rangle$, that is, $s_\square$ differs from s by the flipping of a single plaquette. $\Omega_\square(s)$ denotes the diagonal entries of the operator introduced in Eq. (4.10).

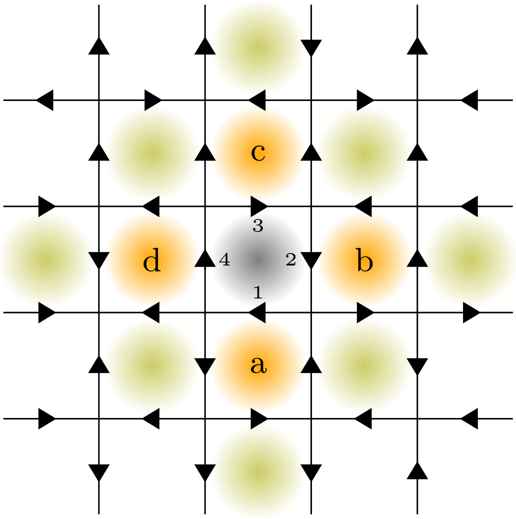

Figure 4.2: Convention for the definition of the operators in Eqs. (4.11)–(4.14). The projectors in these equations are defined on the bonds of the neighboring plaquettes (orange), except for those that are shared with the reference plaquette (gray). Labeling of plaquettes (a, b, c, d) and of spins within a plaquette $(1, 2, 3, 4)$, is done according to their relative position as shown in this figure. Plaquettes in orange are relevant for first-order cumulants, whereas second-order cumulants involve also the plaquettes in green.

Following the prescription given by Eqs. (3.76) and (3.77), we can introduce a variational parameter for each one of the nine possible values ($[-4, \dots, 4]$) that the integer-valued function $\omega_\square(s)$ can take. Thus, using the short-hand notation

$$\eta^{(1)}_{\omega_\square(s)}(t) := \sum_{\omega=-4}^{4} \delta_{\omega_\square(s),\omega}\eta^{(1)}_{\omega}(t), \tag{4.16}$$

we can write down the corresponding *variational* effective Hamiltonian as

$$\tilde{\mathcal{H}}^{(1)}_{\mathrm{QLM}} = i\frac{\mathcal{J}}{\lambda}\sum_{\square}\left(\frac{\psi_0(s_\square)}{\psi_0(s)} \times (\mathcal{F}_\square(s))^2\eta^{(1)}_{\omega_\square(s)}(t)\right), \tag{4.17}$$

which contains up to nine independent (assuming translational invariance) “first-order” variational parameters $\eta^{(1)}_{\omega}(t)$. On the other hand, the “zeroth-order” contribution reads

$$\tilde{\mathcal{H}}^{(0)}_{\mathrm{QLM}} = \ln(\psi_0(s)) - iE_s\eta^{(0)}(t), \tag{4.18}$$

with a single variational parameter $\eta^{(0)}(t)$ and E_s satisfying $H_0|s\rangle = E_s|s\rangle$ and being dimensionless. Thus, a VCN built upon the zeroth- and first-order cumulants reads

$$\mathcal{H}^{(1)}_{\mathrm{QLM}} = \tilde{\mathcal{H}}^{(0)}_{\mathrm{QLM}} + \tilde{\mathcal{H}}^{(1)}_{\mathrm{QLM}}. \tag{4.19}$$

The wave function amplitudes are thus approximated by

$$\psi\big(s;\eta(t)\big) = \exp\Big[\mathcal{H}^{(1)}_{\text{QLM}}\big(s;\eta(t)\big)\Big], \tag{4.20}$$

which are time-evolved according to the TDVP of Section 3.4.2. The first-order VCN defined above contains a maximum coupling distance (along either the i or j direction) between plaquettes equal to 2. Indeed, for a given plaquette $\Box$, the function $\omega_\Box(s)$ involves only the nearest neighboring plaquettes that are shown in Fig. 4.2. Thus, when plugged into the expression of the classical network, this gives rise to terms where the plaquettes that are separated the most are, for example, b and d in Fig. 4.2. In terms of parallel spins [for example, spins on links $(\mathbf{r},j)$ and $(\mathbf{r}+l\hat{i},j)$, with l an integer], the maximal coupling distance is equal to 3.

Finally, let us note that the ansatz (4.19) can be explicitly recast as a classical Ising-like spin model with multiple (up to 16) spin interaction terms. Indeed, this can be achieved by rewriting the constraints in Eq. (4.16) in terms of the projectors $P^{\uparrow,\downarrow}_{p,i}$. For instance, for $\omega=4$, we have

$$\delta_{\omega_\Box(s),\omega=4} = P^{\downarrow}_{\Box,1}P^{\downarrow}_{\Box,2}P^{\uparrow}_{\Box,3}P^{\uparrow}_{\Box,4}P^{\uparrow}_{a,1}P^{\uparrow}_{a,2}P^{\downarrow}_{a,4}P^{\uparrow}_{b,1}P^{\uparrow}_{b,2}P^{\downarrow}_{b,3}P^{\uparrow}_{c,2}P^{\downarrow}_{c,3}P^{\downarrow}_{c,4}P^{\uparrow}_{d,1}P^{\downarrow}_{d,3}P^{\downarrow}_{d,4}. \tag{4.21}$$

4.3.2 Second-order ansatz

For most of the numerical results we shall present next, it becomes important to make use of a second-order VCN. Thus, let us show explicitly how to construct such ansatz. The second-order correction to the cumulant expansion is proportional to [see Eqs. (3.63) and (3.65)]:

$$\exp\left[-\left(\frac{\mathcal{J}}{\lambda}\right)^2\int_0^t dt'\int_0^{t'} dt''\left(\frac{\langle s|V(t')V(t'')|\psi_0\rangle}{\langle s|\psi_0\rangle}-\frac{\langle s|V(t')|\psi_0\rangle\langle s|V(t'')|\psi_0\rangle}{\langle s|\psi_0\rangle^2}\right)\right]. \tag{4.22}$$

Let us compute the two integrands separately. Using the solutions in Eq. (4.9), we have

$$\frac{\langle s|V(t')V(t'')|\psi_0\rangle}{\langle s|\psi_0\rangle} = \sum_{\Box',\Box''}\frac{\psi_0(s_{\Box',\Box''})}{\psi_0(s)}\mathcal{F}_{\Box'}(s)^2\mathcal{F}_{\Box''}(s_{\Box'})^2\mathrm{e}^{i\lambda\omega_{\Box'}(s)t'}\mathrm{e}^{i\lambda\omega_{\Box''}(s_{\Box'})t''}, \tag{4.23}$$

$$\frac{\langle s|V(t')|\psi_0\rangle\langle s|V(t'')|\psi_0\rangle}{\langle s|\psi_0\rangle^2} = \sum_{\Box',\Box''}\frac{\psi_0(s_{\Box'})\psi_0(s_{\Box''})}{\psi_0(s)^2}\mathcal{F}_{\Box'}(s)^2\mathcal{F}_{\Box''}(s)^2\mathrm{e}^{i\lambda\omega_{\Box'}(s)t'}\mathrm{e}^{i\lambda\omega_{\Box''}(s)t''}, \tag{4.24}$$

where $|s_{\Box',\Box''}\rangle \equiv (U_{\Box'}+U^{\dagger}_{\Box'})(U_{\Box''}+U^{\dagger}_{\Box''})|s\rangle$.

Let us note at this point the following aspect concerning the locality of the second-order cumulant. Each of the two contributions, Eqs. (4.23) and (4.24), might, in principle, give rise to couplings at all distances. However, when we subtract them to form the overall second-order correction [see Eq. (4.22)], most of the resulting terms cancel out, leaving only couplings up to some (local) coupling distance. For instance, if we consider the initial state $|{\rightarrow}\rangle$ in Eq. (3.67)—an equal-weight superposition of all spin configurations—the ratios of initial amplitudes in the equations above reduce to 1. Then, one can easily verify that the only nonvanishing contributions in the sums over all plaquette pairs, $\sum_{\square',\square''}$, arise from overlapping plaquettes, that is, plaquettes sharing one common link (gray and orange plaquettes in Fig. 4.2) or from plaquettes connected by a common neighboring plaquette (gray and green plaquettes in Fig. 4.2). In effect, for plaquettes separated by more than one intermediate plaquette (that is, plaquettes outside the colored region in Fig. 4.2), we have that $\mathcal{F}_{\square''}(s_{\square'}) \equiv \mathcal{F}_{\square''}(s)$ and $\omega_{\square''}(s_{\square'}) \equiv \omega_{\square''}(s)$, and hence, Eqs. (4.23) and (4.24), become identical. In this case, the coupling distance (along either the $\hat{\imath}$- or $\hat{\jmath}$- direction) is equal to 4 for plaquettes, and equal to 5 for parallel spins. We note that this remark also holds for other initial states that can be written as a product of local terms, as long as supports of sufficiently separated local terms do not overlap with each other, as is the case for all initial states considered in throughout this chapter.

Now let us convert the second-order pCN into a second-order VCN. In the same spirit as for the first-order ansatz, the integrals involved in the second-order correction can be written as

$$\int_0^t \mathrm{d}t' \int_0^{t'} \mathrm{d}t'' \mathrm{e}^{i\lambda\omega_{\square'}(s)t'} \mathrm{e}^{i\lambda\omega_{\square''}(s_{\square'})t''} = \sum_{\omega_1,\omega_2=-4}^{4} \Bigg\{ \delta_{\omega_{\square'}(s),\omega_1} \delta_{\omega_{\square''}(s_{\square'}),\omega_2} \times \int_0^t \mathrm{d}t' \int_0^{t'} \mathrm{d}t'' \mathrm{e}^{i\lambda\omega_1 t'} \mathrm{e}^{i\lambda\omega_2 t''} \Bigg\}, \tag{4.25}$$

for Eq. (4.23), and likewise for Eq. (4.24). In this case, there are (not more than) 81 possible combinations of the tuple (ω_1, ω_2); hence, we introduce a second-order variational parameter $\eta^{(2)}_{\omega_1,\omega_2}(t)$ for each of those possible values. Thus, using the short-hand notation

$$\eta^{(2)}_{\omega_{\square'}(s),\omega_{\square''}(s_{\square'})}(t) := \sum_{\omega_1,\omega_2=-4}^{4} \delta_{\omega_{\square'}(s),\omega_1} \delta_{\omega_{\square''}(s_{\square'}),\omega_2} \eta^{(2)}_{\omega_1,\omega_2}(t), \tag{4.26}$$

and upon integrating Eq. (4.23), one can make the substitution

$$\int_0^t dt' \int_0^{t'} dt'' \frac{\langle s|V(t')V(t'')|\psi_0\rangle}{\langle s|\psi_0\rangle} \longleftarrow \sum_{\square',\square''} \frac{\psi_0(s_{\square',\square''})}{\psi_0(s)} \mathcal{F}_{\square'}(s)^2 \mathcal{F}_{\square''}(s_{\square'})^2 \eta^{(2)}_{\omega_{\square'}(s)\omega_{\square''}(s_{\square'})}(t). \tag{4.27}$$

Analogously, the corresponding substitution of Eq. (4.23), is

$$\int_0^t dt' \int_0^{t'} dt'' \frac{\langle s|V(t')|\psi_0\rangle\langle s|V(t'')|\psi_0\rangle}{\langle s|\psi_0\rangle^2} \longleftarrow \sum_{\square',\square''} \Bigg\{ \frac{\psi_0(s_{\square'})\psi_0(s_{\square''})}{\psi_0(s)^2} \mathcal{F}_{\square'}(s)^2 \times \mathcal{F}_{\square''}(s)^2 \tilde{\eta}^{(2)}_{\omega_{\square'}(s),\omega_{\square''}(s)}(t) \Bigg\}, \tag{4.28}$$

with $\tilde{\eta}^{(2)}_{\omega_{\square'}(s),\omega_{\square''}(s)}(t)$ defining a further 81 variational parameters. Combining the previous two equations, we obtain the full (variational) second-order classical Hamiltonian:

$$\begin{aligned}\tilde{\mathcal{H}}^{(2)}_{\mathrm{QLM}} = &-\frac{\mathcal{J}^2}{\lambda^2} \sum_{\square',\square''} \left(\frac{\psi_0(s_{\square',\square''})}{\psi_0(s)} \mathcal{F}_{\square'}(s)^2 \mathcal{F}_{\square''}(s_{\square'})^2 \eta^{(2)}_{\omega_{\square'}(s),\omega_{\square''}(s_{\square'})}(t) \right) \\ &+ \frac{\mathcal{J}^2}{\lambda^2} \sum_{\square',\square''} \left(\frac{\psi_0(s_{\square'})\psi_0(s_{\square''})}{\psi_0(s)^2} \mathcal{F}_{\square'}(s)^2 \mathcal{F}_{\square''}(s)^2 \tilde{\eta}^{(2)}_{\omega_{\square'}(s),\omega_{\square''}(s)}(t) \right).\end{aligned} \tag{4.29}$$

Thus, to second-order in the underlying cumulant expansion, a VCN is defined by the following effective Hamiltonian

$$\mathcal{H}^{(2)}_{\mathrm{QLM}} = \tilde{\mathcal{H}}^{(0)}_{\mathrm{QLM}} + \tilde{\mathcal{H}}^{(1)}_{\mathrm{QLM}} + \tilde{\mathcal{H}}^{(2)}_{\mathrm{QLM}}, \tag{4.30}$$

with the expressions given in Eqs. (4.18), (4.17), and (4.29). The wave function amplitudes are thus approximated by

$$\psi(s;\eta(t)) = \exp\left[\mathcal{H}^{(2)}_{\mathrm{QLM}}(s;\eta(t))\right], \tag{4.31}$$

which are time-evolved according to the TDVP of Section 3.4.2.

Let us also point out that we restrict the resulting VCNs to have the same locality as the underlying pCNs; that is, the sums over plaquette $\square''$ in (4.29) are restricted to the nearest or next-nearest neighbors of plaquette $\square'$ (see Fig. 4.2).

4.4 Quantum dynamics in the QLM

We now aim to characterize the nonequilibrium dynamics of the QLM. In particular, we are interested in studying the unitary dynamics generated by the Hamiltonian in Eq. (4.1), starting from the initial states discussed below. As anticipated, we compute the quantum dynamics with the VCNs in Eqs. (4.20) and Eq. (4.31), which are time-evolved using the TDVP of Section 3.4.2. Unless otherwise stated, in all the examples discussed in this section, the TDVP equations are solved using a 4th-order Runge-Kutta integrator with step size $\Delta t = 0.1\lambda^{-1}$. Also, periodic boundary conditions are used in all the examples shown below.

4.4.1 Initial states for unitary evolution

We consider the following initial states. First, we consider an equally weighted superposition of all spin configurations, which has been previously introduced in Eq. (3.67), but that we write here for convenience

$$|\psi_0\rangle = |{\rightarrow}\rangle = \bigotimes_i \tfrac{1}{\sqrt{2}}\Big(|{\uparrow_i}\rangle + |{\downarrow_i}\rangle\Big), \tag{4.32}$$

where $|{\uparrow_i}\rangle$ and $|{\downarrow_i}\rangle$ are the two basis states at link i. This state is distributed over all superselection sectors of the model.

The second initial condition that we shall regard is

$$|\psi_0\rangle = |{\rightarrow}\rangle_{\mathrm{FF}}, \tag{4.33}$$

which is a projection of $|{\rightarrow}\rangle$ to a single "fully-flippable" (FF) sector, defined as the zero-charge zero-flux sector. $|{\rightarrow}\rangle_{\mathrm{FF}}$ is an equal-weighted superposition of all states from the FF sector (that is, the Rokhsar-Kivelson state [44] for the FF sector).

While $|{\rightarrow}\rangle$ is a product state, $|{\rightarrow}\rangle_{\mathrm{FF}}$ is entangled. Nevertheless, $|{\rightarrow}\rangle$ can be continuously connected to a product state from the same FF sector via

$$|\psi_0(\alpha)\rangle = \bigotimes_i \Big[\sin\big(\alpha + \tfrac{\pi}{4}\big)|\mathrm{FF}_i\rangle + \cos\big(\alpha + \tfrac{\pi}{4}\big)|\overline{\mathrm{FF}}_i\rangle\Big], \tag{4.34}$$

with $\alpha \in [0, \pi/4]$. Here, $|\mathrm{FF}_i\rangle$ and $|\overline{\mathrm{FF}}_i\rangle$ denote the local spin orientations of the two states with all plaquettes flippable and therefore with checkerboard-alternating clockwise (FF_i) and anticlockwise ($\overline{\mathrm{FF}}_i$) orientations. By construction, $|\psi(\alpha = 0)\rangle = |{\rightarrow}\rangle$ and $|\psi(\alpha = \pi/4)\rangle = |\mathrm{FF}\rangle \equiv \bigotimes_i |\mathrm{FF}_i\rangle$. Importantly, the states $|\psi(\alpha)\rangle$ are spatially uniform. The resulting dynamics for $\alpha = 0$ is displayed in Fig. 4.1(b), where we monitor the spatiotemporal buildup of quantum correlations. We will identify the limited spatial propagation with nonergodic behavior below.

It will be also of interest to look at the unitary dynamics starting from nonuniform initial states. In particular, we shall consider nonuniform initial states created by adding a line defect with subextensive energy contribution to the states in Eqs. (4.32) and (4.33). This is achieved by applying the operator

$$\mathcal{P} = \prod_{\square\in\mathscr{C}_0} 1 + (U_\square + U_\square^\dagger)^2, \tag{4.35}$$

where $\mathscr{C}_d$ denotes the set of plaquettes in the dth column. Thus, $\mathcal{P}|\psi_0\rangle$ represents one of the states in Eqs. (4.32) and (4.33) with a line energy defect along the zeroth column.

Before analyzing in detail the quantum dynamics in truly 2D geometries, we benchmark the VCN method for the QLM in quasi-1D structures.

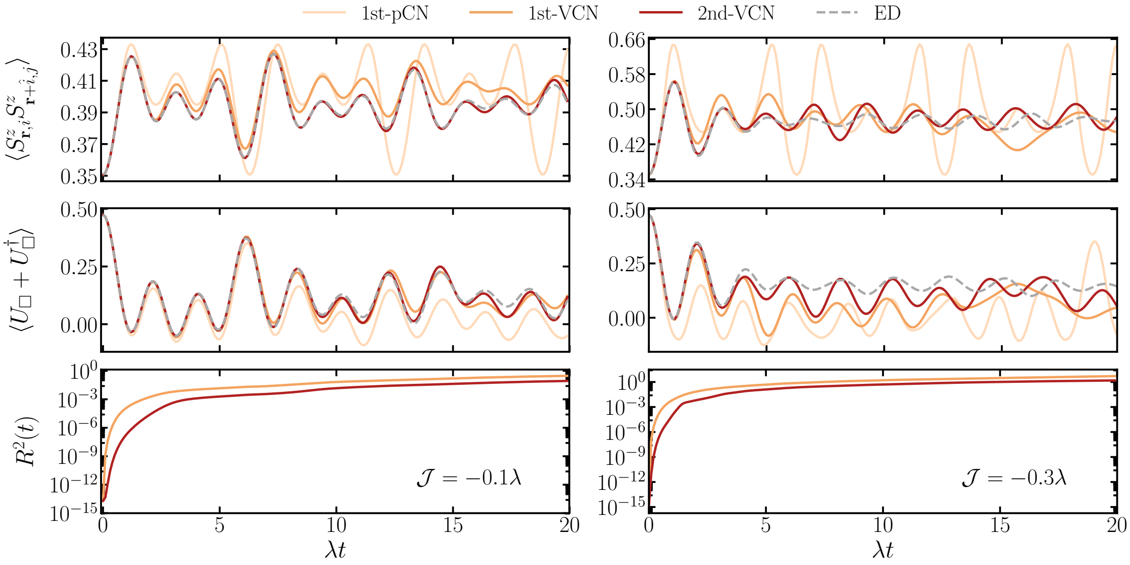

Figure 4.3: Comparison of perturbative, variational, and exact dynamics in a quasi-1D ladder of 10×2 plaquettes (40 spins): Left and right columns show the unitary dynamics generated by the Hamiltonian in Eq. (4.1) with $\mathcal{J}/\lambda = -0.1$ and $\mathcal{J}/\lambda = -0.3$, respectively, starting from $|{\rightarrow}\rangle_{\text{FF}}$. Upper row: Dynamics of the nearest-neighbor spin-spin correlator $\langle S^z_{\mathbf{r},i} S^z_{\mathbf{r}+\hat{i},j} \rangle$. Middle row: Dynamics of the (dimensionless) mean kinetic energy per plaquette $\langle U_\square + U^\dagger_\square \rangle$. Lower row: Integrated residuals $R^2(t)$, of the first- and second-order VCNs.

4.4.2 Benchmarks in quasi-1D ladders

In this section we provide benchmarks for the VCN method for the problem at hand. To this end we consider dynamics computed via the VCNs in Eqs. (4.20) and Eq. (4.31), and the initial states in Eqs. (4.32) and (4.33) and nonuniform initial states of the type $\mathcal{P}|\psi_0\rangle$. This is done in stripe-like geometries of size $L_x \times L_y$ plaquettes, with $L_x = 10, 12$ and $L_y = 2$. Beyond first- and second-order ansätze, we use the partial third-order ansatz, where we take into account a subset of all third-order terms (it is computationally hard to deal with all of them). During the evolution we sample various observables using the Monte Carlo method, as explained in Section 3.4.

We compare the VCN results with the results of exact diagonalization (see Section 3.2). When we consider the FF sector, that is, the initial states $|{\rightarrow}\rangle_{\text{FF}}$ or $\mathcal{P}|{\rightarrow}\rangle_{\text{FF}}$, it is possible to do conventional ED, since the dimension of the FF sector is $\dim(\mathscr{H}_{\text{FF}}) = 17906, 147578$ for system sizes 10×2 and 12×2, respectively. Since in this case the number of states for the 10×2 system is relatively small, in the TDVP calculations, we can also carry out an exact enumeration of states; that is, we can explicitly sum over all relevant spin configurations in expressions such as the expectation value of observables [see for example Eq. (3.39)], rather than performing a Monte Carlo sampling. Let us recall that we can restrict ourselves to the FF sector as different superselection sectors are not mixed during unitary dynamics. On the other hand, when we consider the initial states $|{\rightarrow}\rangle$ or $\mathcal{P}|{\rightarrow}\rangle$,

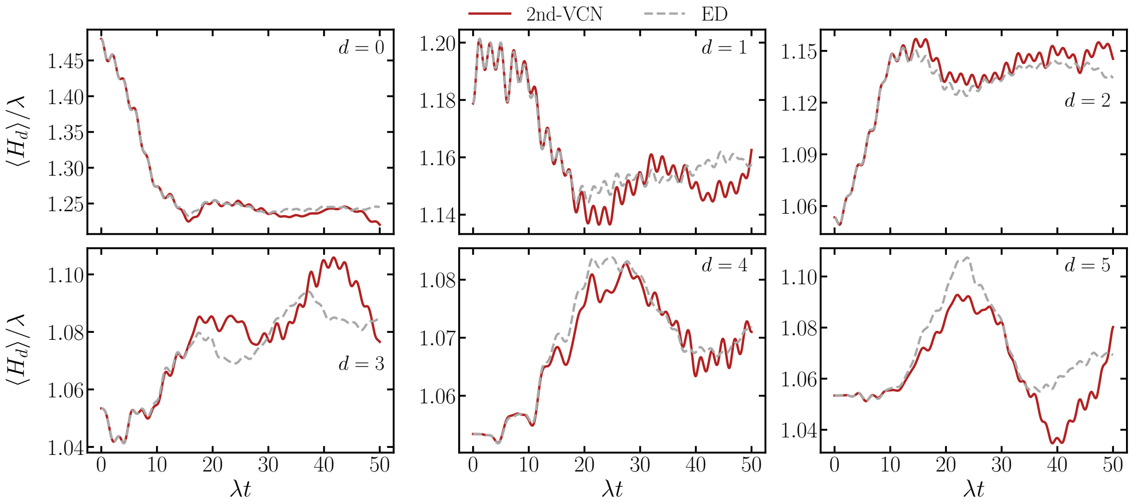

Figure 4.4: Energy of the dth column with $d = 0, \ldots, 5$, in the time evolution from the nonuniform initial state $\mathcal{P}|{\rightarrow}\rangle_{\mathrm{FF}}$, containing an excess of energy around $d = 0$ (see main text), in a quasi-1D ladder of 10×2 plaquettes (40 spins) with $\mathcal{J}/\lambda = -0.1$. We compare the TDVP solution using a second-order VCN [Eq. (4.31)] with ED results.

which involve all superselection sectors, and therefore, the whole Hilbert space whose dimension is $\dim(\mathscr{H}) = 2^{40}, 2^{48}$ for the considered system sizes, we are forced to use a different approach. Namely, we sample a random sector, perform the ED-evolution within the sector and then average over 10^6 sectors (effective "disorder realizations").

We present results for correlation functions and single-plaquette observables. Further, we analyze the error by computing either the integrated residual error [see Eq. (3.54)] or the error production rate [see Eq. (3.55)].

First, in Figs. 4.3 and 4.4, we present the results for a quasi-1D ladder of 10×2 plaquettes, for the initial states $|{\rightarrow}\rangle_{\mathrm{FF}}$ or $\mathcal{P}|{\rightarrow}\rangle_{\mathrm{FF}}$. More specifically, in Fig. 4.3, we

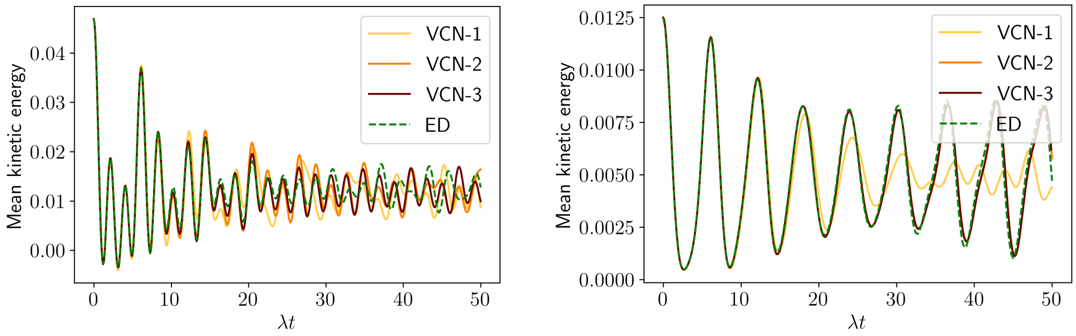

Figure 4.5: Dimensionless mean kinetic energy per plaquette $-\frac{\mathcal{J}}{\lambda}\langle U_\square + U_\square^\dagger\rangle$ for the uniform initial states $|{\rightarrow}\rangle_{\mathrm{FF}}$ (left) and $|{\rightarrow}\rangle$ (right) in a quasi-1D ladder of 12×2 plaquettes (48 spins). Comparison of ED (dashed green line) versus first-, second- and partial third-order VCN (solid lines).

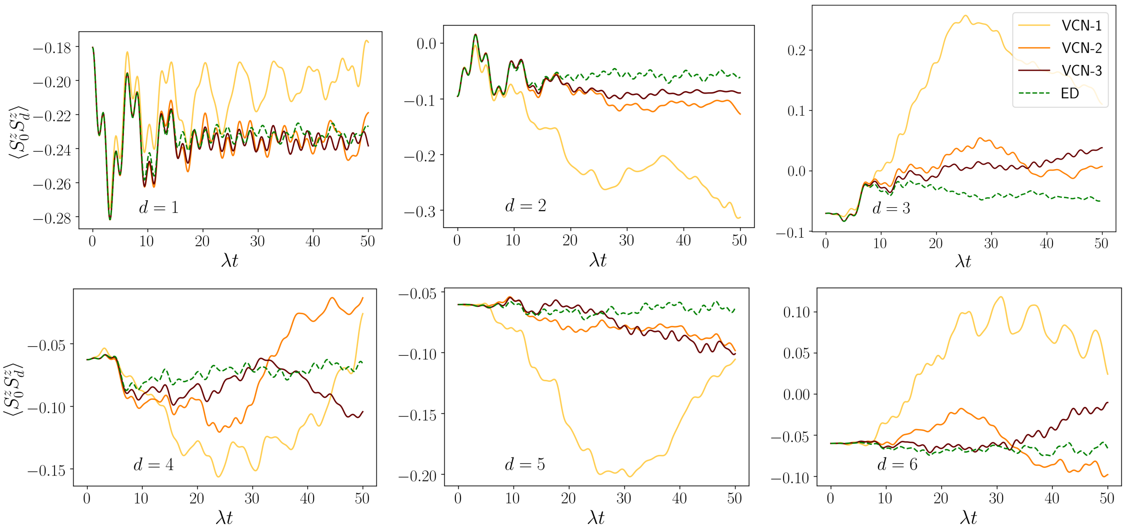

Figure 4.6: Correlation function $\langle S_0^z(t) S_d^z(t) \rangle$ for $d = 1, ..., 6$ for the uniform initial state $|{\rightarrow}\rangle_{\mathrm{FF}}$ in a quasi-1D ladder of 12×2 plaquettes (48 spins). Comparison of ED (dashed green line) and VCN (solid lines).

compare the dynamics computed with ED, a first-order pCN, a first-order VCN [Eq. (4.20)], and a second-order VCN [Eq. (4.31)], for the initial state $|{\rightarrow}\rangle_{\mathrm{FF}}$. The observables analyzed here are the nearest-neighbor spin-spin correlation function $\langle S^z_{\mathbf{r},i} S^z_{\mathbf{r}+\hat{\imath},j} \rangle$ (or, $\langle S_1^z S_2^z \rangle$, with the convention in Fig. 4.2), and the mean kinetic energy (up to a factor of $-\mathcal{J}$) per plaquette $\langle U_\square + U_\square^\dagger \rangle$. Besides, we also show the integrated relative residuals $R^2(t)$ of the first- and second-order VCNs as a measure of their accuracy. We show results with $\mathcal{J}/\lambda = -0.1$ (left column) and $\mathcal{J}/\lambda = -0.3$ (right column). As expected, it is the second-order VCN that provides the most accurate results. This can be seen from both the evolution of the observables and the growth of the residuals. In particular, for $\mathcal{J}/\lambda = -0.1$, the second-order VCN captures remarkably well correlations at short distances (left column, upper row), as well as the oscillatory behavior of off-diagonal observables (left column, middle row), in the entire range of accessed timescales $\lambda t = 20$. As discussed in Section 3.5, for a bigger strength of the perturbation $\mathcal{J}/\lambda = -0.3$, the description in terms of all of the considered wave functions, breaks down at earlier times. Yet, the second-order VCN still yields a rather excellent agreement with ED up to significant timescales $\lambda t \sim 7$. In all cases, the VCNs outperform the first-order pCN regarded here.

As we will argue below the dynamics in the FF sector is presumably ergodic. This is illustrated here in that the oscillations of both $\langle S^z_{\mathbf{r},i} S^z_{\mathbf{r}+\hat{\imath},j} \rangle$ and $\langle U_\square + U_\square^\dagger \rangle$ decay towards some steady-state value. Importantly, such decay of the oscillations is captured by the TDVP solutions. On the contrary, the pCN fails to capture this crucial feature, although it gets right the frequency of the oscillations up to considerable timescales.

In Fig. 4.4, we compare the dynamics computed with ED and a second-order VCN, for the initial state $\mathcal{P}|{\rightarrow}\rangle_{\mathrm{FF}}$. Here we look at the time evolution of the total energy of the dth

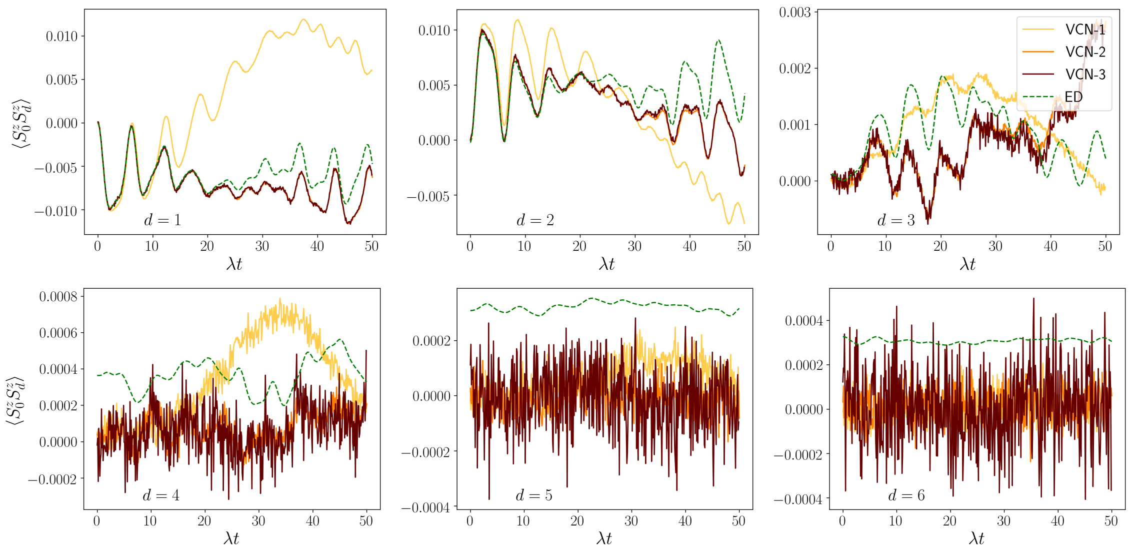

Figure 4.7: Correlation function $\langle S_0^z(t) S_d^z(t) \rangle$ for $d = 1, ..., 6$ for the uniform initial state $|{\rightarrow}\rangle$ in a quasi-1D ladder of 12 × 2 plaquettes (48 spins). Comparison of sector-sampled ED (dashed green line) and VCN (solid lines). In the initial state $|{\rightarrow}\rangle$ spins are non-correlated, that is, $\langle S_0^z(0) S_d^z(0) \rangle = 0$ so for $d = 4 - 6$ (lower panel) we see mostly only random noise in both ED and MC samplings.

column, which is given by

$$H_d = \sum_{\square \in \mathscr{C}_d} -\mathcal{J}(U_\square + U_\square^\dagger) + \lambda (U_\square + U_\square^\dagger)^2. \tag{4.36}$$

We observe that the second-order VCN captures quite well, in a quantitative way, the propagation of the line defect at all distances up to a time $\lambda t \approx 20$. After this point, the TDVP solution is not exact anymore, but it still follows qualitatively the exact dynamics to the largest accessed time, $\lambda t = 50$.

The results for the 12×2 system are displayed in Figs. 4.5–4.9. These results show that up to a timescale $\lambda t \simeq |\lambda / \mathcal{J}| \approx 10$, the VCN method works very well for both the single-plaquette observables (Fig. 4.5 and 4.8) and the long-distance correlators (Figs. 4.6 and 4.7), which is also manifested in the fact that the error production rate remains small till $\lambda t \approx 10$ and starts to grow significantly after that (Fig. 4.9). This means that up to these times the VCN wave functions capture the quantum states almost entirely. Nevertheless we see that VCNs can capture the single-plaquette observables up to much longer times, especially the average behavior with smoothed out high-frequency oscillations (Fig. 4.5). It is important to underline that VCNs can capture quantitatively the activation dynamics, while the dynamics after the activation is captured qualitatively as shown in Fig. 4.8, where we look at the spreading of the (normalized) column energy

$$\varepsilon_d(t) = \frac{\langle H_d(t) \rangle - H_{\text{av}}}{H_{\text{av}}}, \tag{4.37}$$

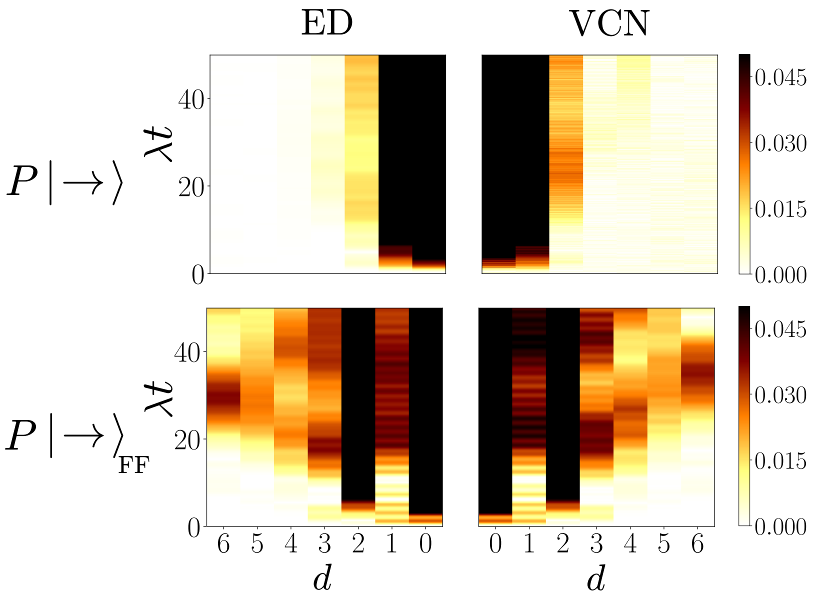

Figure 4.8: Normalized deviation of energy of dth column from its initial value $|\varepsilon_d(t) - \varepsilon_d(0)| = (\langle H_d(t)\rangle - H_d(0))/H_{\mathrm{av}}$, for the non-uniform initial states $\mathcal{P}|\!\rightarrow\rangle$ (upper panel) and $\mathcal{P}|\!\rightarrow\rangle_{\mathrm{FF}}$ (lower panel), in a quasi-1D ladder of 12 × 2 plaquettes (48 spins). Comparison of ED (left panel) and second-order VCN (right panel).

where $H_{\mathrm{av}} = \langle H\rangle/L$ denotes the expected value of $\langle H_d(t)\rangle$ in the long-time limit when the system thermalizes (L is the number of columns). Importantly, Fig. 4.8 already shows us that the system features two very different dynamical phases, which we will discuss in detail in the following section.

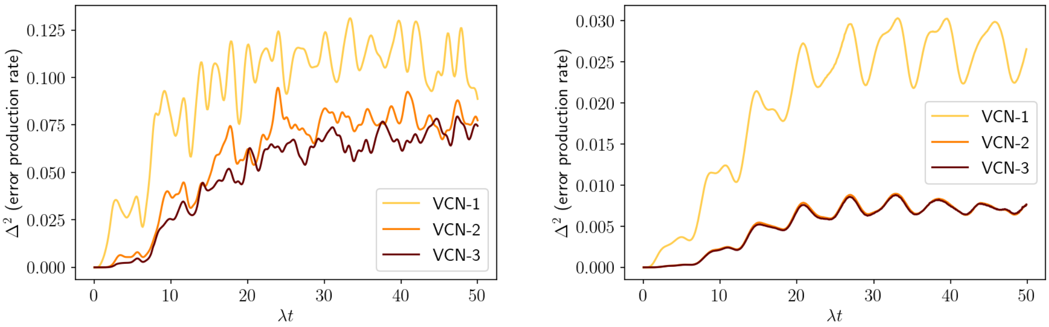

Figure 4.9: Error production rate for uniform states $|\!\rightarrow\rangle_{\mathrm{FF}}$ (left) and $|\!\rightarrow\rangle$ (right) for the first-, second- and third-order VCN wave functions.

4.4.3 Localized and ergodic dynamics in 2D

Using the VCNs introduced above, we now compute the nonequilibrium dynamics in the QLM, in truly 2D setups. We start by studying the spatiotemporal buildup of quantum correlations, measured via $\langle S_0^z(t) S_d^z(t)\rangle$, upon initializing the system in the state $|\!\rightarrow\rangle$ in Eq. (4.32). The result is shown in Fig. 4.1(b) for a system with 80 × 80 plaquettes (12800

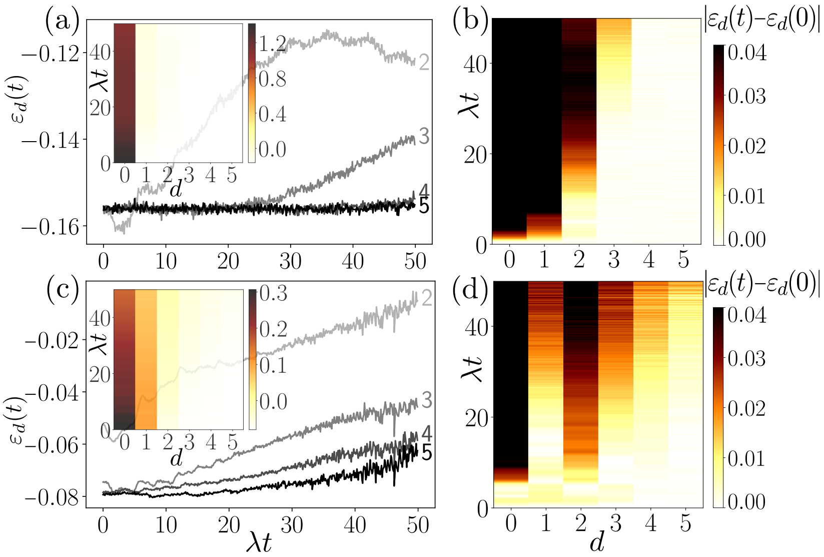

Figure 4.10: Quantum energy dynamics for line defects created in the $|{\rightarrow}\rangle$ (upper panel) and $|{\rightarrow}\rangle_{\mathrm{FF}}$ (lower panel) initial states, displaying the normalized plaquette energy of dth column $\varepsilon_d(t)$ [Eq. (4.37)]. (a), (c) $\varepsilon_d(t)$ for different columns $d = 2-5$ where darker colors refer to larger distances from the initial defect. Insets show the same data including $d = 0,1$ in a color plot. (b), (d) Absolute deviation of $\varepsilon_d(t)$ from the initial value $\varepsilon_d(0)$. (b) Signal propagation for $|{\rightarrow}\rangle$ showing a strong bending of the light cone indicating localized behavior and (d) for $|{\rightarrow}\rangle_{\mathrm{FF}}$ consistent with linear propagation indicative of ergodic behavior. For all the plots $J/\lambda = -0.1$ and system size 10×10.

spins), where one can see that correlations emerge only over a limited spatial distance suggesting nonergodic behavior. We proceed by further corroborating this observation by other measures. Namely, we study energy transport in the QLM by creating initial conditions with a spatial energy inhomogeneity in the form of a line defect with subextensive energy contribution and use the character of energy propagation to distinguish between ergodic and localized dynamics. As already mentioned in the previous section, we can create such states by applying the operator $\mathcal{P}$ in Eq. (4.35) to the initial states in Eqs. (4.32) and (4.33). Concretely, in Fig. 4.10, we plot the (normalized) column energy $\varepsilon_d(t)$ in Eq. (4.37). We checked that other choices of the excitation operator $\mathcal{P}$ (diagonal or nondiagonal) increasing the amplitudes of configurations with flippable plaquettes at $d = 0$ do not qualitatively affect the results we present next.

Comparing Figs. 4.10(a) and 4.10(c), we observe that the dynamics differs qualitatively for the two initial conditions, as already anticipated in Fig. 4.8. Let us stress that the Hamiltonian parameters are identical for the situations displayed in Figs. 4.10(a) and 4.10(c). While for $|\psi_0\rangle = |{\rightarrow}\rangle$ energy transport is highly suppressed and only visible on short distances [Fig. 4.10(a)], the opposite happens for $|\psi_0\rangle = |{\rightarrow}\rangle_{\mathrm{FF}}$. This becomes even more apparent in Figs 4.10(b) and 4.10(d), where $\varepsilon_d(t)$ relative to the initial value $\varepsilon_d(0)$ is shown, therefore more directly highlighting energy propagation. While for $|{\rightarrow}\rangle_{\mathrm{FF}}$ we identify a linearly propagating front, for $|{\rightarrow}\rangle$ we observe a strong bending. We argue below that this front for $|{\rightarrow}\rangle$ can extend only to a finite region as a consequence of disorder-free localization.

4.5 Bound on quantum dynamics by a correlated percolation problem

The qualitative difference in the quantum dynamics for the initial states $|{\rightarrow}\rangle$ and $|{\rightarrow}\rangle_{\mathrm{FF}}$ originates from a dynamical transition, which one can study systematically upon tuning the parameter α for the initial state (4.34). For this purpose, we employ an unconventional correlated classical percolation problem and establish a bound on the quantum localized-ergodic transition in the QLM providing a strong numerical evidence for an extended nonergodic phase as a consequence of disorder-free localization.

We illustrate the idea for the initial state $|{\rightarrow}\rangle$, distributed over all superselection sectors. Consider a typical (random) sector from this distribution (Fig. 4.11(a)). Such sector exhibits many background charges $q_{\mathbf{r}}$ whenever the “two-in two-out” rule at vertex $\mathbf{r}$ is violated. Importantly, these background charges (constants of motion by gauge invariance) impose strong kinetic constraints. For instance, $q_{\mathbf{r}} = \pm 2$ implies that neighboring spins either all point inward or outward, hence the adjacent plaquettes remain unflippable forever. The influence of $q_{\mathbf{r}} = \pm 1$ charges is more subtle. They make at least two adjacent plaquettes unflippable, while their positions might change over time.

The question we address now is whether these constraints are so strong to fragment the square lattice into sets of kinetically disconnected islands or whether one can contain an extensive (percolating) connected cluster. For that purpose we study an unconventional percolation problem using an infinite-temperature classical MC simulation. We start from the initial condition (4.34), sampling a random basis state (and thus a sector) with a distribution set by the amplitudes in $|\psi(\alpha)\rangle$. Then we determine which parts of the systems are kinetically connected, using MC search with random plaquette flips. The simulation is stopped when every plaquette is flipped either 0 or more than some fixed threshold ($= 100$) number of times (or after 10^{11} MC steps if this condition is still not satisfied). As a result we find the number of performed flips for each plaquette [Fig. 4.11(b)]. Repeating this procedure for different initial configurations at a given α and scanning α, we finally obtain the percolation probability [Fig. 4.11(c)]. Most importantly, one can observe a clear evidence for a percolation threshold $\alpha_c \approx 0.25$. Although the simulation termination condition is chosen such as to minimize the number of potentially missed “weak connections” between flippable clusters, we cannot exclude the possibility of such misses. While we do not expect a significant impact deep in the respective phases, this caveat might become important in the vicinity of α_c, thus we restrain ourselves from studying the critical behavior.

Since $\alpha_c > 0$, the initial state $|\psi(\alpha = 0)\rangle = |{\rightarrow}\rangle$ corresponds to the classically non-percolating side of the transition, while from $\alpha_c < \pi/4$ it follows that state $|\psi(\alpha = \pi/4)\rangle =$

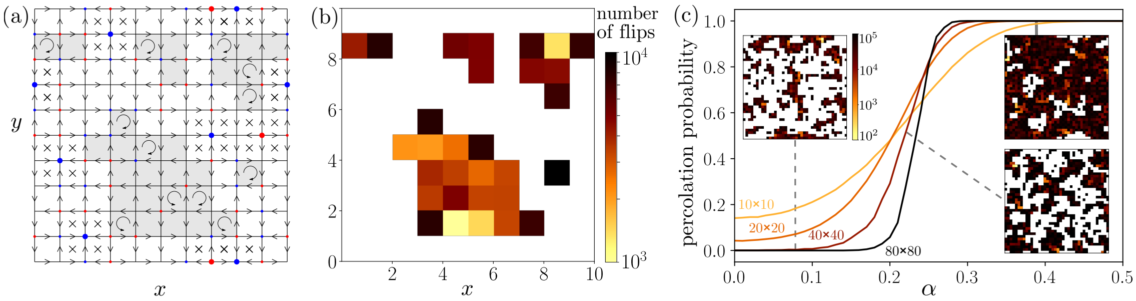

Figure 4.11: Classical correlated percolation problem implying a quantum nonergodic phase in the QLM. (a) Typical spin configuration sampled from $|\rightarrow\rangle$ with arrows showing the local spin orientation and circular arrows flippable plaquettes. Red and blue disks denote positive and negative background charges, respectively. Crosses indicate plaquettes blocked by charges $q = \pm 2$. Grey color indicates plaquettes that can become flippable in the course of the evolution. (b) Result of the Monte Carlo simulation starting from the state (a). The colormap shows the number of times that the individual plaquettes were flipped in the course of the simulation; white color stands only for plaquettes, that have never been flipped. c) Percolation probability vs α. The insets show typical configurations below, at, and above the percolation threshold $\alpha_c \approx 0.25$ for a 40×40 system.

$|\mathrm{FF}\rangle$ and all other states from the FF-sector (including $|{\rightarrow}\rangle_{\mathrm{FF}}$) lie on the percolating side. This classical threshold is imprinted in the quantum dynamics and ultimately leads to the strong localization observed in propagation of correlations [Fig. 4.1(b)] and of the energy [Fig. 4.10(a) and 4.10(b)] for $|{\rightarrow}\rangle$. For the FF-sector state $|{\rightarrow}\rangle_{\mathrm{FF}}$ there is no percolation constraint, which allows propagation of the signal to long distances [Fig. 4.10(c) and 4.10(d)]. We emphasize that this analysis sets only a lower bound onto the true quantum transition localization-delocalization threshold $\alpha_c^{(q)}$, since the quantum system might be still localized due to interference case by the kinetic $\mathcal{J}$-term even on the classically percolating side.

4.6 Summary and outlook

In this chapter, we have shown that genuinely interacting 2D homogeneous LGTs can become nonergodic as a consequence of disorder-free localization. This is especially surprising since the conventional many-body localization is theoretically conjectured to be unstable in 2D at elevated energy densities [184, 185], implying that gauge invariance/constraints represent a different and probably more robust mechanism of ergodicity breaking as compared to disorder. The key element of our analysis is a bound on the localization-delocalization transition based on a classical correlated percolation problem implying a strong fragmentation of Hilbert space into kinetically disconnected regions. This observation is supported by studying the quantum dynamics of the model, where we find that the propagation of line defects gives rise to very distinctive light cone structures in the respective localized and ergodic phases.

Regarding the quantum dynamics simulations, we used the method of variational classical networks introduced in the previous chapter. In this regard, we found that the resulting VCNs for the QLM are highly nonconventional spin models; see, for example, Eq. (4.21). Yet, the same general ideas to build VCNs (see Section 3.5) apply in their construction. We illustrated this by explicitly building the first- and second-order VCNs, which were then used for computing the dynamics of the QLM. In particular, we made sure to benchmark our method in different scenarios for the problem at hand, for example by comparing against ED results in quasi-1D geometries. We found that even in the FF sector, which constitutes one of the most challenging scenarios for our method, as it embodies considerable quantum correlations that propagate throughout the entire system, the VCN method performs remarkably well starting from both uniform and nonuniform initial states. In particular, we found that second-order VCNs yield very accurate results for short-range correlations and local off-diagonal observables, and that they were able to account for the propagation features of line defects in the nonuniform initial states, which as we have mentioned is crucial for distinguishing localized and ergodic behavior. Overall, this problem allowed us to verify the main features and accuracy of the VCN method in a more challenging model than the 1D TFIM studied in Section 3.5.4.

Both the percolation analysis as well as the VCN method can be directly applied to other quantum many-body systems with finite-dimensional local Hilbert spaces independent of dimensionality, such as 3D quantum spin ice systems, which might be an interesting scope of the developed techniques in the future. Further, it might be interesting to explore how the classical and quantum transition thresholds are related to each other as well as to determine their respective critical behaviors, and whether the disorder-free localization scenario holds also in the presence of matter degrees of freedom. Finally, our theoretical analysis appears within reach of future experiments: significant efforts in the last years have explored routes to realize the QLM model experimentally in systems of Rydberg atoms [190, 191] as a next step after the recent experimental advances on 1D LGTs [33, 37–41] (see also Section 2.5).

Chapter 5

Real-time dynamics of string breaking in quantum spin chains

The content of this chapter is mainly based on Ref. [1].

We now turn our attention to another important nonequilibrium process in gauge theories, namely, *string breaking dynamics.* As mentioned in the introduction, string breaking is a key dynamical process in theories featuring confinement, such as quantum chromodynamics [4–6], where two static charges, for instance a heavy quark-antiquark pair, are connected by a flux tube or *string.* The picture was historically developed in analogy with ordinary superconductivity and the so-called Meissner effect, where the magnetic field is squeezed into magnetic fluxes due to Cooper-pair condensation [4, 5, 281]. In the confining phase of the gauge theory, which occurs naturally in the strong-coupling regime, the gauge field exhibits large spatial fluctuations such as monopoles that also condense [53], giving rise to a squeezed one-dimensional electric flux line or string. The string can, however, break beyond a critical distance, as the creation of new, light particle-antiparticle pairs becomes more favourable [82, 84, 93, 282, 283]. This mechanism is precisely referred to as string breaking. Its static properties have been investigated extensively [82–89] while recently also its dynamics has attracted increased attention [21, 31, 90–102]. Importantly, many aspects of confinement cannot only be realized in gauge theories, but also in conventional quantum spin chains [54–75, 77], as pointed out in Chapter 1. Yet, it has remained an open question whether quantum spin models can also inherit the fundamental dynamical process of string breaking.

In this chapter we address this question and show that string breaking can indeed occur in paradigmatic quantum Ising chains. Here, the elementary excitations are domain walls which can exhibit confining potentials induced either by symmetry-breaking fields [55, 57, 68] or long-range interactions [70]. As a particular consequence, the phenomenology

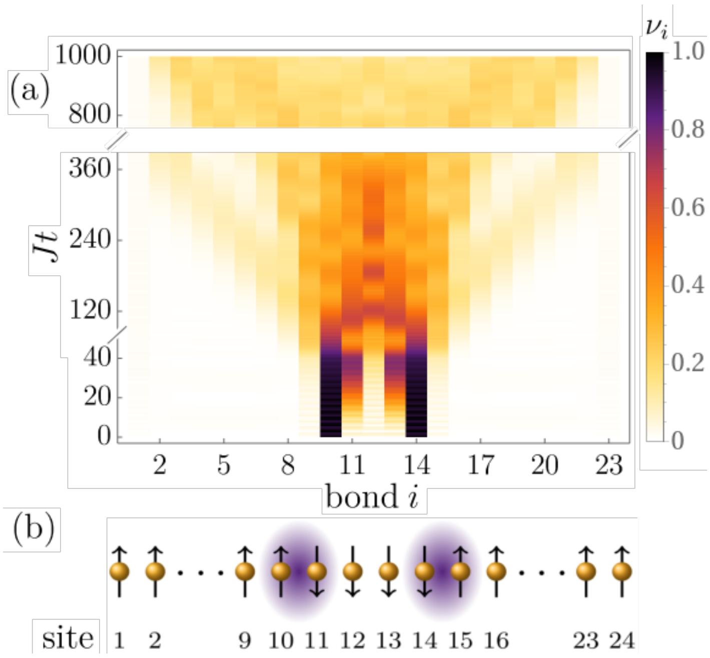

Figure 5.1: Real-time dynamics of string breaking in the short-range Ising chain with $L = 24, h_x/J = 0.2, h_z/J = 1$ and an initial distance $\ell = 4$ between two domain walls. (a) Dynamics of the domain wall density $\nu_i(t)$ displaying two stages of string breaking. First, the initial domain walls remain static for a long time with dynamics occurring in the connecting string. Second, the string breaks on longer time scales by forming bound pairs of domain walls. The initial string state is schematically depicted in (b).

of string breaking not only obtains a significantly broadened scope towards the realm of quantum many-body theory but also brings it within reach of experiments in quantum simulators such as systems of Rydberg atoms or trapped ions. As our main observation, we find that string breaking takes place as a two-stage process (see Fig. 5.1): In the first stage the two initial charges remain essentially static and stable on a time scale which can depend crucially on the initial domain wall separation. In this regime, we observe, however, that the connecting string can become a dynamical object. We develop an effective description for this string motion, which turns out to exhibit strong kinetic constraints. The resulting reduced models allow us to obtain analytical access for instance on time scales of string breaking or on bounding the maximum number of particle-antiparticle pairs created during string motion. We further observe that the string motion also leads to a heterogeneous spatiotemporal profile of quantum correlations. While the regions outside of the string essentially remain uncorrelated, the string itself can develop strong quantum correlations. In the second stage, the string eventually breaks at a time scale, which can grow by orders of magnitude upon increasing the separation of the initial domain walls. While we present our findings for two particular quantum Ising chains, we argue that our observations also generalize to other systems such as one-dimensional confining gauge theories. We further discuss how our results on string breaking can be realized in systems of Rydberg atoms and trapped ions.

The chapter is organized as follows. In Section 5.1, we start by introducing the model Hamiltonians that are considered in this chapter, and by defining the quench protocols and measured observables. We present a summary of our main results in Section 5.2. We then further elaborate on these results in Sections 5.3 and 5.4. In particular, in Section 5.3, we analyze the first stage of string breaking. In this part, we develop some effective descriptions for the string motion during this stage (Sections 5.3.1 and 5.3.3), which give us access to analytical predictions such as a bound on the maximum charge density that can be created (Section 5.3.2) and the typical timescales of string breaking (Section 5.3.4). We also provide a field-theoretical description, which is needed when considering the continuum limit, in Section 5.3.5. The second stage is discussed in Section 5.4. Some concluding remarks, including possible experimental implementations of the phenomenology studied in this chapter, are given in the last section.

5.1 Models and quench dynamics

In this section, we introduce the models, quench protocol, and measured observables considered for this part of this thesis.

5.1.1 Quantum Ising chains

We study the real-time dynamics of string breaking in two quantum spin models with distinct features. In the first place, we consider a quantum Ising chain with nearest-neighbor interactions in both transverse and longitudinal magnetic fields, with strength h_x and h_z, respectively,

$$H_{\text{short}} = -J\sum_{i=1}^{L-1}\sigma_i^z\sigma_{i+1}^z - h_x\sum_{i=1}^{L}\sigma_i^x - h_z\sum_{i=1}^{L}\sigma_i^z. \tag{5.1}$$

The second model is a quantum spin chain with long-range interactions,

$$H_{\text{long}} = -J\sum_{i<j}^{L}\frac{1}{r_{ij}^{\alpha}}\sigma_i^z\sigma_j^z - h_x\sum_{i=1}^{L}\sigma_i^x, \tag{5.2}$$

where σ_i^{μ} ($\mu = x, y, z$) denotes, as in previous chapters, the Pauli matrices acting on site i, r_{ij} is the distance between sites i and j, $\alpha > 1$ determines the power-law decay of the long-range interactions (the case $\alpha \in [0, 1]$ is avoided so as to ensure a well-defined thermodynamic limit [70, 284]), L is the size of the system, and the ferromagnetic coupling $J > 0$ sets the overall energy scale. For the short-range model in Eq. (5.1), we use open boundary conditions, since this choice resembles the conditions in relevant experimental platforms, which are discussed subsequently. We have, however, checked that our results do not rely on this particular choice. On the other hand, we consider periodic boundary conditions for the long-range model in Eq. (5.2), where $r_{ij} = \min(|i-j|, L-|i-j|)$, as this model is more sensitive to finite-size effects. As in the previous chapters of this thesis, we use units such that the reduced Planck's constant $\hbar$ and the lattice spacing a are both set to 1.

In their respective ground states, both models feature a ferromagnetic phase for sufficiently weak transverse fields h_x, with domain walls as the elementary excitations. In the short-range model, this is the case in the limit of vanishing longitudinal field h_z, whereas for the system in Eq. (5.2) when the power-law decay $\alpha > 2$ of the interactions is sufficiently rapid. Upon adding h_z [55, 57, 68] or upon decreasing α into the range $\alpha < 2$ [70], the domain walls develop a confining potential with the interaction energy between two domain walls increasing as a function of their distance similar in phenomenology to confinement in gauge theories.

In spite of their similarities, we also note important conceptual differences between the two models. The short-range model has a two-fold degenerate ground state at $h_z = 0$, which is split by the addition of the longitudinal field. Then, the domain wall excitations are points along the chain where the spin tunnels between the two ground states. Since one of the ground states is now higher in energy, two domain walls separated by a string of length $\ell \gg 1$ have an energy cost E proportional to ℓ. In contrast, the ground state of H_{long} is always exactly two-fold degenerate in its ferromagnetic phase, but confinement between domain walls is driven by *frustration* between segments of the chain with opposite magnetization and long-range ferromagnetic couplings. For the Hamiltonian in Eq. (5.2), the energy cost of separating two domain walls a distance $\ell \gg 1$ scales as $E \propto \ell^{2-\alpha}$ ($\log \ell$ for $\alpha = 2$) [70]. Therefore, the long-range model can interpolate between logarithmic and linear confinement, which are both realized in lattice gauge theories [13]; yet we will see that string breaking proceeds in most of the aspects similarly in both models, suggesting that the developed picture is general for theories featuring confinement.

Finally, let us also notice that previous works have explored connections between Ising models and confining field theories. In particular, duality transformations have been established [13, 194, 199, 200] between short-range Ising models and some lattice gauge theories (see also Section 2.3). Similar dualities are expected to hold for the long-range case. Moreover, in Ref. [285] it is discussed how the short-range model in Eq. (5.1), could be mapped into a gauge theory and be used to describe the low-energy physics of the one-dimensional massive Schwinger model. Additionally, there is a recent concrete theoretical proposal [286] to realize certain lattice gauge theories using the system (5.1), in the context of quantum simulators. Thereupon, quantum Ising chains do constitute reasonable lattice theories to study the dynamics of confinement and string breaking.

5.1.2 Quench protocol and measured observables

We study the dynamics of string breaking by initializing the spin chains in a product state with a specific magnetization profile, as shown in Fig. 5.1(b). All spins are pointing ↑ except within a central region of variable length ℓ where the spins are taken to be ↓. This generates a state with exactly two domain walls connected by a string. This setup not only represents a direct realization of the desired particle-antiparticle pair but is also motivated by the classes of initial conditions that can be prepared experimentally in quantum simulators such as Rydberg atoms or trapped ions; see, for instance [170–172]. Let us note that this type of string-like states, as well as excitations with a larger number of strings, have been found to also play an important role in quantum spin dynamics beyond confinement, in other models of quantum magnetism such as the one-dimensional spin-1/2 Heisenberg model [287, 288].

Next, the system is evolved with one of the Hamiltonians in Eqs. (5.1) or (5.2). In either case, the transverse field is chosen sufficiently weak so that the elementary domain wall excitations are still almost point-like particles. This setup represents a quantum quench from an excited eigenstate beyond the ground state manifold in the limit of $h_x = 0$ to the respective quantum Ising models. In general, we solve this dynamical problem by means of exact diagonalization techniques (see Section 3.2 in Chapter 3) supported by effective analytical descriptions that will be presented in more detail below. Note that, in the regime of stronger transverse fields, domain walls cannot simply be treated as point-like particles; instead, they become extended objects. We will provide a brief discussion on the dynamics of kinks with a finite width in Section 5.3.5.

We characterize the resulting dynamics through different observables. On the one hand, we study the dynamics and creation of the elementary excitations by computing the local density of kinks

$$\nu_i(t) = \frac{1}{2}\langle 1 - \sigma_i^z(t)\sigma_{i+1}^z(t)\rangle, \tag{5.3}$$

measuring the presence or absence of a domain wall at the given bond $(i, i+1)$.

Further, we aim to explore the spatiotemporal structure of quantum correlations during string breaking dynamics. For that purpose we study the nearest-neighbor connected correlation function:

$$\mathcal{C}_i(t) = \langle \sigma_i^z(t)\sigma_{i+1}^z(t)\rangle - \langle \sigma_i^z(t)\rangle\langle \sigma_{i+1}^z(t)\rangle. \tag{5.4}$$

Lastly, we also quantify quantum correlations by looking at the half-chain entanglement entropy. To compute this quantity, we partition the system across its center, such that the two resulting subsystems A and B, are the left and right halves of the chain, respectively. Then, the half-chain entanglement entropy is given by the von Neumann entropy of one of

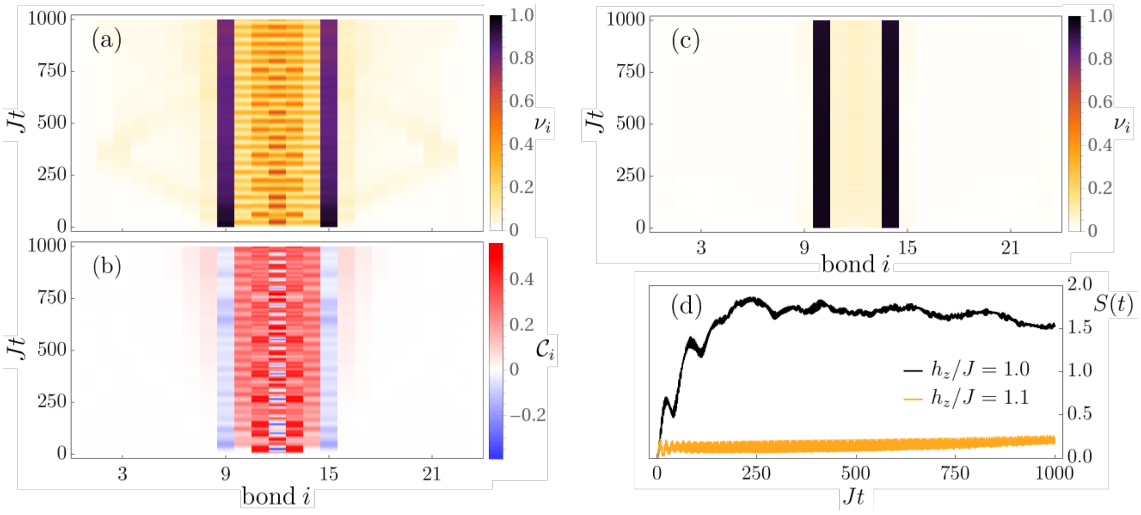

Figure 5.2: (Left) String motion in the short-range model with $L = 24$, $h_x/J = 0.2, h_z/J = 1$, and an initial separation of the domain walls $\ell = 6$. Dynamics of (a) the domain wall density $\nu_i(t)$, and (b) the nearest-neighbor connected correlator $\mathcal{C}_i(t)$. (Right) Suppression of string motion and string breaking in the short-range model with $L = 24$, $h_x/J = 0.2, \ell = 4$. Dynamics of (c) the domain wall density $\nu_i(t)$ with $h_z/J = 1.1$, and (d) the half-chain entanglement entropy $S(t)$ with $h_z/J = 1$ (resonant) and $h_z/J = 1.1$ (off-resonant). Similar off-resonant behavior is also observed with values of h_z/J smaller than 1. The resonant curve in (d) corresponds to the quench displayed in Fig. 5.1.

the two parts [289] (see also Appendix A), say A, that is,

$$S(t) \equiv S(\rho_A(t)) = -\mathrm{Tr}_A(\rho_A(t) \ln \rho_A(t)), \tag{5.5}$$

where $\rho_A(t) = \mathrm{Tr}_B(|\Psi(t)\rangle\langle\Psi(t)|)$ is the reduced density matrix of the left half of the chain, and $|\Psi(t)\rangle$ describes the (pure) quantum state of the entire system at time t. This entanglement entropy measures the amount of quantum correlations established between the two halves of the chain.

5.2 Summary of main results

We start by outlining the main findings of this chapter, which will be analyzed in more detail in the following sections. We show the characteristic patterns of string breaking for the short-range and long-range quantum Ising chains in Figs. 5.1, 5.2 and Fig. 5.3, respectively. As a central observation, the phenomenon of string breaking takes place as a two-stage process. In the first stage, the two kinks remain essentially static, while the connecting string can become a dynamical object, see, in particular, Figs. 5.2(a) and 5.3(a). We find that in the short-range Ising chain the stability of the initial kinks crucially depends on their initial distance ℓ. Upon changing separation from $\ell = 4$, Fig. 5.1, to $\ell = 6$, Figs. 5.2(a) and 5.2(b), the time range of their stability jumps from a time $Jt \approx 40$ to

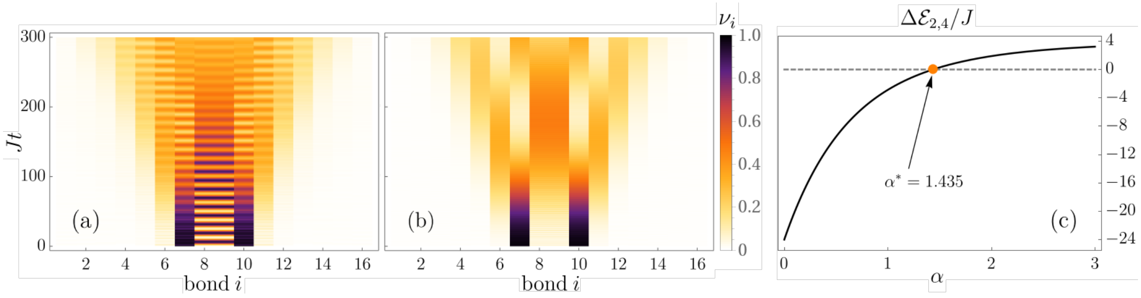

Figure 5.3: Real-time dynamics of string breaking in the long-range Ising model. (a) String breaking as a two-stage process when the exponent $\alpha = 1.435$ is such that a resonance condition is satisfied. (b) String breaking also takes place with an non-resonant exponent $\alpha = 1.1$. Note the lack of transient string oscillations, as opposed to the resonant case. Both instances show the domain-wall dynamics $\nu_i(t)$, for a system of size $L = 17$, and $\ell = 3$, $h_x/J = 0.25$. (c) Graphical solution of the resonance condition for the example in (a). $\Delta\mathcal{E}_{2,4}$ is the energy difference (in units of J) between the initial state with two kinks and a four-kink state, in which the central spin is flipped.

a value which is not anymore visible on the accessed time scales. It is one of the main goals of this work to provide a physical picture for this stability and to describe the string motion in this regime.

While the two initial kinks can remain stable for a long time, we observe that the connecting string can undergo complex dynamics, see Figs. 5.2(a) and 5.2(b), in particular, which we explain in more detail via an effective description in Section 5.3.1. Especially for the case of long-lived initial kinks, particle-antiparticle pairs are created and annihilated in a complex oscillatory pattern without being able to induce a breaking of the string. Conversely, outside of the initial string, the system remains almost inert with only some slight dynamics induced by the quench such as the ballistic motion of a bound pair of two domain walls, an analog of a meson, in Fig. 5.2(a). Finally, we find that there are also parameter regimes where the string does not display dynamics during the initial stage, see Fig. 5.2(c) and the short-time behavior in Fig. 5.3(b). This latter feature will also be captured in our effective model, which shows that the dynamics of the string is too constrained in this case to induce oscillatory behavior.

A further important finding of this work is representatively shown in Fig. 5.2(b). During the first stage, the dynamics in the string not only generates particles but also significant quantum correlations, while these are absent outside of the central region, yielding a characteristic spatiotemporal correlation pattern. Consequently, the recently observed entanglement growth during string breaking in gauge theories [31, 93, 95, 100, 102] can be understood to be initially caused by the generation of these strong correlations inside of the string, while the outside remains effectively decoupled. Notice that this implies that the mesons travelling ballistically in Fig. 5.2(a), which are merely produced by the quench dynamics, are essentially decoupled from the inside of the string.

5.3 First stage: string motion

Let us now focus on the first stage of string breaking. As a central observation, the two initial kinks can remain static for long times, which allows us to develop simplified effective descriptions in this regime.

Importantly, for the short-range Ising chain the system effectively decomposes into three disconnected spatial regions, in particular, because no quantum correlations are generated between them, see Fig. 5.2(b). Since the outside essentially remains static, we will now focus on the dynamics of the string itself, which in this decomposition, is now an object with a fixed spatial extent determined by the initial spin configuration and therefore the initial spatial separation ℓ of the kinks. Specifically, we will describe the string dynamics in the following by the Hamiltonians in Eqs. (5.1) and (5.2) on a chain of ℓ sites and initial condition $|\Psi_0\rangle = \bigotimes_{m=1}^{\ell} |\downarrow\rangle_m$. Let us point out that we have to impose a magnetic boundary condition at the ends, since the first and last spin of the string have to remain inert due to the requirement that the two initial domain walls are static. This can be achieved by skipping the transverse-field term or by adding a strong longitudinal field to those lattice sites.

For the long-range model, an analogous decomposition is not possible. However, we still observe that the spatial region outside of the initial string remains almost inert. Therefore, one can develop an effective description which keeps the spins outside of the string frozen and the spins inside the string as dynamical objects.

5.3.1 Effective description of the string dynamics

As argued in Section 5.1.1, the considered quantum Ising chains exhibit confinement dynamics whenever $h_x \ll J$ and therefore whenever quantum fluctuations are weak. We take this as a starting point to organize the Hilbert space for the string dynamics. Specifically, we will decompose the state space into sectors with different numbers of domain walls. For that purpose, we introduce operators $\mathcal{P}_k$ projecting onto the subspace of k kinks. This allows us to represent the effective Hamiltonian $\mathcal{H}_{\text{eff}}$ for the string as:

$$\mathcal{H}_{\text{eff}} = \sum_{k \in \mathcal{I}} \mathcal{H}_k + \sum_{k \neq k'} \mathcal{V}_{k,k'} , \tag{5.6}$$

where $\mathcal{H}_k = \mathcal{P}_k H \mathcal{P}_k$ denotes the projection of the full Hamiltonians in Eqs. (5.1) and (5.2) onto the subspace with k kinks. Accordingly, $\mathcal{V}_{k,k'} = \mathcal{P}_k H \mathcal{P}_{k'} + \mathcal{P}_{k'} H \mathcal{P}_k$, stands for the coupling between such subspaces and $\mathcal{I} = \{2, 4, \dots, k_{\max}\}$ is the index set labeling the allowed kink sectors up to the number of kinks $k_{\max}$, that maximally fit into the string upon respecting the boundary condition, which is $k_{\max} = \ell - 2$ when ℓ is even and $k_{\max} = \ell - 1$ when ℓ is odd.

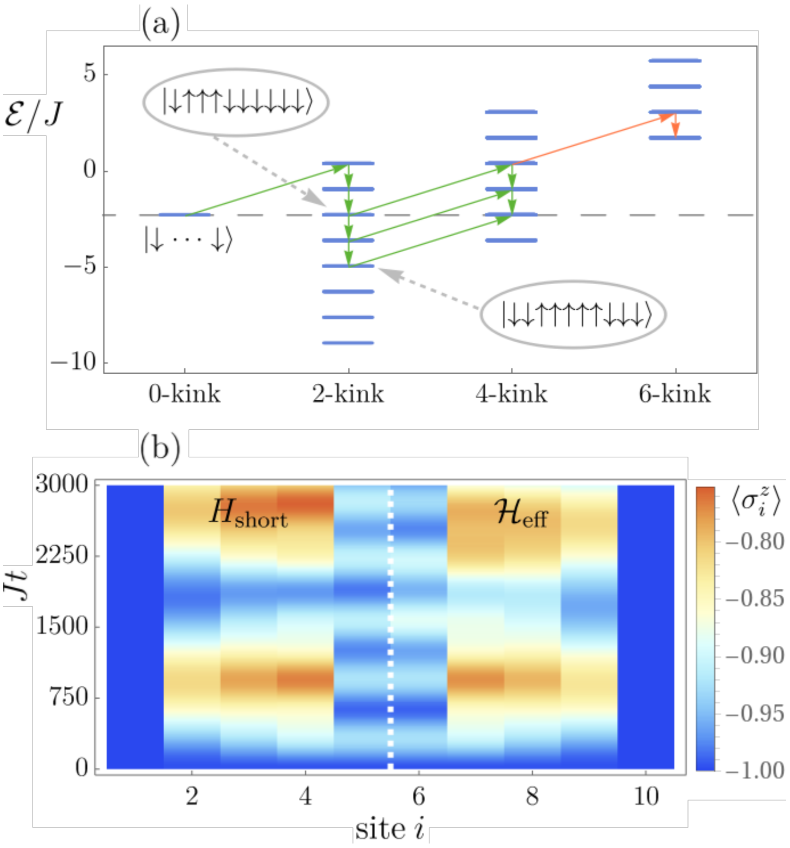

Figure 5.4: Effective description of the string motion in the short-range model during the first stage. (a) Decomposition of the effective Hamiltonian $\mathcal{H}_{\text{eff}}$ into different kink sectors. The arrows indicate allowed transitions induced by single-spin flips via the transverse field. Paths yielding virtual transitions between resonant states are shown in green. Orange arrows indicate transitions towards a non-resonant sector. Two spin configurations within the 2-kink sector are shown, as an example, as well as their location in the energy ladder. (b) Comparison of the exact magnetization dynamics $\sigma_i^z(t)$ (left) to the effective description including all kink sectors up to k^* (right), with $\ell = 10$, $h_x/J = 0.075$, and $h_z/J = 2/3$.

By decomposing the Hamiltonian into these kink sectors one obtains a representation as depicted in Fig. 5.4(a) for the short-range model in Eq. (5.1). The overall picture, however, does not change for the long-range case. The general structure of $\mathcal{H}_k$ can be divided into a diagonal part $\mathcal{E}_k$ in the spin configurations and an off-diagonal one, which is proportional to h_x and acts as a hopping term for the kinks. The transitions between different kink sectors contained in $\mathcal{V}_{k,k'}$ are driven by single-spin flips induced by the transverse field, which can only connect spin configurations that differ by exactly two domain walls. In Appendix B, show explicitly how to construct all the different terms in Eq. (5.6).

Let us now more specifically analyze the structure of the diagonal part of $\mathcal{H}_k$. For the short-range model, it reads:

$$\mathcal{E}_k(\mathcal{S}) = -J(\ell - 1) + 2Jk - h_z(\ell - 2l_{\mathcal{S}}), \tag{5.7}$$

where k and $l_{\mathcal{S}}$ denote the number of kinks and the number of ↓ spins in the given spin configuration $\mathcal{S}$, respectively. The sector of $k = 0$ kinks only contains one configuration $\mathcal{S} = |\downarrow \ldots \downarrow\rangle$, that is, the initial condition. Since kinks can only be generated in pairs, the next higher sector is the $k = 2$ one. The respective two domain walls can reside on various different bonds with an energy that depends linearly on their distance, which is the defining feature of confinement and which leads to a tower of states as depicted in Fig. 5.4(a), similarly also for the higher kink sectors.

For the long-range system, the energy of a particular spin configuration is not a simple explicit function of the parameters ℓ, k, and $l_{\mathcal{S}}$ [70]. Instead, we numerically obtain the energy for a given kink sector using the formula

$$\mathcal{E}_k(\mathcal{S}) = -J \sum_{i<j}^{L} \frac{s_i(\mathcal{S}) s_j(\mathcal{S})}{r_{ij}^{\alpha}}, \tag{5.8}$$

where $s_i(\mathcal{S}) = \pm 1$ is the value of the spin on site i corresponding to the configuration $\mathcal{S}$. Unlike the short-range case, this will depend on ℓ, k, and $l_{\mathcal{S}}$ nonlinearly, and notably the influence of boundary effects can be significant, as a general feature of long-range systems.

Transitions induced by the transverse field across configurations that live in a given sector (and therefore leave the number of domain walls invariant) have the only consequence that they move domain walls between neighboring lattice sites. As the domain walls are confined, such a motion always costs energy so that the respective process is off-resonant and therefore only yields perturbative corrections. For the short-range model, this can be alternatively seen by recognizing that the diagonal part $\mathcal{E}_k$ resembles a Wannier-Stark ladder of charged particles in an electric field [290] as a function of both k and $l_{\mathcal{S}}$. Here, the role of the field is taken over either by the coupling J or the longitudinal field h_z. The off-diagonal part of $\mathcal{H}_k$ induces motion on this Wannier-Stark ladder for a fixed k via h_x by flipping individual spins. As known from the Wannier-Stark problem, however, this motion is always off-resonant and therefore only slightly perturbs the eigenstates of $\mathcal{E}_k$. This holds, in particular, in the limit of weak kinetic energy, which is guaranteed in our problem as $h_x \ll J$, see the discussion in Section 5.1. It will therefore be sufficient for the moment to ignore this motion within sectors of a given number of kinks k.

Similar representations of Hamiltonians in kink sectors have been introduced and used for the effective description of systems with confinement [59, 60, 70, 71]. Here, however, we not only restrict to low-kink sectors as in previous works but rather consider the full decomposition. As we will show, this turns out to be important for the description of the string dynamics because many resonant spin configurations $\mathcal{S}$ can appear across different kink sectors, which become crucial to describe the string motion.

At this point it becomes important to distinguish two different classes of parameter sets. Depending on the choice of Hamiltonian parameters, spin configurations in the higher-kink sectors can either be off-resonant or degenerate with the initial string. This distinction, which determines whether higher-kink sectors contribute perturbatively or non-perturbatively to the string dynamics, will become crucial to identify situations where string motion is suppressed or induced, as explained below. For the short-range model, resonances can occur whenever

$$\frac{h_z}{J} = \frac{k}{\ell - l_{\mathcal{S}}}, \tag{5.9}$$

where $1+k/2 \leq l_{\mathcal{S}} \leq \ell-k/2$. In the case of the long-range interacting model, the resonance condition corresponds to matching the energy for two different configurations $\mathcal{E}_k(\mathcal{S}_1) = \mathcal{E}_{k'}(\mathcal{S}_2)$. The location of the resonance can be easily determined by numerically comparing the energy difference between kink sectors; see Fig. 5.3(c) for a particular example of tuning α to obtain a degeneracy. Notice that by taking into account the off-diagonal transverse-field contributions within fixed kink sectors, the energy levels in Eq. (5.8) get broadened so that the resonance condition does not require fine-tuning.

When the parameters are such that there are no resonances, the string becomes inert and only acquires perturbative corrections from higher-kink sectors. An example of such a scenario is shown in Fig. 5.3(b) for the long-range model, where not only the initial charges remain static but also the string is almost inactive. Note, however, that in this example the string eventually breaks. The situation changes drastically in the short-range model where only a slight departure away from the resonance condition yields a suppression of both string motion and string breaking, at least, up to the accessible time scales, see Fig. 5.2(c) in comparison to Fig. 5.1(a). While the suppression of transport and particle production in the non-resonant short-range model were recently reported [71, 291], here we also find that the spreading of quantum information is drastically reduced in the off-resonant case as compared to the resonant one, see Fig. 5.2(d) where the dynamics of the half-chain entanglement entropy is shown.

Regarding the resonant case, which is illustrated in Figs. 5.1, 5.2(a), 5.2(b), and 5.3(a), the situation is again completely different, since the string can develop complex motion. Importantly, this dynamics is dominantly driven by all those spin configurations across all kink sectors which are resonant with the initial string configuration, as we will show in Section 5.3.3.

It might appear as a fine-tuning problem to achieve resonant configurations. However, let us now argue that the resonant case is at least as generic as the off-resonant one. First of all, the absence of a resonance we attribute to a lattice effect. Due to a nonzero lattice spacing, the energy in the string develops a granular structure allowing only discrete values. This changes when going towards a continuum limit where this granularity is gradually washed out. Therefore, for small lattice spacings resonances become much more likely. Furthermore, notice that taking into account the broadening of the energy levels due to quantum fluctuations in $\mathcal{H}_k$ makes the resonance conditions more generic.

In the following, we will analyze the implications of the effective model in more detail by first deriving a bound on particle creation in the string and second by analyzing the dynamics in the resonant subspace.

5.3.2 Bound on particle production

As emphasized before, the string dynamics is dominated by the resonant subspaces across the different kink sectors. This immediately has an important consequence: there always exists a maximum kink sector k^* that is resonantly coupled to the initial string. This imposes a constraint on the number of domain walls K that can be generated during real-time evolution.

To obtain such a bound for the short-range model, let us note that the leading-order energy of a spin configuration is given by Eq. (5.7), whereas the energy of the initial string is $\mathcal{E}_0 = -J(\ell-1)+\ell h_z$. Thus, imposing the resonance condition $\mathcal{E}_0 \equiv \mathcal{E}(\mathcal{S})$ and solving for k, yields

$$k = \frac{h_z}{J}(\ell - l_{\mathcal{S}}). \tag{5.10}$$

On the other hand, k and $l_{\mathcal{S}}$ are not independent. Indeed, one can readily show that

$$l_{\mathcal{S}} \geq l_{\mathcal{S}}^{\min}(k) := 1 + \frac{k}{2}. \tag{5.11}$$

Combining (5.10) and (5.11) gives a bound, in terms of ℓ and h_z, on the number of kinks K that is possible to produce inside the string, provided that the resonance condition is met, namely

$$K \leq k^* := \left\lfloor \frac{2(\ell-1)}{1+2J/h_z} \right\rfloor_{\text{even}}, \tag{5.12}$$

where $2J/h_z$ is one of the rational numbers allowed by Eq. (5.9) and is also such that k^* is at least equal to 2. Here, the notation $\lfloor x \rfloor_{\text{even}}$ stands for the largest even integer smaller than or equal to x. Importantly, $k^* \leq k_{\max}$ can be much smaller than the maximum number of kinks $k_{\max}$ that fit in a string of given length ℓ ignoring the resonance condition, especially upon decreasing the value of the longitudinal field h_z where $k^* \propto h_z/J$ implying a small kink density. As anticipated before, $k_{\max} = \ell - 2$ if ℓ is even and $k_{\max} = \ell - 1$ when ℓ is odd.

Let us note that the origin of the bound (5.12) can be directly understood from Fig. 5.4 where we depict the structure of the energy levels for the short-range model. The creation of two new kinks costs at least an energy $4J$. As a consequence, the minimum energy at a given kink sector has to increase for higher k up to the point where the tower is shifted out of resonance, which marks the maximum number of domain walls which can be potentially generated. Of course, these considerations neglect the influence of off-diagonal spin flips in $\mathcal{H}_k$ so that the bound only holds in the limit of weak transverse fields and might yield corrections for larger h_x. The derived bound represents a constraint on the generation of new kinks, which restricts the formation of composite mesonic objects of bound domain wall pairs and hence might significantly slow down string breaking.

One particular implication of this bound is a controlled criterion for truncating the sums in Eq. (5.6) incorporating all non-perturbative effects, that is, what is the maximum kink sector that has to be taken into account for the description of the string dynamics. In order to assess and illustrate the approach presented here, in Fig. 5.4(b) we show the dynamics of the mean on-site magnetization $\langle \sigma_i^z(t) \rangle$, of a string of length $\ell = 10$ in a longitudinal field $h_z/J = 2/3$, a value for which the resonance condition is met. As implied by the bound (5.12) and shown in Fig. 5.4(a), here $k^* = 4$, so that the corresponding reduced model simply reads $\mathcal{H}_{\text{eff}} = \mathcal{H}_0 + \mathcal{H}_2 + \mathcal{H}_4 + \mathcal{V}_{0,2} + \mathcal{V}_{2,4}$. As can be observed, the reduced model captures the main features of the exact dynamics.

For the long-range model, it is, in principle, possible to get more than two states with resonant energies after we impose $\mathcal{E}_k(\mathcal{S}_1) = \mathcal{E}_{k'}(\mathcal{S}_2)$ and choose α accordingly. However, due to the nonlinear nature of the energy function of the long-range model, given by Eq. (5.8), it becomes more challenging to get a strict bound on the number of resonantly accessible domain walls. Let us point out that, it is, however, still possible to determine numerically the maximum kink sector simply by scanning the energy in Eq. (5.8) in all relevant kink sectors to identify degeneracies with the initial string state.

5.3.3 Dynamics in resonant subspace

The full solution of the Hamiltonian in Eq. (5.6) may still require exponential resources in the string length ℓ. Here, we aim to show that a further reduction is possible beyond the restriction onto the maximum kink sector k^* that has been taken into account already in the previous Section. Specifically, it is possible to obtain an effective description of the resonant subspace alone, which as we show provides further insights during the first stage of the string dynamics.

The central property that we will use in the following is that all spin configurations outside of the resonant subspace can be treated perturbatively in h_x/J, by recalling that the transitions between spin configurations are driven by the transverse field, which has to be chosen to satisfy $h_x \ll J$. However, in general, the challenge is that, in principle, exponentially many paths exist in the energy level diagram such as in Fig. 5.4(a) that can connect different resonant configurations by virtual transitions. It is clear, nonetheless, that those paths that require overcoming large energy differences are less relevant than the others. It turns out that the identification of the “shortest paths” that are contributing dominantly depends on the details of the chosen parameters.

For the short-range model, we indicate in Fig. 5.4(a) with arrows the shortest paths in the energy diagram for one particular case of a string of length $\ell = 10$ with $h_z/J = 2/3$ connecting dominantly the different resonant sectors in terms of single-spin flips. We can then ignore all states not contained in this shortest paths selection, since they will only contribute subdominantly yielding only further perturbative corrections. The remaining off-resonant spin configurations can then be eliminated perturbatively by means of a Schrieffer-Wolff transformation [292, 293], as explained below.

Schrieffer-Wolff transformation

Here we explain the main idea of a Schrieffer-Wolff transformation [292, 293] and then apply it for the problem at hand. Let us consider a Hamiltonian of the form

$$H = H_0 + \gamma V, \tag{5.13}$$

where the eigenvalues $\{\epsilon_\mu\}$ and eigenstates $\{|\mu\rangle\}$ of H_0 are known, that is,

$$H_0 = \sum_\mu \epsilon_\mu |\mu\rangle\langle\mu|. \tag{5.14}$$

Our task is to carry out a unitary transformation, with generator S, such that the rotated Hamiltonian

$$\tilde{H} = \mathrm{e}^S (H_0 + \gamma V)\mathrm{e}^{-S} = H_0 + \gamma V + [S, H_0] + \gamma[S, V] + \frac{1}{2}[S, [S, H_0]] + \cdots \tag{5.15}$$

has no off-diagonal terms to first order. This is accomplished by choosing S such that

$$[S, H_0] = -\gamma V, \tag{5.16}$$

that is,

$$S_{\mu\nu} = \gamma \frac{V_{\mu\nu}}{\epsilon_\mu - \epsilon_\nu} \tag{5.17}$$

in the H_0 eigenbasis, and provided that the right-hand side is finite. Thus, Eq. (5.15) becomes

$$\tilde{H} = H_0 + \frac{1}{2}\gamma[S, V] + \mathcal{O}(\gamma^3). \tag{5.18}$$

Now let us apply this technique to the problem at hand. The starting point is the effective Hamiltonian $\mathcal{H}_{\text{eff}}$ as given in Eq. (5.6), including contributions up to the k^* sector where k^* is determined as explained in the previous section [see Eq. (5.12)]. We bear in mind that at this stage we only considered states that are involved in the shortest paths mentioned before. The projected Hamiltonians $\mathcal{H}_k$ contain a diagonal part, given essentially by Eq. (5.7), and an off-diagonal part. Here we collect the diagonal terms in H_0 and put the off-diagonal part of the $\mathcal{H}_k$'s together with the terms $\mathcal{V}_{k,k'}$ (all having to do with the transverse field h_x) in the perturbation term γV, with h_x/J playing the role of the small parameter γ. Note that, after performing the Schrieffer-Wolff transformation,

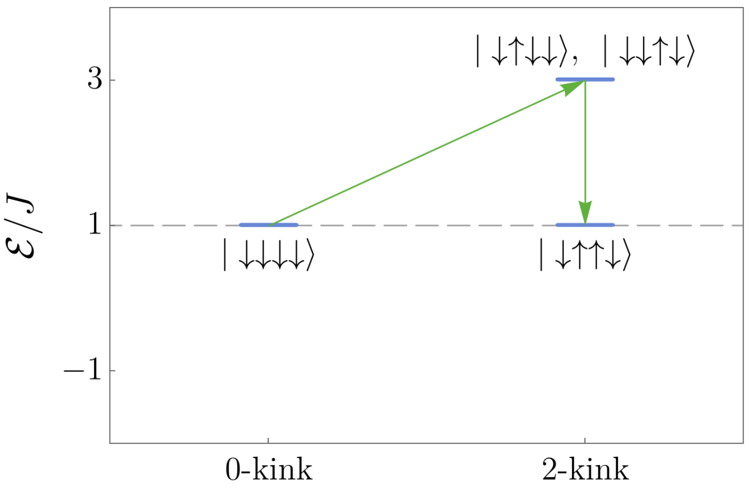

Figure 5.5: Decomposition of the effective Hamiltonian into the possible kink sectors, in the short-range model with $\ell = 4$ and $h_z/J = 1$.

the second-order term, $\frac{1}{2}\gamma[S, V]$, will contain effective couplings between resonant states in adjacent kink subspaces, which are then used to build the effective theory. In the following, we illustrate this procedure with two concrete examples.

String of length $\ell = 4$ in a field $h_z/J = 1$ (short-range model)

First, we apply this approach to the string of the example shown in Fig. 5.1, that is, we consider a string of length $\ell = 4$ in a longitudinal field $h_z/J = 1$. In this case, the configuration space associated to the effective Hamiltonian in Eq. (5.6) consists of four configurations, one in the zeroth-kink sector $|\downarrow\downarrow\downarrow\downarrow\rangle$ (initial string), and three more in the two-kink sector $|\downarrow\uparrow\downarrow\downarrow\rangle, |\downarrow\downarrow\uparrow\downarrow\rangle, |\downarrow\uparrow\uparrow\downarrow\rangle$. As shown in Fig. 5.5, these four configurations are involved in the shortest paths connecting the resonant states $|\Psi_0\rangle = |\downarrow\downarrow\downarrow\downarrow\rangle$ and $|\Psi_1\rangle = |\downarrow\uparrow\uparrow\downarrow\rangle$.

The diagonal part, Eq. (5.7), of the effective Hamiltonian $\mathcal{H}_{\text{eff}}$, in matrix representation, is

$$H_0 = \begin{pmatrix} 4\frac{h_z}{J} - 3 & 0 & 0 & 0 \\ 0 & 2\frac{h_z}{J} + 1 & 0 & 0 \\ 0 & 0 & 2\frac{h_z}{J} + 1 & 0 \\ 0 & 0 & 0 & 1 \end{pmatrix}, \tag{5.19}$$

whereas the off-diagonal part reads

$$\gamma V \equiv \frac{h_x}{J} \begin{pmatrix} 0 & -1 & -1 & 0 \\ -1 & 0 & 0 & -1 \\ -1 & 0 & 0 & -1 \\ 0 & -1 & -1 & 0 \end{pmatrix}.$$

The generator of the Schrieffer-Wolff transformation, Eq. (5.17), is

$$S = \frac{h_x}{J}\begin{pmatrix} 0 & \frac{1}{4-2h_z/J} & \frac{1}{4-2h_z/J} & 0 \\ -\frac{1}{4-2h_z/J} & 0 & 0 & -\frac{1}{2h_z/J} \\ -\frac{1}{4-2h_z/J} & 0 & 0 & -\frac{1}{2h_z/J} \\ 0 & \frac{1}{2h_z/J} & \frac{1}{2h_z/J} & 0 \end{pmatrix}. \tag{5.20}$$

We now compute the second-order term, $\frac{1}{2}\gamma[S,V]$, from which we will obtain an effective model for the resonant subspace. We have

$$\frac{1}{2}\cdot\frac{h_x}{J}[S,V] = \begin{pmatrix} a & 0 & 0 & b \\ 0 & d & d & 0 \\ 0 & d & d & 0 \\ b & 0 & 0 & c \end{pmatrix}, \tag{5.21}$$

where

$$\begin{aligned} a &= -2\frac{(h_x/J)^2}{4-2h_z/J}, \qquad & b &= -\frac{(h_x/J)^2}{2h_z/J} - \frac{(h_x/J)^2}{4-2h_z/J}, \\ c &= -2\frac{(h_x/J)^2}{2h_z/J}, \qquad & d &= \frac{(h_x/J)^2}{2h_z/J} - \frac{(h_x/J)^2}{4-2h_z/J}. \end{aligned} \tag{5.22}$$

Thus, in the resonant subspace the problem reduces to that of a two-state system with Hamiltonian

$$\tilde{\mathcal{H}}_{\text{eff}} = \begin{pmatrix} a & b \\ b & c \end{pmatrix}. \tag{5.23}$$

This problem can be resolved exactly. Indeed, the time-evolved wave function can be written as

$$|\psi(t)\rangle = c_1(t)|\downarrow\downarrow\downarrow\downarrow\rangle + c_2(t)|\downarrow\uparrow\uparrow\downarrow\rangle, \tag{5.24}$$

with the initial condition $c_1(0) = 1, c_2(0) = 0$. The time-dependent probability for being found in each of the two states is then given by Rabi's formula (see for example Ref. [294]):

$$|c_2(t)|^2 = \frac{1}{2}\left(1 - \cos\left[2\left(\frac{h_x}{J}\right)^2 Jt\right]\right) = \sin^2\left[\left(\frac{h_x}{J}\right)^2 Jt\right], \tag{5.25}$$

This equation tells us that the system will be oscillating between the two states with a period given by $JT = \pi/(h_x/J)^2$ (see Fig. 5.6). Further, one can predict analytically the time scale at which the new kinks are generated in the string. This happens when the spin configuration with two kinks in the interior of the string is maximally populated for the

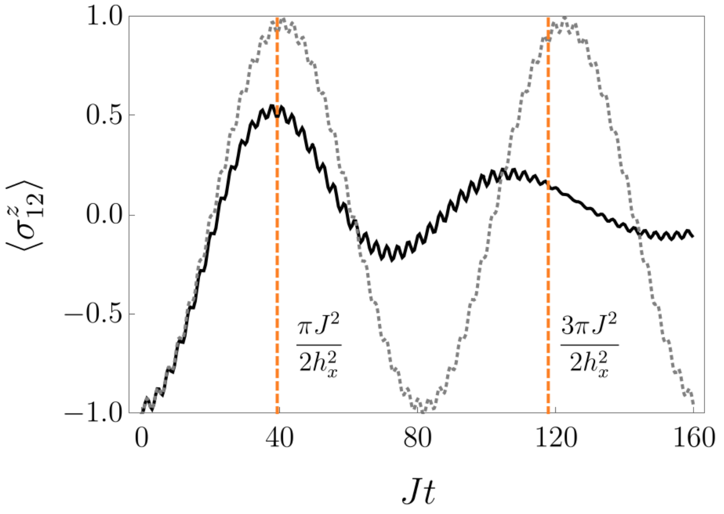

Figure 5.6: Dynamics of mean local magnetization at site 12, $\langle\sigma_1 2^z(t)\rangle$, in a chain of size $L = 24$, with a central string of length $\ell = 4$, for the short-range model (5.1) with $h_x/J = 0.2, h_z/J = 1$. The black curve shows the complete solution obtained by ED, whereas the gray dotted curve is the perturbative solution where we only consider the string alone with fixed kinks at the boundaries (also computed via ED). The difference between the orange dashed lines gives the period as predicted by the effective model for the resonant states.

first time. According to our model, this occurs at

$$Jt^* = \frac{\pi}{2(h_x/J)^2} \approx 39.3, \tag{5.26}$$

which is in excellent agreement with the results shown in Fig. 5.1. In Section 5.3.4, we investigate the accuracy of this prediction at increasing transverse-field strength. Let us already note at this point that the present analysis also has central implications for the second stage of string breaking, that will be discussed in Section 5.4.

String of length $\ell = 3$ in the long-range model with $\alpha = 1.435$

In the long-range model, the resonant dynamics are especially simple because the resonant subspace only contains two states. For the particular case chosen in Fig. 5.3(a), the transition between the two states requires flipping only one spin in the center of the string. In such a case, the oscillation period between these two states can be directly calculated (see Fig. 5.7). Following steps similar to those of the previous example, one finds that the time at which the higher-kink state inside the string is maximally populated is $Jt^* = \pi/(h_x/J) \approx 12.57$ for the parameters used in Fig. 5.3(a), which is in perfect agreement with ED results of the many-body Hamiltonian.

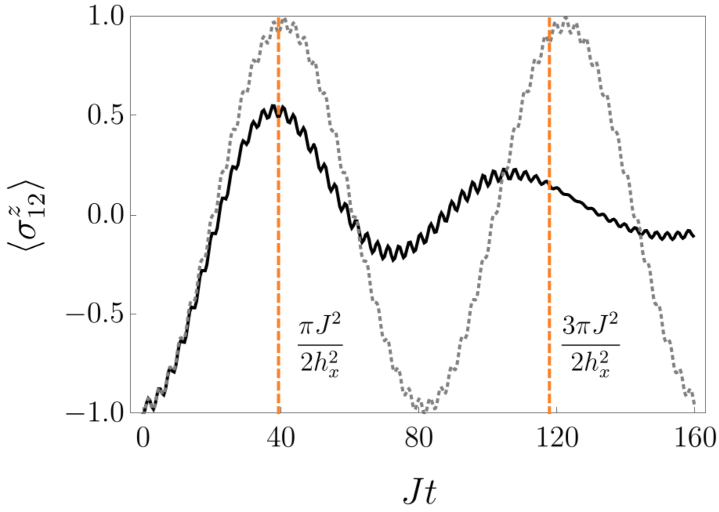

Figure 5.7: Dynamics of mean local magnetization at site 9, $\langle \sigma_9^z(t) \rangle$, within a string of length $\ell = 3$, embedded in the center of a chain with $L = 17$ spins, for the long-range model (5.2) with $h_x/J = 0.25, \alpha = 1.435$. The black curve is the complete solution obtained by ED. The difference between two consecutive orange dashed lines gives the period as predicted by the effective model for the resonant states.

Let us emphasize that the analytical estimates of the typical time scales for the onset of string breaking, which are obtained with our effective description, go beyond the estimates for the non-resonant scenario as reported in Ref. [291].

5.3.4 Typical timescale for the onset of string breaking

The timescales necessary for the observation of string breaking can be tuned upon increasing the strength of the transverse field. Here, we illustrate this point concretely for the short-range model. Moreover, we employ the effective model in the resonant subspace discussed above to obtain an analytical prediction for the relevant timescale. Thus, let us consider a similar setting as in Fig. 5.1, namely, we study the quench dynamics to $h_x/J = 0.2, h_z/J = 1$, in the short-range model, starting from a string state with a central string of length $\ell = 4$, embedded in a chain of $L = 12$ spins with open boundary conditions. As shown in Section 5.3.3, for this particular setting, our effective description maps the problem onto a two-level system. The breaking of the string is thus expected when the "broken-string" configuration, $|{\downarrow\uparrow\uparrow\downarrow}\rangle$, is maximally populated for the first time, for that represents the moment when two new kinks are created right next to the original ones. According to our effective model, this occurs at a timescale given in Eq. (5.26).

In Fig. 5.8, we show the domain-wall dynamics obtained via ED at three different values of the transverse-field strength, namely, $h_x/J = 0.3, 0.4$, and 0.5, with the predicted typical timescales being $Jt^* \approx 17.45, 9.82$, and 6.28, respectively. We observe that these predicted values give a remarkably good estimate of the onset of string breaking, even at relatively

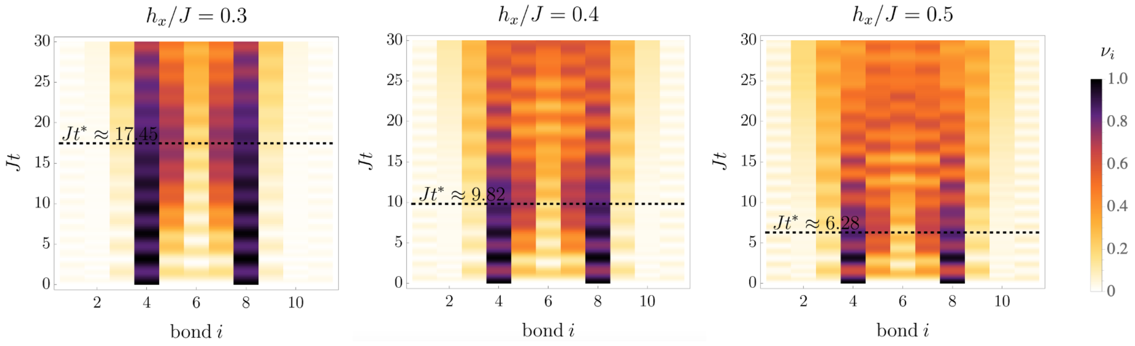

Figure 5.8: Timescales for the onset of string breaking in the short-range Ising model with $L = 12, h_z/J = 1$ and an initial distance $\ell = 4$ between two domain walls, at increasing transverse-field strength $h_x/J = 0.3, 0.4$, and 0.5. The black dashed lines indicate the predicted typical timescale from the effective model in the resonant subspace.

large transverse fields. Overall, these results show that by increasing the strength of the transverse field, it could be, in principle, possible to bring the whole phenomenology of string breaking within the reach of current technologies in quantum simulators.

5.3.5 Field-theoretical approach and extended kinks in the short-range model

In the majority of this chapter, we have worked close to the limit $h_x \approx 0$ for the short-range model, Eq. (5.1). Directly at $h_x = 0$, the kinks are given by product states, $\sigma_i^z = \pm 1$, but at $h_x > 0$ single local kinks are generally complicated states which are not easily constructed, even with the exact analytic solutions to this Hamiltonian in the deconfined ($h_z = 0$) limit.

Here, we construct approximate kinks which are still product states, but better approximate the actual kinks of the model. A simple ansatz is to take

$$|\mathcal{K}\rangle = \bigotimes_j \Big[\cos\theta_j|+\rangle + \sin\theta_j|-\rangle\Big], \tag{5.27}$$

where $\sigma^z|\pm\rangle = \pm|\pm\rangle$, and we choose the expectation value on each site to be the position-space profile of the kinks:

$$\langle\mathcal{K}|\sigma_j^z|\mathcal{K}\rangle = \cos 2\theta_j = F(x_j). \tag{5.28}$$

We take $F(x)$ to vanish at the position of the kink (which should be at the half-way point between two lattice sites). This equation only determines $\sin\theta_j$ up to a sign; if we are working with $h_x, J > 0$, we should choose the sign which makes $\langle\sigma_j^x\rangle = \sin 2\theta_j$ positive. We furthermore want the state to approach the exact magnetization of the Ising chain far away from the position of any kinks:

$$\lim_{x\to\pm\infty} F(x) = \pm N_0. \tag{5.29}$$

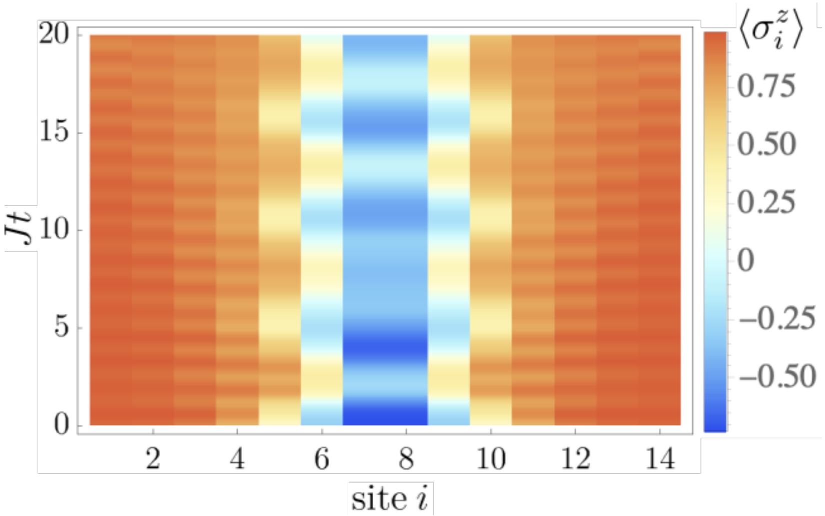

Figure 5.9: Evolution of the mean on-site magnetization $\langle\sigma_i^z(t)\rangle$ in the short-range model (5.1) with $h_x/J = 0.45, h_z/J = 0.6$, taking into account the approximate expression for the extended kinks [Eq. (5.33)].

We can determine N_0 directly from the exact solution [275], namely

$$N_0 = \left[1 - (h_x/J)^2\right]^{1/8}. \tag{5.30}$$

In addition, we would like the profile $F(x)$ to have a finite width around the position of the kink. This width should be on the order of

$$W \sim \frac{v}{E_{\mathcal{K}}}, \tag{5.31}$$

where v is a characteristic velocity in the system and $E_{\mathcal{K}}$ is the energy of the kink. Here, we can take some intuition from the exact dispersion of the model,

$$\epsilon_\kappa = 2\sqrt{J^2 + h_x^2 - 2h_x J\cos\kappa}, \tag{5.32}$$

where $\kappa \in [-\pi, \pi]$.

So one sees that the energy gap of the system is $\Delta = 2(J - h_x)$, and that the low-momentum dispersion takes the form $\sqrt{\Delta + v^2\kappa^2} \approx \Delta + v^2\kappa^2/2\Delta$, identifying $v = 2\sqrt{h_x J}$. So in principle we could build any function $F(x)$ which approaches $\pm N_0$ away from positions of kinks and vanishes along a width of order $W \sim \sqrt{h_x/J}/(1-h_x/J)$ in units of the lattice spacing.

We propose the following single-kink ansatz:

$$F(x) = \pm N_0 \tanh\left[\frac{3E_{\mathcal{K}}}{4N_0^2 v}(x - x_0)\right]. \tag{5.33}$$

This functional form was inspired by the semiclassical static solution for kinks in scalar ϕ^4 quantum field theory. This theory describes the short-range Ising chain at couplings h_x/J such that the correlation length is large compared with the lattice spacing, and furthermore we can treat this theory perturbatively in its interactions if we are not too close to the phase transition ($h_x = J$). In these limits, the kinks are given by the field configurations of Eq. (5.33) [295]. This expression also reduces to a step function in the limit $h_x \to 0$, as expected. The expression $E_{\mathcal{K}}$ is the exact energy of the kink, but at our level of approximation we simply take $E_{\mathcal{K}} = \Delta$. Numerical results using these approximate kinks are shown in Fig. 5.9, where we take $h_x/J = 0.45$ and $h_z/J = 0.6$. We find similar behavior to that seen in the small h_x limit, where the string undergoes dynamical oscillations, but the location of the initial kinks remains approximately static. In principle, one may perform similar experiments for higher transverse fields in the long-range model after numerically obtaining reasonable values for N_0, v, and $E_{\mathcal{K}}$ and a similar ansatz to the above, although we have not done so here. This provides some evidence that the dynamics described in the previous sections of this chapter survives into the many-body regime, where h_x is not small.

5.4 Second stage: string breaking

While the final string breaking can be prolonged to long times, see Fig. 5.2, it is known especially for the short-range model that the system is ergodic and thermalizing [296], although long-lived nonequilibrium states have been recently discussed in this system [297–299] and delayed thermalization observed in the long-range model [300]. However, in general, we expect that the considered models will eventually restore a homogeneous state where the string has to be broken. For the case displayed in Fig. 5.1, we indeed observe that at long times the system becomes homogeneous with some remaining spatiotemporal fluctuations expected for systems of finite size [301].

Eventually, the string breaks by the formation of mesons, that is, bound pairs of domain walls involving, in particular, the two initial kinks. Strings can, in principle, break both for the case of resonant motion, see Fig. 5.1(a) and Fig. 5.3(a), as well as when the parameters are chosen such that the resonance condition for the string motion is not satisfied, see Fig. 5.3(b). The latter case seems to be especially applicable to the long-range model, since when the resonance condition is not met in the short-range model, string breaking may only occur after an exponentially long time, see Fig. 5.2(c) and Refs. [71, 291]. Furthermore, we also observe another significant difference between the long- and short-range models. While the time scale of string breaking does not seem to depend crucially on varying the parameters for the long-range interacting case, see Fig. 5.3, for the short-range Ising chain string breaking can be delayed by orders of magnitude in Fig. 5.2(a) by only changing the initial string length from $\ell = 4$ to $\ell = 6$.

As we aim to argue in the following, the delayed string breaking and meson formation for large string lengths ℓ in the short-range model is not only caused by the energy costs for particle creation due to the large kink mass as in the Schwinger mechanism [79, 302]. We rather observe that there are, in particular, strong kinetic constraints imposed by the dynamics in the resonant subspace. First of all, the considerations from Section 5.3.3 imply that only a limited subset of spin and therefore domain wall configurations is kinetically accessible. In this context, we find that there are mainly two different scenarios.

On the one hand, the resonant subspace might be such that a configuration with newly generated domain walls close to the initial kinks can be reached. This makes the meson formation very efficient. Such a case is displayed in Fig. 5.1, where we find that the time scale for string breaking coincides with the time scale of reaching the respective resonant domain wall configuration. In Section 5.3.4, we have discussed that from the effective description the latter time scale is $Jt^* = \pi/(2(h_x/J)^2) \approx 39.3$ matching the data in Fig. 5.1 obtained using exact diagonalization.

On the other hand, the resonant subspace can induce kinetic constraints so that only domain walls at larger distances from the initial kinks can be generated. In this context, the general bound on domain wall production derived in Eq. (5.12) provides some general implications. In particular, for weak symmetry-breaking fields h_z the maximally accessible kink density in the string becomes proportional to h_z/J implying that the typical distance between the generated domain walls is large. This makes it difficult for the system to efficiently form mesons of two kinks at a short separation.

For the long-range case, only a single higher-kink configuration can be resonant with the initial string, unless we fine-tune multiple parameters. As a consequence, we have not identified a case where the time scales associated with kink dynamics and string breaking have been related to each other. For the resonant case displayed in Fig. 5.3(a), this explains why there are a large number of oscillations before string breaking, which is analogous to what is seen for the short-range case displayed in Fig. 5.2(a). In addition, for generic parameters, the long-range model has no resonances and string breaking occurs with no transient string oscillations, as shown in Fig. 5.3(b). For the short-range model, the minimal energy gap between two spin configurations is always a constant value, see Fig. 5.4(a). However, for the long-range Hamiltonian, due to the nonlinear nature of the energy expression Eq. (5.8), the spacing between higher energy states can be extremely small. Due to this nature, the string can still break relatively fast, even without satisfying a resonant condition, see Fig. 5.3(b).

5.5 Summary and outlook

In this chapter, we have shown that string breaking can occur dynamically in quantum Ising chains where domain walls develop a confining potential induced either by a symmetry-breaking longitudinal field [55, 57, 68] or by long-range interactions [70]. Our main observation is that this phenomenon can be described as a two-stage process. During the first stage, a pair of initial kinks effectively acts as static external charges. The connecting string, however, can become a dynamical object and develops complex dynamics. To approximate this dynamics, we have derived an effective kinetically constrained model in the resonant subspace. In particular, we have obtained a bound on the maximal number of kinks that can be dynamically generated, and, for some cases, obtained a quantitative estimate for the time scale of final string breaking. We have argued that the large time scales for eventual string breaking are not only caused by the energy costs for pair creation due to the large mass of particles as in the Schwinger mechanism [79, 302]. We rather find that the effective model in the resonant subspace also imposes strong kinetic constraints. In this context, a natural question is to what extent the observed slow string breaking dynamics can be related to the slow relaxation observed previously in kinetically constrained models [31, 110, 112, 118, 123, 124, 126–128, 131, 169, 303–306]. In this respect, the non-resonant local dynamics in the short-range model seems to be even more constrained, with both particle production and spreading of quantum information being strongly suppressed.

While all of our analysis has been carried out for quantum Ising models, it can be equally well applied also to lattice gauge theories. For instance, it might be particularly interesting to explore the constrained dynamics in the resonant subspaces for such systems, as well as the string stability after a quench, as a function of the separation. A further interesting route might be the extension of our analysis to string breaking dynamics in higher-dimensional systems, which is certainly much more challenging. Importantly, long strings or flux tubes connecting far distant static background charges can still behave as effectively one-dimensional [307], which might make our analysis also applicable in this case and therefore relevant for high-energy physics.

Our finding, that the phenomenology of string breaking dynamics cannot only be realized in gauge theories but also in systems with less complexity such as spin chains, implies that this phenomenon might be more directly accessible experimentally. The dynamics in spin chains has already been successfully studied in various quantum simulator experiments [167, 169–172, 174–176, 179, 181], while lattice gauge theories are much more challenging to realize, as gauge invariance is difficult to enforce, with, however, some notable recent efforts[33–42] (see also Section 2.5). More specifically, we now outline how our results might be observable in Rydberg atom and trapped ion quantum simulators within the current scope of technology. Both platforms support, in principle, the initial preparation of any targeted product state [170–172] such as those with two domain walls, as depicted in Fig. 5.1(b). Since the strength of next-nearest-neighbor interactions in Rydberg atoms is just about 1.6% of the nearest-neighbor value [174], it is safe to neglect interactions beyond nearest neighbors up to timescales $Jt \sim 100$. Therefore, this type of platform can be used to probe short-range Ising chains [169, 171, 174–176, 179] as in Eq. (5.1), up to the mentioned timescales. On the other hand, long-range interacting Ising models find a natural implementation in systems of trapped ions with a tunable power-law exponent [167, 170, 172]. As a matter of fact, two recent experiments have already observed the confinement of domain walls in the systems herein considered and in the aforementioned experimental platforms [77, 181], showing the feasibility to observe string breaking in the models in Eqs. (5.1) and (5.2) in future experiments. However, the timescales necessary for the observation of string breaking in the numerical data we show in this work are rather large compared to what has been achieved experimentally. Importantly, these timescales can be significantly tuned by increasing the transverse-field strength h_x, as long as h_x does not exceed a critical value beyond which domain walls cease to be elementary excitations of the Ising model; see Section 5.3.4. We emphasize that, even in the regime of strong transverse-field, where domain walls can no longer be regarded as point-like particles, one can use a field-theoretical approach to takes into account the finite width of kinks. As shown in Section 5.3.5, this yields a similar description to the one at weak fields. On the other hand, what might be certainly experimentally observable is the constrained dynamics during the first stage where interesting and complex dynamical patterns are realized, see Fig. 5.2. Moreover, both considered experimental platforms allow for local readouts which make all the quantities discussed in this work measurable.

Finally, let us remark that, although our effective models allow us to elucidate various interesting aspects of the first stage of string breaking, and even to predict typical timescales for the final breaking of the string, a complete understanding of the second stage remains a challenge for techniques relying on classical resources. In this sense, the experimental perspectives with quantum simulators discussed above are crucial, as it is this approach that stands as the most promising route for deepening our understanding of hard problems such as string breaking dynamics, in a foreseeable future.

Chapter 6

Conclusions and Outlook

In this thesis, we have studied two concrete nonequilibrium dynamical phenomena in LGTs and related quantum spin models. Our main findings are the demonstration of nonergodic behavior in a 2D interacting LGT and the observation and characterization of dynamical string breaking in quantum Ising chains. Further, we have introduced a numerical method for computing the real-time evolution of correlated quantum systems. In addition, we have also discussed possible routes for the experimental realization with quantum simulators of the studied problems using current and future technologies.

We have also included a concise introduction to LGTs in Chapter 2, where we discuss the basic structure of an LGT in the Hamiltonian formulation using both Wilson's and quantum link approaches. Because of its central importance to the main subject of this work, this chapter also touches upon some of the state-of-the-art quantum simulator experiments of LGTs. Regarding the computational part, in Chapter 3, we have also described a few state-of-the-art techniques for simulating strongly interacting quantum models. Namely, we have reviewed exact diagonalization techniques, time evolution with matrix product states, and time evolution with different types of classical networks such as artificial neural networks. This short review thus paves the way for introducing the method of VCNs, which is one of the main contributions of this thesis as mentioned before.

Let us now summarize the main original results presented in this thesis and discuss possible extensions to be addressed in future work. The nonequilibrium dynamics of the 2D U(1) QLM was the subject of Chapter 4. Here, we showed that such an interacting 2D LGT can exhibit nonergodic behavior, in the absence of disorder, due to the mechanism of disorder-free localization. The importance of this finding can be better understood by making a couple of remarks on the role of *dimensionality* in localization phenomena. While the effect of dimensionality is well understood in the single-particle phenomenon of Anderson localization [308, 309], it is less clear what happens in interacting theories. For example, while there is a consensus about the existence of many-body localization [115–117] in 1D, it is still debated whether this phenomenon survives in 2D [168, 184–186].

Regarding disorder-free localization, all previous works had focused either on 1D systems or noninteracting theories in higher dimensions. Thus, prior to the work presented here (see also Ref. [2]), the central question about the role of dimensionality in the particular case of disorder-free localization has remained open. As mentioned before, our work answers this question by showing that such a mechanism is not destroyed by interactions in two spatial dimensions. This seems to suggest that *local constraints* due to *gauge invariance* give rise to an ergodicity-breaking mechanism that is seemingly more robust than the more conventional disorder-induced many-body localization. Further, we were able to put a bound on the localization transition through a mapping onto a classical correlated percolation problem in Section 4.5. Let us recall that a such bound constitutes only a lower bound for the true quantum-mechanical transition, that is, it might be possible that the system becomes localized on the percolating side of the transition due to interference effects, as the system is still inhomogeneous in a given superselection sector. However, determining the true quantum threshold is a far more challenging problem and hence remains a target for future studies.

There are two important tools for the analysis performed in this part of the present thesis. First, the method of VCNs, which was introduced in Chapter 3 (see specifically Section 3.5) and that allowed us to study the quantum dynamics of the 2D QLM in an efficient manner. To this end, we have explicitly built the relevant variational ansätze, whose construction, although not trivial, comprises a manageable degree of complexity. In particular, we were able to study quantum quenches in the 2D QLM starting from representative initial states of both the ergodic phase and the localized phase, up to considerably long timescales. The second important tool is a classical correlated percolation problem, which allowed us to put a bound on the localization-delocalization transition. Further, we showed that the latter analysis also implies a *fragmentation* of the Hilbert space into kinetically disconnected regions. Importantly, both the VCN method and the classical percolation analysis can be applied to other quantum many-body systems in two and higher-dimensions.

Now let us discuss several aspects of the problem disucussed in Chapter 4 that could be the subject of future research. In the first place, since our main result relies on the bound obtained via the percolation argument, it would be interesting to carefully characterize the nature of the observed (classical) percolation transition. Let us note here that such a characterization is not essential in *qualitatively* determining the localization-delocalization transition of interest. However, we believe that this is a very interesting problem on its own that deserves a more thorough analysis. Moreover, it would also be interesting to study the true quantum localization transition, as mentioned before. This, however, looks at the moment like a quite challenging problem, as it can be understood from related studies on 1D systems featuring many-body localization. On the other hand, let us recall that here we considered a *pure* LGT, that is, a gauge theory without matter degrees of freedom. In this respect, it is an intriguing question whether or not the conclusions discussed above also hold in the presence of matter. This problem, although clearly more challenging, should be approachable with the tools and methodology employed in this work. Finally, as mentioned above, the tools developed for this part of the present thesis can be applied to other systems in two and higher dimensions. Here, 3D quantum spin ice models appear as a particularly interesting target for future investigations. Potential applications, however, are not limited to LGTs but extend to the more general realm of quantum many-body systems. Some systems that could be addressed with the techniques developed here include 2D bosonic and fermionic Hubbard models as well as other systems featuring kinetic constraints. Lastly, as discussed in Section 4.6, the theoretical analysis presented here lies within reach of future experiments with quantum simulators. In particular, we have mentioned recent potential routes with Rydberg-atom quantum simulators [190, 191].

The second problem that was tackled in this work regards the real-time dynamics of string breaking in quantum spin chains. As discussed in Chapter 5 (see also Ref. [1]), here, we showed that such a dynamical phenomenon of fundamental importance in high-energy physics, can also take place in quantum Ising models where domain walls get confined either by a symmetry-breaking field or by long-range interactions. As a central observation, we identified two distinct stages occurring during this process. First, the initial kinks effectively act as static external charges, whereas the connecting string may display non-trivial dynamics and stron quantum correlations. To understand this motion, a kinetically constrained model was derived. Within this effective description, we were able to obtain a bound on the maximal number of kinks that can be dynamically generated, and, in some cases, a quantitative estimate for the timescale of final string breaking. As an important remark, we observed that this effective model in the resonant subspace imposes strong kinetic constraints, which may lead to significantly large timescales for the eventual string breaking. As pointed out in the concluding section of Chapter 5, a natural question to be addressed in future investigations is precisely to what extent the observed slow string breaking dynamics can be related to the slow relaxation observed previously in kinetically constrained models [31, 110, 112, 118, 123, 124, 126–128, 131, 169, 303–306].

As mentioned before (see particularly Sections 2.3.1 and 5.1.1), the quantum Ising models considered in this part share deep connections with certain LGTs (see also Refs. [76, 103]). While such connections highlight the relevance of our findings to the field of nonequilibrium dynamics in LGTs, our analysis can equally be directly applied to LGTs themselves as well, as pointed out in Section 5.5. For instance, the study of the constrained dynamics in the resonant subspace of LGTs could be particularly interesting. Naturally, the extension towards higher dimensions remains one of the main goals for future research. However, here, let us mention again that for such higher-dimensional systems, it has been found that long strings connecting far distant static charges can be effectively treated as one-dimensional objects [307]. The latter observation might also make our work directly relevant to more realistic scenarios in high-energy physics. On the other hand, the fact that the phenomenology of string breaking dynamics can also be realized in quantum Ising chains can be very useful for the experimental accessibility of this phenomenon. In effect, as we have mentioned in Chapter 1 and Section 5.5, the dynamics in quantum spin chains has already been successfully studied in various quantum simulator experiments [167, 169–172, 174–176, 179, 181]. In contrast, the quantum simulation of LGTs is a more challenging problem due to the difficulty of experimentally enforcing gauge invariance, with, however, a few remarkable pioneering efforts [11, 33–43]. In Section 5.5, we have discussed some routes for the possible implementation of the studied Ising models (and the measurement of the relevant observables) in Rydberg-atom and trapped-ion quantum simulators within the current scope of technology. Further, in Section 5.3.4, we have explained how the timescales for string breaking could be tuned to adapt to what is currently possible experimentally. In this respect, let us mention again that the constrained dynamics taking place during the first stage of string breaking might be certainly experimentally observable.

All in all, we remain certain that the problems addressed in this work clearly show the type of prolific phenomenology appearing in the study of nonequilibrium dynamics in LGTs. Moreover, we believe that our observations, analysis, as well as the tools developed here could serve as starting point and/or motivation to tackle other interesting problems in the realms of LGT and quantum many-body dynamics.

Appendix A

Schmidt decomposition and entanglement entropy

The singular value decomposition used in Chapter 3 for the construction of MPS and MPO, is also a fundamental ingredient for another important factorization, the so-called *Schmidt decomposition*, which in turn is useful for computing a measurement of entanglement in the form of the *von Neumann entropy*, a quantity of interest in the characterization of the dynamics discussed in Chapter 5. This is how it works. Let us consider a bipartition of our system as schematically shown in Fig. A.1. We can then write a general pure state for the whole system as

$$|\psi\rangle = \sum_{i=1}^{\dim(\mathscr{H}_L)} \sum_{j=1}^{\dim(\mathscr{H}_R)} a_{ij} |i\rangle_L |j\rangle_R, \tag{A.1}$$

where $\mathscr{H}_{L/R}$ denotes the Hilbert space of the subsystem L/R, with orthonormal basis $\{|i\rangle_L\}$ and $\{|j\rangle_R\}$, respectively. Note that the Hilbert space of the whole system is $\mathscr{H} = \mathscr{H}_L \otimes \mathscr{H}_R$. We also note that the two-index objects a_{ij} can be regarded as the entries of a matrix A, for which we can use the SVD formula (3.21), so that we get

$$|\psi\rangle = \sum_{i=1}^{\dim(\mathscr{H}_L)} \sum_{j=1}^{\dim(\mathscr{H}_R)} \sum_{\alpha=1}^{r} U_{i\alpha} \Sigma_\alpha V^*_{j\alpha} |i\rangle_L |j\rangle_R, \tag{A.2}$$

where r is the rank of A and gives the number of nonzero singular values. Defining

$$|\alpha\rangle_L := \sum_{i=1}^{\dim(\mathscr{H}_L)} U_{i\alpha} |i\rangle_L, \qquad |\alpha\rangle_R := \sum_{j=1}^{\dim(\mathscr{H}_R)} V^*_{j\alpha} |j\rangle_R, \tag{A.3}$$

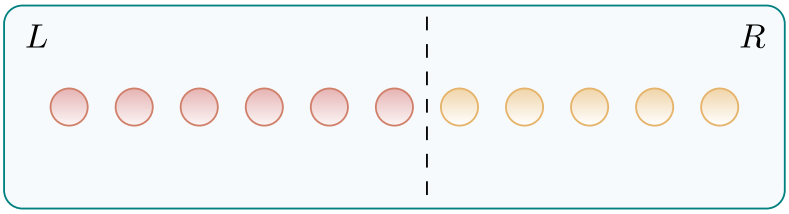

Figure A.1: Schematic illustration of a partition of a one-dimensional lattice into two subsystems L and R.

we arrive at the Schmidt decomposition:

$$|\psi\rangle = \sum_{\alpha=1}^{r} \Sigma_\alpha |\alpha\rangle_L |\alpha\rangle_R. \tag{A.4}$$

It is important to notice that the sets $\{|\alpha\rangle_{L/R}\}$ also form orthonomal bases due to the properties of U and V.

The importance of the Schmidt decomposition resides on the fact that it gives access to a direct readout of the *entanglement* of the quantum state under consideration, which gives us a measurement of the amount of *non-local* information and *non-classical* correlations that are contained in such a state. To see how to access the entanglement properties of a state, let us consider the reduced density operators of the subsystems L and R, namely

$$\rho_L := \mathrm{Tr}_R|\psi\rangle\langle\psi| = \sum_{\alpha=1}^{r} \Sigma_\alpha^2 |\alpha\rangle_{LL}\langle\alpha|, \qquad \rho_R := \mathrm{Tr}_L|\psi\rangle\langle\psi| = \sum_{\alpha=1}^{r} \Sigma_\alpha^2 |\alpha\rangle_{RR}\langle\alpha|, \tag{A.5}$$

which encode the entire physical content of the subsystems L and R, respectively.

One possible measurement of entanglement is given by the von Neumann entropy [234, 289] of one of the two subsystems, say L,

$$S_L := -\mathrm{Tr}_L\big[\rho_L \ln(\rho_L)\big] = -\sum_{\alpha=1}^{r} \Sigma_\alpha^2 \ln(\Sigma_\alpha^2), \tag{A.6}$$

and likewise for S_R. In either case $S_L = S_R$ because of the eigenvalues identity of the reduced density matrices; see Eq. (A.5).

A very useful application of Eq. (A.6) is that it allows us to understand the maximal amount of entanglement that can be encoded by an MPS.[1] To illustrate this point, let us consider a singlet state of a two-spin-1/2 system, that is,

$$|\psi\rangle = \frac{1}{\sqrt{2}}\Big[|\uparrow\downarrow\rangle - |\downarrow\uparrow\rangle\Big]. \tag{A.7}$$

---

[1] Note that entanglement is basis-dependent. Thus, it is understood that such statements are meant for "a given basis".

A straightforward calculation using Eq. (A.5) shows us that the reduced density matrix for one of the two sites is already in diagonal form, namely, $\rho_1 = \rho_2 = \mathrm{diag}(1/2, 1/2)$. Therefore, Eq. (A.6) yields

$$S_1 = S_2 = -2 \cdot \frac{1}{2} \ln(2^{-1}) = \ln(2). \tag{A.8}$$

On the other hand, it is known [260] that $\ln(2)$ is the maximum entanglement possible for a two-spin state. Further, this is achieved if and only if the reduced density matrices are *maximally mixed* (identical eigenvalues and hence minimal amount of local information). This result can be generalized to reduced density operators of dimension D, that is, an MPS of dimension D as well. We thus have that the maximum entanglement that can be encode by such a state is

$$S_{\mathrm{vN}} = -D \cdot \frac{1}{D} \ln(D^{-1}) = \ln(D). \tag{A.9}$$

Appendix B

Effective Hamiltonian for string breaking dynamics in short-range quantum Ising models

In this Appendix, we explicitly show how to construct the different terms that appear in Eq. (5.6) of Chapter 5. Here we regard the short-range model whose Hamiltonian is given by Eq. (5.1). Let us recall that here we consider a chain of length ℓ, with a magnetic boundary condition imposed at the ends, and that the reference state is the initial string, that is, $|\Psi_0\rangle = \bigotimes_{m=1}^{\ell} |{\downarrow}\rangle_m$.

The projected model in the 0-kink sector reads

$$\mathcal{H}_0 = \mathcal{P}_0 H \mathcal{P}_0 = \mathcal{E}_0 |\Psi_0\rangle\langle\Psi_0|, \tag{B.1}$$

where $\mathcal{P}_0 = |\Psi_0\rangle\langle\Psi_0|$ is the projector onto the 0-kink sector, and $\mathcal{E}_0 = -J(\ell-1) + \ell h_z$ is the energy of the initial string.

Let us now look at the two- and four-kink sectors. Elements of the 2-kink subspace are labeled by two quantum numbers j_1 and j_2, such that $|j_1, j_2\rangle = |{\downarrow} \cdots {\downarrow}_{j_1} {\uparrow} \cdots {\uparrow} {\downarrow}_{j_2} \cdots {\downarrow}\rangle$, with $j_1 = 1, \ldots, \ell-2$ and $j_2 = j_1+2, \ldots, \ell$. The 2-kink projected Hamiltonian acts on $|j_1, j_2\rangle$ as

$$\begin{aligned} \mathcal{H}_2 |j_1, j_2\rangle = \mathcal{E}_2(j_1, j_2)|j_1, j_2\rangle - h_x\big[&|j_1+1, j_2\rangle + |j_1-1, j_2\rangle \\ &+ |j_1, j_2+1\rangle + |j_1, j_2-1\rangle\big], \end{aligned} \tag{B.2}$$

where the diagonal term is $\mathcal{E}_2 = -J(\ell-5) - h_z[\ell - 2(l_1+l_2)]$, and $l_1 = j_1$, $l_2 = \ell - j_2 + 1$ are the lengths of the two resulting strings.

The 4-kink model requires four quantum numbers: $|j_1, j_2, l_2, j_3\rangle = |{\downarrow} \cdots {\downarrow}_{j_1} {\uparrow} \cdots {\uparrow} {\downarrow}_{j_2} \cdots {\downarrow}_{(j_2+l_2-1)} {\uparrow} \cdots {\uparrow} {\downarrow}_{j_3} \cdots {\downarrow}\rangle$, with indices taking the possible values $j_1 = 1, \ldots, \ell-4$,

$j_2 = j_1 + 2, \ldots, \ell - 2$, $j_3 = j_2 + 2, \ldots, \ell$, $l_2 = 1, \ldots, j_3 - j_2 - 1$. The action of the 4-kink projected Hamiltonian on $|j_1, j_2, l_2, j_3\rangle$ is given by

$$\begin{aligned}\mathcal{H}_4|j_1, j_2, l_2, j_3\rangle &= \mathcal{E}_4(j_1, j_2, l_2, j_3)|j_1, j_2, l_2, j_3\rangle - h_x\big[|j_1 + 1, j_2, l_2, j_3\rangle \\ &+ |j_1 - 1, j_2, l_2, j_3\rangle + |j_1, j_2 + 1, l_2 - 1, j_3\rangle + |j_1, j_2 - 1, l_2 + 1, j_3\rangle \\ &+ |j_1, j_2, l_2 + 1, j_3\rangle + |j_1, j_2, l_2 - 1, j_3\rangle + |j_1, j_2, l_2, j_3 + 1\rangle \\ &+ |j_1, j_2, l_2, j_3 - 1\rangle\big], \end{aligned} \tag{B.3}$$

where $\mathcal{E}_4(j_1, j_2, l_2, j_3) = -J(\ell - 9) - h_z[\ell - 2(l_1 + l_2 + l_3)]$, and $l_1 = j_1$, $l_3 = \ell - j_3 + 1$.

The off-diagonal elements of these projected Hamiltonians act as effective hopping terms for the kinks. Yet, in order to fully account for string breaking, we need to take into account the couplings between sectors. Such transitions are induced by the transverse field and are given by

$$\mathcal{V}_{0\to 2} = \mathcal{P}_2 H \mathcal{P}_0 = -h_x \sum_{j_1=1}^{\ell-2} |j_1, j_1 + 2\rangle\langle\Psi_0|, \tag{B.4}$$

and likewise for $\mathcal{V}_{2\to 0}$, so that $\mathcal{V}_{0,2} = \mathcal{V}_{0\to 2} + \mathcal{V}_{2\to 0}$. Analogously, the coupling between the 2- and 4-kink subspaces is given by

$$\begin{aligned}\mathcal{V}_{2\to 4} &= \mathcal{P}_4 H \mathcal{P}_2 \\ &= -h_x \Bigg[\sum_{j_1=1}^{\ell-4} \sum_{j_2=j_1+2}^{\ell-2} \sum_{j_3=j_2+2}^{\ell} |j_1, j_2, 1, j_3\rangle\langle j_1, j_3| \\ &+ \sum_{j_1=1}^{\ell-4} \sum_{j_3=j_1+4}^{\ell} \sum_{l_2=1}^{j_3-j_1-3} |j_1, j_1 + 2, l_2, j_3\rangle\langle j_1 + l_2 + 1, j_3| \\ &+ \sum_{j_1=1}^{\ell-4} \sum_{j_2=j_1+2}^{\ell-2} \sum_{j_3=j_2+2}^{\ell} |j_1, j_2, j_3 - j_2 - 1, j_3\rangle\langle j_1, j_2|\Bigg], \end{aligned} \tag{B.5}$$

and likewise for $\mathcal{V}_{4\to 2}$. Terms involving a higher number of kinks can be derived in a similar manner.

Bibliography

[1] R. Verdel, F. Liu, S. Whitsitt, A. V. Gorshkov, and M. Heyl, Phys. Rev. B **102**, 014308 (2020).

[2] P. Karpov, R. Verdel, Y.-P. Huang, M. Schmitt, and M. Heyl, Phys. Rev. Lett. **126**, 130401 (2021).

[3] R. Verdel, M. Schmitt, Y.-P. Huang, P. Karpov, and M. Heyl, Phys. Rev. B **103**, 165103 (2021).

[4] T. Cheng and L. Li, *Gauge theory of elementary particle physics* (Clarendon Press, Oxford, 1984).

[5] K. Huang, *Quarks, leptons and gauge fields*, 2nd Ed. (World Scientific, Singapore, 1992).

[6] I. Aitchison and A. Hey, *Gauge theories in particle physics. volume ii: qcd and the electroweak theory*, 3rd Ed. (Institute of Physics Publishing, Bristol, 2004).

[7] E. Fradkin, *Field theories of condensed matter physics*, 2nd ed. (Cambridge University Press, 2013).

[8] A. Altland and B. D. Simons, *Condensed matter field theory*, 2nd ed. (Cambridge University Press, 2010).

[9] C. Nayak, S. H. Simon, A. Stern, M. Freedman, and S. Das Sarma, Rev. Mod. Phys. **80**, 1083 (2008).

[10] A. Kitaev, Annals of Physics **303**, 2 (2003).

[11] K. J. Satzinger, Y. Liu, A. Smith, C. Knapp, M. Newman, C. Jones, Z. Chen, C. Quintana, X. Mi, A. Dunsworth, C. Gidney, I. Aleiner, F. Arute, K. Arya, J. Atalaya, R. Babbush, J. C. Bardin, R. Barends, J. Basso, A. Bengtsson, A. Bilmes, M. Broughton, B. B. Buckley, D. A. Buell, B. Burkett, N. Bushnell, B. Chiaro, R. Collins, W. Courtney, S. Demura, A. R. Derk, D. Eppens, C. Erickson, E. Farhi, L. Foaro, A. G. Fowler, B. Foxen, M. Giustina, A. Greene, J. A. Gross, M. P. Harrigan, S. D. Harrington, J. Hilton, S. Hong, T. Huang, W. J. Huggins, L. B. Ioffe, S. V. Isakov, E. Jeffrey, Z. Jiang, D. Kafri, K. Kechedzhi, T. Khattar, S. Kim, P. V. Klimov, A. N. Korotkov, F. Kostritsa, D. Landhuis, P. Laptev, A. Locharla,

E. Lucero, O. Martin, J. R. McClean, M. McEwen, K. C. Miao, M. Mohseni, S. Montazeri, W. Mruczkiewicz, J. Mutus, O. Naaman, M. Neeley, C. Neill, M. Y. Niu, T. E. O'Brien, A. Opremcak, B. Pató, A. Petukhov, N. C. Rubin, D. Sank, V. Shvarts, D. Strain, M. Szalay, B. Villalonga, T. C. White, Z. Yao, P. Yeh, J. Yoo, A. Zalcman, H. Neven, S. Boixo, A. Megrant, Y. Chen, J. Kelly, V. Smelyanskiy, A. Kitaev, M. Knap, F. Pollmann, and P. Roushan, arXiv e-prints, arXiv:2104.01180 (2021).

[12] M. Kaku, *Quantum field theory: a modern introduction* (Oxford Univ. Press, New York, NY, 1993).

[13] J. B. Kogut, Rev. Mod. Phys. **51**, 659 (1979).

[14] L. P. Kadanoff, Rev. Mod. Phys. **49**, 267 (1977).

[15] C Rebbi, *Lattice gauge theories and monte carlo simulations* (World Scientific, Singapore, 1983).

[16] M. Creutz, L. Jacobs, and C. Rebbi, Physics Reports **95**, 201 (1983).

[17] I. Montvay and G. Munster, *Quantum fields on a lattice*, Cambridge Monographs on Mathematical Physics (Cambridge University Press, 1997).

[18] M. Dalmonte and S. Montangero, Contemporary Physics **57**, 388 (2016).

[19] M. C. Banuls, K. Cichy, J. I. Cirac, K. Jansen, and S. Kühn, PoS **LATTICE2018**, 022 (2019).

[20] M. Carmen Bañuls and K. Cichy, Reports on Progress in Physics **83**, 024401, 024401 (2020).

[21] D. Banerjee, M. Dalmonte, M. Müller, E. Rico, P. Stebler, U.-J. Wiese, and P. Zoller, Phys. Rev. Lett. **109**, 175302 (2012).

[22] E. Zohar, J. I. Cirac, and B. Reznik, Phys. Rev. Lett. **110**, 125304 (2013).

[23] U.-J. Wiese, Annalen der Physik **525**, 777 (2013).

[24] L. Tagliacozzo, A. Celi, P. Orland, M. W. Mitchell, and M. Lewenstein, Nature Communications **4**, 2615 (2013).

[25] E. Zohar, J. I. Cirac, and B. Reznik, Phys. Rev. A **88**, 023617 (2013).

[26] D. Marcos, P. Widmer, E. Rico, M. Hafezi, P. Rabl, U.-J. Wiese, and P. Zoller, Annals of Physics **351**, 634 (2014).

[27] E. Zohar, J. I. Cirac, and B. Reznik, Reports on Progress in Physics **79**, 014401 (2015).

[28] C. Muschik, M. Heyl, E. Martinez, T. Monz, P. Schindler, B. Vogell, M. Dalmonte, P. Hauke, R. Blatt, and P. Zoller, New Journal of Physics **19**, 103020 (2017).

[29] J. Bender, E. Zohar, A. Farace, and J. I. Cirac, New Journal of Physics **20**, 093001 (2018).

[30] M. C. Bañuls, R. Blatt, J. Catani, A. Celi, J. I. Cirac, M. Dalmonte, L. Fallani, K. Jansen, M. Lewenstein, S. Montangero, C. A. Muschik, B. Reznik, E. Rico, L. Tagliacozzo, K. Van Acoleyen, F. Verstraete, U.-J. Wiese, M. Wingate, J. Zakrzewski, and P. Zoller, The European Physical Journal D **74**, 165 (2020).

[31] F. M. Surace, P. P. Mazza, G. Giudici, A. Lerose, A. Gambassi, and M. Dalmonte, Phys. Rev. X **10**, 021041 (2020).

[32] T. Armon, S. Ashkenazi, G. García-Moreno, A. González-Tudela, and E. Zohar, arXiv e-prints, arXiv:2107.13024 (2021).

[33] E. A. Martinez, C. A. Muschik, P. Schindler, D. Nigg, A. Erhard, M. Heyl, P. Hauke, M. Dalmonte, T. Monz, P. Zoller, and R. Blatt, Nature **534**, 516 (2016).

[34] H.-N. Dai, B. Yang, A. Reingruber, H. Sun, X.-F. Xu, Y.-A. Chen, Z.-S. Yuan, and J.-W. Pan, Nature Physics **13**, 1195 (2017).

[35] L. W. Clark, B. M. Anderson, L. Feng, A. Gaj, K. Levin, and C. Chin, Phys. Rev. Lett. **121**, 030402 (2018).

[36] N. Klco, E. F. Dumitrescu, A. J. McCaskey, T. D. Morris, R. C. Pooser, M. Sanz, E. Solano, P. Lougovski, and M. J. Savage, Phys. Rev. A **98**, 032331 (2018).

[37] C. Kokail, C. Maier, R. van Bijnen, T. Brydges, M. K. Joshi, P. Jurcevic, C. A. Muschik, P. Silvi, R. Blatt, C. F. Roos, and P. Zoller, Nature **569**, 355 (2019).

[38] F. Görg, K. Sandholzer, J. Minguzzi, R. Desbuquois, M. Messer, and T. Esslinger, Nature Physics **15**, 1161 (2019).

[39] C. Schweizer, F. Grusdt, M. Berngruber, L. Barbiero, E. Demler, N. Goldman, I. Bloch, and M. Aidelsburger, Nature Physics **15**, 1168 (2019).

[40] A. Mil, T. V. Zache, A. Hegde, A. Xia, R. P. Bhatt, M. K. Oberthaler, P. Hauke, J. Berges, and F. Jendrzejewski, Science **367**, 1128 (2020).

[41] B. Yang, H. Sun, R. Ott, H.-Y. Wang, T. V. Zache, J. C. Halimeh, Z.-S. Yuan, P. Hauke, and J.-W. Pan, Nature **587**, 392 (2020).

[42] Z.-Y. Zhou, G.-X. Su, J. C. Halimeh, R. Ott, H. Sun, P. Hauke, B. Yang, Z.-S. Yuan, J. Berges, and J.-W. Pan, arXiv e-prints, arXiv:2107.13563 (2021).

[43] G. Semeghini, H. Levine, A. Keesling, S. Ebadi, T. T. Wang, D. Bluvstein, R. Verresen, H. Pichler, M. Kalinowski, R. Samajdar, A. Omran, S. Sachdev, A. Vishwanath, M. Greiner, V. Vuletic, and M. D. Lukin, arXiv e-prints, arXiv:2104.04119 (2021).

[44] D. S. Rokhsar and S. A. Kivelson, Phys. Rev. Lett. **61**, 2376 (1988).

[45] R. Moessner and S. L. Sondhi, Phys. Rev. Lett. **86**, 1881 (2001).

[46] R. Moessner, S. L. Sondhi, and E. Fradkin, Phys. Rev. B **65**, 024504 (2001).

[47] G. Misguich, D. Serban, and V. Pasquier, Phys. Rev. Lett. **89**, 137202 (2002).

[48] M. Hermele, M. P. A. Fisher, and L. Balents, Phys. Rev. B **69**, 064404 (2004).

[49] N. Shannon, G. Misguich, and K. Penc, Phys. Rev. B **69**, 220403(R) (2004).

[50] L. Savary and L. Balents, Reports on Progress in Physics **80**, 016502 (2016).

[51] A. Lopez and E. Fradkin, Phys. Rev. B **44**, 5246 (1991).

[52] S. Sachdev, Reports on Progress in Physics **82**, 014001 (2018).

[53] I. Ichinose and T. Matsui, Modern Physics Letters B **28**, 1430012 (2014).

[54] B. M. McCoy and T. T. Wu, Phys. Lett. B **72**, 219 (1977).

[55] B. M. McCoy and T. T. Wu, Phys. Rev. D **18**, 1259 (1978).

[56] M. Greiter, Phys. Rev. B **66**, 054505 (2002).

[57] S. B. Rutkevich, J. Stat. Phys. **131**, 917 (2008).

[58] B. Lake, A. M. Tsvelik, S. Notbohm, D. A. Tennant, T. G. Perring, M. Reehuis, C. Sekar, G. Krabbes, and B. Büchner, Nature Physics **6**, 50 (2010).

[59] R. Coldea, D. A. Tennant, E. M. Wheeler, E. Wawrzynska, D. Prabhakaran, M. Telling, K. Habicht, P. Smeibidl, and K. Kiefer, Science **327**, 177 (2010).

[60] S. B. Rutkevich, J. Stat. Mech. **2010**, P07015 (2010).

[61] I. Bose and A. K. Pal, Eur. Phys. J. B **77**, 139 (2010).

[62] J. A. Kjäll, F. Pollmann, and J. E. Moore, Phys. Rev. B **83**, 020407 (2011).

[63] Z. Cai, C. Wu, and U. Schollwöck, Phys. Rev. B **85**, 075102 (2012).

[64] C. M. Morris, R. Valdés Aguilar, A. Ghosh, S. M. Koohpayeh, J. Krizan, R. J. Cava, O. Tchernyshyov, T. M. McQueen, and N. P. Armitage, Phys. Rev. Lett. **112**, 137403 (2014).

[65] B. Grenier, S. Petit, V. Simonet, E. Canévet, L.-P. Regnault, S. Raymond, B. Canals, C. Berthier, and P. Lejay, Phys. Rev. Lett. **114**, 017201 (2015).

[66] Z. Wang, J. Wu, S. Xu, W. Yang, C. Wu, A. K. Bera, A. T. M. N. Islam, B. Lake, D. Kamenskyi, P. Gogoi, H. Engelkamp, N. Wang, J. Deisenhofer, and A. Loidl, Phys. Rev. B **94**, 125130 (2016).

[67] A. K. Bera, B. Lake, F. H. L. Essler, L. Vanderstraeten, C. Hubig, U. Schollwöck, A. T. M. N. Islam, A. Schneidewind, and D. L. Quintero-Castro, Phys. Rev. B **96**, 054423 (2017).

[68] M. Kormos, M. Collura, G. Takács, and P. Calabrese, Nature Physics **13**, 246 (2017).

[69] M. C. Diamantini, C. A. Trugenberger, and V. M. Vinokur, Communications Physics **1**, 77 (2018).

[70] F. Liu, R. Lundgren, P. Titum, G. Pagano, J. Zhang, C. Monroe, and A. V. Gorshkov, Phys. Rev. Lett. **122**, 150601 (2019).

[71] P. P. Mazza, G. Perfetto, A. Lerose, M. Collura, and A. Gambassi, Phys. Rev. B **99**, 180302(R) (2019).

[72] A. Lerose, B. Zunkovic, A. Silva, and A. Gambassi, Phys. Rev. B **99**, 121112(R) (2019).

[73] T. Sulejmanpasic, H. Shao, A. W. Sandvik, and M. Ünsal, Phys. Rev. Lett. **119**, 091601 (2017).

[74] W. J. Gannon, I. A. Zaliznyak, L. S. Wu, A. E. Feiguin, A. M. Tsvelik, F. Demmel, Y. Qiu, J. R. D. Copley, M. S. Kim, and M. C. Aronson, Nature Communications **10**, 1123 (2019).

[75] L. Vanderstraeten, E. Wybo, N. Chepiga, F. Verstraete, and F. Mila, Phys. Rev. B **101**, 115138 (2020).

[76] A. Lerose, F. M. Surace, P. P. Mazza, G. Perfetto, M. Collura, and A. Gambassi, Phys. Rev. B **102**, 041118(R) (2020).

[77] J. Vovrosh, H. Zhao, J. Knolle, and A. Bastianello, arXiv e-prints, arXiv:2108.03976 (2021).

[78] J. Kogut and L. Susskind, Phys. Rev. D **9**, 3501 (1974).

[79] J. Schwinger, Phys. Rev. **82**, 664 (1951).

[80] N. B. Narozhny and A. M. Fedotov, The European Physical Journal Special Topics **223**, 1083 (2014).

[81] G. Baur, K. Hencken, and D. Trautmann, Physics Reports **453**, 1 (2007).

[82] O. Philipsen and H. Wittig, Phys. Rev. Lett. **81**, 4056 (1998).

[83] O. Philipsen and H. Wittig, Phys. Lett. B **451**, 146 (1999).

[84] F. Knechtli and R. Sommer, Phys. Lett. B **440**, 345 (1998).

[85] F. Knechtli and R. Sommer, Nucl. Phys. B **590**, 309 (2000).

[86] M. Lüscher and P. Weisz, J. High Energy Phys. **2002**, 049 (2002).

[87] F. Gliozzi and A. Rago, Nucl. Phys. B **714**, 91 (2005).

[88] G. S. Bali, H. Neff, T. Düssel, T. Lippert, and K. Schilling, Phys. Rev. D **71**, 114513 (2005).

[89] M. Pepe and U.-J. Wiese, Phys. Rev. Lett. **102**, 191601 (2009).

[90] F. Hebenstreit, J. Berges, and D. Gelfand, Phys. Rev. Lett. **111**, 201601 (2013).

[91] V. Kasper, F. Hebenstreit, and J. Berges, Phys. Rev. D **90**, 025016 (2014).

[92] S. Kühn, E. Zohar, J. I. Cirac, and M. C. Bañuls, J. High Energy Phys. **2015**, 130 (2015).

[93] T. Pichler, M. Dalmonte, E. Rico, P. Zoller, and S. Montangero, Phys. Rev. X **6**, 011023 (2016).

[94] V. Kasper, F. Hebenstreit, M. Oberthaler, and J. Berges, Phys. Lett. B **760**, 742 (2016).

[95] B. Buyens, J. Haegeman, F. Hebenstreit, F. Verstraete, and K. Van Acoleyen, Phys. Rev. D **96**, 114501 (2017).

[96] Y. Kuno, S. Sakane, K. Kasamatsu, I. Ichinose, and T. Matsui, Phys. Rev. D **95**, 094507 (2017).

[97] P. Sala, T. Shi, S. Kühn, M. C. Bañuls, E. Demler, and J. I. Cirac, Phys. Rev. D **98**, 034505 (2018).

[98] D. Spitz and J. Berges, Phys. Rev. D **99**, 036020 (2019).

[99] J. Park, Y. Kuno, and I. Ichinose, Phys. Rev. A **100**, 013629 (2019).

[100] G. Magnifico, M. Dalmonte, P. Facchi, S. Pascazio, F. V. Pepe, and E. Ercolessi, Quantum **4**, 281 (2020).

[101] S. Notarnicola, M. Collura, and S. Montangero, Phys. Rev. Research **2**, 013288 (2020).

[102] T. Chanda, J. Zakrzewski, M. Lewenstein, and L. Tagliacozzo, Phys. Rev. Lett. **124**, 180602 (2020).

[103] P. I. Karpov, G. Y. Zhu, M. P. Heller, and M. Heyl, arXiv e-prints, arXiv:2011.11624 (2020).

[104] F. M. Surace and A. Lerose, New Journal of Physics **23**, 062001 (2021).

[105] A. Milsted, J. Liu, J. Preskill, and G. Vidal, arXiv e-prints, arXiv:2012.07243 (2020).

[106] D. G. Figueroa, A. Florio, and M. Shaposhnikov, J. High Energy Phys. **2019**, 142 (2019).

[107] I. H. Kim and J. Haah, Phys. Rev. Lett. **116**, 027202 (2016).

[108] A. Smith, J. Knolle, D. L. Kovrizhin, and R. Moessner, Phys. Rev. Lett. **118**, 266601 (2017).

[109] A. Smith, J. Knolle, R. Moessner, and D. L. Kovrizhin, Phys. Rev. Lett. **119**, 176601 (2017).

[110] M. Brenes, M. Dalmonte, M. Heyl, and A. Scardicchio, Phys. Rev. Lett. **120**, 030601 (2018).

[111] A. Smith, J. Knolle, R. Moessner, and D. L. Kovrizhin, Phys. Rev. B **97**, 245137 (2018).

[112] A. Russomanno, S. Notarnicola, F. M. Surace, R. Fazio, M. Dalmonte, and M. Heyl, Phys. Rev. Research **2**, 012003 (2020).

[113] I. Papaefstathiou, A. Smith, and J. Knolle, Phys. Rev. B **102**, 165132 (2020).

[114] P. A. McClarty, M. Haque, A. Sen, and J. Richter, Phys. Rev. B **102**, 224303 (2020).

[115] D. Basko, I. Aleiner, and B. Altshuler, Annals of Physics **321**, 1126 (2006).

[116] R. Nandkishore and D. A. Huse, Annual Review of Condensed Matter Physics **6**, 15 (2015).

[117] D. A. Abanin, E. Altman, I. Bloch, and M. Serbyn, Rev. Mod. Phys. **91**, 021001 (2019).

[118] C. J. Turner, A. A. Michailidis, D. A. Abanin, M. Serbyn, and Z. Papić, Nature Physics **14**, 745 (2018).

[119] C.-J. Lin and O. I. Motrunich, Phys. Rev. Lett. **122**, 173401 (2019).

[120] T. Iadecola and M. Schecter, Phys. Rev. B **101**, 024306 (2020).

[121] A. Hudomal, I. Vasić, N. Regnault, and Z. Papić, Communications Physics **3**, 99 (2020).

[122] H. Zhao, J. Vovrosh, F. Mintert, and J. Knolle, Phys. Rev. Lett. **124**, 160604 (2020).

[123] A. Prem, J. Haah, and R. Nandkishore, Phys. Rev. B **95**, 155133 (2017).

[124] P. Sala, T. Rakovszky, R. Verresen, M. Knap, and F. Pollmann, Phys. Rev. X **10**, 011047 (2020).

[125] S. Pai and M. Pretko, Phys. Rev. Lett. **123**, 136401 (2019).

[126] S. Pai, M. Pretko, and R. M. Nandkishore, Phys. Rev. X **9**, 021003 (2019).

[127] V. Khemani, M. Hermele, and R. Nandkishore, Phys. Rev. B **101**, 174204 (2020).

[128] M. van Horssen, E. Levi, and J. P. Garrahan, Phys. Rev. B **92**, 100305(R) (2015).

[129] N. Pancotti, G. Giudice, J. I. Cirac, J. P. Garrahan, and M. C. Bañuls, Phys. Rev. X **10**, 021051 (2020).

[130] S. Roy and A. Lazarides, Phys. Rev. Research **2**, 023159 (2020).

[131] Z. Lan, M. van Horssen, S. Powell, and J. P. Garrahan, Phys. Rev. Lett. **121**, 040603 (2018).

[132] Z. Fodor and C. Hoelbling, Rev. Mod. Phys. **84**, 449 (2012).

[133] A. Nakamura, Phys. Lett. B **149**, 391 (1984).

[134] K. Fukushima and T. Hatsuda, Reports on Progress in Physics **74**, 014001 (2010).

[135] H.-T. Ding, F. Karsch, and S. Mukherjee, International Journal of Modern Physics E **24**, 1530007 (2015).

[136] G. S. Bali and K. Schilling, Phys. Rev. D **46**, 2636 (1992).

[137] R. Sommer, Nuclear Physics B **411**, 839 (1994).

[138] G. S. Bali, H. Neff, T. Düssel, T. Lippert, and K. Schilling, Phys. Rev. D **71**, 114513 (2005).

[139] T. M. R. Byrnes, P. Sriganesh, R. J. Bursill, and C. J. Hamer, Phys. Rev. D **66**, 013002 (2002).

[140] T. Sugihara, J. High Energy Phys. **2005**, 022 (2005).

[141] M. C. Bañuls, K. Cichy, J. I. Cirac, and K. Jansen, J. High Energy Phys. **2013**, 158 (2013).

[142] L. Tagliacozzo, A. Celi, and M. Lewenstein, Phys. Rev. X **4**, 041024 (2014).

[143] E. Rico, T. Pichler, M. Dalmonte, P. Zoller, and S. Montangero, Phys. Rev. Lett. **112**, 201601 (2014).

[144] B. Buyens, J. Haegeman, K. Van Acoleyen, H. Verschelde, and F. Verstraete, Phys. Rev. Lett. **113**, 091601 (2014).

[145] T. Felser, P. Silvi, M. Collura, and S. Montangero, Phys. Rev. X **10**, 041040 (2020).

[146] D. Robaina, M. C. Bañuls, and J. I. Cirac, Phys. Rev. Lett. **126**, 050401 (2021).

[147] G. Magnifico, T. Felser, P. Silvi, and S. Montangero, Nature Communications **12**, 3600 (2021).

[148] E. A. Calzetta and B.-L. B. Hu, *Nonequilibrium Quantum Field Theory*, Cambridge Monographs on Mathematical Physics (Cambridge University Press, 2008).

[149] M. Troyer and U.-J. Wiese, Phys. Rev. Lett. **94**, 170201 (2005).

[150] J. I. Cirac and P. Zoller, Nature Physics **8**, 264 (2012).

[151] I. M. Georgescu, S. Ashhab, and F. Nori, Rev. Mod. Phys. **86**, 153 (2014).

[152] S. Lloyd, Science **273**, 1073 (1996).

[153] D. Jaksch, C. Bruder, J. I. Cirac, C. W. Gardiner, and P. Zoller, Phys. Rev. Lett. **81**, 3108 (1998).

[154] D. Porras and J. I. Cirac, Phys. Rev. Lett. **92**, 207901 (2004).

[155] M. Lewenstein, A. Sanpera, and V. Ahufinger, *Ultracold atoms in optical lattices: simulating quantum many-body systems* (OUP Oxford, 2012).

[156] J. I. Cirac and P. Zoller, Phys. Rev. Lett. **74**, 4091 (1995).

[157] R. Blatt and C. F. Roos, Nature Physics **8**, 277 (2012).

[158] A. A. Houck, H. E. Türeci, and J. Koch, Nature Physics **8**, 292 (2012).

[159] A. Aspuru-Guzik and P. Walther, Nature Physics **8**, 285 (2012).

[160] M. Greiner, O. Mandel, T. W. Hänsch, and I. Bloch, Nature **419**, 51 (2002).

[161] T. Kinoshita, T. Wenger, and D. S. Weiss, Nature **440**, 900 (2006).

[162] W. S. Bakr, A. Peng, M. E. Tai, R. Ma, J. Simon, J. I. Gillen, S. Fölling, L. Pollet, and M. Greiner, Science **329**, 547 (2010).

[163] J. Simon, W. S. Bakr, R. Ma, M. E. Tai, P. M. Preiss, and M. Greiner, Nature **472**, 307 (2011).

[164] S. Hild, T. Fukuhara, P. Schauß, J. Zeiher, M. Knap, E. Demler, I. Bloch, and C. Gross, Phys. Rev. Lett. **113**, 147205 (2014).

[165] S. S. Kondov, W. R. McGehee, W. Xu, and B. DeMarco, Phys. Rev. Lett. **114**, 083002 (2015).

[166] H. Labuhn, D. Barredo, S. Ravets, S. de Léséleuc, T. Macrì, T. Lahaye, and A. Browaeys, Nature **534**, 667 (2016).

[167] J. Smith, A. Lee, P. Richerme, B. Neyenhuis, P. W. Hess, P. Hauke, M. Heyl, D. A. Huse, and C. Monroe, Nature Physics **12**, 907 (2016).

[168] J.-y. Choi, S. Hild, J. Zeiher, P. Schauß, A. Rubio-Abadal, T. Yefsah, V. Khemani, D. A. Huse, I. Bloch, and C. Gross, Science **352**, 1547 (2016).

[169] H. Bernien, S. Schwartz, A. Keesling, H. Levine, A. Omran, H. Pichler, S. Choi, A. S. Zibrov, M. Endres, M. Greiner, V. Vuletić, and M. D. Lukin, Nature **551**, 579 (2017).

[170] P. Jurcevic, H. Shen, P. Hauke, C. Maier, T. Brydges, C. Hempel, B. P. Lanyon, M. Heyl, R. Blatt, and C. F. Roos, Phys. Rev. Lett. **119**, 080501 (2017).

[171] M. Marcuzzi, J. Minář, D. Barredo, S. de Léséleuc, H. Labuhn, T. Lahaye, A. Browaeys, E. Levi, and I. Lesanovsky, Phys. Rev. Lett. **118**, 063606 (2017).

[172] J. Zhang, G. Pagano, P. W. Hess, A. Kyprianidis, P. Becker, H. Kaplan, A. V. Gorshkov, Z. X. Gong, and C. Monroe, Nature (London) **551**, 601 (2017).

[173] P. Bordia, H. Lüschen, S. Scherg, S. Gopalakrishnan, M. Knap, U. Schneider, and I. Bloch, Phys. Rev. X **7**, 041047 (2017).

[174] J. Zeiher, J.-y. Choi, A. Rubio-Abadal, T. Pohl, R. van Bijnen, I. Bloch, and C. Gross, Phys. Rev. X **7**, 041063 (2017).

[175] V. Lienhard, S. de Léséleuc, D. Barredo, T. Lahaye, A. Browaeys, M. Schuler, L.-P. Henry, and A. M. Läuchli, Phys. Rev. X **8**, 021070 (2018).

[176] S. de Léséleuc, S. Weber, V. Lienhard, D. Barredo, H. P. Büchler, T. Lahaye, and A. Browaeys, Phys. Rev. Lett. **120**, 113602 (2018).

[177] D. Barredo, V. Lienhard, S. de Léséleuc, T. Lahaye, and A. Browaeys, Nature **561**, 79 (2018).

[178] S. Erne, R. Bücker, T. Gasenzer, J. Berges, and J. Schmiedmayer, Nature **563**, 225 (2018).

[179] E. Guardado-Sanchez, P. T. Brown, D. Mitra, T. Devakul, D. A. Huse, P. Schauß, and W. S. Bakr, Phys. Rev. X **8**, 021069 (2018).

[180] E. Guardado-Sanchez, A. Morningstar, B. M. Spar, P. T. Brown, D. A. Huse, and W. S. Bakr, Phys. Rev. X **10**, 011042 (2020).

[181] W. L. Tan, P. Becker, F. Liu, G. Pagano, K. S. Collins, A. De, L. Feng, H. B. Kaplan, A. Kyprianidis, R. Lundgren, W. Morong, S. Whitsitt, A. V. Gorshkov, and C. Monroe, Nature Physics, `10.1038/s41567-021-01194-3` (2021).

[182] D Banerjee, F.-J. Jiang, P Widmer, and U.-J. Wiese, Journal of Statistical Mechanics: Theory and Experiment **2013**, P12010 (2013).

[183] S Chandrasekharan and U.-J Wiese, Nuclear Physics B **492**, 455 (1997).

[184] W. De Roeck and F. m. c. Huveneers, Phys. Rev. B **95**, 155129 (2017).

[185] W. De Roeck and J. Z. Imbrie, Philosophical Transactions of the Royal Society A: Mathematical, Physical and Engineering Sciences **375**, 20160422 (2017).

[186] T. B. Wahl, A. Pal, and S. H. Simon, Nature Physics **15**, 164 (2019).

[187] M. Schmitt and M. Heyl, SciPost Phys. **4**, 013 (2018).

[188] G. Carleo and M. Troyer, Science **355**, 602 (2017).

[189] M. Schmitt and M. Heyl, Phys. Rev. Lett. **125**, 100503 (2020).

[190] A. Celi, B. Vermersch, O. Viyuela, H. Pichler, M. D. Lukin, and P. Zoller, Phys. Rev. X **10**, 021057 (2020).

[191] A. W. Glaetzle, M. Dalmonte, R. Nath, I. Rousochatzakis, R. Moessner, and P. Zoller, Phys. Rev. X **4**, 041037 (2014).

[192] K. G. Wilson, Phys. Rev. D **10**, 2445 (1974).

[193] A. Polyakov, Phys. Lett. B **59**, 82 (1975).

[194] F. J. Wegner, Journal of Mathematical Physics **12**, 2259 (1971).

[195] G. De las Cuevas, W. Dür, H. J. Briegel, and M. A. Martin-Delgado, Phys. Rev. Lett. **102**, 230502 (2009).

[196] J. B. Kogut, Rev. Mod. Phys. **55**, 775 (1983).

[197] J. Kogut and L. Susskind, Phys. Rev. D **11**, 395 (1975).

[198] E. Fradkin and L. Susskind, Phys. Rev. D **17**, 2637 (1978).

[199] D. Horn, M. Weinstein, and S. Yankielowicz, Phys. Rev. D **19**, 3715 (1979).

[200] R. Balian, J. M. Drouffe, and C. Itzykson, Phys. Rev. D **11**, 2098 (1975).

[201] L. Susskind, Phys. Rev. D **16**, 3031 (1977).

[202] B. Bernevig and T. Hughes, *Topological insulators and topological superconductors* (Princeton University Press, 2013).

[203] D. R. Hofstadter, Phys. Rev. B **14**, 2239 (1976).

[204] Y.-P. Huang, D. Banerjee, and M. Heyl, Phys. Rev. Lett. **122**, 250401 (2019).

[205] P. Emonts and E. Zohar, SciPost Phys. Lect. Notes, 12 (2020).

[206] D. Horn, Phys. Lett. B **100**, 149 (1981).

[207] P. Orland and D. Rohrlich, Nuclear Physics B **338**, 647 (1990).

[208] R. Brower, S. Chandrasekharan, and U.-J. Wiese, Phys. Rev. D **60**, 094502 (1999).

[209] P. Anderson, Materials Research Bulletin **8**, 153 (1973).

[210] J. V. José, L. P. Kadanoff, S. Kirkpatrick, and D. R. Nelson, Phys. Rev. B **16**, 1217 (1977).

[211] J. M. Kosterlitz and D. J. Thouless, Journal of Physics C: Solid State Physics **6**, 1181 (1973).

[212] S. Elitzur, Phys. Rev. D **12**, 3978 (1975).

[213] M. A. Levin and X.-G. Wen, Phys. Rev. B **71**, 045110 (2005).

[214] A. H. Guth, Phys. Rev. D **21**, 2291 (1980).

[215] M. E. Peskin, Phys. Lett. B **94**, 161 (1980).

[216] S. Chandrasekharan, Nuclear Physics B - Proceedings Supplements **73**, 739 (1999).

[217] R. P. Feynman, International Journal of Theoretical Physics **21**, 467 (1982).

[218] J. C. Halimeh and P. Hauke, Phys. Rev. Lett. **125**, 030503 (2020).

[219] K. Stannigel, P. Hauke, D. Marcos, M. Hafezi, S. Diehl, M. Dalmonte, and P. Zoller, Phys. Rev. Lett. **112**, 120406 (2014).

[220] L. Barbiero, C. Schweizer, M. Aidelsburger, E. Demler, N. Goldman, and F. Grusdt, Science Advances **5**, `10.1126/sciadv.aav7444` (2019).

[221] D. González-Cuadra, A. Dauphin, P. R. Grzybowski, M. Lewenstein, and A. Bermudez, Phys. Rev. B **102**, 245137 (2020).

[222] D. González-Cuadra, A. Bermudez, P. R. Grzybowski, M. Lewenstein, and A. Dauphin, Nature Communications **10**, 2694 (2019).

[223] M. D. Lukin, M. Fleischhauer, R. Cote, L. M. Duan, D. Jaksch, J. I. Cirac, and P. Zoller, Phys. Rev. Lett. **87**, 037901 (2001).

[224] M. A. Cazalilla and J. B. Marston, Phys. Rev. Lett. **88**, 256403 (2002).

[225] G. Vidal, Phys. Rev. Lett. **91**, 147902 (2003).

[226] G. Vidal, Phys. Rev. Lett. **93**, 040502 (2004).

[227] A. J. Daley, C. Kollath, U. Schollwöck, and G. Vidal, J. Stat. Mech., P04005 (2004).

[228] S. R. White and A. E. Feiguin, Phys. Rev. Lett. **93**, 076401 (2004).

[229] F. Verstraete, J. J. García-Ripoll, and J. I. Cirac, Phys. Rev. Lett. **93**, 207204 (2004).

[230] M. Zwolak and G. Vidal, Phys. Rev. Lett. **93**, 207205 (2004).

[231] S. Paeckel, T. Köhler, A. Swoboda, S. R. Manmana, U. Schollwöck, and C. Hubig, Annals of Physics **411**, 167998 (2019).

[232] D. Perez-Garcia, F. Verstraete, M. M. Wolf, and J. I. Cirac, Quantum Info. Comput. **7**, 401–430 (2007).

[233] F. Verstraete, V. Murg, and J. Cirac, Advances in Physics **57**, 143 (2008).

[234] U. Schollwöck, Annals of Physics **326**, January 2011 Special Issue, 96 (2011).

[235] S. Czischek, M. Gärttner, and T. Gasenzer, Phys. Rev. B **98**, 024311 (2018).

[236] G. Fabiani and J. H. Mentink, SciPost Phys. **7**, 4 (2019).

[237] G. Fabiani and J. H. Mentink, SciPost Phys. **7**, 4 (2019).

[238] I. López Gutiérrez and C. B. Mendl, arXiv e-prints, arXiv:1912.08831 (2019).

[239] H. Burau and M. Heyl, Phys. Rev. Lett. **127**, 050601 (2021).

[240] S.-H. Lin and F. Pollmann, arXiv e-prints, arXiv:2104.10696 (2021).

[241] D. Hofmann, G. Fabiani, J. H. Mentink, G. Carleo, and M. A. Sentef, arXiv e-prints, arXiv:2105.01054 (2021).

[242] A. W. Sandvik, AIP Conference Proceedings **1297**, 135 (2010).

[243] V. Murg, F. Verstraete, and J. I. Cirac, Phys. Rev. A **75**, 033605 (2007).

[244] J. Hauschild, F. Pollmann, and F. Heidrich-Meisner, Phys. Rev. A **92**, 053629 (2015).

[245] M. P. Zaletel, R. S. K. Mong, C. Karrasch, J. E. Moore, and F. Pollmann, Phys. Rev. B **91**, 165112 (2015).

[246] T. Hashizume, I. P. McCulloch, and J. C. Halimeh, arXiv e-prints, arXiv:1811.09275 (2018).

[247] P. Czarnik, J. Dziarmaga, and P. Corboz, Phys. Rev. B **99**, 035115 (2019).

[248] C. Hubig and J. I. Cirac, SciPost Phys. **6**, 31 (2019).

[249] A. Kshetrimayum, M. Goihl, and J. Eisert, Phys. Rev. B **102**, 235132 (2020).

[250] C. Hubig, A. Bohrdt, M. Knap, F. Grusdt, and J. I. Cirac, SciPost Phys. **8**, 21 (2020).

[251] T. Hashizume, J. C. Halimeh, and I. P. McCulloch, Phys. Rev. B **102**, 035115 (2020).

[252] B. Kloss, D. R. Reichman, and Y. B. Lev, SciPost Phys. **9**, 70 (2020).

[253] J. Richter, T. Heitmann, and R. Steinigeweg, SciPost Phys. **9**, 31 (2020).

[254] P. Kramer and M. Saraceno, *Geometry of the Time-Dependent Variational Principle in Quantum Mechanics* (Springer, Berlin, Heidelberg, 1981).

[255] J.-H. Jung and J. D. Noh, Journal of the Korean Physical Society **76**, 670 (2020).

[256] A. M. Läuchli, J. Sudan, and R. Moessner, Phys. Rev. B **100**, 155142 (2019).

[257] C. Lanczos, Journal of research of the National Bureau of Standards **45**, 255 (1950).

[258] T. J. Park and J. C. Light, The Journal of Chemical Physics **85**, 5870 (1986).

[259] S. R. White, Phys. Rev. Lett. **69**, 2863 (1992).

[260] U. Schollwöck, "DMRG: Ground States, Time Evolution, and Spectral Functions", in *Emergent Phenomena in Correlated Matter*, Vol. 3, edited by E. Pavarini, E. Koch, and U. Schollwöck, Schriften des Forschungszentrums Jülich. Reihe modeling and simulation (Forschungszentrum Jülich GmbH Zentralbibliothek, Verlag, Jülich, Sept. 23, 2013), 16.1–16.34.

[261] E. H. Lieb and D. W. Robinson, Communications in Mathematical Physics **28**, 251 (1972).

[262] M. Fagotti and P. Calabrese, Phys. Rev. A **78**, 010306 (2008).

[263] M. Fishman, S. R. White, and E. Miles Stoudenmire, arXiv e-prints, arXiv:2007.14822 (2020).

[264] F. Becca and S. Sorella, "Variational monte carlo", in *Quantum monte carlo approaches for correlated systems* (Cambridge University Press, 2017), 103–130.

[265] D. Landau and K. Binder, *A guide to monte carlo simulations in statistical physics* (Cambridge University Press, USA, 2005).

[266] R. Jastrow, Phys. Rev. **98**, 1479 (1955).

[267] G. Carleo, F. Becca, M. Schiró, and M. Fabrizio, Scientific Reports **2**, 243 (2012).

[268] G. Carleo, F. Becca, L. Sanchez-Palencia, S. Sorella, and M. Fabrizio, Phys. Rev. A **89**, 031602 (2014).

[269] B. Blaß and H. Rieger, Scientific Reports **6**, 38185 (2016).

[270] G. Carleo, L. Cevolani, L. Sanchez-Palencia, and M. Holzmann, Phys. Rev. X **7**, 031026 (2017).

[271] R. G. Melko, G. Carleo, J. Carrasquilla, and J. I. Cirac, Nature Physics **15**, 887 (2019).

[272] N. Le Roux and Y. Bengio, Neural Computation **20**, 1631 (2008).

[273] R. Kubo, Journal of the Physical Society of Japan **17**, 1100 (1962).

[274] J. Wei and E. Norman, Journal of Mathematical Physics **4**, 575 (1963).

[275] P. Pfeuty, Annals of Physics **57**, 79 (1970).

[276] S. Sachdev, *Quantum phase transitions*, 2nd ed. (Cambridge University Press, Cambridge, 2011).

[277] M. Heyl, A. Polkovnikov, and S. Kehrein, Phys. Rev. Lett. **110**, 135704 (2013).

[278] M. Heyl, Reports on Progress in Physics **81**, 054001 (2018).

[279] M. J. P. Gingras and P. A. McClarty, Reports on Progress in Physics **77**, 056501 (2014).

[280] M. Stern, C. Castelnovo, R. Moessner, V. Oganesyan, and S. Gopalakrishnan, Phys. Rev. B **104**, 115114 (2021).

[281] M. Creutz, *Quarks, gluons and lattices*, Cambridge Monographs on Mathematical Physics (Cambridge Univ. Press, Cambridge, UK, June 1985).

[282] F. Gliozzia and P. Provero, Nucl. Phys. B **556**, 76 (1999).

[283] F. Gliozzi and P. Provero, Nucl. Phys. B - Proceedings Supplements **83-84**, Proceedings of the XVIIth International Symposium on Lattice Field Theory, 461 (2000).

[284] S. A. Cannas and F. A. Tamarit, Phys. Rev. B **54**, R12661 (1996).

[285] R. Shankar and G. Murthy, Phys. Rev. B **72**, 224414 (2005).

[286] J. Zhang, J. Unmuth-Yockey, J. Zeiher, A. Bazavov, S.-W. Tsai, and Y. Meurice, Phys. Rev. Lett. **121**, 223201 (2018).

[287] Z. Wang, J. Wu, W. Yang, A. K. Bera, D. Kamenskyi, A. T. M. N. Islam, S. Xu, J. M. Law, B. Lake, C. Wu, and A. Loidl, Nature **554**, 219 (2018).

[288] W. Yang, J. Wu, S. Xu, Z. Wang, and C. Wu, Phys. Rev. B **100**, 184406 (2019).

[289] L. Tagliacozzo, T. R. de Oliveira, S. Iblisdir, and J. I. Latorre, Phys. Rev. B **78**, 024410 (2008).

[290] G. H. Wannier, Phys. Rev. **117**, 432 (1960).

[291] W. De Roeck and V. Verreet, arXiv e-prints, arXiv:1911.01998 (2019).

[292] J. R. Schrieffer and P. A. Wolff, Phys. Rev. **149**, 491 (1966).

[293] B. Mühlschlegel, Z. Phys. A **208**, 94 (1968).

[294] J. J. Sakurai, *Modern quantum mechanics; rev. ed.* (Addison-Wesley, Reading, MA, 1994).

[295] R. Rajaraman, *Solitons and Instantons: An Introduction to Solitons and Instantons in Quantum Field Theory* (North-Holland, Amsterdam, 1982).

[296] H. Kim and D. A. Huse, Phys. Rev. Lett. **111**, 127205 (2013).

[297] M. C. Bañuls, J. I. Cirac, and M. B. Hastings, Phys. Rev. Lett. **106**, 050405 (2011).

[298] A. J. A. James, R. M. Konik, and N. J. Robinson, Phys. Rev. Lett. **122**, 130603 (2019).

[299] N. J. Robinson, A. J. A. James, and R. M. Konik, Phys. Rev. B **99**, 195108 (2019).

[300] B. Neyenhuis, J. Zhang, P. W. Hess, J. Smith, A. C. Lee, P. Richerme, Z.-X. Gong, A. V. Gorshkov, and C. Monroe, Science Advances **3**, `10.1126/sciadv.1700672` (2017).

[301] L. D'Alessio, Y. Kafri, A. Polkovnikov, and M. Rigol, Adv. Phys. **65**, 239 (2016).

[302] F. Sauter, Z. Phys. **69**, 742 (1931).

[303] D. Bulmash and M. Barkeshli, arXiv e-prints, arXiv:1806.01855 (2018).

[304] G. De Tomasi, D. Hetterich, P. Sala, and F. Pollmann, Phys. Rev. B **100**, 214313 (2019).

[305] T. Rakovszky, P. Sala, R. Verresen, M. Knap, and F. Pollmann, Phys. Rev. B **101**, 125126 (2020).

[306] C. J. Turner, A. A. Michailidis, D. A. Abanin, M. Serbyn, Phys. Rev. B **98**, 155134 (2018).

[307] M. Lüscher, Nucl. Phys. B **180**, 317 (1981).

[308] P. W. Anderson, Phys. Rev. **109**, 1492 (1958).

[309] E. Abrahams, P. W. Anderson, D. C. Licciardello, and T. V. Ramakrishnan, Phys. Rev. Lett. **42**, 673 (1979).

Versicherung

Hiermit versichere ich, Roberto Verdel Aranda, dass ich die vorliegende Arbeit ohne unzulässige Hilfe Dritter und ohne Benutzung anderer als der angegebenen Hilfsmittel angefertigt habe; die aus fremden Quellen direkt oder indirekt übernommenen Gedanken sind als solche kenntlich gemacht. Die Arbeit wurde bisher weder im Inland noch im Ausland in gleicher oder ähnlicher Form einer anderen Prüfungsbehörde vorgelegt. Diese Arbeit wurde unter der wissenschaftlichen Betreuung von Dr. Markus Heyl und Prof. Dr. Roderich Moessner am Max-Planck Institut für Physik komplexer Systeme in Dresden angefertigt. Ich erkläre hiermit, dass keine früheren erfolglosen Promotionsverfahren stattgefunden haben. Ich erkenne die Promotionsordnung der Fakultät für Mathematik und Naturwissenschaften der Technische Universität Dresden an.

Unterschrift
Dresden, September 2021